ABSTRACT

Title of dissertation: INVESTIGATION OF AERODYNAMICS OF FLAPPING WINGS FOR MICRO AIR VEHICLE APPLICATIONS

Ria P. Malhan, Doctor of Philosophy, 2013

Dissertation directed by: Dr. Inderjit Chopra
Department of Aerospace Engineering

A coupled CFD-CSD solver was used to simulate the aerodynamics of a flexible flapping wing. The CFD solver is a compressible RANS (Reynolds Averaged Navier Stokes) solver. Multibody dynamics solver 'MBDyn', was used as the structural solver to take into account non linear shell straining, making it possible to analyze low aspect ratio wings with large deformations. Validation of the two codes was carried out independently. The solvers were then coupled using python and validated against prior experiments and analysis on spanwise and chordwise flexible wings.

As realistic MAV wings are extremely flexible and lightweight, under the effect of high inertial and aerodynamic forces, they undergo large non linear deformations over a flap cycle. However, there is a dearth of experimental data on well characterized flapping wings (with known structural and mass properties) at MAV-scale Reynolds numbers. Systematic experiments were carried out on rigid and flexible flapping wings in an open jet wind tunnel and forces

were measured using a test bed. Pure flapping of rigid wings did not generate sufficient propulsive force and may not be a viable configuration. Passive pitching of rigid wing generated both, target vertical and propulsive forces. Dynamic wing twist was then incorporated using flexible wings. A flexible wing was fabricated using a combination of unidirectional carbon fiber strips (chordwise ribs), carbon rod (leading edge spar) and mylar film (membrane). Structural model of the wing (combination of beam and shell elements) was developed and then coupled to the CFD model. CFD-CSD analysis of flexible wing was carried out and good correlation was obtained for all the configurations. This comprehensive experimental data set can also be used to validate other aeroelastic analyses of the future. Further, the analysis was used to gain more insights into flow physics. It was observed that as a result of flexibility, by taking advantage of unsteady flow features, a lighter, simpler mechanism could be used to generate larger forces than a rigid wing. The validated, comprehensive analysis developed in this work may serve as a design tool for deciding configurations and wing kinematics of next generation MAVs.

INVESTIGATION OF AERODYNAMICS OF FLAPPING WINGS FOR MICRO AIR VEHICLE APPLICATIONS

by

Ria P. Malhan

Dissertation submitted to the Faculty of the Graduate School of the
University of Maryland, College Park in partial fulfillment
of the requirements for the degree of
Doctor of Philosophy
2013

Advisory Committee:
Dr. Inderjit Chopra, Chair/Advisor
Dr. James D. Baeder
Dr. J. Gordon Leishman
Dr. Anya R. Jones
Dr. Ramani Duraiswami

To my parents and brother

Acknowledgments

First and foremost I would like to thank my advisor, Dr. Inderjit Chopra. This work would not have been possible without his belief in me, support and encouragement. His dedication, work ethic and discipline have always been a source of inspiration. I am extremely grateful to him for giving me this opportunity. I am very grateful to Dr. James Baeder. His insights and guidance gave a new dimension to my research.

I would also like to thank my other committee members, Dr. J. Gordon Leishman, Dr. Anya R. Jones and Dr. Ramani Duraiswami for evaluating my research and providing constructive inputs. I owe my gratitude to Dr. Masarati for the structural modeling part of my research and all the help he has provided.

I have been lucky to have two wonderful mentors, Dr. Moble Benedict and Dr. Vinod Lakshminarayan. They have both been instrumental in this work and helped me to learn and evolve. Moble has also been my friend and helped me through all the personal and professional ups and downs. I am thankful to Dr. Nagaraj for his insights and encouragement throughout my stay here.

I would also like to thank my close friends, Dr. Arun Jose, Bhaskar Adhikari, Dr. Monica Syal, Dr. Deepa Subramanian, Dr. Asitav Mishra, Dr. Vikram Hrishikeshavan and Kumar Ravichandran for making me feel special and loved.

Finally, I would like to thank my family: my parents and brother. My parents have sacrificed a lot and it is all thanks to them for making me the person I am today. I am immensely proud of my baby brother who has now matured into a fine young man and been my strength throughout. It was my family's collective dream to see me earn this degree. Their unconditional love has helped me overcome all the tough times. Words cannot express the love, gratitude and respect I have for them.

Thank you God for giving me an amazing family, friends and professors and helping me achieve this milestone in my life.

Table of Contents

List of Tables

List of Figures

Nomenclature

a	Speed of sound, m/s
AR	Aspect Ratio
b	Width of plate, m
c	Airfoil chord, m
C_p	Pressure coefficient, $\frac{p-p_\infty}{\frac{1}{2}\rho V_\infty^2}$
C_x	Sectional propulsive force coefficient
C_z	Sectional vertical force coefficient
C_X	Propulsive force coefficient, $\frac{F_X}{\frac{1}{2}\rho U_\infty^2 cS}$
C_Z	Vertical force coefficient, $\frac{F_Z}{\frac{1}{2}\rho U_\infty^2 cS}$
E	Young's Modulus, Pa
F_X	Propulsive force
F_Z	Vertical force
f	Flapping frequency, Hz
h	Plunge displacement (non dim. by chord)
h_o	Plunge amplitude (non dim. by chord)
k	Reduced frequency, $\omega c/2V_\infty$
l	Length of plate, m
M_∞	Free stream Mach number, V_∞/a
P	Pressure
Re	Reynolds number

t	Time, secs
t_h	Thickness of plate, m
S	Wing span, m
V_∞	Free stream velocity, m/s
V_{tip}	Tip speed, m/s
α	Angle of attack
γ_o	Flapping amplitude, deg
γ	Flapping angle, deg
ϕ	Phase difference between pitch and plunge, deg
θ	Pitch angle, deg
θ_o	Fixed pitch angle, deg
θ_a	Pitch amplitude, deg
ω	Rotational speed, rad/sec

List of Abbreviations

CFD	Computational Fluid Dynamics
FSI	Fluid-Structure Interaction
IVP	Initial Value Problem
MAV	Micro-Aerial Vehicles
MLS	Moving Least Squares
MSD	Multibody System Dynamics
NS	Navier-Stokes

PDMS Polydimethylsiloxane

RBF Radial Basis Functions

URANS Unsteady Reynolds-Averaged Navier-Stokes

VL Vortex Lattice

Chapter 1

Introduction

The growing interest in unmanned aircrafts, especially for surveillance and reconnaissance missions in confined areas, has spurred research activities in the area of Micro Air Vehicles (MAVs). In 1997, the Defense Advanced Research Projects Agency (DARPA) initiated a program to develop MAVs for various missions. DARPA defined an MAV in terms of size, gross weight and payload - requiring that the maximum dimension in any direction be less than 15 cm, gross weight of less than 100 grams, with up to 20 grams devoted to payload, and the MAV should be able to reach altitudes of up to 100 m [1]. MAVs can be considered as aerial robots or 6 degree of freedom machines which are required to carry out a variety of missions. Potential applications for MAVs, both military and civilian, are numerous. A few applications are: search and rescue, biochemical sensing, power line inspection, targeting, fire rescue, communications and traffic monitoring (Figure 1.1). MAVs can also be used in police missions to track criminals on the run and keep an eye on crowded events. Depending on the mission, payloads may consist of video cameras, chemical sensors and communication devices. Some missions may require MAVs to operate in dull, dangerous and dirty environments like inside caves and tunnels, as shown in Figure 1.2.

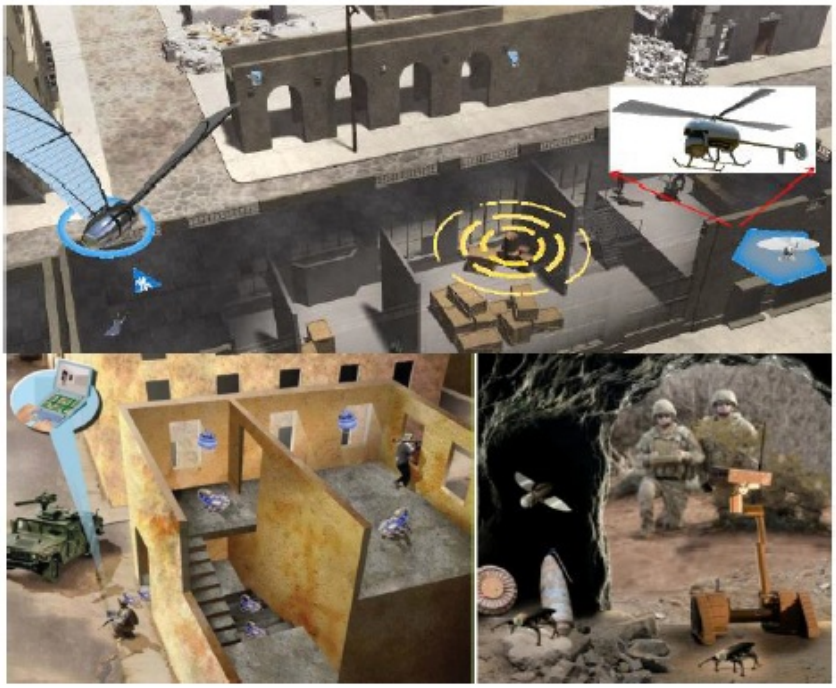

Figure 1.1: **MAV scenarios**

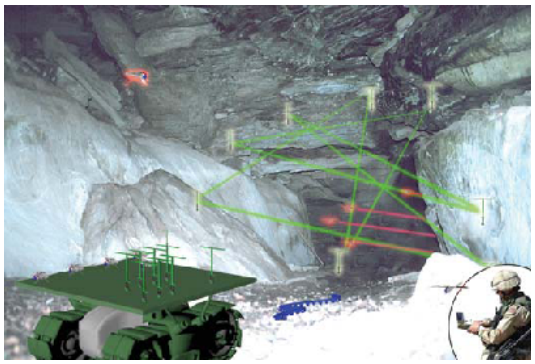

Figure 1.2: **MAV operation in caves and tunnels**

In order to successfully carry out these missions, we need MAVs that are compact, maneuverable, can operate in constrained environments, efficient (with good hover and loiter endurance), have low noise signature and low detectability, and superior tolerance to wind gusts. Rapid advances in micro-electronics and manufacturing techniques of miniaturized components in the

past decade have fueled the development of MAVs. For example, muscle wire and magnet-coil actuators are being used, which are lighter and smaller than traditional servo actuators; and cameras and chemical sensors have decreased dramatically in size and weight due to advances in electronics. Lithium batteries have replaced Nickel-Metal Hydride batteries. These Lithium batteries have energy and power densities that far exceed Nickel-Metal Hydride batteries and can be made very small. As a result of all these advances, different types of MAVs are being built and tested. MAVs can be classified into three main categories: Fixed wing, Rotary Wing and Bio-inspired MAVS. Some of the current MAVs are described next.

1.1 Fixed Wing MAVs

Fixed wing MAVs are relatively less complex, efficient (longer endurance), have good stability characteristics and can be more easily controlled than other MAVs. AeroVironment developed the widely successful Black Widow (Figure 1.3), a 6-in span, fixed-wing MAV using multidisciplinary design optimization for determining the different components that would result in the best configuration [2]. It weighs around 80 grams and has an endurance of 30 minutes. The platform was then designed to deliver live images in real-time via a custom-made color camera and transmitter. Research from the Black Widow developed into AeroVironment's WASP MAV. In August of 2002, the WASP set a record for MAV endurance with flight duration of 1 hour 47 minutes [3].

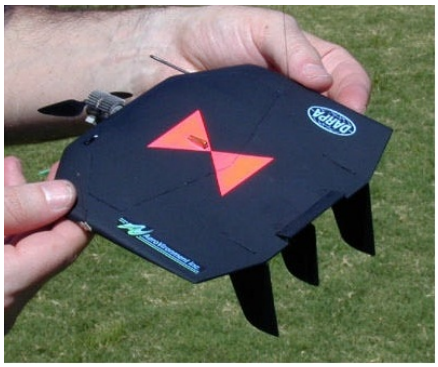

(a) **Black Widow** [2]

(b) **Wasp** [3]

Figure 1.3: **Fixed wing MAVs (AeroVironment)**

National Aerospace Laboratories, India recently built the Black Kite MAV (Figure 1.4) with a wingspan of 30 cm, endurance of 30 minutes and range of 2 km. It can carry a daytime camera and uses piezoelectric vibrating surface for flow control [4].

The University of Arizona has developed several $6 - 12$ inch span fixed-wing MAVs. Four MAV wind-tunnel models were built with $3, 6, 9$, and 12% camber, and tested in a Low Speed Wind Tunnel. The 3% camber wing gives the best lift-to-drag ratio of the four cambers and was considered to be the optimal choice for high-speed, efficient flight. It was observed that the 6 and 9% camber wings gave the best low-speed performance because of their high lift-to-drag ratios and mild pitching moments near their stall angles of attack [5, 6].

The University of Florida developed several flexible-wing design MAVs with wing spans ranging from 5 inches to 18 inches. Two versions of a flexible wing, a batten reinforced version and a perimeter reinforced version, were

Figure 1.4: **Black Kite (National Aerospace Laboratories, India)** [4]

compared to a nominally rigid version in the wind tunnel using a combination of loads testing, 3-D visual image correlation for deformation measurements and flow visualization. Increases in maximum coefficient of lift, as well as improvements in pitch stability were demonstrated for the perimeter reinforced version, whereas gust alleviation was demonstrated for the batten reinforced wing [7].

Active areas of research in fixed wing MAVs are on implementing various forms of biologically-inspired morphing techniques to optimize performance, employing lightweight and flexible membrane wings [8-15], and determining stability characteristics of fixed wing designs and propeller designs [16]. Despite this abundance of research, both experimentally and computationally [17, 18], fixed-wing MAVs lack the ability to hover or fly at low speeds and therefore, are not applicable for operations in constrained areas.

1.2 Rotary Wing MAVs

The main advantage of rotary wing MAVs is their ability to hover. A lot of work has been done at the University of Maryland on rotary wing MAVs. The first configuration was a single rotor with active turning vanes in the slipstream to counteract the rotor torque. It had a 2-bladed, teetering hinge rotor with a diameter of 25 cm. The vehicle had a total weight of 240 g and flew successfully in hover [19, 20].

The second configuration was a micro coaxial rotor system (MICOR) having two counter-rotating rotors of 9-in diameter, weighing 145 g, a payload capacity of 20 g, and an endurance of 10 minutes. The two counter-rotating rotors negate the need for a tail rotor, which allows the design to be more compact. Significant effort was put into the rotor blade design of MICOR, resulting in a figure of merit increase from 0.42 to 0.64 through parametrically investigating the effects of airfoil camber, leading edge shape, and blade planform shape [21]. Although it has a highly improved rotor design, its 10 minute hover endurance is relatively low.

A fully functional shrouded rotory wing vehicle was also designed at University of Maryland that weighed about 280 g (244 mm rotor diameter). The shrouded rotor had a 30% increase in power loading in hover compared to an unshrouded rotor. Due to the stiff, lightweight shroud construction, a net payload benefit of $20 - 30$ g was achieved [22].

Various commercial RC helicopters have also been successfully built but

Figure 1.5: **Tishrov (University of Maryland)** [22]

have limited endurance. For example, Air Hogs Havoc Heli [23] weighs 10 grams with 130 mm main rotor span. The helicopter is controlled by an infrared controller, with two channels (one for the main rotor and one for the tail rotor) allowing independent user control of throttle (main rotor RPM) and tail rotor RPM. It is designed for indoor flying, but can also be flown outdoors in calm conditions with minimal lighting. It is made of tough EPP (expanded polypropylene) foam and comprises a lithium polymer rechargeable battery and 2 micro motors. The helicopter is recharged by plugging it into the controller. Charging generally takes $10 - 15$ minutes and will give the Havoc Heli a flight duration anywhere between 5 to 7 minutes. Range is limited due to the use of infrared instead of the more common radio frequency remote control. MSRP is between 20 and 40 USD.

Unless carefully designed, rotors can suffer from performance degradation at low Reynolds numbers because their airfoils operate in a more challenging flow environment. Scaling down rotor blades and using low Reynolds number

airfoils results in figures of merit in the range of 0.4 to 0.5, a value far less than the full scale value of about 0.8. Due to dominant viscous effects of low Reynolds number flow regimes at which these rotors operate, these MAVs suffer from low hover endurance. Additionally, they have limited forward flight speeds compared to fixed wing MAVs. From a flight mechanics perspective, there is significant cross coupling in lateral and longitudinal motions and these vehicles are inherently unstable. Therefore stability augmentation of a rotary-wing system can be quite challenging. Additionally, these vehicles are quite sensitive to wind gusts [22, 24].

Another type of rotary-wing MAV that has been the subject of much research recently, is the quad rotor helicopter. Quad rotors offer a wide range of benefits as these vehicles have large operational envelopes, having high agility and thrust to weight ratios as well as superior flight stability [24]. Quad rotors are inherently neutrally stable and the small quad rotors tend to have very fast dynamics that can make them difficult to control. Therefore, many studies focus on accurate dynamics modeling so that better control schemes can be implemented [25, 26].

Researchers at Stanford University [27] developed the Mesicopter (Figure 1.6), a meso-scale quad-rotor electric helicopter that operated at a Reynolds number of approximately 5000. Each of the four rotors of the Mesicopter had a diameter of 1.5 cm, and the total weight was 3 grams. The project's main driving application is the deployment of a huge number of micro vehicles over large areas or planets to gather atmospheric and meteorological data.

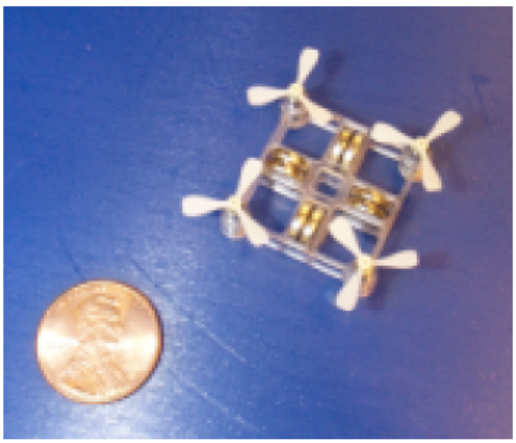

Figure 1.6: **Mesicopter (Stanford University)** [27]

A 50 gram micro quad rotor vehicle was developed at the University of Maryland in collaboration with Daedalus Flight Systems [26] to meet requirements set forth by the Army. The vehicle under investigation was designed to be extremely small and lightweight so that it can be operated in constrained environments and indoors. Specifically, the primary constraint placed on this design was that the platform must fit within a 150 mm by 150 mm (6 in by 6 in) square box, including the rotors (Figure 1.7).

Due to their ease of construction, quadrotor aircraft are frequently used as amateur model aircraft projects. Various commercial quad rotors are available in the market. The Parrot AR.Drone [28] is a radio controlled flying quadrotor helicopter built by the French company Parrot. The drone is designed to be controlled with iOS devices (such as the iPhone, iPad, or iPod Touch) and with Android devices (such as the HTC Hero and the Sony Ericsson Xperia). It is made of plastic and foam and about a foot (30 cm) long. The structure is constructed of carbon-fibre tubes. With a weight of 420 grams

it can maintain flight for about 12 minutes with a speed of 5 m/s.

There are two main disadvantages of quad rotors that could limit their success. In particular, quad rotors mean four motors that are very power consuming [29]. Furthermore, motors are, in general, heavy and difficult to miniaturize. Therefore this configuration may not be suitable when the main target is to maximize flying time.

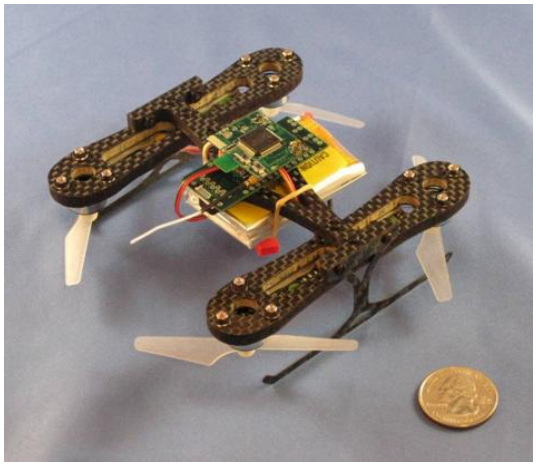

Figure 1.7: **DFS/UMD Micro Quad** [25]

1.3 Motivation for Bio-Inspired Flapping Wing MAVs

Both fixed wings and rotary wings appear to provide well-known technologies, but all the flight envelope specifications of MAVs cannot be achieved using these scaled down concepts. This motivated researchers to investigate alternative typologies.

Figure 1.8 shows mass versus wing span for different natural and man-made flyers [30]. It is interesting to note that there exists a trend line between

all these flyers. With their size and weight constraints, MAVs lie in between large insects and small birds. Figure 1.9 shows gross weight versus Reynolds Numbers for different flyers, and again, MAVs lie in the same Reynolds Number regime as large insects and small birds [24]. The basic idea for bio-inspired MAVs is to adapt from nature and use similar flying technique as insects and birds: flapping wings. At MAV scales, flapping-wing vehicles may offer many advantages and superior flight stability in gusty environments over fixed wing/rotary-wing vehicles such as high maneuverability and efficiency. Also, flapping wing aircraft have the potential to take-off and land vertically and can blend more easily into the environment. Recently, a lot of studies have been carried out in order to investigate the efficiency of such concepts and the possibility to reproduce them in the laboratory. In fact, the principal motivation seems to be the possibility of integrating vertical and propulsive forces together with stability and control mechanisms [31].

With the introduction of a constantly accelerating and decelerating wing, the aerodynamics of such vehicles is highly unsteady in addition to the high viscous effects because of low operating Reynolds numbers. Insects and birds make use of different unsteady lift mechanisms to make their flight possible. These unsteady aerodynamic effects need to be investigated thoroughly in order to understand them and use them to our advantage while building the next generation MAVs.

The first step towards building a flapping wing MAV is to understand the kinematics and aerodynamics of natural flyers. Natural flyers can be di-

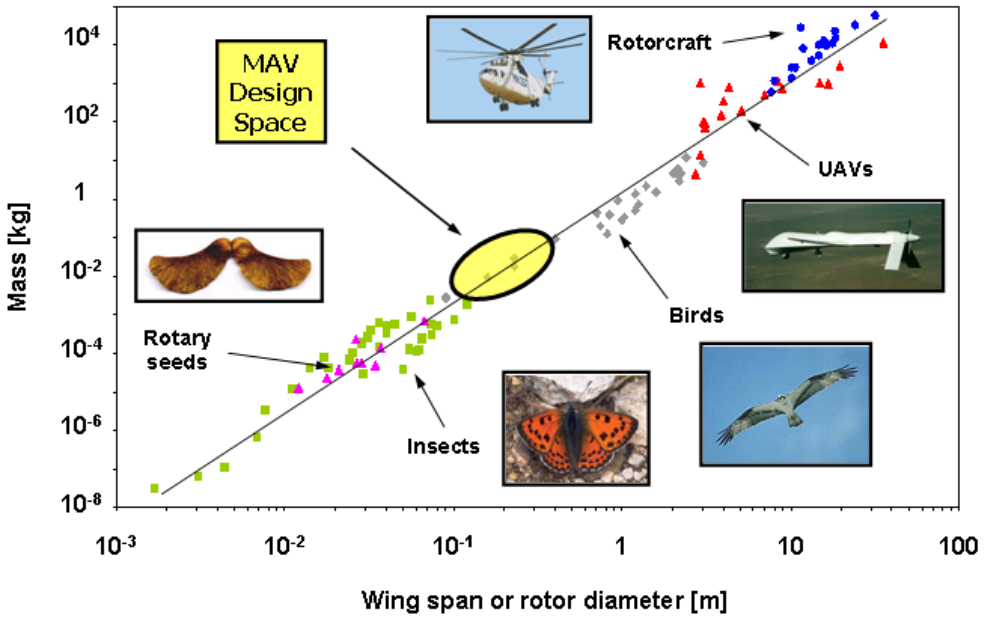

Figure 1.8: **Mass v/s wing span for different flyers [30]**

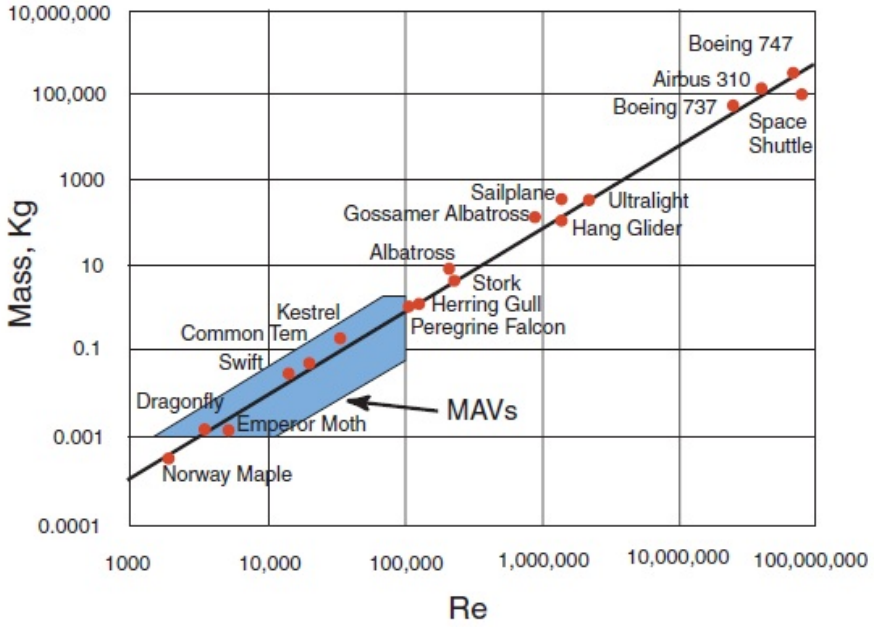

Figure 1.9: **Mass v/s** *Re* **for different flyers [24]**

vided into two main categories, avian and insect. Birdlike vehicles are called ornithopters and insect-like vehicles are called entomopters. These two sub

classes of flapping wings have significantly different features. Ornithopters, like the majority of birds, generate vertical force by flapping wings up and down with synchronized small variations of angle of incidence. This method of propulsive thrust generation requires forward flight similar to fixed-wing MAVs. As a result, ornithopters cannot hover, and they need to obtain an initial airspeed before taking off. Entomopters use the kinematics of insects for flying, meaning a large and rapid change of angle of incidence. Due to this large angle variation between the upstroke and downstroke, this technique is sometimes also referred to as pitch reversal. Compared to how birds fly, they are able to generate much more vertical force and, thus, are able to execute VTOL and hovering [29]. Some further details of insect and avian flight are mentioned next.

1.3.1 Insect Flight

Insect flight is characterized by high speed movement, in terms of both normalized flight speed and wing beat frequency, at low Reynolds numbers. The insect wing beat is powered by two different sets of muscles in the thorax: direct and indirect [32]. Direct muscles are attached directly to the wing, whereas indirect muscles lie within the thorax without any 'direct' link to the wings and manipulate the thorax shape instead. Larger insects (e.g. locusts, moths and dragonflies) with lower wing beat frequencies use both indirect and direct muscles for flight, while smaller insects (with higher wing beat

frequencies) predominantly use indirect muscles for flapping their wings. The general principle within the thorax for both types of muscles is for sets to be arranged in an antagonistic manner, i.e. muscles alternately contract and relax to produce the elevation or depression of the wing. Wing rotation about its longitudinal axis is induced at the wing hinge. The thorax constitutes a highly efficient mechanically resonant system acting as an energy storage device during contraction and relaxation cycles. In addition to these power muscles, insects also have steering muscles that control the wing orientation and rotation. All these muscles combine to give insects the ability to flap their wings through complex trajectories at high frequencies.

Each wing beat can be broken down into a downstroke and upstroke with translation movements and rotational stages interconnecting them. The flapping motion is more than just a simple repeating down and up stroke and is commonly described using several kinematic parameters like stroke amplitude, wing beat frequency, wing angle of attack, stroke plane angle, downstroke/upstroke ratio, wing tip trajectory, timing for wing rotation. Values for these parameters vary in insects, depending upon the flight speed and maneuvering actions (e.g. forward, pitch, yaw, roll and hovering). The kinematic parameters may vary asymmetrically across a pair of wings depending on the maneuvers. The most common wing tip trajectory is a curved ellipse or figure-of-eight as shown in Figure 1.10. In addition to the controlled wing kinematics, the wings themselves passively flex and twist in order to maximize the lift to drag ratio. Typical wing kinematic parameter values for insects are listed in

Table 1.1. The complexity in insect wing flapping mechanisms and the control of stable flight make the task of replicating it extremely challenging in MAV design [32].

Table 1.1: **Typical wing kinematic parameters for large hovering insects** [32]

Kinematic Parameter	**Typical Value**
Angle of Attack, α	30°
Stroke Amplitude, Φ	120°
Wing Beat Frequency, n	$20 - 40$ Hz for large insects
Stroke Timing, d/u	$1 - 1.1$
Stroke Plane Angle, β	$10^\circ \rightarrow 50^\circ$ (flt. speed: $0 \rightarrow$ max)
Body Angle, χ	$50^\circ \rightarrow 10^\circ$ (flt. speed: $0 \rightarrow$ max)

Now, consider the aerodynamics of insects. Quasi steady analysis cannot explain the forces produced by insect wings. The enhanced aerodynamic performance of insects results from unsteady lift mechanisms such as delayed stall, rotational circulation, and wake capture [34, 35], shown schematically in Figure 1.11. Delayed stall functions during the translation portions of the stroke, when the wings sweep through the air with a large angle of attack, causing a leading edge vortex to form. In contrast, rotational circulation and wake capture generate aerodynamic forces during stroke reversals, when the

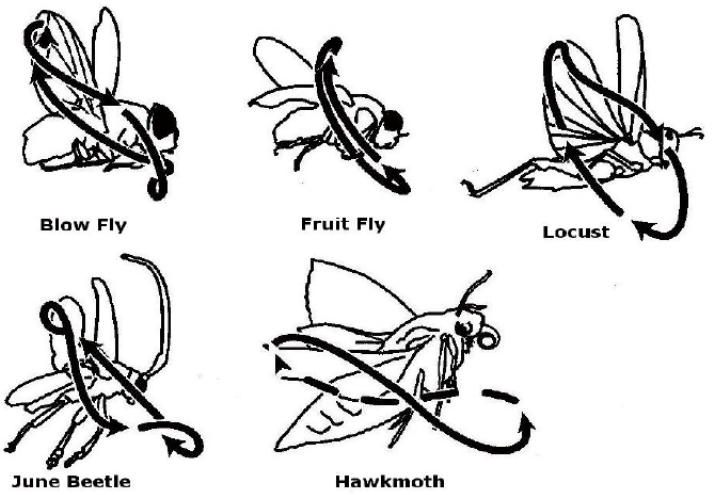

Figure 1.10: **Insect wing tip trajectories [33]**

wings rapidly rotate and change direction. Rotational circulation occurs at the end of each upstroke and downstroke when the wing flips to change direction. This rotation provides additional circulation, which augments the lift. Wake capture also happens during the wing rotation. At the beginning of each stroke, the wing passes through the wake of the previous stroke such that the increased airflow adds additional lift. In addition to contributing to the lift required to keep an insect aloft, these two rotational mechanisms provide a means by which the insect can modulate the direction and magnitude of forces during steering maneuvers.

Insects that do not rotate their wings at the end of each upstroke and downstroke utilize the clap-fling mechanism where two identical wings begin their motions in a clapped position [36]. The two wings then split apart by rotating about their trailing edges. This phase of the wings' motion is called the fling phase. A transient circulation is formed around each wing in the fling

phase. Immediately after the fling phase the two wings separate, each carrying a bound vortex with it. This is the separation phase of the motion cycle. The wing produces lift directed upward and normal to the horizontal direction of the wing's motion during this phase.

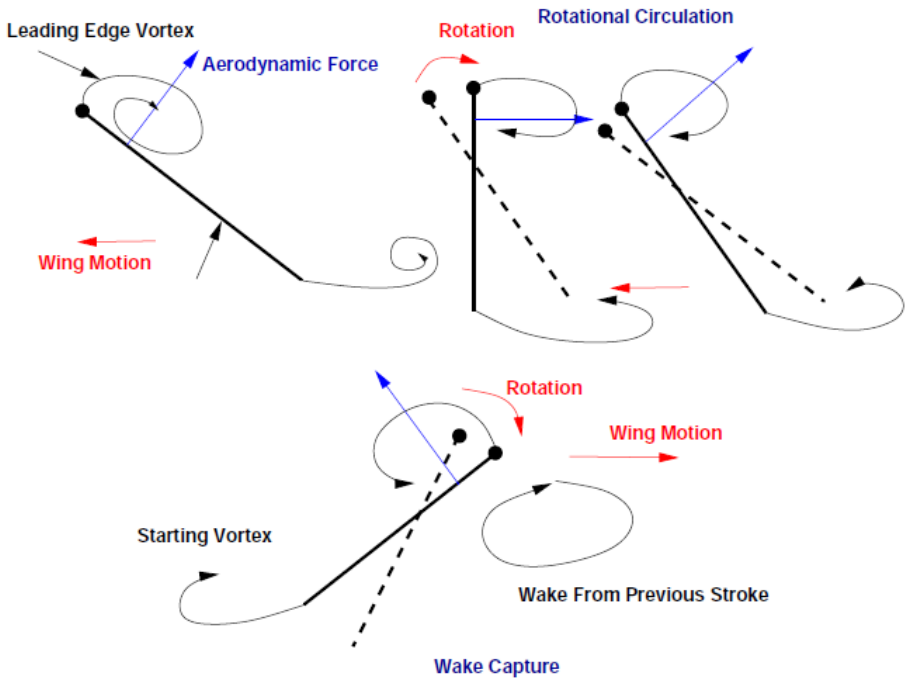

Figure 1.11: **Unsteady lift mechanisms in insects** [34]

1.3.2 Avian Flight

The second type of kinematics in natural flyers is the avian or bird kinematics. In addition to flapping wings up and down (mostly in a vertical plane), birds sweep wings forward and back, twist along the span and fold them to adjust the wetted area [37]. Compared to human arm, bird skeleton has a shortened humerus bone in proportion to the radius and ulna, and the wrist and fingers (called hand wing) are fused to support the weight of the primary

feathers and provide strength to the wing tip [38] as shown in Figure 1.12. Every bird species has different proportions in the arm and hand bones which are optimized for its dominant flight mode. Figure 1.13 shows scaled wing skeletons of some birds. The hand wing shown between the two vertical lines provides the dynamic control for the bird and can comprise upto 80% of the wing length for small birds (like hummingbirds), which fly in highly unsteady conditions such as hover. Arm bones in larger birds (like hawks) compose 40% to 60% of the total wing length because they fly at higher Reynolds numbers in quasi steady flows and use prolonged gliding. Slow flapping or gliding flight modes benefit from a larger region of secondary and tertiary feathers that can act like a fixed wing. The longer arm wing also allows for more bending and spanning to reduce drag on the upstroke and vary the wing area [38].

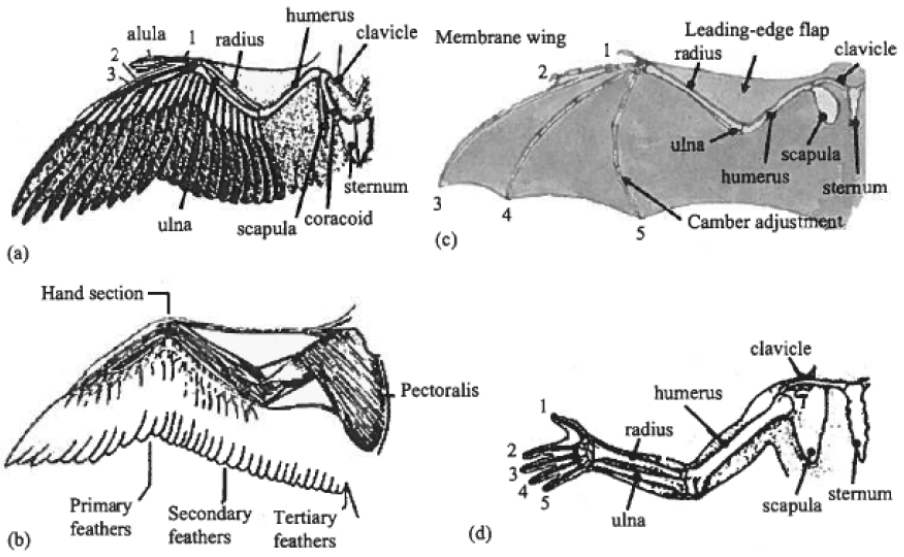

Figure 1.12: **Schematics for (a), (b) a bird wing, (c) bat wing, (d) human arm [38]**

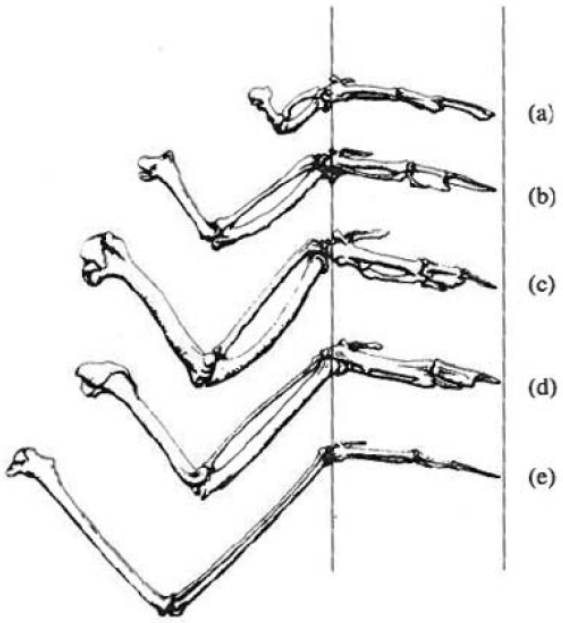

Figure 1.13: **Proportion of hand wing to arm wing, for (a) Calliope hummingbird; (b) Rock dove; (c) Blue grouse; (d) Starling; (e) Albatross [40]**

A bird has approximately 75 different muscles to control the movements of its different body parts [39]. Collectively, the muscles are concentrated near the bird's center of gravity. Birds power their flight primarily by pectoralis muscle, which is the largest muscle and constitutes $8 - 11\%$ body mass (Figure 1.14). These muscles provide the power for the downstroke of the wing and thus, bear most of the burden of supporting a bird in flight. The supracoracoideus, a smaller muscle (about one-fifth the size of the pectoralis), is the primary wing elevator during upstroke. Besides these two major muscles, there are numerous other smaller muscles, which assist in modulating wing orientation and controlling wing shape.

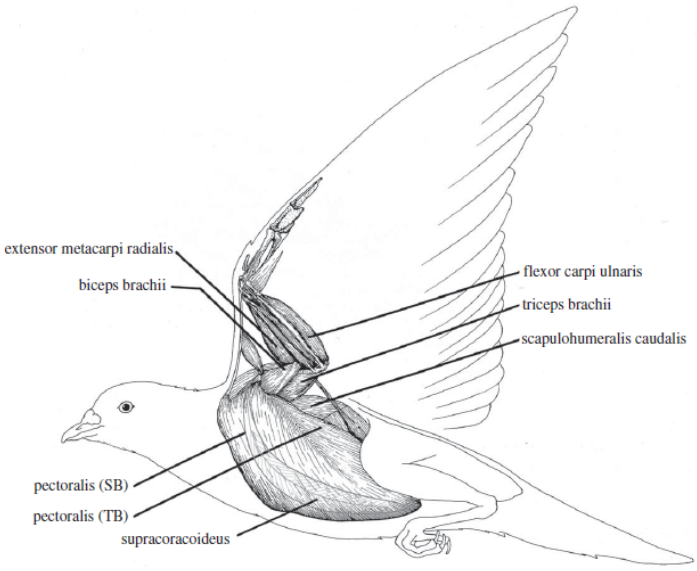

Figure 1.14: **Anatomical organization of avian wing musculature showing key muscles [39]**

The flapping motion is of primary importance because it generates the vertical and propulsive forces that enable flight. Near the wing tips where the vertical induced flow from flapping motion is large, the leading edge of the wing must pitch into the flapping direction to maintain attached flow [41]. Therefore the pitching motion is also critical to achieve flight. The forces generated by a positively cambered flapping wing during upstroke and downstroke are shown in Figure 1.15. Maintaining positive angle of attack during upstroke requires significant upward twist because the downward inflow angle due to the flapping motion increases with increasing span position. If a positive angle of attack is achieved, the lifting force will be upwards and backward, increasing the drag on the wing. However, if the angle of attack on upstroke is negative, the lift vector will be negative and forward, creating thrust but also causing negative

lift. During downstroke, the wing is always at a positive angle of attack with significant upward inflow near the wing tip. The relative inflow tilts the lift vector forward so that it produces thrust, especially near the wing tip. This reasoning shows how the motion of the wing tip is instrumental in increasing thrust and decreasing drag, while the interior of the wing primarily produces lift [41].

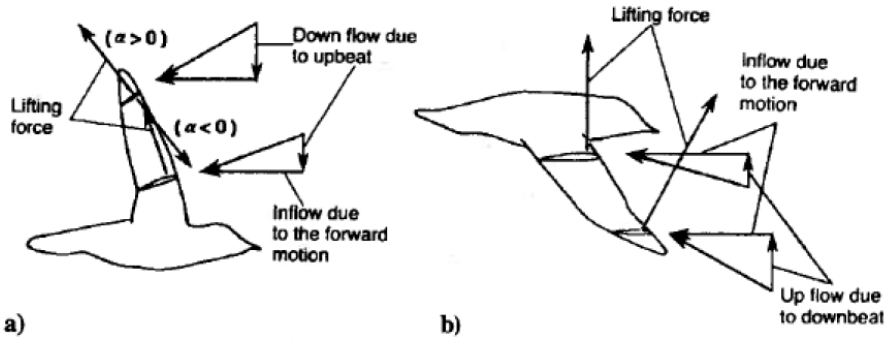

Figure 1.15: **Forces generated by a flapping wing during a) upstroke and b) downstroke [41]**

Each bird uses a different type of wing motion to fly, and they are generally categorized by the path of the wing tip during one beating cycle [40], as shown in Figure 1.16. Wing tip paths also vary based on flight modes including taking off and landing or flight speeds. Two common tip path shapes are ovals and figure eights. The line connecting the top and bottom of the tip path is called the stroke plane; it varies from vertical for forward flight to horizontal for hovering.

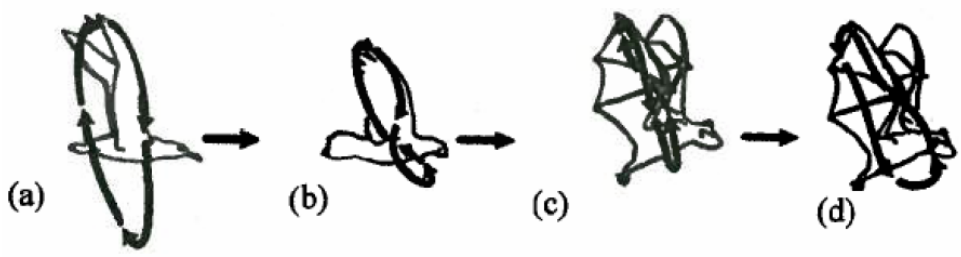

Figure 1.16: **Tip paths for (a) albatross, fast gate; (b) pigeon, slow gate; (c) horseshoe bat, fast gate; (d) horseshoe bat, slow gate** [40]

1.4 Bio-Inspired Flapping Wing MAVs

As mentioned earlier, for the small scale of MAVs, flapping wing vehicles may be the preferred approach because of their abundance in nature, and their ability to harness low Reynolds number unsteady vortex lift effects and gust tolerance capabilities. They can blend more naturally into the outdoor environment, providing camouflage and there is a wealth of biological inspiration to draw upon. This section highlights some of the current flapping-wing MAVs.

1.4.1 Insect-Based MAVs

Insect-based MAVs offer the advantage of having the potential to hover; however, because they operate at low Reynolds numbers where viscous effects dominate, they require high flapping frequencies and consume large amounts of power. Their small size also restricts their payload capacity. Additionally, the highly evolved motions involved with insect flight renders mechanical replica-

tion difficult and costly in terms of weight. Insects quickly rotate and reverse direction between the upstrokes and downstrokes and produce lift based on unsteady mechanisms described earlier (in Section 1.3.1). Despite the complexities associated with insect flight, MAVs have been developed based on both the clap-fling and rotational lift mechanisms.

Figure 1.17: **Mentor (University of Toronto) [42]**

A hovering MAV called MENTOR [42] was developed at the University of Toronto's Institute for Aerospace Studies, based on clap-fling mechanism with biplane wings as shown in Figure 1.17. It had a 30 cm wingspan and weighed 580 g. MENTOR could fly for 10 min, but because of the clapping of its wings, had a large noise signature. It was the first flapping-wing aircraft to hover under its own power. It used a single four-bar based mechanisms for flapping all the four wings and a set of four vanes for directional control.

UC Berkeley is developing the Micromechanical Flying Insect (MFI) [43]. It employs insect-based phasing between wing flapping and rotational motions in order to achieve flight control. The goal of the MFI project is the fabrication of an electromechanical device capable of autonomous flight and complex behaviors, mimicking a blowy Calliphora insect, which has a mass of 100 mg, wing length of 11 mm, wing beat frequency of 150 Hz and actuator power of 10 mW.

Tarascio et al. [30] conceptualized a hybrid, insect-based MAV called the Thrust Augmented Entomopter (TAE). The configuration utilized flapping wings to hover, and a pusher propeller for thrust in forward flight. The wings would be configured for minimum power requirements in hover, and would not flap during forward flight. The concept had an estimated weight of 160 g, and a wingspan of 218 mm.

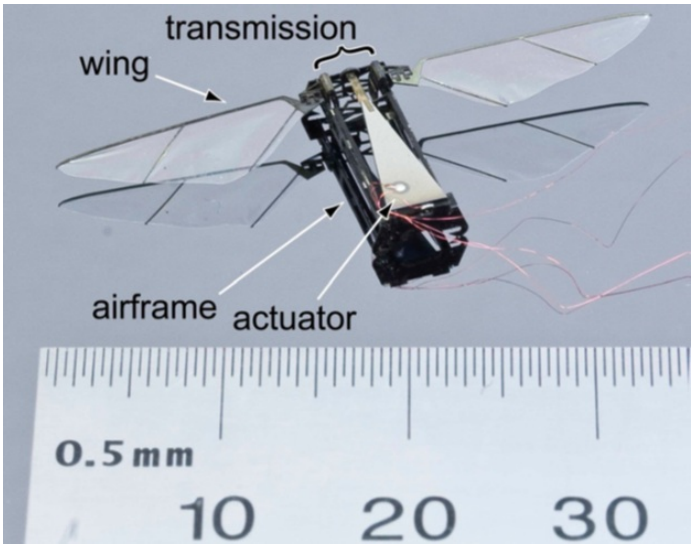

Figure 1.18: **Microrobot (Harvard University) [44]**

Wood at the Harvard Microrobotics Lab of Harvard University [44], has recently designed a biologically inspired microrobot and demonstrated controlled vertical flight in hover. The vehicle weighs 56 mg and the wings are flapped in an insect like manner by the action of a single piezoelectric actuator (Figure 1.18). A piezoelectric actuator is used because at this scale, it is not feasible to have an electric motor powering the wings through a system of gears. Due to the fact that these materials are typically brittle and have high operation frequencies and stresses, it uses a miniature transmission manufactured from carbon fiber flexures. They have demonstrated uncontrolled free flight in hover only with altitude control. When the robot flapped its wings, the flapping induced inertial and aerodynamic forces that caused the wings to passively rotate. In turn, the passive rotation created a non-zero angle of attack during the wing stroke, which produced vertical force. In general, the faster the wings flapped (i.e., the higher the frequency and/or the amplitude of their stroke angle), the greater the vertical force. Further, when the researchers caused a disturbance by blowing air from a hose at the microrobot, the microrobot was able to withstand the disturbance. In addition, the 56 mg microrobot is capable of generating vertical forces of up to 3.6 times its own weight, meaning it could carry a payload including steering components, sensors, and power sources.

Perhaps the most notable flapping wing MAV built to date is the Nano Hummingbird [47], a small hovering ornithopter, which was developed as a part of the Defense Advanced Research Projects Agency (DARPA) Nano Air

Vehicle (NAV) program. It had a mass of 19 g, a wingspan of 16.5 cm, and the ability to hover for several minutes, fly forward up to 6.7 m/s, and transmit live color video to a remote ground station. Additionally, the vehicle demonstrated the ability to perform controlled hovering flight for the first time. It has a highly advanced design with superior flight stability, but requires sophisticated on-board stabilization. The Hummingbird can fly indoors as well as outdoors, but can only handle wind speeds of 5 mph which would be a limitation to outdoor operation on windy or gusty days.

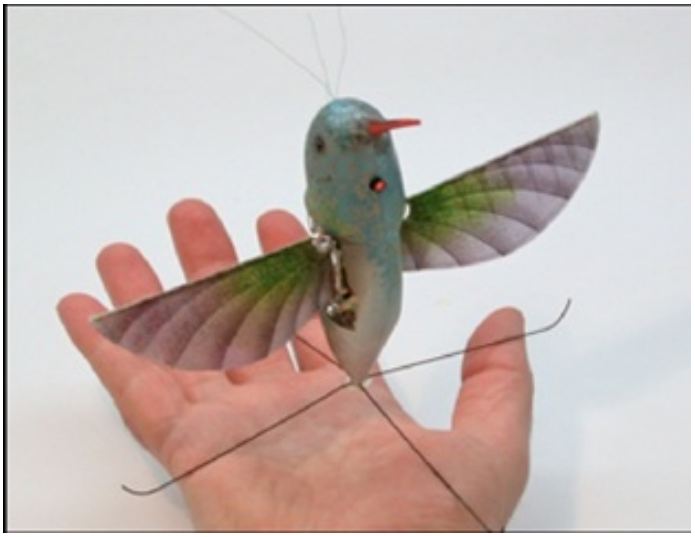

Figure 1.19: **Nano Hummingbird (AeroVironment)** [**47**]

1.4.2 Avian Based MAVs

The advantage of employing avian-based flight is that the aerodynamics can be simplified by using simple up-down flapping motion with flexible membrane wing skins. The use of a flexible membrane allows the wing to passively change its relative angle of attack and camber during the stroke cycle.

This is the mechanism by which commercially-available ornithopters operate. Although this simplification is adequate for producing vertical and propulsive forces, birds still have an advantage in their ability to adjust their flapping scheme for different flight regimes. A lot of research is being carried out on how to incorporate more aspects of avian flight.

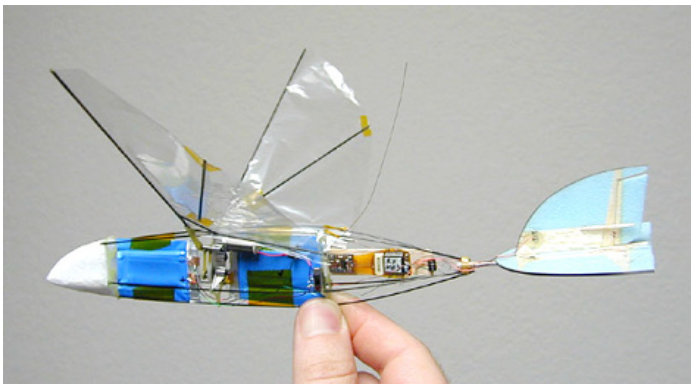

Figure 1.20: **Microbat (AeroVironment) [45]**

A battery powered ornithopter with MEMS wings was developed by AeroVironment called the Microbat [45]. The wings were constructed using titanium-alloy metal as wingframe and parylene C as wing membrane. Several MEMS wings were fabricated with parameters, such as chord and spar widths, membrane thickness, number of spars, and sweep angle, varied. Super capacitor-powered and battery-powered ornithopters were built. The best free flight duration of 9 seconds and 18 seconds were achieved by super capacitor powered (weighing 6.5 grams, 14 cm wing span) and battery-powered ornithopters (weighing 10.6 g, 14 cm wing span), respectively.

Another ornithopter recently developed was the DelFly [46] at Delft University. It had two sets of flapping wings, which allowed it to fly both, fast for-

ward flight missions and very slow, loitering missions. DelFly uses traditional fixed wing control surfaces: it has an elevator and a rudder that are controlled by magnetic actuators. It had a 350 mm wingspan, flapping frequency of 6 Hz, and weight of 17 g and carried a video camera payload, allowing it to recognize targets. It had an endurance of 12 minutes at a cruise speed of 1.8 m/s.

Figure 1.21: **Delfly (Delft University) [46]**

1.5 Technical Challenges

Despite the ongoing work on building flapping wing MAVs, none have been able to achieve controlled flight for more than a few minutes. Development and operation of MAVs in real environment requires overcoming a range of technical barriers. These include issues such as small-scale power generation and storage, navigation and communications, and efficient propulsion and aerodynamics [33]. Additionally, it is quite challenging to replicate wing kinematics and flight control of natural flyers to withstand gust and achieve maneuverability. All these challenges are discussed below. One of the most in-

teresting and least understood aspect of small-scale flight is the aerodynamics. This is discussed towards the end of this section in greater detail.

1.5.1 System Integration

Physical integration of various components at an MAV scale vehicle is much more challenging than in a larger aircraft. Various sensors and modules for flight altitude, flight stability, speed, control and associated signal processing units have to be light weight and consume minimum power and must be integrated into a much smaller volume. On-board processor and communications electronics are critical links between the sensor systems and the ground station, and they are vital to the flight and propulsion control systems. Many of the system functions can be provided by microelectronics or MEMS-based components, which have advanced significantly in past few years.

Separate modules for each function would consume more volume than may be available. The multi-functionality required by the MAV weight and power constraints may be achieved by a highly integrated design, with physical components serving multiple purposes, or accomplishing multiple and often diverse functions. For example, wings may also serve as antennae or as sensor apertures. Power source may be integrated with the fuselage structure, and so on. This kind of design clearly requires a lot of innovation and improvisation. Figure 1.22 highlights the complexity of the problem and shows how miniaturization has slowed down over the past few years [33].

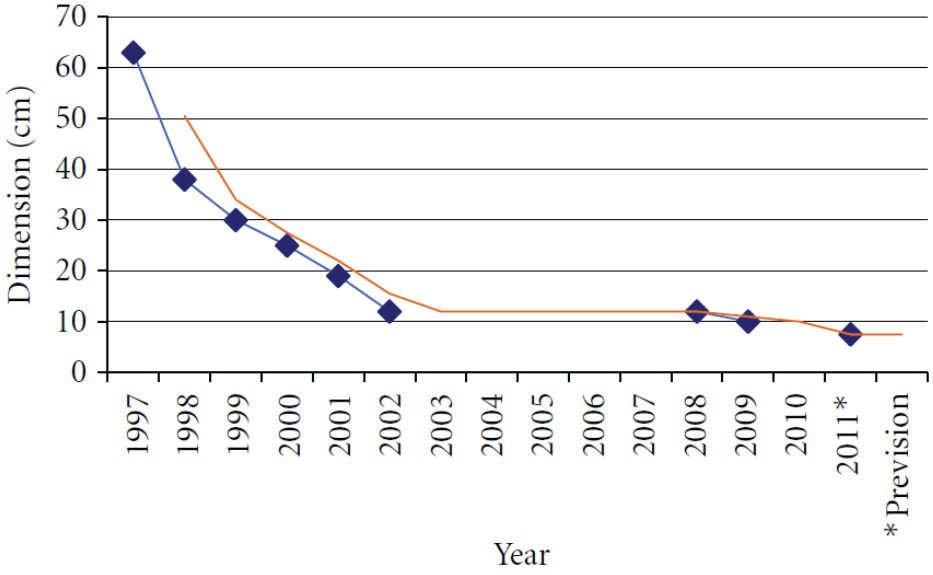

Figure 1.22: **MAV development: dimension reduction [33]**

1.5.2 Propulsive Systems

Electric motors are the most prevalent and easiest way for producing motion in all three types of MAVs (fixed wing, rotary wing and flapping wing). They offer high efficiency, reliability and ease of control. Coreless motors are more suitable since they are lighter and smaller than direct current (DC) iron-core motors. Coreless motors do not have an iron core, hence, there are no iron losses thereby leading to higher efficiency. Furthermore, since the rotor is light, it has small inertia that allows extremely fast acceleration and deceleration. The main disadvantage is that due to lack of iron core in the center, such motors reduce heat dissipation and thus are suitable for small and low power motors. Other options are miniaturized Internal Combustion Engines ICEs (successfully built already) but difficult to integrate and their main drawback

is that they are very noisy, which limits a lot of military applications where stealth is extremely important [48]. Also they become inefficient at lower size. Micro-gas turbines could be another alternative. Despite significant efforts by numerous groups [49, 50, 51], no commercial MEMS gas turbine generators are currently available. Another possibility is to include a hybrid system, such as electric motors and combustion engines [52]. Although this technique has been already used with good results in larger air vehicles, it is not suitable for MAVs that have strict constraints on both weight and size.

1.5.3 Energy Storage

Energy storage is required on board to power the motors, electronic circuits, sensors, actuators, and the communication devices. Batteries are commonly used in the current MAVs. Furthermore, the energy density of the batteries has steadily increased and size has reduced during the past ten years, due to progresses in consumer electronics industry (especially cell phones). Ni-Cd batteries have now almost completely been replaced by more energy dense lithium-based batteries that also are less toxic [53]. Furthermore, the most advanced batteries (intelligent batteries) include circuitry that optimizes the cells' discharge curves with respect to the loads. They make use of various battery-related characteristics such as charge recovery effect, to enhance battery lifetime and ensure safe operation [54]. However, the most advanced batteries still provide much lower energy densities than traditional sources,

such as gasoline or methanol as shown in Figure 1.23.

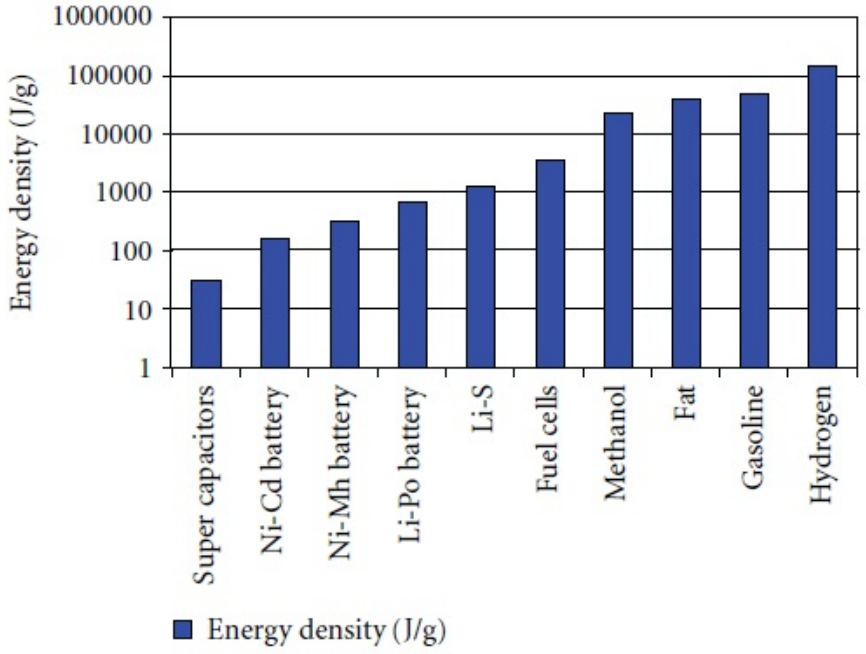

Figure 1.23: **Energy densities of various energy storage systems [33]**

Another area of active research is fuel cells. A fuel cell system is conceptually a type of battery in which the fuel is transformed into electric current trough an electrochemical process. There are several kinds of fuel cells, which mainly differ with respect to the principle of energy conversion. Currently, the most promising fuel cells for MAVs are proton exchange membrane (PEM) fuel cell and direct methanol fuel cell (DMFC). Though a lot of work is required before fuel cells become common place, they are already available in the market [55]. An example of an MAV powered by a fuel cell is "The Hornet", developed in 2003 by DARPA, it uses absolutely no batteries, capacitors, or other sources of energy (except fuel cells). The Hornet has a wingspan of 38

cm and a total weight of the vehicle around 170 g, including fuel cell [33]. Ultracapacitors and solar cells are other potential sources, which are under investigation [56].

1.5.4 Sensors and Actuators

Sensors can roughly be divided into two categories. The first ones contain the sensors that are necessary for flight control, the second ones are sensors that are a part of the payload and provide mission-specific information. Examples are cameras, microphones, gas sensors, biological sensors, radiation sensors, etc. Depending on the applications, most MAVs typically include one or more of these data sensors. Important selection criteria for the choice of sensor are small dimensions, low weight, and low power consumption.

Actuators are needed for different on board applications. They are used for flight control, (e.g. making the vehicle turn), for operating the sensors like movable cameras or for building useful tools, such as micropliers for picking up samples, etc. Linear actuators are the most suitable solution for flapping wing systems. Although a lot of studies are being carried out on new materials and new concepts for linear actuators, all the existing prototypes have limited maximum elongation and/or long response time that limit the applicability [33]. Another possible solution is using microservo actuators that are rotary actuators. They consist of a small electric motor, with some cogwheels that form a microgear. Other micro motor technologies, such as piezoelectric

Table 1.2: **Qualitative summary of linear actuators [32]**

Linear Actuator	**Advantages**	**Disadvantages**
Piezoelectric Ceramic	Excellent performance except strain output. Strain magnitude can be modified using bender arrangement.	Require high activation voltage.
Shape Memory Alloy	Excellent performance except frequency range.	Poor fatigue life.
Magnetostrictor	Excellent performance except strain output.	Require high activation voltage and bulky.
Solenoid	High strain.	Low energy density.
Electroactive polymers	Certain EAPs match muscle for performance.	Only ionic EAPs operate on low voltage. Novel technology, not widely available.

motors or shape alloy motors, are still under development, and they are yet not matured enough for MAV application [57, 58]. Tables 1.2 and 1.3 show a qualitative summary of some linear and rotary actuators.

Table 1.3: **Qualitative summary of rotary actuators [32]**

Rotary Actuator	**Advantages**	**Disadvantages**
Brushed DC motor	Simple operation, no driver electronics required.	Size and mass may be an issue.
Brushless DC motor	Miniature size and mass.	Driver electronics required.
Piezoelectric motor	Miniature size and mass. High torque at all speeds.	Product choice limited. High voltage and driver electronics required.
Micro ICE	High power density and efficiency.	Novel technology, under development.

1.5.5 Low Reynolds Number Aerodynamics

Reynolds number (Re) is a non-dimensionalized parameter that can be seen in Navier-Stokes equations. Navier-Stokes equations are the fluid flow equations and have the following form for an incompressible fluid [59]:

$$\frac{\partial(u)}{\partial(t)} + (u \cdot \bigtriangledown)\, u = \bigtriangledown p + \frac{1}{Re} \bigtriangledown^2 u \tag{1.1}$$

where, $\bigtriangledown$ is the spatial gradient operator normalized by some length scale (L), u is the velocity vector normalized by some velocity scale (U), t is the time normalized by the convective time scale (L/U), p is the pressure (normalized by the dynamic pressure ρU^2), and ρ is the fluid density. The Re is defined as:

$$Re = (\frac{\rho U L}{\mu}) \tag{1.2}$$

where μ is the fluid viscosity. Since the numerator is composed of mass, velocity and size, and the denominator consists of viscosity, Reynolds number can be thought of as the ratio of inertial forces to viscous forces in the flow.

The combination of small scale and low velocities in MAVs results in a flight regime with very low Reynolds numbers. As was seen in Figure 1.9, MAVs lie within the shaded region at the lower left corner of the graph, bounded by Re between $2,000$ and $100,000$. This places MAVs in a completely different regime from conventional aircrafts. The biggest challenge facing MAV designs, therefore, pertains to their aerodynamics.

When Re is small, the flow is laminar and smooth, viscosity is dominant and it distributes and transports momentum throughout the flow. With sufficiently small Re, the Laplacian term on the right hand side governs the fluid dynamics, and the non-linear term on the left hand side will not significantly affect the flow. Laminar flows, with the limit Re approaching zero, can often be solved analytically, and computational solutions can be found with direct simulations of the Navier-Stokes equations. When inertial forces dominate (high Re), non-linear terms on the left will start to influence the dynamics and the the flow becomes turbulent and disorganized because local increases in momentum cause instability. At sufficiently high Re, the non-linear terms dominate, and the fluid is considered fully turbulent. Direct simulation of tur-

bulent flows are computationally expensive and are currently not practical for aircraft design. However, many approximations of the characteristics of turbulent flow have been developed, and these can be implemented in computational algorithms to obtain solutions that are close enough to experimental results. The use of these approximations has led to great advances in the design and performance of large, high-speed aircraft that operate at high Re.

When the chord based Reynolds number of an airfoil (defined as $Re_c = \frac{\rho U_\infty c}{\mu}$) is greater than 10^6, most of the boundary layer on the wing is turbulent, and the laminar and transitional regions have relatively little effect on the forces on the wing. Thus, computations can use approximations and simplified models for the turbulent boundary layer and thereby obtain acceptable results. When $Re_c < 10^3$, due to high viscosity, the flow over typical airfoils will not transition to turbulence, and it can be solved with direct simulation. Thus, $10^3 < Re_c < 10^6$ is a transitional region for airfoils and wings. It is the region where laminar, transitional and turbulent flow all have a significant effect on the forces generated by the wing, and each must be modeled accurately [59]. Since this happens to be the range of Reynolds Number in which MAVs operate, the aerodynamics in this regime needs to be understood properly.

The first detailed study of aerodynamics within this range of Re was conducted by Schmitz during the 1930's [60]. In a wind tunnel, the forces generated by airfoils in the range $2 \times 10^4 < Re < 2 \times 10^5$ were measured for three airfoil shapes: a thin flat plate, a thin cambered plate, and a thick

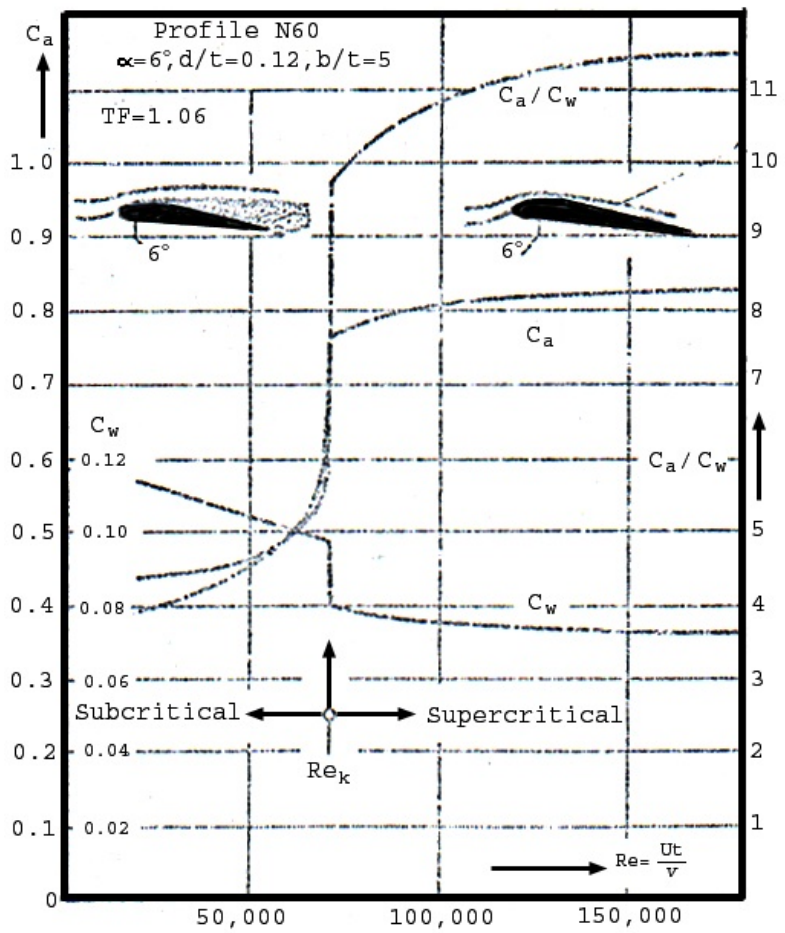

Figure 1.24: **The critical** Re **and the maximum lift and minimum drag coefficient (**c_a **and** c_w**) of the N60 airfoil across its critical** Re [60]

cambered airfoil (the N60). The key observation was that thick cambered airfoils have a critical Re where the performance changes drastically. Figure 1.24 shows c_a (German convention for c_l) and c_w (c_d) for the N60 airfoil across a range of Re. Above the critical Re range, the lift-to-drag ratio is much higher than the values below the critical Re. This critical Re range is similar to the transitional Re range described above for a flat plate boundary layer. When an airfoil is below its critical Re range, the flow is dominated by viscous forces

and remains laminar over the entire airfoil. Above this range, the flow will transition to turbulence somewhere on the airfoil. Schmitz's results were verified and expanded upon by Abbott [61], Riegels [62] and Althaus [63]. For most airfoil sections, the critical Reynolds number is in the range $10^4 - 10^6$. By plotting the lift-to-drag ratios of airfoils across this range of Reynolds number, McMasters generalized these results in 1979 with a wide band as shown in Figure 1.25 [64]. It was also observed that smooth airfoils, in general, have a higher maximum lift-to-drag ratio than rough airfoils at high Re. However, at Re below 10^5, the lift-to-drag ratios of rough airfoils does not drop as sharply as smooth airfoils.

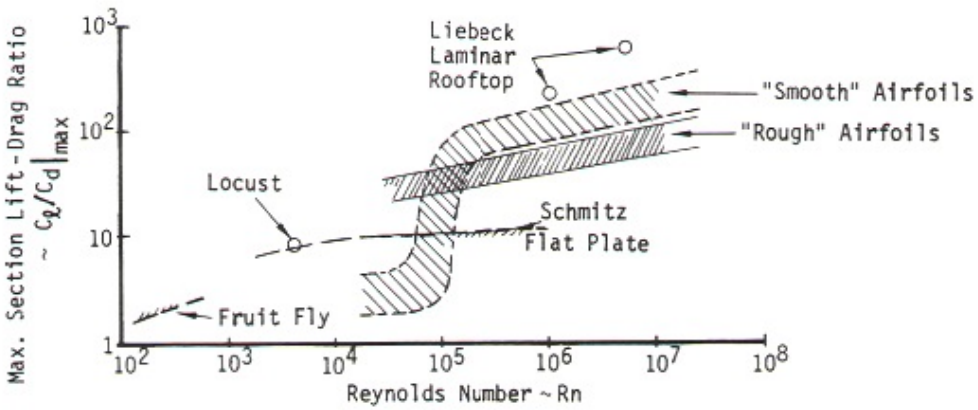

Figure 1.25: **Maximum Lift-to-Drag vs Reynolds number [64]**

Mueller conducted both, visualization and force measurements to understand the cause for this performance decrease at low Re [65]. His studies were focused on measuring the lift and drag forces on the NACA 663-018 airfoil (symmetric, 18% thick) at $4\times10^4 < Re < 4\times10^5$. The lift measurements made at $Re = 4\times10^4$ show a dramatic change at $\alpha = 8°$, as shown in Figure 1.26(a).

At $Re > 10^5$ however, the lift coefficient was found to increase linearly with α (as it does at all larger Re). Using smoke visualization, Mueller showed that the drastic increase in lift coefficient found at $Re = 4 \times 10^4$ and $\alpha = 8\,\text{deg}$ is due to the formation of a Laminar Separation Bubble (LSB) at this angle of attack. An LSB is demonstrated in Figure 1.27. It typically begins with a laminar boundary layer that encounters an adverse pressure gradient, which causes the boundary layer to separate. The laminar separated shear flow is unstable and transitions to a turbulent separated shear flow. The turbulence then transports momentum from the free-stream, across the shear layer, and down towards the surface. When the momentum transport is sufficient, the turbulent boundary layer is considered to be reattached to the surface, thus closing the separation bubble [66].

Using a highly sensitive force balance, Laitone acquired some of the most reliable data on forces generated by low Re wings [67]. Lift and drag were measured on a thin wedge (which approximated a flat plate), a 5% cambered plate, and the NACA 0012 at angles of attack from zero lift to well beyond stall. The range of Re was $2 \times 10^4 - 7 \times 10^4$ and he demonstrated a variety of results that are peculiar to this range of Re. The first result is that at $Re = 2 \times 10^4$, the 5% cambered plate achieves the highest lift-to-drag ratio, while the NACA 0012 had the lowest, even lower than a simple thin wedge. This is shown in Figure 1.28. In addition, it was also observed that the NACA 0012 has a higher lift coefficient when it is placed backwards in the flow, that is, when the trailing edge is used as the leading edge. These results indicate

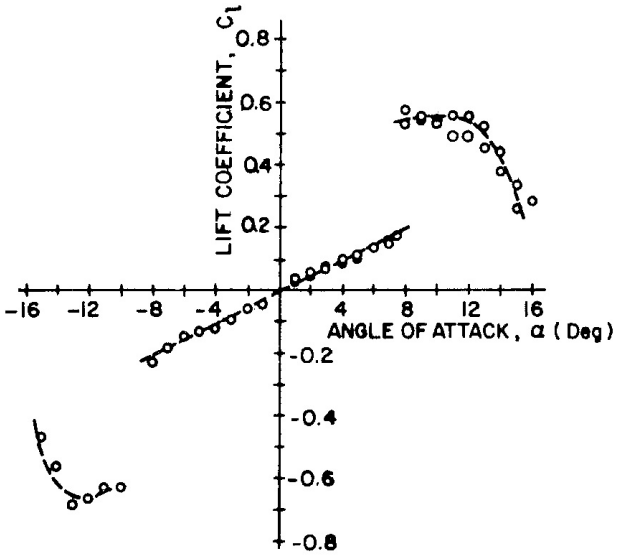

(a) $Re = 4 \times 10^4$

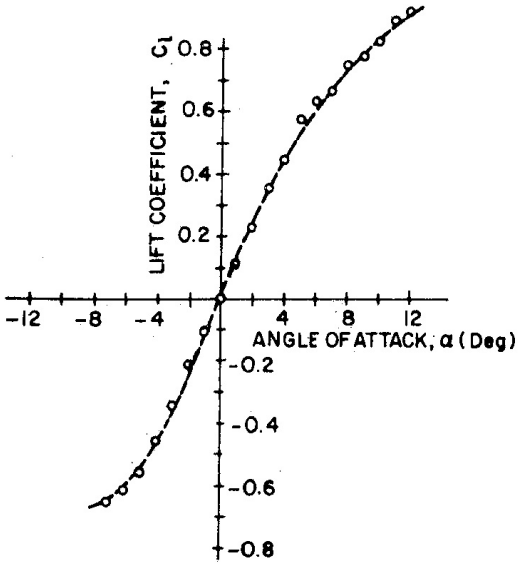

(b) $Re = 4 \times 10^5$

Figure 1.26: **Lift curves for NACA 663-018 airfoil at different** Re**[65]**

that a small leading edge radius is preferred at this range of Re.

The above studies were for 2D airfoils. However, for MAVs, we need to consider low aspect ratio wings operating in low Reynolds numbers.

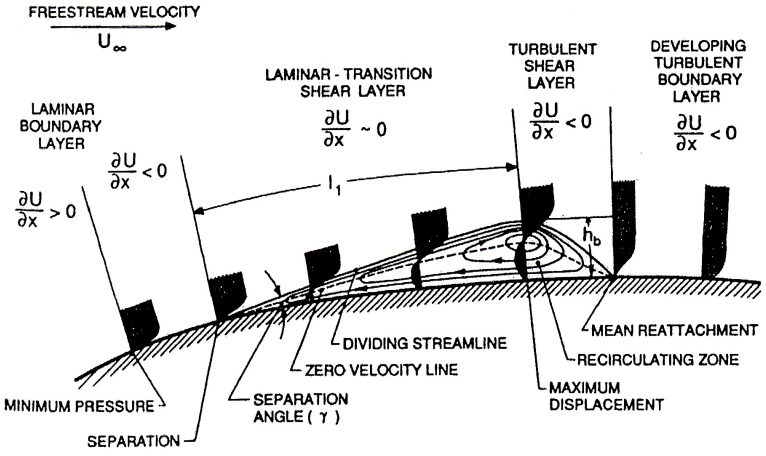

Figure 1.27: **Description of a laminar separation bubble [65]**

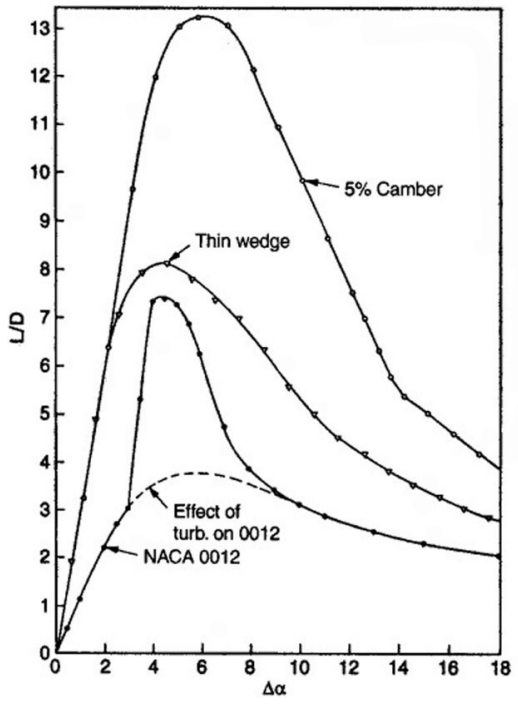

Figure 1.28: **Lift to Drag ratio for three airfoil shapes (Laitone[67])**

Experiments were carried out by Pelletier et al. [68] to study the lift, drag, and pitching moment characteristics of low aspect ratio wings operating at Reynolds numbers in the range of $6 \times 10^4 - 2 \times 10^5$. Wind-tunnel tests were

carried out on wings with aspect ratios between 0.5 and 3. Some results are shown in Figure 1.29. The key conclusions are as follows. A reduction in the lift curve slope with decreasing aspect ratio was observed. Furthermore, as the aspect ratio was decreased, the linear region of the lift coefficient versus angle of attack (α) curve became longer and α_{stall} increased. Moreover, there was no abrupt stall for low aspect ratio wings. For these low aspect ratios, the lift coefficient often reached a plateau and then remained relatively constant, or even started to increase, for increasing angles of attack.

1.5.6 Leading Edge Vortex

Previous studies on insect flight have shown that using quasi-steady values of lift and drag coefficients underestimate forces in flapping flight, mainly because it cannot account for additional lift created by unsteady phenomena. Unsteady lift coefficients appeared to be a factor of 2.5 higher than steady-flow coefficients [69].

Unsteady flapping wings show the formation of a leading edge vortex (LEV), which is another type of laminar separation, followed by reattachment to the airfoil surface. This LEV is formed in flapping wings due to separation at the sharp leading edge of a wing during the flapping strokes. In the downstroke, for example, the separation rolls up on top of the wing, and forms a vortex near the leading edge. The flow outside the vortex is able to reattach to the airfoil surface. The reason for the roll up of the separation may be due to the

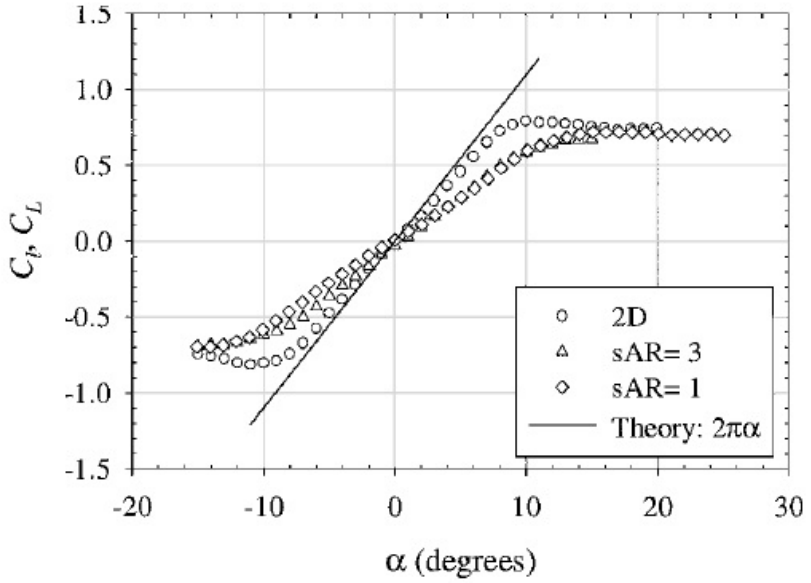

(a) $Re = 8 \times 10^4$

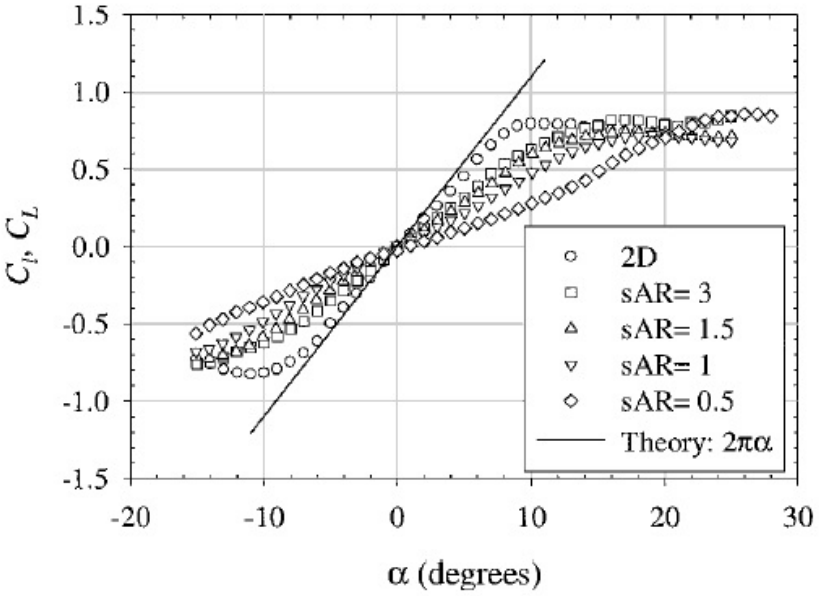

(b) $Re = 1.4 \times 10^5$

Figure 1.29: **Lift curves for flat plate [68]**

stabilizing effects of span-wise flow from the wing center to the wing tip. This span-wise flow causes the vortex to form a helical shape as it travels down

the span. Many studies on biological flying systems (especially insects) have revealed that a dominant feature of the flow physics of a flapping wing at low Re is the formation of an LEV [70, 71, 72, 35].

Therefore, while studying flapping wings at low Reynolds numbers, all the complex aerodynamic phenomenon needs to be thoroughly investigated and high fidelity tools are required to be able to model them accurately.

1.6 Review of Experimental Studies on Flapping Wings

A number of experimental studies have been carried out to understand the aerodynamics of flapping wings. Knoller [73] and Betz [74] were the first to identify that positive propulsive thrust is produced due to pure plunging motion of a wing in free-stream as it results in an effective angle of attack during both the up-stroke and downstroke. Katzmayer [75] experimentally verified this fact in 1922 by measuring the propulsive thrust from a stationary wing placed in a sinusoidally oscillating wind stream. This is known as the Knoller-Betz or Katzmayer effect.

Pitching/plunging airfoils at high Reynolds numbers (on the order of million) were studied in detail while investigating dynamic stall of helicopter blades. The formation of a leading edge vortex due to flow separation was found to have significant effect on the blade aerodynamics. This leads to forces and moments that are very different from static stall values. McCroskey [76] and Carr [77] provided comprehensive reviews on this topic. While this work

can serve as a starting point for investigating flapping wing MAV aerodynamics, the Reynolds number regime is at least one to two orders of magnitude higher than that of MAVs. Recently, several experiments were carried out in the lower Reynolds number regime on flapping wings.

Anderson et al. [78] performed experiments on propulsive thrust-producing harmonically oscillating 2D airfoils. Force and power measurement, as well as flow visualization was carried out in order to classify the principal characteristics of the flow around and in the wake of the airfoil. Visualization data was obtained using digital particle image velocimetry at Reynolds number 1100, and force and power data were measured at Reynolds number $40,000$. Visualization results elucidated the basic mechanisms involved for high efficiency and showed that conditions of high efficiency are associated with the formation on alternating sides of the foil of a moderately strong leading-edge vortex per half-cycle, which is convected downstream and interacts with trailing-edge vorticity, resulting eventually in the formation of a reverse Karman street. The phase angle between transverse oscillation and angular motion was found to be a critical parameter affecting the interaction of leading-edge and trailing edge vorticity, as well as the efficiency of propulsion.

Experiments were carried out by Jones et al. [79] to investigate the ability of a sinusoidally plunging airfoil to produce propulsive thrust, known as the Knoller-Betz or Katzmayr effect, mentioned earlier. Water-tunnel experiments were performed providing flow visualization and Laser Doppler Velocimetry data of the unsteady wakes formed by the plunging foils. Vortical structures

and time-averaged velocity profiles in the wake were compared with numerical computations from a previously developed inviscid, unsteady panel code that utilized a nonlinear wake model. Qualitative and quantitative comparisons were excellent at low reduced frequencies and Strouhal numbers, indicating that the formation and evolution of the propulsive thrust-indicative wake structures are primarily inviscid phenomena. Results at Strouhal numbers greater than about 1.0 (based on plunge amplitude) demonstrated non-symmetric, deflected wake patterns, where both an average propulsive thrust and an average vertical force were produced and could not be explained using unsteady panel method.

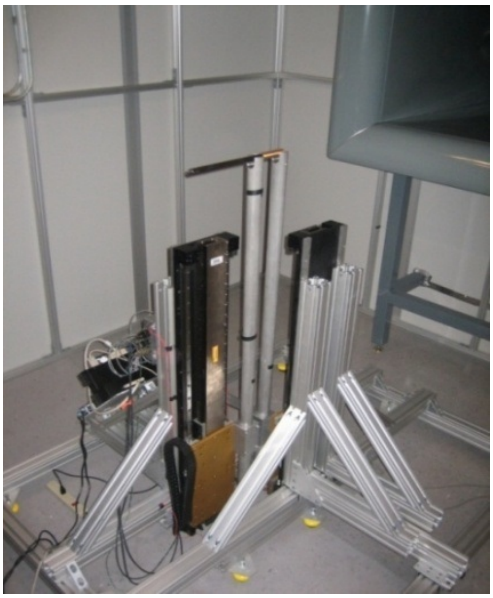

Figure 1.30: **Experimental test setup at University of Florida [80]**

Since MAV flapping wings generally have a very low aspect ratio, it may be expected that 3D effects will have an important role to play. Hart et al. [80] carried out experiments on a rigid wing in a wind tunnel (Figure 3.19). PIV

and aerodynamic loads data were used to study the effects of varying the phase between pitching and plunging cycles for a flat plate with an aspect ratio 2 at a chord based Reynolds number of $40,000$. It was shown that for a pure plunging case, the unsteady fluid phenomena delayed stall and increased the maximum coefficient of lift by 68%. Even though this study provided good data for computational validation, it did not provide full details of the flow physics.

Recently, experiments were carried out by Yuan et al. (Figure 1.31) on root based flapping, which closely mimic the kinematics of avian flight (Figure 3.26). The wing had a spanwise tapered planform and the airfoil section was NACA 0005. These experiments were carried out in a water tunnel and instantaneous forces were measured using two small one-component strain gauge balances to measure the vertical and propulsive forces. No flow visualization data was presented for this 3D wing.

It should be noted that all these studies were based on rigid wings. In addition to the basic flap kinematics, birds and insects employ large scale deformation of their wing geometries to improve the aerodynamic efficiency through neuromuscular control and through the aeroelastic response of the wings. Wang et al. [82] measured the kinematics of dragonfly flight for forward and maneuvering flight conditions. Their results showed that the camber varied significantly from 0.1c to 0.12c due to wing flexibility during the flapping cycle. They also conducted flow analysis of a 2-D model of a dragonfly with and without camber variation and showed that camber significantly affected the

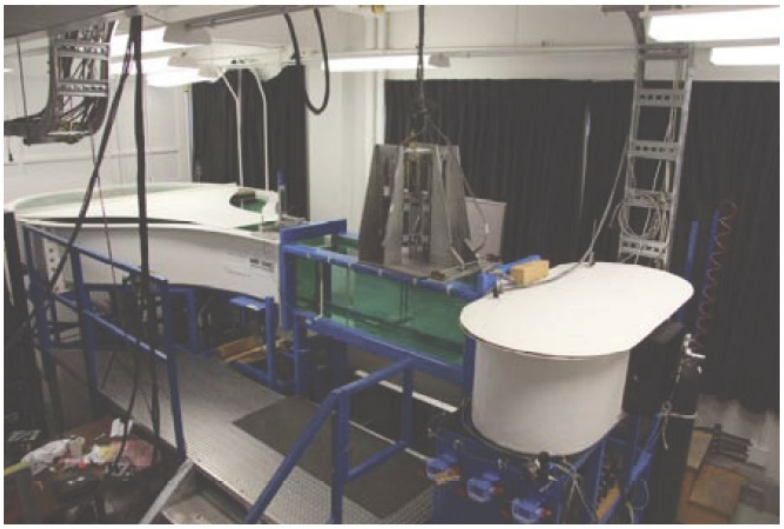

Figure 1.31: **Experimental test setup at National Research Council Canada [81]**

vertical force generated. The study on a hovering hummingbird by Tobalske et al. [83] showed the importance of camber on vertical force generation. Despite the kinematic symmetry of the upstroke and downstroke, the hummingbird generates 75% of the vertical force during the downstroke due to positive camber and only 25% during the upstroke due to the absence of a negative camber. Liu et al. [84] measured the wing geometry and kinematics of a seagull, merganser, teal, and owl and observed that the wing sections are highly cambered (0.085C) and are similar to the low-Reynolds-number airfoils. The wing deformation of birds and insects significantly affects the stability and strength of the LEV and force production. Therefore, it may be beneficial to include the effects of wing flexibility. The studies mentioned next focused on flexible flapping wings.

Frampton et al. [85] explored passive aeroelastic tailoring for optimal flapping wings in hover. A rig for measuring the propulsive thrust generated and power consumed by several wings was developed. All wings had rectangular planform, 6 in span and an aspect ratio of 2.3. The wings were stiffened by carbon-fiber ribs of varying width and thickness and covered with Mylar film. The wing natural bending and torsion frequencies were passively tailored in this way. The key observation was that a wing with bending and torsion motion in phase produces the largest propulsive thrust whereas a wing with the torsional motion lagging the bending motion by 90° results in best efficiency.

Combes et al. [86] carried out experiments to examine the contributions of aerodynamic and inertial elastic forces to wing bending in the Hawkmoth Manducasexta in hover. Fresh Manduca wings were attached to a motor and flapped at a realistic wing-beat frequency and stroke amplitude. The wing bending in normal air was compared with that in helium (approximately 15% air density), in which the contribution of fluid-dynamic forces to wing deformations is significantly reduced. This 85% reduction in air density produced only slight changes in the pattern of Manduca wing deformations, suggesting that fluid dynamic forces have a minimal effect on wing bending. A simplified finite element model of a wing was also used to show that the differences observed between wings flapped in air versus helium are most likely due to fluid damping, rather than to aerodynamic forces. This suggests that damped finite element models of insect wings (with no fluid dynamic forces included) may be able to predict overall patterns of wing deformation prior to calculations of

aerodynamic forces, facilitating integrative models of insect flight.

Singh [34] developed a passive pitch, bi-stable flapping mechanism to simulate insect wing kinematics in hover as shown in Figure 1.32. This setup was used to measure the propulsive forces generated by the flapping wing mechanism along with the flapping and pitching motions at the wing base at flap frequencies up to 12 Hz. The average air loads were measured using a custom built load cell with highly sensitive piezo-resistive strain gauges. The key observations were that the inertial loads constituted the major portion of the total loads acting on the flapping wings tested on the mechanism and that for all the wings tested, the propulsive thrust dropped at higher frequencies. Further, they found that at such frequencies, the light-weight and highly flexible wings used in the study exhibited significant aeroelastic effects.

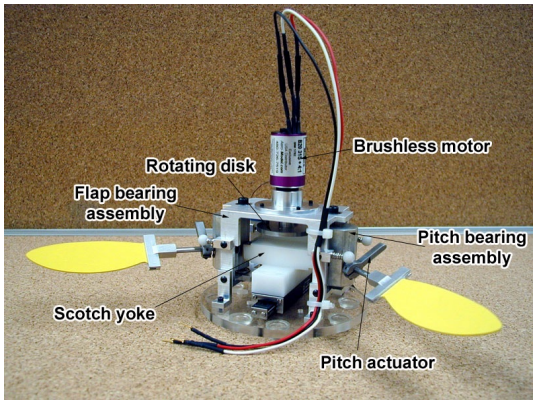

Figure 1.32: **Passive pitch, bi-stable flapping mechanism [34]**

Very few studies have been carried out on flexible flapping wings in forward flight. Wind tunnel tests were carried out by Ho et al. [87] for a variety of flap frequencies and freestream velocities on rigid and flexible wings. It was

concluded that a stiff wing in the spanwise direction near the leading edge is advantageous in terms of vertical force in the unsteady flow domain, while one that is spanwise flexible causes a sharp drop in vertical force for unsteady conditions. In terms of propulsive thrust, experiments indicated that the wing stiffness, particularly near the trailing edge, determined the final propulsive thrust output.

Heathcote et al. [88] carried out an experimental study of the effect of spanwise flexibility on the propulsive thrust, power-input, and propulsive efficiency of a rectangular wing with an aspect ratio of 6. The wing was oscillated in heave at one end in a water tunnel over a Reynolds number range of $10,000$-$30,000$. A two-component force balance was used to obtain the propulsive thrust and efficiency characteristics of the wing (Figure 1.33). Three wings of varying spanwise stiffness were tested: a rigid wing, flexible wing and highly flexible wing. All the wings were rigid in the chordwise direction. When the propulsive thrust coefficient was plotted against reduced frequency, a limited degree of flexibility was observed to be greatly beneficial. A propulsive thrust benefit of 50% was observed for a wing of intermediate flexibility. For a highly flexible wing, however, the tip was observed to move out of phase with the root, and a reduced propulsive thrust coefficient was recorded. PIV measurements at a number of spanwise locations showed a reverse von Karman vortex street near the wing root, resembling the flow pattern observed in 2-D studies in the literature. The initial rise in propulsive thrust coefficient with the introduction of spanwise flexibility was seen from the vorticity fields to arise from an in-

crease in the effective heave amplitude. Excessive spanwise flexibility was seen to lead to large tip phase lags, where the root and tip moved in opposite directions for significant portions of the stroke. The corresponding vorticity fields revealed the formation of vorticity of one type near the root, and of opposite type near the tip, leading to a fragmented and weak vorticity pattern. Significantly lower propulsive thrust coefficients, and diminished efficiency, were observed in this regime. The findings of this paper suggest that birds, bats and insects may benefit aerodynamically from the flexibility of their wings. From a design aspect, flexibility may benefit MAVs both aerodynamically and in the inherent lightness of flexible structures. This experimental study has been used for validating many aeroelastic analyses because it is one of the very few studies where the flexible wings were structurally characterized.

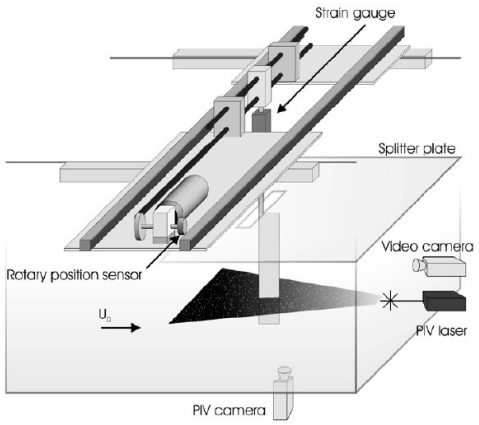

Figure 1.33: **Water tunnel test set up at University of Bath [88]**

Even though experiments can provide a wealth of information, it is quite challenging to carry out detailed flow measurement and hence, to understand the flow physics at low Reynolds numbers. In addition to the low

Reynolds Numbers, flapping wings are continuously accelerating and decelerating. Therefore, it is extremely difficult to separate out the aerodynamic forces from the large inertial forces. Further, flow visualization can only be carried out for a limited number of spanwise locations. Therefore, experiments may be complimented by analysis to get a better understanding of the flow physics of flapping wing MAVs.

1.7 Review of Numerical Studies on Aerodynamics of Flapping Wings

DeLaurier developed an aerodynamic model for large aspect ratio harmonically flapping wings in forward flight using modified strip theory approach [89] as shown in Figure 1.34. Vortex-wake effects, partial leading edge suction and post stall behavior were accounted for in the model. Also, contributions of sectional mean angle of attack, mean camber, and skin friction drag were added, which allowed this model to be used for the calculation of average vertical force, as well as the propulsive thrust, power required and propulsive efficiency of a flapping wing in steady level flight. The wing's aspect ratio is assumed large enough that the flow over each section is essentially chordwise (in the mean-stream direction). However, this assumption is not valid for MAVs as they have low aspect ratio wings.

Singh developed an unsteady aerodynamic model based on indicial functions to be able to analyze insect wing aerodynamics in hover [34]. The model

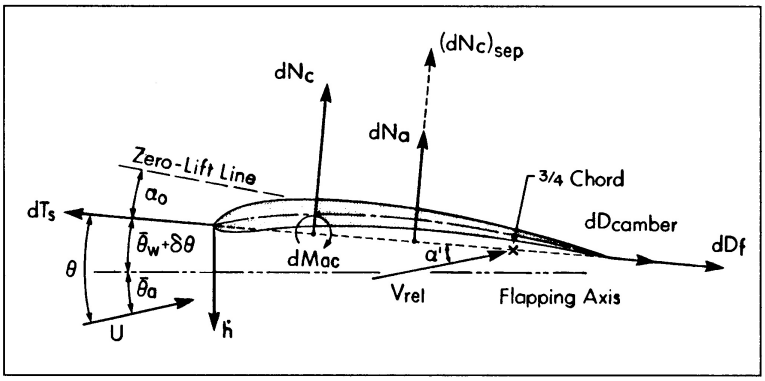

(a) **Wing section aerodynamic forces and motion variables**

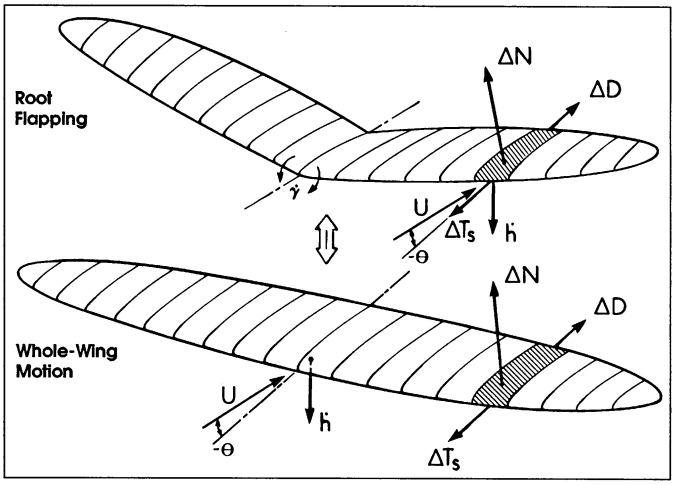

(b) **Assumed strip theory equivalence to whole wing motion**

Figure 1.34: **Modified strip theory (DeLaurier)**[89]

was built by taking into account the contributions of the following components: translation and rotational circulation based on thin airfoil theory with wing elasticity effects included, effect of a leading edge vortex on the wing determined by using Polhamaus' leading edge suction analogy for delta wings at high angles of attack, non-circulatory forces based on thin airfoil theory, effect of starting vortex on the translational and rotational circulation accounted for

by using the Wagner function and effect of the shed wake and a tip vortex, accounted for by using the Kussner function. The induced flow velocity was determined based on momentum considerations. The model was validated with the experimental data for Robofly wings moving at very low frequency in oil [35]. Key observations of this validation study are as follows. The ideal translatory lift coefficient, obtained from thin airfoil theory was inadequate to capture the aerodynamic forces because this coefficient did not capture the lift stall shown by experimental data at angles of attack greater than 45°. The predictions improved when the experimental lift and drag coefficients were used in the analysis (which might not be available for a general case). Even with the experimental force coefficients, there were discrepancies between the predictions and experiment at the beginning and end of each stroke. Another important assumption in this analysis was that the inflow was considered to be uniform.

It should be noted that though these analytical methods are computationally inexpensive, they are not able to capture all the viscous, unsteady aerodynamic effects of flapping, low aspect ratio MAV wings. Most of the simplified models are applicable to cases where there is a small change in angle of attack. However, a flapping wing operates at large flap amplitudes and as a result experience large values of effective angle of attack. The flow is highly unsteady, often accompanied by the formation of leading edge vortices. For low reduced frequencies, the flow that develops over the flapping wing is essentially quasi-steady: the aerodynamic state at a given time step

is mostly influenced by the wing shape at that time step. As the reduced frequency increases, unsteady effects become important, the influence of the wake is stronger, and the forces at a time step are substantially affected by the wing shape at previous time steps. Wake terms provide the only connection between the forces generated at disparate time steps and must be included to compute accurate sensitivities. Vortex Lattice Methods have also been used to analyze flapping wings and is a much simpler method than a CFD analysis. It can calculate the flow characteristic fast, and it doesn't require large computer resources, but it provides only a moderate level of fidelity.

A design optimization study was carried out by Stanford et al. [90] where computational framework capable of obtaining the derivative of a time-averaged force quantity (vertical force, propulsive thrust, power, propulsive efficiency) with respect to the shape of a flapping wing at any time step was developed using an unsteady vortex lattice method. The design was performed with a gradient-based optimization, where gradients are computed using an analytical sensitivity analysis. It was noted by the authors that these results obtained using the vortex lattice method for the morphing designs are only of a moderate fidelity. It is important to incorporate the higher-fidelity aerodynamic solvers to ascertain the accuracy of low-fidelity models.

For a complete solution of the viscous, non-linear flow equations or the Navier-Stokes equations, a Computational Fluid Dynamics (CFD) analysis appears appropriate. A lot of research has been carried out on 2D CFD analysis of pitching/plunging airfoils. One such study was carried out by Tuncer et

al. [91, 92] on NACA 0012 airfoil in pure plunge mode using a thin-layer Navier Stokes solver. Unsteady flow-fields were computed at the free-stream Mach number of 0.3, Reynolds number of 10^6, and the Baldwin-Lomax turbulence model was employed. Parametric variation of the frequency and amplitude of the pure plunge oscillation showed that dynamic stall is encountered as soon as the non-dimensional plunge velocity exceeds the approximate value of 0.35.

Numerical simulations of dynamic stall phenomena at Re of 10^5 of an airfoil oscillating in a combined plunge plus pitch kinematics with some phase difference, were performed with a Navier-Stokes solver by Isogai et al. [93] Propulsive efficiency and propulsive thrust were calculated for various combinations of the phase difference and reduced frequency for two different amplitude ratios. Highest efficiency was observed for the case in which the pitching oscillation advances 90° ahead of the heaving oscillation and the reduced frequency is at some optimum value.

Limited work has been done on 3D flapping wings. Some important 3D CFD studies are highlighted next.

Visbal et al. [94] carried out high-fidelity implicit large-eddy simulation of a pure plunging airfoil at low-Reynolds-number conditions ($Re_c < 6 \times 10^4$). Calculations were performed first for a SD7003 airfoil section at an angle of attack $\alpha_0 = 4°$, plunging with reduced frequency, k=3.93 and amplitude $h_o/c = 0.05$. A comparison of the instantaneous spanwise vorticity component obtained from both 2-D and 3-D calculations is shown at a given phase of the plunging motion in Figure 1.35. For $Re_c = 10^4$, the 2-D and 3-D results are

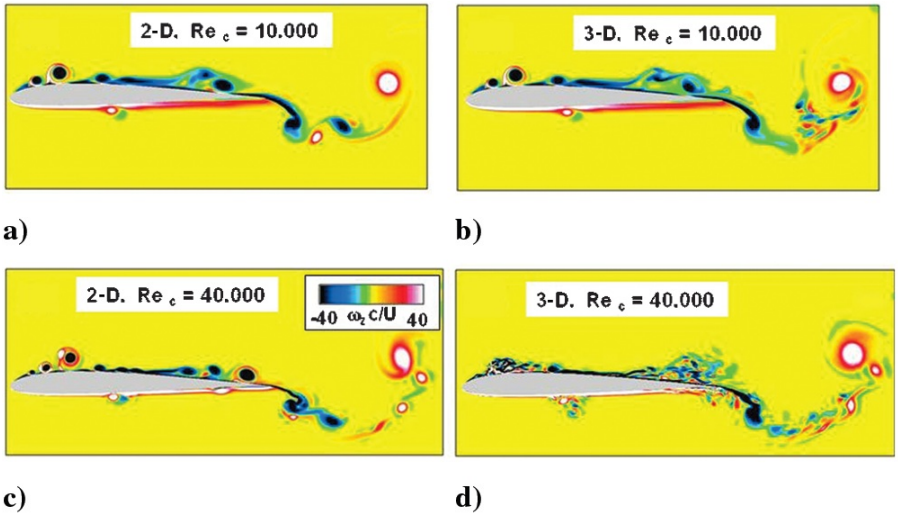

Figure 1.35: **Comparison of instantaneous spanwise vorticity for 2-D and 3-D simulations,** $k = 3.93$**,** $\alpha_o = 4°$**.**

found to be in close agreement with each other over a significant portion of the airfoil. The leading-edge vortex formation, in particular, exhibits a well-defined and persistent two-dimensional character. Some minor discrepancies exist in the aft portion near the trailing edge, as well as in the near wake due to incipient transitional effects. Therefore, for the given plunging parameters and $Re_c = 10^4$, the flow structure is effectively laminar, and predictable to a great extent by the two dimensional computational approach. As the Reynolds number is increased to 4×10^4, significant differences emerge between 2-D and 3-D results. The coherent vortices observed in the 2-D simulations break down in the spanwise direction. As a second example, the suppression of stall at high angle of attack ($\alpha_o = 14°$) was investigated using high-frequency, small-amplitude vibrations ($k = 10$, $h_o/c = 0.005$). At $Re_c = 6 \times 10^4$, separation was completely eliminated in a time-averaged sense, and the mean propulsive

drag was reduced by approximately 40%.

A dynamic unstructured grid based high-order spectral difference (SD) method was developed recently by Yu et al. [95] to solve the three dimensional compressible Navier-Stokes (N-S) equations. The capability of the developed solver in handling complex vortex-dominated flow was demonstrated via the simulations of the three dimensional flapping-wing problems at low Reynolds and Mach numbers. Furthermore, based on the aerodynamic force results, it was found that the pure plunging motion is not conducive to the propulsive performance. A combined plunging and pitching motion can drastically increase the propulsive thrust generated.

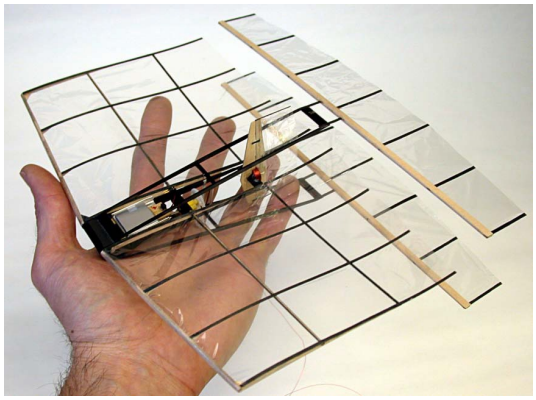

Figure 1.36: **NPS Flapping wing MAV [96]**

The low Reynolds number aerodynamics of a flapping wing MAV developed at Naval Postgraduate School (NPS) by Max Platzer and Kevin Jones as shown in Figure 1.36 was studied numerically by Lim et al. [96] The dynamic mesh simulation model of the full multi-wing configuration, which consists of a fixed wing and a pair of aft position, opposed pitch/plunge flapping wings.

This model was developed using an advanced CFD-ACE+ code which is a commercially available software. Results were compared to past experimental observations and provided impetus for future computational optimization studies on the NPS flapping wing MAV.

Computations on a rigid plate in pure plunge and combined pitch and plunge were carried out at University of Michigan [97]. They used a RANS solver to simulate the experiments carried out by Hart et al. [80], mentioned earlier in Section 1.6 and satisfactory correlation was obtained.

CFD analysis on 3D wing was also carried out by Yuan et al. [81]. They simulated their root own flapping experiments on rigid wings (mentioned earlier). A highly 3D flow field was observed for this root flapping case. Compared with the 2D results, the 3D calculations clearly over-predicted the force generation. The authors noted that this is a warning sign for engineering design that one cannot simply rely on the 2D results without consideration of the 3D effects of a low-aspect-ratio wing.

1.8 Review of Aeroelastic Analysis of Flapping Wings

Aeroelastic analysis of flexible flapping wings is a very active area of research and a lot of studies of varying fidelity have been carried out over the past decade.

Tang et al. [98] analyzed flexible 2D airfoils using a Navier-Stokes solver in conjunction with finite element method with beam elements. The key ob-

servations are as follows. Firstly, while a flexible airfoil deforms in response to aerodynamic loading, it also exhibits an equivalent pitching motion, which in turn modifies the effective angle of attack, affecting the vertical and propulsive forces significantly. Secondly, in response to the aerodynamic loading, a flexible airfoil performs a passive pitching motion to change the effective angle of attack, causing noticeable differences in vertical and propulsive force generation. Thirdly, within the range of the flexibility considered, the flow fields are quite similar for all cases. Even at $Re = 100$, in the plunging motion, the force acting on airfoil is dominated by pressure and the viscous force is of little impact on the overall vertical and propulsive force generation. Detailed airfoil shape is secondary compared to the equivalent angle of attack.

Liani et al. [99] modeled the aerodynamics based on assumptions of inviscid flow using 2D unsteady panel methods and structural dynamics using a linear finite element model based on beam theory. Stall could not be predicted using this model, limiting the amplitude of oscillations for calculating the aeroelastic response to small values. They main observation was that aerodynamic forces increased when wing flexibility is taken into account.

Singh [34] developed an aeroelastic analysis where an in-house structural solver was coupled it an unsteady aerodynamic analysis based on indicial functions (mentioned earlier in Section 1.7). The structural solver was based on linear finite element plate analysis. It was validated with prior research on rotating plates and in-house experiments. He used this code to simulate experiments of flexible isotropic plates undergoing insect kinematics in hover.

The main conclusion from this study was that aerodynamic loads cannot be neglected while computing the wing response.

Willis et al. [100] presented a multi-fidelity computational framework capable of modeling flapping wing vehicles. A nonlinear beam model was coupled to one of the following aerodynamic models (with increasing fidelity): wake only method, lifting line method, panel method and high order discontinuous Galerkin methods for solving the Navier Stokes equation. The idea was that low fidelity tools can be applied to gain insights into the parametric dependencies and provide a good initial guess for higher fidelity solvers. Such an approach presents an opportunity for computational savings and provides the ability to understand flapping flight physics. However, since this analysis used a beam model, it cannot be applied to low aspect ratio MAV flapping wings.

Kim et al. [101] used an aerodynamic model based on modified strip theory (developed by DeLaurier [89], mentioned in Section 1.7), which was further improved to take into account relatively high angles of attack and dynamic stall effects induced by pitching and plunging motions. A reduced structural model of a rectangular flapping wing was established by using flexible multibody dynamics. Validation of analysis was carried out with experiments at low flapping frequencies.

Smith et al. [102] simulated a tethered moth's flapping wings using an unsteady aerodynamic panel method and a finite element method (with a combination of beam and membrane elements). This study highlighted the importance of including the wake in the unsteady analysis of flexible wings.

However, it did not account for separation at the leading edge, resulting in poor correlation of computed forces with experimental results.

Gopalakrishnan et al. [103] evaluated the effects of wing deformation by coupling a large-eddy simulation solver with a linear elastic membrane model. Same grid distribution was used in both the solvers eliminating the need for fluid-structure interpolation. Inertial forces due to flapping were neglected in computing the deformations. Different membrane prestresses were investigated to obtain a desired camber in response to the aerodynamic pressure. It was observed that the wing camber increased the vertical and propulsive force significantly. Its main limitation is the use of a linear structural solver which cannot be used for wings undergoing large deformations.

A realistic flapping wing MAV is highly anisotropic with different flexibilities in the spanwise and chordwise directions. In order to generate sufficient forces, the wings operate at high flap frequencies and flap and pitch amplitudes. Being extremely lightweight and flexible, under the effect of large inertial forces (due to continuous starting and stopping of wings between the downstroke and upstroke), these wings undergo large non-linear deformations. Therefore, in order to be able to simulate a realistic flexible wing, non-linearities in both the structures and fluids must be modeled accurately for these low aspect ratio wings.

All the analyses mentioned above suffered from one or more of the following major limitations:

1. Limited to 2D flow environment

2. Simplistic aerodynamic model (based on unsteady lifting line airfoil theory, unsteady panel methods etc.)

3. Simplistic structural model (based on linear/non-linear beam models, linear plate/membrane models)

4. Simplistic aerodynamic and structural models (both)

Chimakurthi et al. [104] developed a co-rotational structural dynamics solution to analyze shell like flapping wing structures. It was coupled to an in-house incompressible Navier Stokes solver and partially validated with available experimental data of flexible plunging/flapping isotropic wings. Case studies were presented for three different flexible wing configurations: rectangular wings with pure prescribed plunge motion, an elliptic wing with pure prescribed flap rotation, and a rectangular wing with pure prescribed flap rotation. Numerical studies showed that within the range of non-dimensional parameters considered, only a limited amount of spanwise flexibility is favorable for propulsive thrust generation. These results were consistent with prior research by Heathcote et. al [88] (mentioned in Section 1.6). Though this is an excellent study combining high fidelity aerodynamic and structural solvers, it suffered from certain limitations. Firstly, the solver was used to analyze only isotropic wings. Realistic MAV wings, on the other hand are extremely anisotropic and this anisotropy has a large impact on the aeroelasticity of the wings. Secondly, the CFD grid was unable to accommodate moderate to

large deformations. Thirdly, the mapping interface between the solvers was not robust. Finally, the coupled solver was not parallelized making it computationally expensive.

1.9 Need for New Experimental Data

Though a lot of experimental works have been carried out on flapping wings, a large number of them are performed by biologists on insect wings at very low Reynolds numbers (~ 100), which are far below the current MAV regime. In the Reynolds number regime of MAVs ($\sim 10^3 - 10^5$), a number of studies have been carried out on rigid wings. Though these provide some insights into unsteady aerodynamics but many other studies have shown that natural flyers use flexibility to their advantage. It is extremely important to understand not only unsteady aerodynamics, but also the aeroelastic effects need to be modeled in order to be able to accurately predict the performance of flapping wing MAVs. The current flapping wing MAVs are built using membrane wings strengthened by carbon spars and these are normally based on a trial and error approach through experimentally testing a variety of wings and kinematic configurations. In most of these studies, the flexible wings are not even structurally characterized. Therefore, there is clearly a need of reliable experimental data on structurally well characterized realistic, flexible, light weight wings.

1.10 Need for New Aeroelastic Modeling

Experimental testing of different wings is a very time consuming and inefficient way to drive the design of flapping wing MAVs as well as to understand their flow physics. A case in example is the Nano Hummingbird developed by AeroVironment [47], which is possibly the most successful flapping wing MAV to date. It was developed through an experimental trial and error approach. Over 300 different wings were tested before they could achieve a successful configuration. Figure 1.37 shows a sample set of the wings tested.

Further, experiments may not be able to provide the level of details in flow physics, which can be achieved through a high fidelity analysis. Such flow details are necessary to understand the fundamentals of aerodynamics and aeroelasticity of flapping wings.

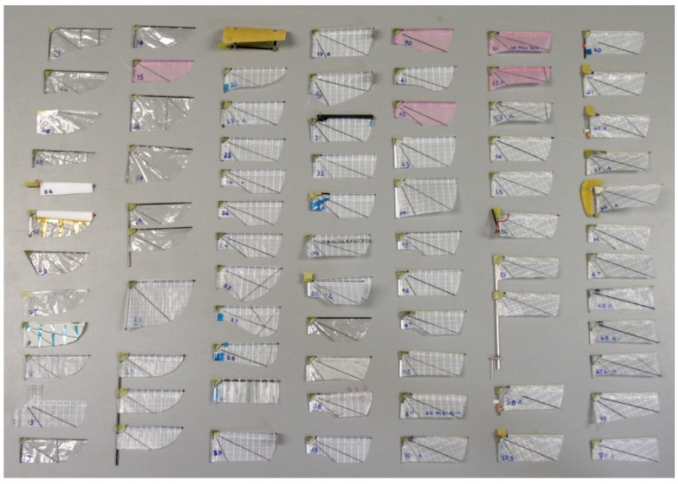

Figure 1.37: **Some examples of wing designs tested during the NAV program [47]**

In recent years, a number of aeroelastic analyses have been developed.

The three major components of the analyses are: the aerodynamic solver, structural solver and the coupling between the solvers. Majority of the analyses either have a simplified aerodynamic model that cannot accurately represent all the unsteady, viscous effects (based on thin airfoil theory, unsteady panel methods, euler methods) or, have a linear finite element structural model (mostly based on beam elements). It should be noted that to model all the complex unsteady and aeroelastic effects of these highly flexible low aspect ratio wings, both the solvers should be of high fidelity and be able to take into account the three dimensional unsteady aerodynamics at low Reynolds numbers as well as large non linear deformations of 2D membrane wings with anisotropic assumption. In addition, the coupling between the two solvers should be consistent and robust.

1.11 Objectives and Approach

The objective of this work is two-fold. The first aim of the current work is to extend the limited body of work on 3D flapping wings and develop a high fidelity CFD-CSD solver to study the performance and flow physics of realistic flexible flapping wing MAVs. Proper understanding of the aerodynamics and aeroelasticity of flapping wings will reduce the developmental time and effort as compared to the most widely used experimental trial and error approach. A high fidelity, well validated solver may then be used to design the next generation flapping wing MAVs. The second objective is to carry out experiments

on realistic flexible wings to determine the kinematics suitable for generating vertical and propulsive forces in forward flight. These wings were then structurally characterized to generate a comprehensive data set, currently scarce in literature, which can be used for validation of aeroelastic analyses of flapping wings. The outline of the approach is as follows.

Earlier work by Lakshminarayan and Baeder [105] demonstrated the capability of using a compressible Reynolds Averaged Navier-Stokes (RANS) solver, called OVERTURNS, to study the flow physics of hovering micro-rotors. This solver is further extended to simulate rigid flapping wings. The CFD methodology is described in Chapter 2. Since this is the first time, OVERTURNS is used for flapping wings, validation is carried out first for pitching/plunging airfoils in 2D flow environment at different Reynolds numbers. Next, 3D validation is carried out for rigid wings with different kinematics. First, pure plunge and combined pitch and plunge cases are analyzed and compared with results by Hart et al. of University of Florida [80]. Next, root based flapping motion is simulated (similar to avian kinematics) in 3D flow environment and validated against the results published by Yuan et al. of National Research Council, Canada [81]. These validation results are presented in Chapter 3.

To include the effect of wing flexibility, a multibody structural solver developed at Politecnico di Milano, called MBDyn, is used. MBDyn has been used for rotary wing applications and had nonlinear beam elements. Beam elements cannot be used to analyze low aspect ratio MAV wings. Therefore,

during this research, the modeling capability of MBDyn was extended to include nonlinear plate/shell elements. The shell model is validated here with prior research as well as in-house experiments on flexible plates. Structural modeling methodology and validation of the solver is presented in Chapter 4.

Once both the aerodynamic and structural solvers were validated independently, they were coupled using a python based framework to obtain a coupled CFD-CSD analysis. In the current literature, there exists very little data on well characterized flexible wings. One such data set was published by Heathcote et al. of University of Bath on spanwise flexible wings. The coupled analysis was used to simulate these simplified configurations and satisfactory validation was obtained. The solver is then used to analyze a chordwise flexible wing. These results form the content of Chapter 5.

There is a dearth of data in prior literature on realistic, flexible, well-characterized MAV scale flapping wings. To fill this void, in-house experiments were carried out in an open-jet wind tunnel on rigid and flexible flapping wings. The flexible wings were also structurally characterized by performing experimental testing and these structural properties were used to develop a model in MBDyn. The structural model was coupled to the CFD solver and a coupled CFD-CSD analysis was carried out. The results were compared with the experiments and this helped to further validate the coupled analysis. Finally, the analysis was used to gain more insights into the flow physics, for example, the pressure coefficient contours at different sections of the wing and at different instants of flap cycle. The instantaneous force variation over a

flap cycle and spanwise force variation is also examined. These results are presented in Chapter 6. Chapter 7 describes the key conclusions from this work and some recommendations for future work.

Chapter 2

Aerodynamic Modeling Methodology

In this work, aerodynamic modeling of flapping wings is carried out using an in-house CFD solver, OVERTURNS. It is a Reynolds Averaged Navier Stokes Solver and has been used extensively for rotary wing applications. During this study, it was extended to flapping wing MAVs.

The fundamental fluid dynamic equations along with the numerical solution algorithms are described in this chapter. The flow domain that is being studied is initially identified. Following this, the details of the mesh system and the connectivity approach is discussed. Subsequently, the flow equations and methodologies available in the existing flow solver are described.

2.1 Flow Domain

The focus of the current work is to simulate the flow-field of flapping wing MAVs. Only one wing is modeled in this study and its surface can be treated as a solid wall. The far-field extent of the modeled domain is limited to a few wing chords from the wing in any direction, because of practical reasons.

Even within the finite domain of interest, the flow solution can be represented only at finite locations. This is achieved by decomposing the flow domain into smaller domains (cells) by generating a grid. The flow variables

represented at each of these grid points constitute the flow solution. The accuracy of the solution is determined by the quality of the grid. A common difficulty in simulating complex geometries is that a single, contiguous grid will not be sufficient to represent all the flow features well enough. For a flapping wing, it is very difficult to obtain a single structured mesh which can represent the wing surface and also preserve important off-surface flow features, like the shed vortices. In such cases, the common approaches used are unstructured meshes, multiblock structured meshes or overlapping chimera structured meshes.

Unstructured meshes are generally considered to be easily adaptable to complex configurations, but they require more memory and are less efficient compared to structured meshes. Using block structured grids, the grid interfaces have to be matched and this makes the grid generation process very complicated.

Overset structured grids have the advantage that different grids can be generated independent of each other and can be placed in the region of interest without any distortion [105]. Due to these advantages, the current work employs overset meshes.

The penalty to pay however, is the additional work required in identifying points of overlap between meshes and interpolation of the solution in this overlap region. Additionally, there is a possibility of a loss of the conservation property of the numerical scheme. However, the resulting errors can be minimized by making sure discontinuous features like shocks and shear layers

do not cross the overlap boundaries and furthermore, ensuring that the mesh cells are of commensurate size in the overlap region [105].

2.2 Mesh Generation

To accurately represent wing surfaces, body conforming structured curvilinear meshes are required. In this study, both 2D and 3D flow environments are analyzed. A hyperbolic mesh generation technique [130] is used to generate 2D C-type meshes(Figure 2.1).

For the 3D wing, the 2D meshes are generated around the airfoil sections at the various spanwise locations, shown in Figure 2.2(a). The C-type meshes are free of a geometrical singularity at the trailing edge, which is a major disadvantage of O-type meshes. Also, the grid clustering at the trailing edge provides good resolution for capturing the shed wake. The C-meshes obtained are stacked in the spanwise direction for the 3D grid.

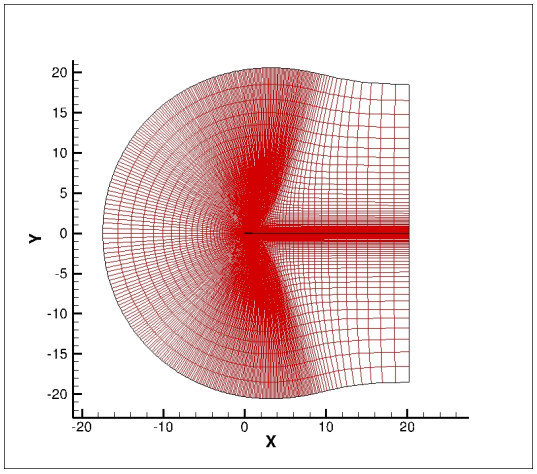

Figure 2.1: **2D C-type mesh**

Near the root and the tip regions, the spanwise sections are rotated and collapsed, thus defining a C-O topology, see Figure 2.2(b). Details of the collapsing technique are described in [131]. Figure 2.3 shows the wing mesh on the surface.

2.3 Overset Grid Methodology

As discussed in the previous sections, finely-spaced wing mesh is overset onto a coarser background mesh to allow for wing motion and maintain computational efficiency while capturing all the flow features. The wing mesh is overset in a background meshes, in order to resolve the vortices. In the current work, a background mesh consists of a cartesian mesh. A sample background mesh with embedded wing mesh is shown in Figure 2.4

In this system, information is transferred between these two meshes through domain connectivity. A "donor" cell on one mesh will give information to a "receiver" cell on the other mesh. Significant effort is made to ensure that the donor and receiver cells are roughly equivalent in size, such that information can be interpolated between meshes without loss of too much accuracy. In addition, a "hole" is cut in the background mesh where the blade mesh is located to maintain consistency of solution in the entire computational domain. Implicit hole-cutting method developed by Lee [124] and refined by Lakshminarayan [105] is used to find the connectivity information between the overset meshes.

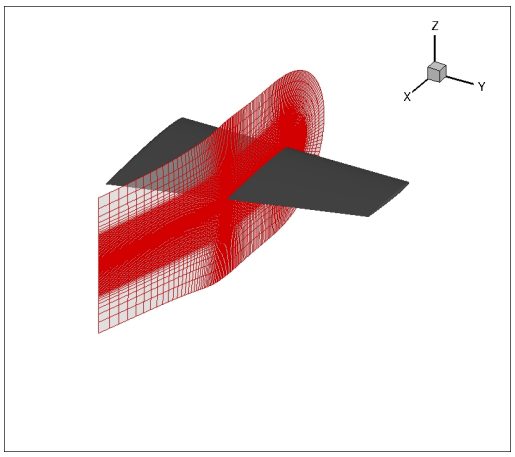

(a) **C-type mesh at one spanwise location**

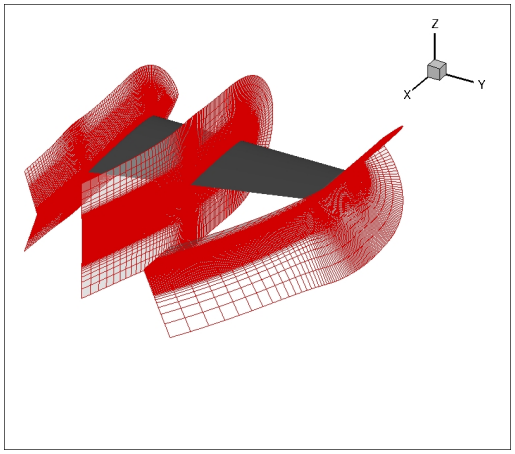

(b) **Near body C-O mesh at root and tip**

Figure 2.2: **C-type meshes at different spanwise locations**

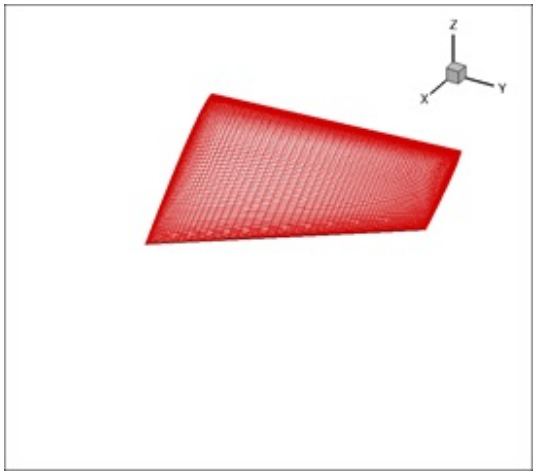

Figure 2.3: **Wing surface mesh**

2.4 Grid Motion

An avian wing has very complex wing motions that is a combination of flapping, pitching and folding of the wing. The two main degrees of freedom, flapping and pitching, are considered here. The wing motion is prescribed and different types of kinematics have been studied in this work:

1. Pure plunge
2. Combined Plunge and Pitch
3. Root Flap
4. Combined Root Flap and Pitch

The parameters for wing motion (flap frequency, plunge (or flap) amplitude, pitch amplitude, phasing between pitch and plunge (or flap)) can be easily changed to generate the required kinematics.

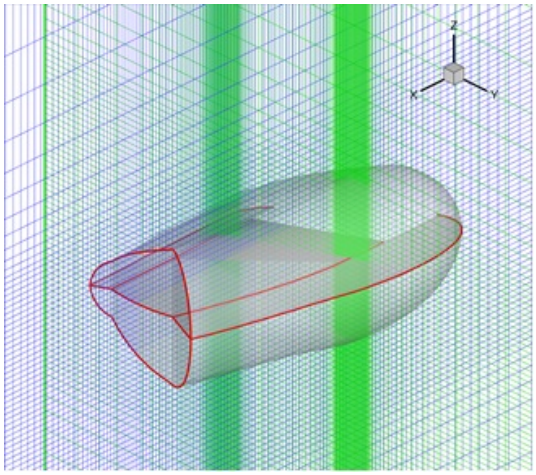

(a)

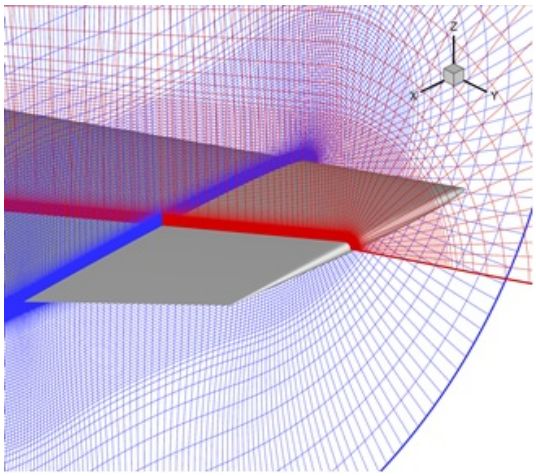

(b)

Figure 2.4: **Wing mesh embedded in background cartesian mesh**

2.5 Flow Solver

Once the grid is generated and grid motions are prescribed, the flow field properties at each grid point within the overset mesh system can be obtained by solving the conservation laws of physics for fluid flow. The following subsections describe these governing equations, as well as certain numerical methods

to ensure their convergence for low-Mach and Reynolds number flight regimes.

2.6 Compressible Navier-Stokes Equations

The flow field information at each point of the CFD grid is obtained by solving the governing flow equations which represent conservation of mass, momentum and energy. The conservation laws can be gathered into a single system of partial differential equations called the Navier Stokes equations. These equations cans be numerically discretized and solved with necessary boundary conditions for the specified geometry. Additional algebraic or differential equations may be required for closure and are mentioned in later sections. The strong conservative law form of the 3-dimensional unsteady compressible Navier Stokes equations in Cartesian coordinates are given by:

$$\frac{\partial Q}{\partial t} + \frac{\partial F_i}{\partial x} + \frac{\partial G_i}{\partial y} + \frac{\partial H_i}{\partial z} = \frac{\partial F_v}{\partial x} + \frac{\partial G_v}{\partial y} + \frac{\partial H_v}{\partial z} + S \tag{2.1}$$

where Q is the vector of conserved variables, F_i, G_i, H_i are vectors representing inviscid fluxes, F_v, G_v, H_v are vectors representing viscous fluxes and S represents the sources terms. The vector of conserved variables is given by:

$$Q = \begin{cases} \rho \\ \rho u \\ \rho v \\ \rho w \\ e \end{cases} \tag{2.2}$$

where ρ is the density, (u, v, w) are the Cartesian velocity components and e is the total energy per unit volume. The flux vectors are given by

$$F_i = \begin{cases} \rho u \\ \rho u^2 + p \\ \rho uv \\ \rho uw \\ u(e + p) \end{cases} \tag{2.3}$$

$$G_i = \begin{cases} \rho v \\ \rho vu \\ \rho v^2 + p \\ \rho vw \\ v(e + p) \end{cases} \tag{2.4}$$

$$H_i = \begin{cases} \rho w \\ \rho w u \\ \rho w v \\ \rho w^2 + p \\ w(e+p) \end{cases} \tag{2.5}$$

$$F_v = \begin{cases} 0 & (2.6) \\ \tau_{xx} \\ \tau_{yx} \\ \tau_{zx} \\ u\tau_{xx} + v\tau_{xy} + w\tau_{xz} - q_z & (2.7) \end{cases}$$

$$G_v = \begin{cases} 0 & (2.8) \\ \tau_{xy} \\ \tau_{yy} \\ \tau_{zy} \\ u\tau_{yx} + v\tau_{yy} + w\tau_{yz} - q_y & (2.9) \end{cases}$$

$$H_v = \begin{cases} 0 & (2.10) \\ \tau_{xz} \\ \tau_{yz} \\ \tau_{zz} \\ u\tau_{zx} + v\tau_{zy} + w\tau_{zz} - q_z & (2.11) \end{cases}$$

where q_z, q_y,q_z are the thermal conduction terms, which can be represented in terms of temperature, T, and the coefficient of thermal conductivity, k, given by:

$$q_i = -k\frac{\partial T}{\partial x_i} \tag{2.12}$$

The pressure, p, is determined by the equation of state for a perfect gas, given by

$$p = (\gamma - 1)\{e - \frac{1}{2}\rho(u^2 + v^2 + w^2)\} \tag{2.13}$$

where γ is the ratio of specific heats, generally taken as 1.4. For a perfect gas, $T = \frac{p}{\rho R}$, where R is the gas constant. With the assumption of Stokes' hypothesis, the mean stress is represented as:

$$\tau_{ij} = \mu[(\frac{\partial u_i}{\partial x_j} + \frac{\partial u_j}{\partial x_i}) - \frac{2}{3}\frac{\partial u_k}{\partial x_k}\delta_{ij}] \tag{2.14}$$

where μ is the laminar viscosity, which can be evaluated using Sutherland's Law.

For the flow solver, the Navier-Stokes equations must be solved in computational space, such that the flux contributions can be defined with respect to the adjacent computational cell faces. Since the equations above are given in physical space (i.e. (x, y, z) coordinates), a curvilinear coordinate transformation must be employed which converts the Navier-Stokes equations to a uniformly spaced Cartesian coordinate system in computational space (i.e.

ξ, η, ζ coordinates). The transformed equations are given by:

$$\frac{\partial \hat{Q}}{\partial t} + \frac{\partial \hat{E}}{\partial \xi} + \frac{\partial \hat{F}}{\partial \eta} + \frac{\partial \hat{G}}{\partial \zeta} = \hat{S} \tag{2.15}$$

where

$$\hat{Q} = \frac{1}{J} Q \tag{2.16}$$

$$\hat{E} = \frac{1}{J} \left(\frac{\partial \xi}{\partial x} E + \frac{\partial \xi}{\partial y} F + \frac{\partial \xi}{\partial z} G \right) \tag{2.17}$$

$$\hat{F} = \frac{1}{J} \left(\frac{\partial \eta}{\partial x} E + \frac{\partial \eta}{\partial y} F + \frac{\partial \eta}{\partial z} G \right) \tag{2.18}$$

$$\hat{G} = \frac{1}{J} \left(\frac{\partial \zeta}{\partial x} E + \frac{\partial \zeta}{\partial y} F + \frac{\partial \zeta}{\partial z} G \right) \tag{2.19}$$

$$\hat{S} = \frac{1}{J} S \tag{2.20}$$

and J represents the Jacobian of the coordinate transformation, defined as:

$$J = det \left(\frac{\partial(\xi, \eta, \zeta)}{\partial(x, y, z)} \right) \tag{2.21}$$

It should be noted that in OVERTURNS, all the variables in the Navier-Stokes equations have been non-dimensionalized; generally, length scales were non-dimensionalized by blade chord and dependent variables are non-dimensionalized by freestream conditions [105].

2.7 Reynolds-Averaged Navier-Stokes Equations

The solution of the Navier-Stokes equation, in the form given in 2.15, has no fundamental difficulties with inviscid or laminar flows. However, a direct simulation of the turbulent flow for MAVs by solving these time-dependent equations (referred to as Direct Numerical Simulation, DNS) is very computationally intensive, an approximation to turbulence is needed. For engineering and physics problems, the Reynolds-Averaged Navier-Stokes (RANS) equations represent an approximation that considerably reduces the amount of calculations needed to solve the governing equations. The RANS equations decompose the flow into mean and fluctuating parts, i.e. any flow variable can be written in the form: $\phi = \bar{\phi} + \phi'$

where $\bar{\phi}$ represents the mean part, and ϕ' is the fluctuating part. The mean part is obtained from Reynolds averaging given by:

$$\bar{\phi} = \frac{1}{\bar{\chi}} \lim_{\Delta t \to \infty} \frac{1}{\Delta t} \int_0^{\Delta t} \chi\phi(t)dt \tag{2.22}$$

where $\chi = 1$, if ϕ is density or pressure and $\chi = \rho$, if ϕ is other variable such as velocity, internal energy, enthalpy and temperature. By definition, the Reynolds average of the fluctuating part is zero.

These decomposed parts, when placed in the Navier-Stokes equations, Eq. 2.15, result in the mathematical description of the mean flow properties. If we drop the bar on the mean flow variables, the resulting equations are the same as the instantaneous Navier-Stokes equations except for additional

terms in the momentum and energy equations; these additional terms are denoted as the Reynolds Stress Tensor, and account for the additional stress due to turbulence. However, these additional Reynolds-stress terms are now unknown, and must be approximated using a turbulence model to achieve closure of the RANS equations.

2.8 Turbulence Model

The turbulent contribution to viscosity is approximated by the Reynolds Stress Term:

$$\tau_{ij}^{R} = -\rho u_i' \bar{u} i_j \tag{2.23}$$

Eq. 2.14 showed the Reynolds stresses with the assumption of isotropic eddy viscosity. Although many turbulence models have been developed to obtain turbulent viscosity, two models available currently in OVERTURNS are the Baldwin-Lomax model [132], and the Spalart Allmaras model [133].

The Baldwin-Lomax (BL) model is a two-layer, algebraic, 0-equation model which uses boundary layer velocity profile to determine eddy viscosity. Baldwin-Lomax model is suitable for high-speed attached flows with thin boundary layers. Though the BL model is not meant for use with unsteady, separated flows, it can still provide a quick preliminary approach to solving turbulent eddy viscosity, especially in cases where robustness is more important than capturing flow physics details.

The Spalart-Allmaras (SA) turbulence model has been used in this work,

is a one-equation model given by:

$$\frac{\partial \bar{\nu}}{\partial t} + V \cdot (\nabla \bar{\nu}) = \frac{1}{\sigma}[\nabla \cdot ((\bar{\nu} + \nu)\nabla \bar{\nu} + c_{b2}(\nabla \nu)^2] + c_{b1}\bar{S}\bar{\nu} - c_{w1} f_w \left[\frac{\bar{\nu}}{d}\right]^2 \quad (2.24)$$

It relates the Reynolds stresses to the mean strain. The turbulent eddy viscosity, ν_t, is obtained by solving the above PDE for a related variable, where the two quantities are related by $\nu_t = \bar{\nu} f_{v1}$. f_{v1} is a function of $\bar{\nu}$ and the molecular viscosity, ν and is defined as:

$$f_{v1} = \frac{\chi^3}{\chi^3 + c_{v1}^3} \quad (2.25)$$

c_{b1}, c_{b2}, and c_{w1} are constants, d is distance from the wall, and V is the mean flow velocity; further details can be found in Reference [133].

Essentially, after loose coupling of this equation to the Navier-Stokes equations, the turbulent eddy viscosity can be obtained, from which the shear stress in the moment and energy equations can be evaluated, thus providing closure for all the variables.

2.9 Spatial Discretization

In OVERTURNS, the baseline algorithm uses a finite volume approach to discretize Equation 2.15 in space and time; the discrete approximation is shown in Equation 2.26. In the finite volume approach, a fictitious control volume is created around each grid point; its boundaries are defined by the midpoints of each line joining the current grid point to its neighboring grid points. At these boundaries, or faces, of the control volume, the fluxes are

evaluated, thus allowing for the conservation equations to be solved within the volume. A schematic is shown in Figure 2.5,

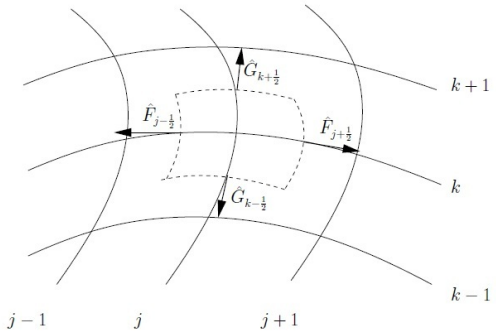

Figure 2.5: **Schematic showing computational cell [105]**

$$\frac{\Delta\hat{Q}}{\Delta t} = -\frac{\hat{E}_{j+\frac{1}{2}} - \hat{E}_{j-\frac{1}{2}}}{\Delta\xi} - \frac{\hat{F}_{k+\frac{1}{2}} - \hat{F}_{k-\frac{1}{2}}}{\Delta\eta} - \frac{\hat{G}_{l+\frac{1}{2}} - \hat{G}_{l-\frac{1}{2}}}{\Delta\zeta} + \hat{S}_{j,k,l} \qquad (2.26)$$

where (j, k, l) are the computational indices corresponding to the $(\xi,\ \eta,\ \zeta)$ coordinate directions. The $(j \pm \frac{1}{2},\ k \pm \frac{1}{2},\ ,\ l \pm \frac{1}{2})$ subscripts denote the values at the cell face. Thus, in the spatial discretization, the inviscid and viscous fluxes are obtained by calculating the fluxes at the interfaces for every cell (j, k, l) in the computational domain.

For the inviscid terms, the flux at the interface is computed using van Leers Monotone Upstream-Centered Scheme for Conservation Laws (MUSCL) scheme [134]. This is a two-step upwind scheme in which the wave propagation property of the inviscid equations is accounted for in the flux calculation, thus making it highly stable. The first step involves evaluating the left and right state at each cell interface using a reconstruction from the respective

cell centers of each state. The second step is to calculate the fluxes at the interface by defining a local Rie-mann problem using the left and right states. In TURNS, Roe flux-difference splitting [135] is used to solve for the flux at the interface:

$$F(q^L, q^R) = \frac{F(q^L) + F(q^R)}{2} - |\hat{A}(q^L, q^R)|\frac{q^R - q^L}{2} \tag{2.27}$$

In the above equation, $\hat{A}$ denotes the Roe-averaged Jacobian matrix and L and R superscripts indicate the left and right states, respectively. Typically Roe's scheme is modified by Turkel to become the Roe-Turkel scheme [136] in order to better approximate low Mach number flow. In low-Reynolds flows with thick boundary layers and large amounts of separation, the viscous terms in the spatial discretization cannot be neglected. Thus, an example viscous term of the form:

$$\frac{\partial}{\partial \xi}\left(\alpha \frac{\partial \beta}{\partial \eta}\right) \tag{2.28}$$

is discretized in TURNS using a second-order central differencing scheme:

$$\frac{1}{\Delta \xi}\left[\left(\alpha_{j+\frac{1}{2},k}\frac{\beta_{j+\frac{1}{2},k+1} - \beta_{j+\frac{1}{2},k}}{\Delta \eta}\right) - \left(\alpha_{j-\frac{1}{2},k}\frac{\beta_{j-\frac{1}{2},k} - \beta_{j-\frac{1}{2},k-1}}{\Delta \eta}\right)\right] \tag{2.29}$$

where

$$\alpha, \beta_{j\pm\frac{1}{2},k} = \frac{\alpha, \beta_{j,k} \pm \alpha, \beta_{j\pm1,k}}{2} \tag{2.30}$$

2.10 Low Mach Preconditioning

Since a flapping wing MAV operates in low-Mach and low-Reynolds Number flight regimes, it is necessary to employ a low-Mach preconditioner to

help maintain accuracy and convergence of the compressible Navier-Stokes flow solver. The discretized form of the compressible Navier-stokes equations does not converge upon the incompressible solution as Mach number approaches zero. Thus, use of the preconditioner resolves this issue and achieves several specific goals, among which two are listed below.

1. Since there is a large difference between eigenvalues in low Mach flows, the solution is computationally stiff and therefore requires more time to reach a steady-state solution. The preconditioner accelerates convergence by bringing the magnitude of the acoustic eigenvalues closer to the convective eigenvalues, thereby reducing stiffness.

2. A low-Mach preconditioner removes scaling inaccuracies between dissipation terms. This is most beneficial near the stagnation term and near surface boundary layers, since the preconditioner makes the pressure terms and convective terms more consistent to each other [139].

In this work, time accurate low Mach preconditioning in dual-time scheme described by Buelow et al. [121] and Pandya et al. [122] is used.

2.11 Implicit Time Marching and Dual Time-Stepping

The spatial discretization as described earlier solves for the fluxes at the right hand side (RHS) of equation 2.26. In most CFD solvers, implicit time marching is preferred over explicit schemes (due to the lack of a numerical

stability limit), for evolution of the conservative variable, $\hat{Q}$ in time. Explicit schemes only solve the governing equations at a later timestep $t + \Delta t$ using information from the current state of the system. However, they require an impractically small Δt to converge stiff problems while keeping the error bounded, and can diverge with a larger timestep size. Implicit methods, conversely, solve simultaneously at both at the current timestep, t, and the next timestep, $t + \Delta t$. Hence, implicit schemes do not suffer from the same stability problems, and a larger timestep can be taken to converge the solution faster. When Equation 2.26 is written in a generic discretized delta form using an implicit algorithm, the following expression is obtained:

$$LHS\Delta\hat{Q}^n = -\Delta t RHS \tag{2.31}$$

where the right-hand side (RHS) represents the fluxes that comprise the "physics" of the problem, and the left-hand side represents the implicit scheme which comprise the "numerics" and determine the rate of convergence. "n" denotes the current timestep. The implicit algorithm produces a large sparse banded matrix, which is then solved to obtain a solution for $\hat{Q}^n$. Typically, approximate factorization methods are used to solve such sparse systems. For time-dependent calculations, such as the unsteady moving mesh problems associated with flapping wings, dual timestepping [137] may be used to aid in convergence. With dual time-stepping, a series of pseudo-timesteps are introduced per physical time step, such that the unsteady problem becomes a pseudo-steady problem. However, care must be taken to ensure that the dual

timestepping scheme undergoes enough sub-iterations such that an accurate transient solution is achieved. Typically, a drop in the unsteady residual of two orders of magnitude is sufficient to ensure that each physical timestep is well-converged.

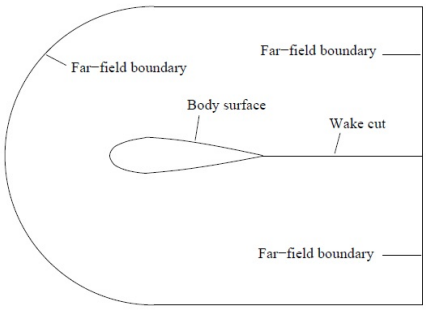

Figure 2.6: **C-mesh topology [105]**

2.12 Boundary Conditions

The governing equations described above are very generic and do not change from one problem to another. Therefore, apart from these conservation equations, initial and boundary conditions are needed to define a problem.

Initial conditions are specified by assigning the density, flow velocities and pressure everywhere in the solution region before the start of the solution procedure. Typically for a flapping wing MAV in forward flight, the initial conditions are set such that the density and pressure and flow velocities are freestream values.

The two common boundary conditions for an external flow are the wall boundary condition and the far-field boundary condition. Wall boundaries are

natural boundaries of the physical domain which arise from the wall surfaces being exposed to the flow. For a viscous fluid which passes a solid wall, the relative velocity between the surface and the fluid directly at the surface is zero. The truncation of the physical domain or system for the purpose of numerical simulation leads to artificial far-field boundaries, where certain physical quantities have to be prescribed. The far-field boundary condition has to fulfill two basic requirements. First, the truncation of the domain should have no notable effects on the flow solution as compared to the infinite domain. Second, any outgoing disturbances must not be reflected back into the flow-field.

Additional boundaries become manifest in the numerical simulation due to the mesh system and grid topology, namely, wake-cut boundary, periodic boundary, boundary between blocks, chimera boundary etc. All of these boundaries are numerical in nature rather than physical.

Typical boundaries found in the solution of the Navier-Stokes equations can be shown on a schematic C-mesh, Figure 2.6. They include wall boundary, far-field boundary and wake cut boundary. A brief numerical description of these boundaries are given below.

2.12.1 Wall Boundary Condition

In this work, all the solid walls are treated as viscous wall. Therefore no-slip condition is applied, which requires the fluid velocity at the wall be equal to the surface velocity. At the solid wall, the density (ρ) is extrapolated (zeroth

order) from the interior of the domain. The pressure (p) is then obtained from the normal momentum equation.

2.12.2 Far-field Boundary Condition

The farfield boundary on the background mesh is placed as far away in the radial direction from body surfaces as computationally practical such that the conditions at these mesh points are very close to freestream. Characteristic-based Riemann invariants [138], which are extrapolated from the interior or the freestream and are based on the direction of the velocity vector and sonic velocity, are used to determine these boundary conditions. Hence, this ensures that there are no spurious wave reflections at the boundary.

2.12.3 Wake Cut Boundary Condition

At the wake cut region, grid planes collapse on to each other. Along these planes, an explicit simple average of the solution from either side is used. Similar boundaries are present at the root and tip of a C-O grid and are treated in the same manner.

2.12.4 Overset Boundary

The overset boundaries are determined by the Implicit Hole-Cutting code, and are used to provide connectivity information between the blade and background meshes. Further details were described earlier in Section 2.3.

Chapter 3

Aerodynamic Analysis of Rigid Wings

OVERTURNS has been used extensively for rotary wing applications. During this study, it was extended to flapping wings for the first time. In order to determine the applicability of OVERTURNS for flapping wing MAVs, validation of the code was carried out for different conditions. First, 2D flow conditions were simulated. Once satisfactory correlation was achieved with prior research, 3D validation for rigid wing kinematics was carried out.

3.1 2D Code Validation for Pitching and Plunging Airfoils

The code was first validated for pure plunge cases at relatively high chord-based Reynolds numbers (10^6) against the simulations carried out by Tuncer et al. [91, 92]. Combined pitch and plunge was then simulated, again at relatively high Reynolds numbers (10^5), and results were validated with those of Isogai et al. [93]. Finally, analysis was carried out for MAV scale Reynolds numbers and results were validated with predictions by Yuan et al. [81].

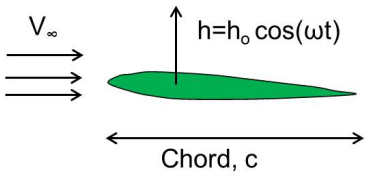

Figure 3.1: **Schematics of plunge kinematics**

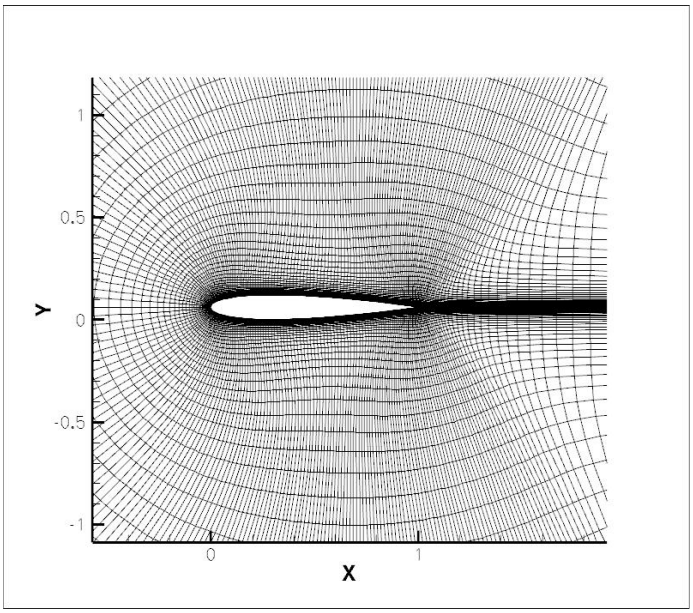

Figure 3.2: **C-grid for NACA 0012**

3.1.1 Pure Plunge ($M = 0.3$, $Re = 10^6$)

First, a flapping NACA0012 airfoil at relatively high Mach number for MAV applications of 0.3, and Reynolds number of 10^6, which was computationally investigated by Tuncer and Platzer [92] was considered. They used a thin layer Navier-Stokes solver to carry out the analysis.

The airfoil kinematics was given by:

$$h = h_o cos(\omega t) \tag{3.1}$$

where, plunge amplitude (h_o) was varied from 0.4 c to 1.4 c, and reduced

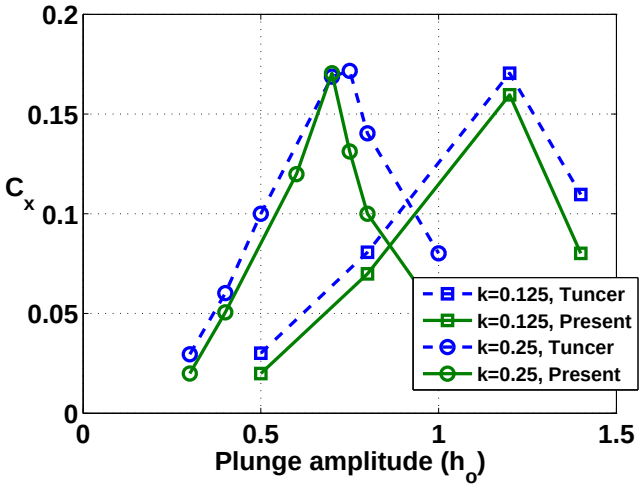

Figure 3.3: **Variation of C_x with plunge amplitude (pure plunge)**

frequencies ($k = 2\pi fc/(2U)$) of 0.125 and 0.25 were considered. A schematics is shown in Figure 3.1 The non-dimensional time for various positions during the flap cycle are as shown in Table 3.1. This convention will be used for all the results.

Table 3.1: **Instantaneous wing positions during flap cycle**

Wing position	**Non-dimensional time (t/T)**
Top of Downstroke	0
Middle of Downstroke	0.25
Bottom of Downstroke	0.5
Middle of Upstroke	0.75

Grid convergence study was carried out for C-type grids with 491×128, 327×85 and 121×62 points. No significant difference was seen between the

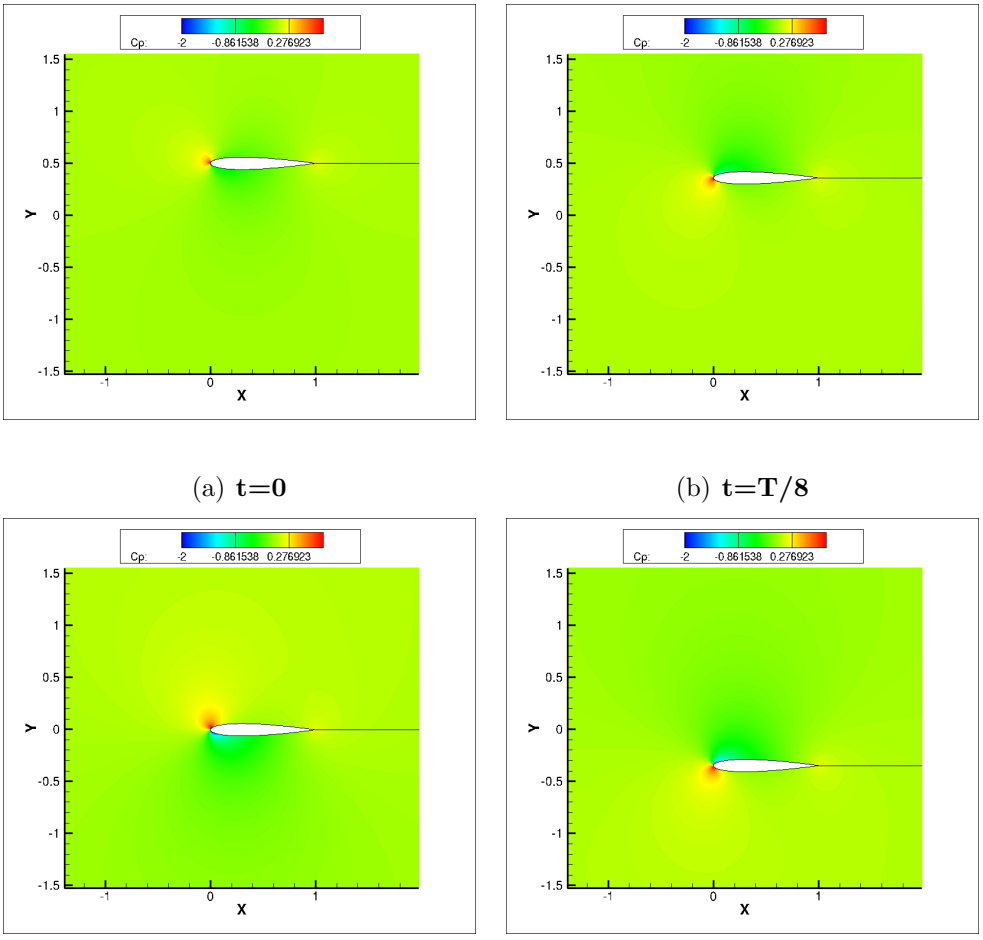

(a) **t=0** (b) **t=T/8**

(c) **t=T/4** (d) **t=3T/8**

Figure 3.4: C_p **contours for pure plunge case (**$k = 0.125, h_o = 0.5$**c)**

first two cases. Results are presented here for the grid with 327 points in the streamwise and 85 points in the normal direction (Figure 3.2).

Figure 3.3 shows the variation of average propulsive force with plunge amplitude for both the reduced frequencies. Good correlation is observed between the results from the present study and those by Tuncer et al. [92]. It can be seen that as the plunge amplitude is increased, the mean propulsive force coefficient (C_x) increases till a certain point and then drops sharply. Fig-

ure 3.4 shows the pressure coefficient contours for the case with $k = 0.125$ and $h_o = 0.5$ c at different instant of the downstroke. There is a formation of small leading edge suction which leads to the positive propulsive force. Figure 3.5 shows the pressure coefficient contours for the same reduced frequency and higher plunge amplitude of 1.2 c. As compared to Figure 3.4, a greater leading suction is formed, which leads to greater propulsive force.

As the plunge amplitude is increased even further, a leading edge vortex is formed over the airfoil. As long as the vortex is ahead of the position of maximum thickness of the airfoil, it produces a positive propulsive force. But, with further increase in plunge amplitude, the leading edge vortex is shed during the flap cycle and moves aft towards the trailing edge. The low pressure center of this aft moving vortex creates a force which is vectored in the negative propulsive direction, thus decreasing the propulsive force. This is illustrated in Figure 3.6, which shows the contour plots of pressure coefficient over the airfoil as it moves during the downstroke, for the case with k = 0.125, $h_o = 1.4$ c.

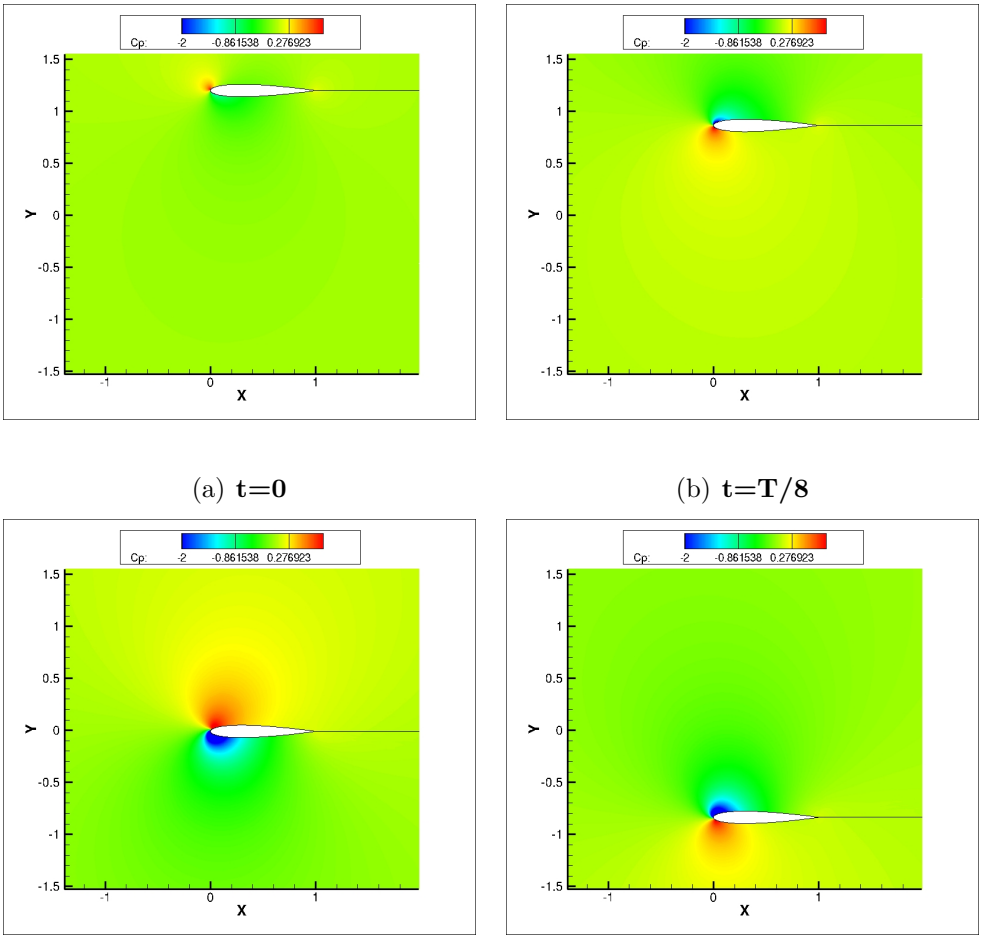

(a) **t=0** (b) **t=T/8**

(c) **t=T/4** (d) **t=3T/8**

Figure 3.5: C_p **contours for pure plunge case (**$k = 0.125, h_o = 1.2$ **c)**

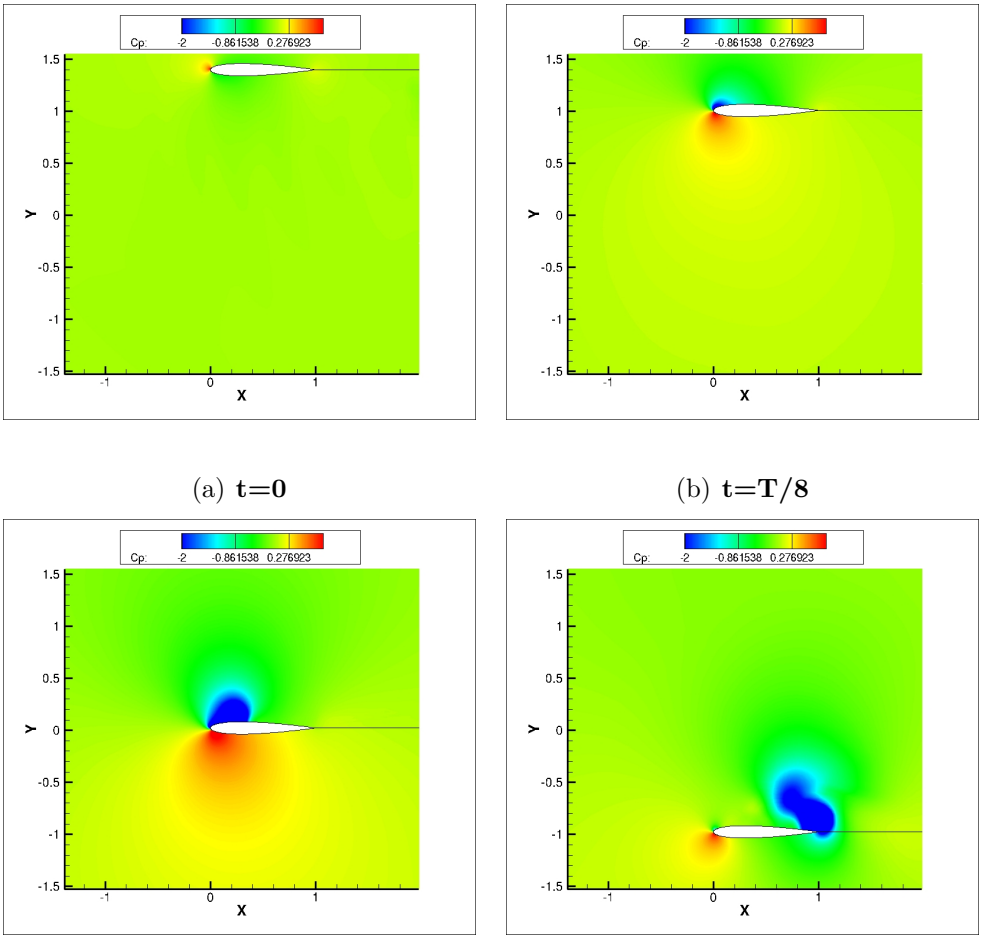

(a) **t=0** (b) **t=T/8**

(c) **t=T/4** (d) **t=3T/8**

Figure 3.6: C_p **contours for pure plunge case (**$k = 0.125, h_o = 1.4$ **c)**

3.1.2 Pure Plunge: Higher Reduced frequency ($M = 0.3$, $Re = 10^6$)

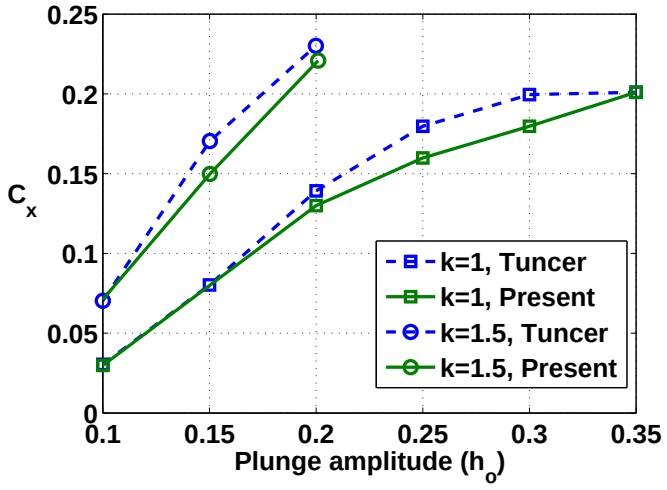

Figure 3.7: **Variation of propulsive force with frequency for higher reduced frequencies (pure plunge)**

Next, higher frequency cases were considered [91] ($k = 1.0$ and 1.5). The onset of dynamic stall did not have a very drastic effect in these cases. As in the previous case, an increase in plunge amplitude leads to an increase in the propulsive force as shown in Figure 3.7. Figures 3.8 and 3.9 show the pressure coefficient contours for the configurations with $k = 1$, and $h_o = 0.1$ c and 0.35 c, respectively. However, unlike the previous case, a sharp drop in propulsive force is not observed as plunge amplitude is increased (Figure 3.7). This is because the leading edge vortex did not have sufficient time to develop and convect aft of the airfoil due to high frequency plunging motion (Figure 3.9). Thus, the suction force due to the vortex is always pointed in the propulsive

direction and we do not see a drop off in the propulsive force. The current simulation predicts this behavior correctly and compares well with the results by Tuncer et al [92].

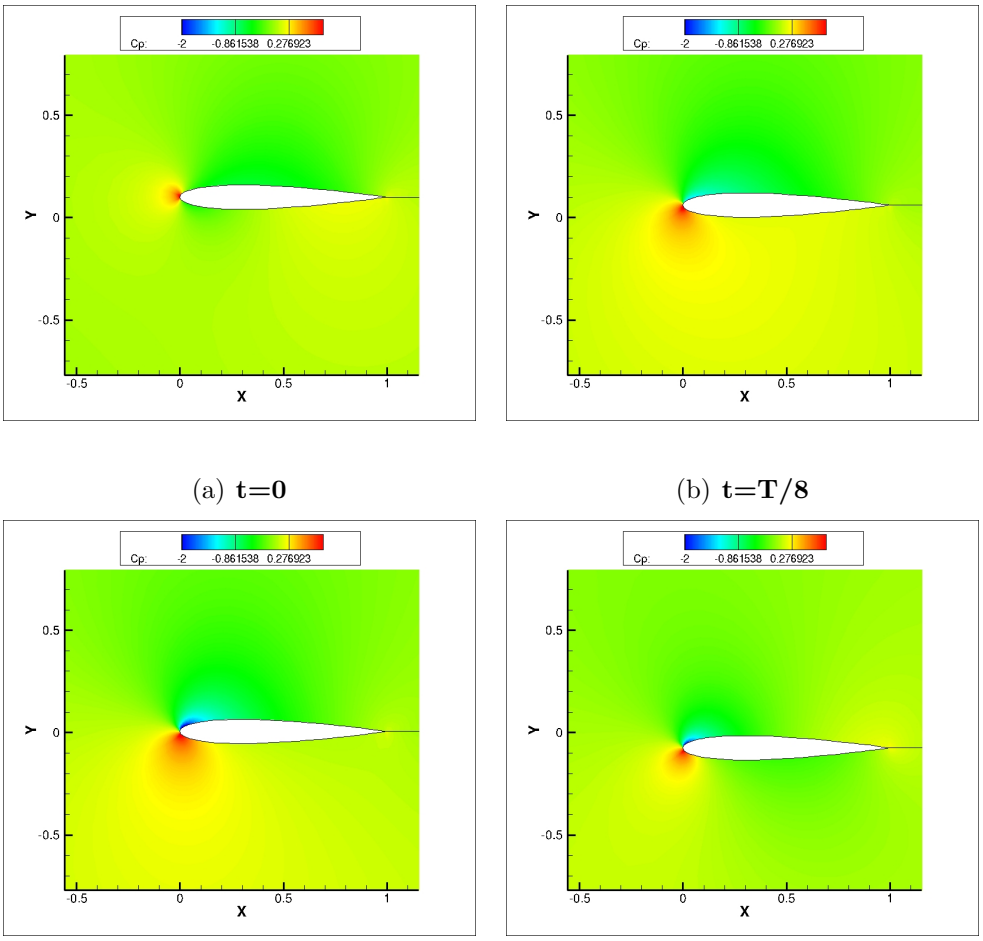

(a) **t=0** (b) **t=T/8**

(c) **t=T/4** (d) **t=3T/8**

Figure 3.8: C_p **contours for pure plunge case (**$k = 1.0, h_o = 0.1$ **c)**

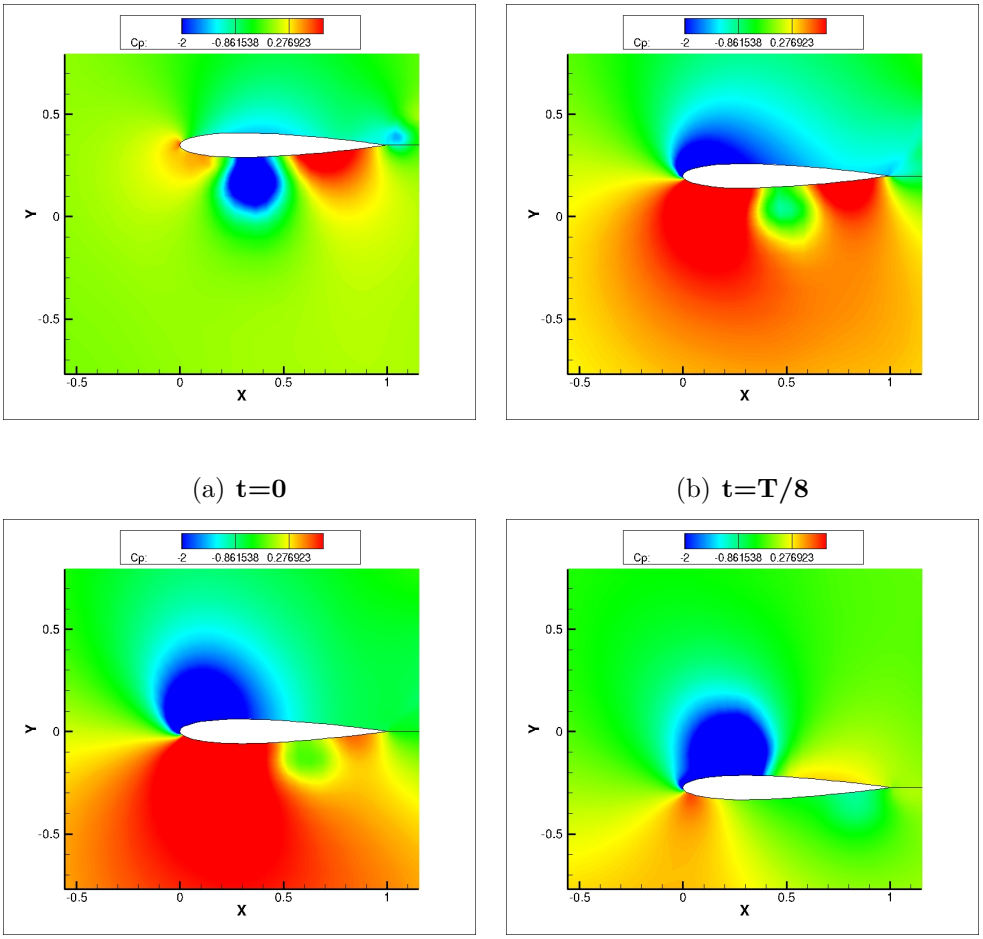

(a) **t=0** (b) **t=T/8**

(c) **t=T/4** (d) **t=3T/8**

Figure 3.9: C_p **contours for pure plunge case (**$k = 1.0, h_o = 0.35$ **c)**

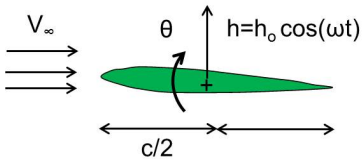

Figure 3.10: **Schematics of plunge plus pitch kinematics**

3.1.3 Combined Pitch and Plunge Motions ($M = 0.3$, $Re = 10^5$)

The third case considered was combined pitch and plunge motion. Validation was carried out with the results by Isogai et al. [93]. The airfoil oscillates in pitch about mid-chord at Mach number of 0.3 and Reynolds number of 10^5. The pitch and plunge motions are given by: $h = h_o cos(kt)$ and $\theta = \theta_o cos(kt + \phi)$.

For the first combined pitch and plunge case, (Case A), h_o = 0.5 c and α_0= 20°, results are shown in Figure 3.11. The phase difference (ϕ) between pitch and plunge determines the effective angle of attack. As the frequency is increased, a shift in phase angle is observed at the frequency at which the highest C_x occurs.

For the second combined pitch and plunge case, (Case B), h_o = 1 c, α_0 = 10°, results are presented in Figure 3.12. Due to higher plunge amplitudes, large-scale leading edge separation occurs. This separation increases as the frequency is increased and thus, reduces the propulsive force. For a phase difference of 90°, the maximum effective angle of attack is reduced and thus stall is avoided. Hence, highest propulsive force is obtained for ϕ = 90°. The results from the current simulation correlate well with those by Isogai et al. [93]

in both the cases.

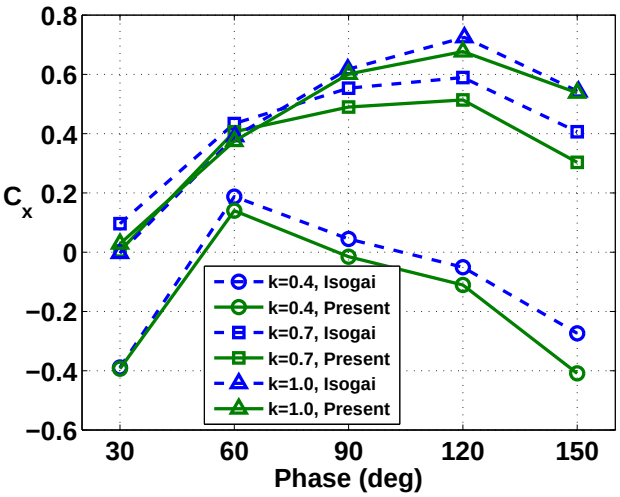

Figure 3.11: **Case A,** $h_o = 0.5$**c and** $\alpha_0 = 20°$ **(combined pitch and plunge)**

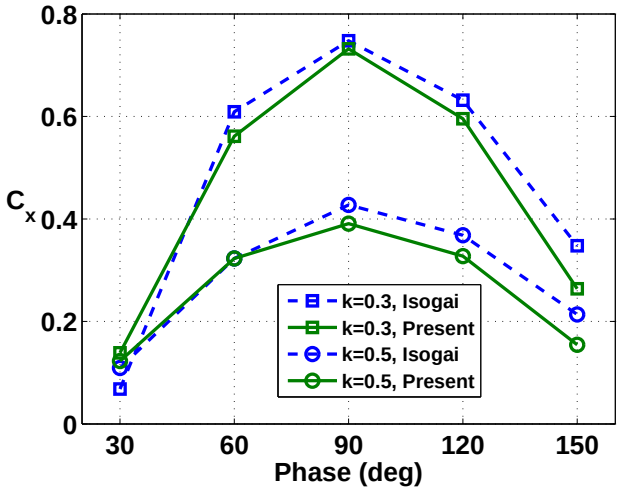

Figure 3.12: **Case B,** $h_o = 1.0$**c and** $\alpha_0 = 10°$ **(combined pitch and plunge)**

To explore the physics in some more detail, the pressure coefficient contours for Case B with $\phi = 30°$ and $90°$ are plotted in Figure 3.13 and 3.14

respectively. As mentioned earlier, by having a phase difference of 90° between the plunge and pitch, the maximum effective angle of attack during the downstroke is reduced and stall can be avoided. It can be seen that as compared to the case with $\phi = 30°$, the leading vortex is more attached to the airfoil for the phase difference of 90°. This leads to a greater propulsive force in the latter case.

It should also be noted that in case of combined pitch and plunge, the direction in which the chordwise force points is a result of the positioning of the leading edge vortex and also the instantaneous pitch angle. Comparing the average propulsive force for combined pitch and plunge motion with that of pure plunge motion, it is observed that in general, the use of combined mechanism can produce higher propulsive force values. Also, if the phasing between pitch and plunge, and the reduced frequency is tailored correctly, the propulsive force generated can be significantly increased. Some more details for the combined pitch and plunge case are given in the next subsection.

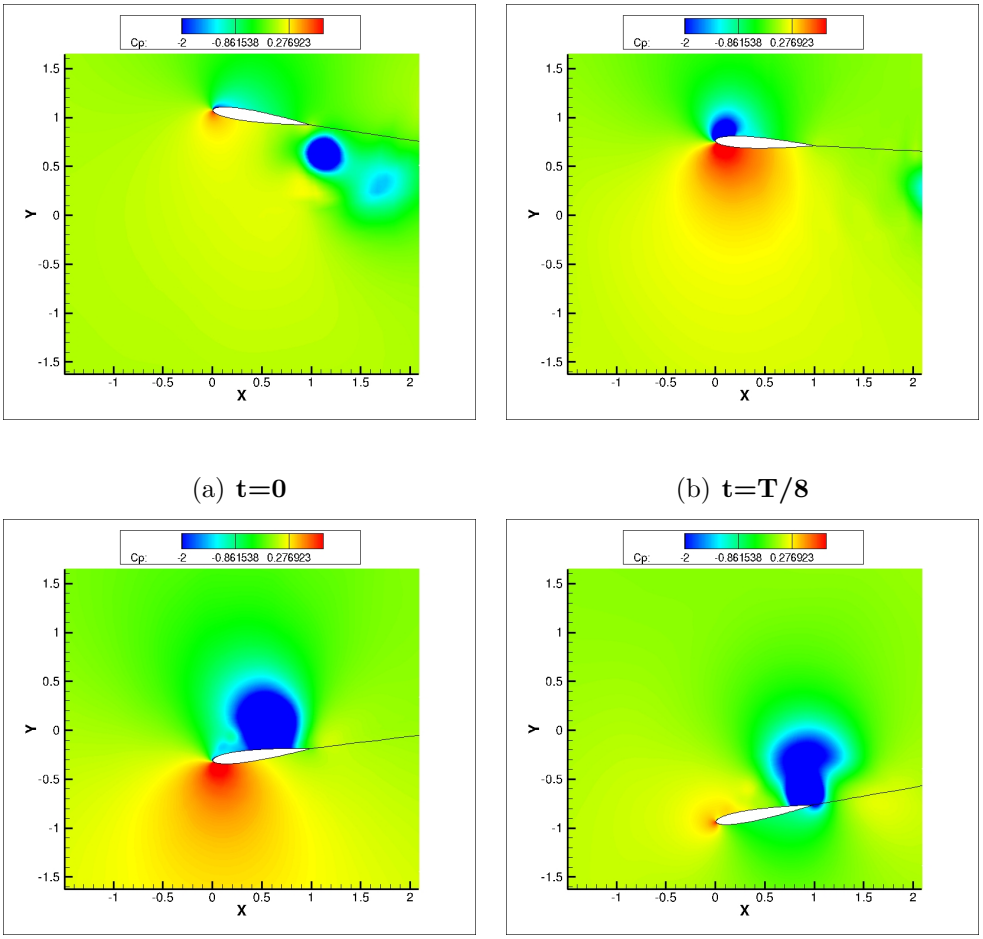

(a) **t=0** (b) **t=T/8**

(c) **t=T/4** (d) **t=3T/8**

Figure 3.13: C_p **contours for plunge + pitch case** ($k = 0.3, \phi = 30°$)

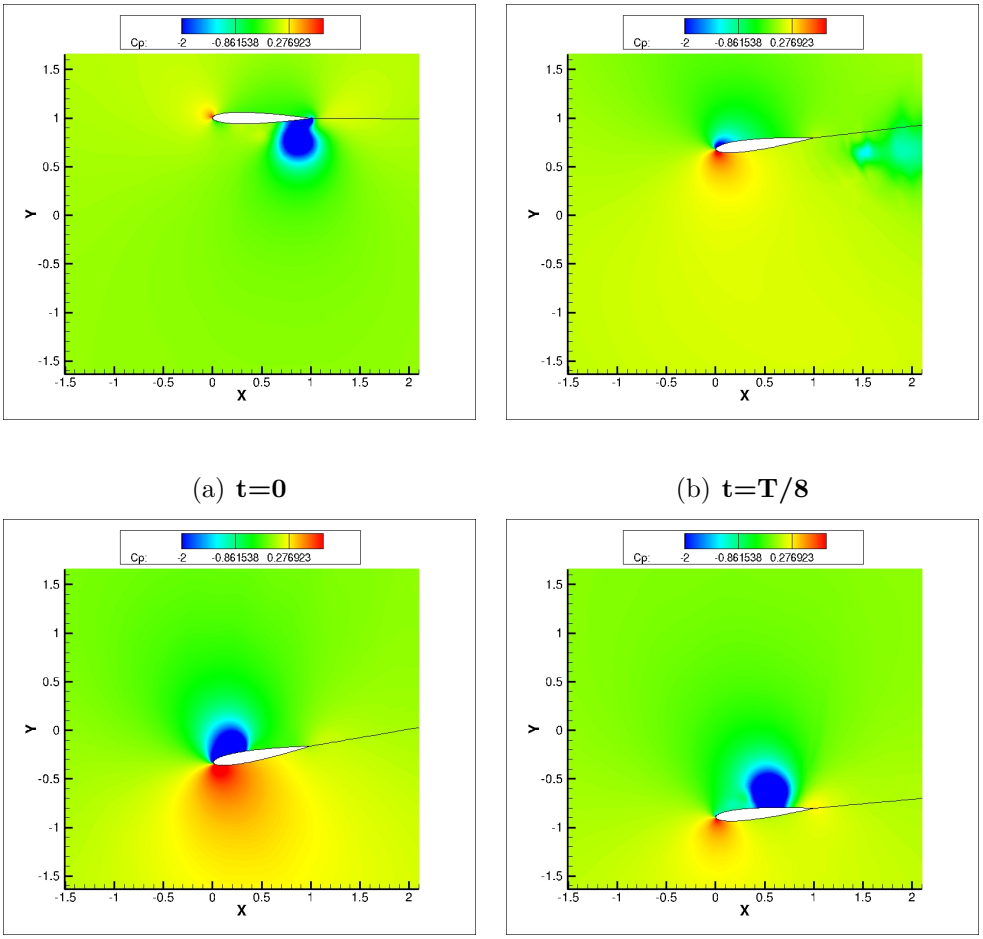

(a) **t=0** (b) **t=T/8**

(c) **t=T/4** (d) **t=3T/8**

Figure 3.14: C_p **contours for plunge + pitch case** ($k = 0.3, \phi = 90°$)

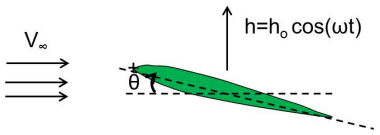

Figure 3.15: **Schematics of plunge plus pitch kinematics for low Re case**

3.1.4 Low Reynolds number case ($Re = 15,000$): Combined Pitch and Plunge

Next, combined pitch and plunge at Reynolds number of $15,000$ (based on maximum plunge velocity) was considered, which is more representative of flapping wing MAVs.

Validation of instantaneous forces was carried out with the 2D simulation done by Yuan et al. [81] for a pitching and plunging NACA 0005 airfoil. The plunge amplitude is one chord and pitching amplitude is 40°. The airfoil oscillates about the leading edge. A schematic is shown in Figure 3.15. The phase difference between the pitch and plunge is 90°. The reduced frequency is 1.6.

Yuan et al. used an incompressible solver for their simulation. Since a compressible solver was used in this study, the freestream Mach number was set to 0.05, which was well within the incompressible limits. The instantaneous vertical and propulsive force variation over a flap cycle from the current simulation was compared with that from Yuan et al. in Figures 3.16 and 3.17, respectively. Note that, $t/T = 0$ corresponds to when the airfoil is at the

highest plunge position.

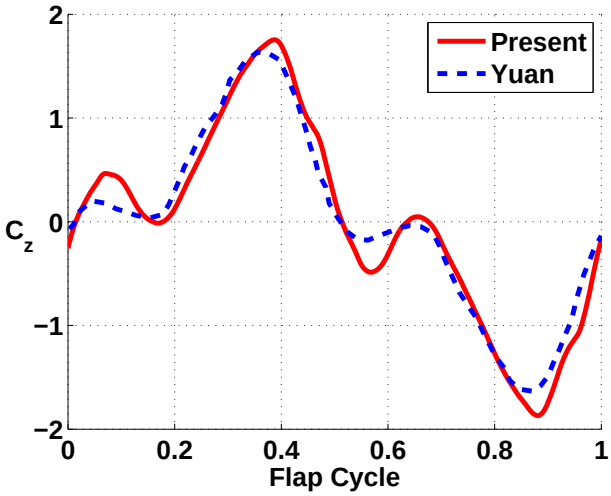

Figure 3.16: C_z **Variation with time for low** Re **(combined pitch and plunge)**

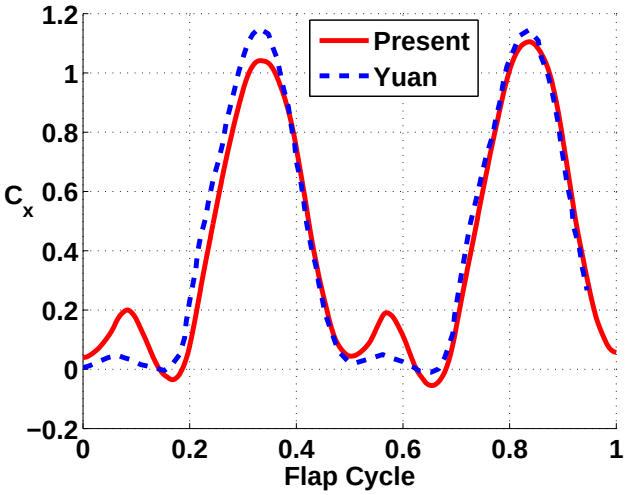

Figure 3.17: C_x **Variation with time for low Re (combined pitch and plunge)**

Satisfactory correlation is obtained with the predictions by Yuan et al. The average force in vertical direction, F_Z is zero because it cancels out in the

upstroke and downstroke. On the other hand, positive propulsive force is generated during both the strokes as a result of the this kinematics and therefore, a net propulsive force is produced over a plunge cycle. The average propulsive force coefficient predicted by the current simulation was 0.40. Though the average vertical force coefficient is zero, the maximum instantaneous vertical force coefficient reaches a value of 1.75 at $t/T = 0.4$ when the effective angle of attack of the airfoil is 38°. Though statically, the airfoil would have stalled at such high angles, due to the unsteady effects, a large unsteady force is obtained in the vertical direction.

A more detailed comparison of the two results was obtained by comparing the contours of pressure coefficient, shown in Figure 3.18 at different instances in time. The pressure coefficient was obtained by normalizing with respect to the maximum plunge velocity. Again, there is satisfactory agreement between the results obtained from the present study and results by Yuan et al., clearly demonstrating the validity of the current methodology. Note that, the present case closely mimics the reference section of the 3D root flapping simulation mentioned in a later section and some discussion on the pressure contour plot will be done at that point (Section 3.2.2).

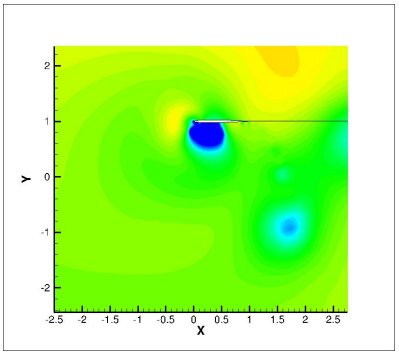

(a) **t=0, Present**

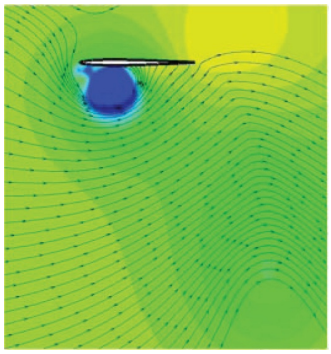

(b) **t=0, Yuan**

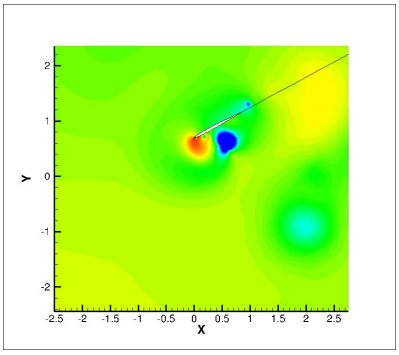

(c) **t=T/8, Present**

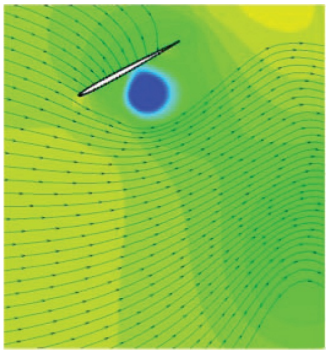

(d) **t=T/8, Yuan**

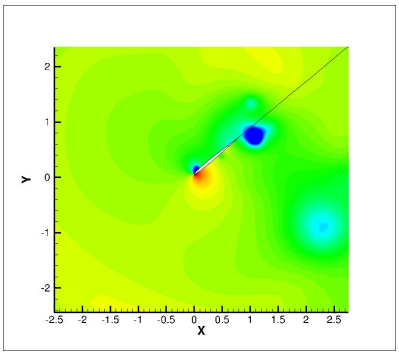

(e) **t=T/4, Present**

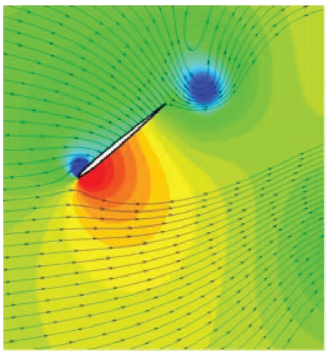

(f) **t=T/4, Yuan**

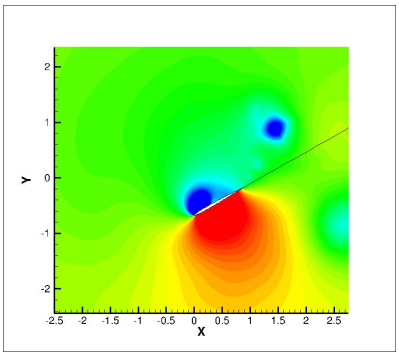

(g) **t=3T/8, Present**

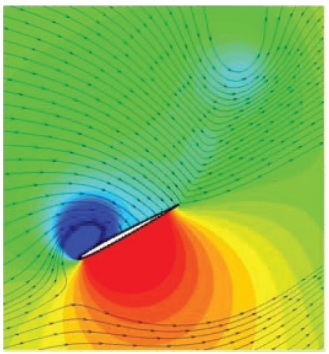

(h) **t=3T/8, Yuan**

Figure 3.18: **Pressure contours for 2D Simulation at low Re (combined pitch and plunge)**

3.2 3D Code Validation

Having obtained good validation for 2D simulation, the next step was to validate the methodology in 3D flow environment. Two types of wing motions were considered. The first motion is the entire wing heaving and pitching. The second type of motion is closer to avian flight with the flapping wing fixed at the root.

3.2.1 Flat plate with Aspect Ratio of 2 (Pitching+Plunging)

3.2.1.1 Description of Test Case

For the first type of motion, wing heaving and pitching, experiments conducted by Hart et al. [80] at UF-REEF low Reynolds number Aerodynamic Characterization Facility (ACF) were simulated. These experiments were carried out on a flat plate with t/c of 3.07% at Reynolds number of $40,000$ based on chord and free stream velocity. A LaVision particle image velocimetery (PIV) system was used to make velocity field measurements around the flat plate at several specific times throughout the wing motion in a streamwise plane at the $3/4^{th}$ spanwise location of the wing. Force data was measured using Applied Aerospaces MC-.10-.375 6-component strain gauge balance. The test set up is shown in Figure 3.19.

The plunge kinematics is defined by

$h = h_o cos(2\pi f t)$

and the pitch kinematics is defined by

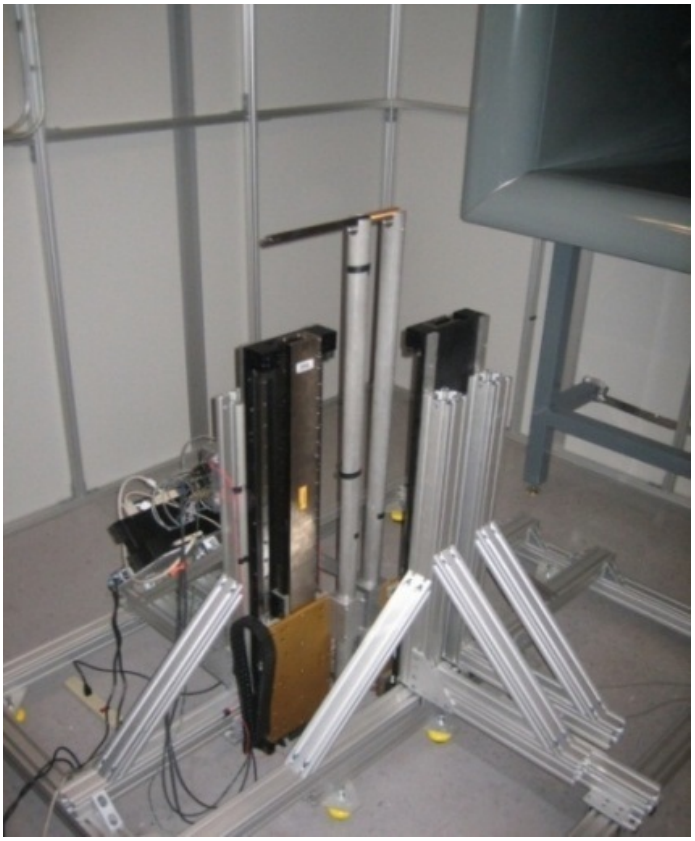

Figure 3.19: **Dynamic Pitch Plunge Rig at University of Florida low Reynolds number Aerodynamic Characterization Facility[80]**

$$\theta = \theta_a cos(2\pi ft + \phi) + \theta_o$$

Two cases were examined: pure plunge (Case 1) and combined pitch and plunge (Case 2). The parameters for the two cases are shown in Table 3.2. The reduced frequency is 0.5. These are same as the canonical problems, which are the subject of AVT-149 NATO task group and were simulated at University of Michigan using a RANS solver [97]. Results from the analysis done at University of Michigan are also presented here for comparison.

Table 3.2: **Parameters for flat plate wing (combined pitch and plunge)**

Case	h_o	**f(Hz)**	θ_o	θ_a	ϕ
1	0.5	2	8	0	0
2	0.5	2	8	8.45	90

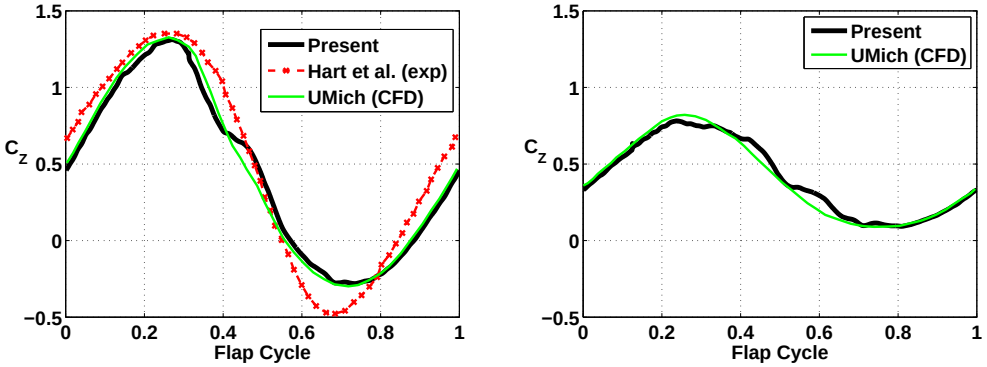

(a) Case 1 (b) Case 2

Figure 3.20: C_Z **variation with time for 3D flat plate**

3.2.1.2 Description of Computational Model

The present simulation was run on a body-fitted curvilinear C-O type blade mesh with clustering at the blade tips, leading edge, and trailing edge to capture all the flow structures. The grid had 277 points in wrap around, 109 points in spanwise and 85 points in normal directions. The outer boundary of the mesh extended to 20 chords away from the blade in all directions. Calculations were done using 1440 iterations per cycle and each iteration used 6 sub-iterations to remove linearization error.

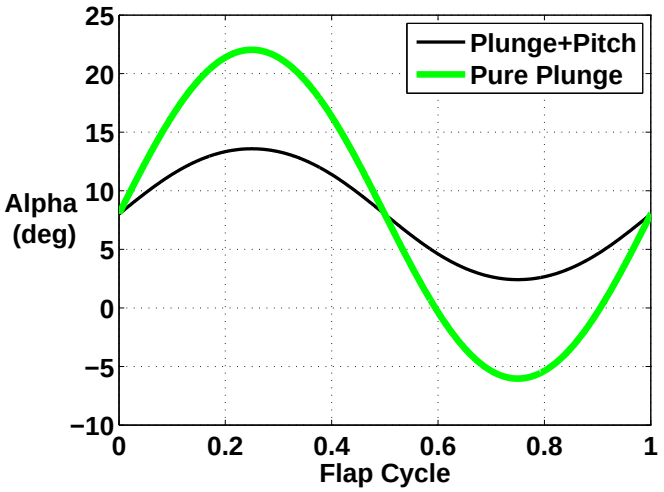

Figure 3.21: **Variation of angle of attack over a flap cycle**

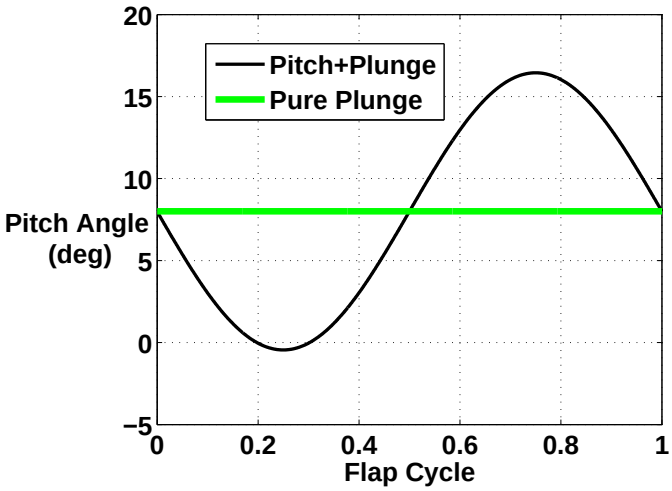

Figure 3.22: **Variation of pitch angle over a flap cycle**

3.2.1.3 Results

Both these cases produce a net force in the vertical direction, F_Z due to the mean positive pitch angle. Figure 3.20 shows the instantaneous vertical force variation over a flap cycle from the present study and prior results. It should be noted that Hart et. al have not presented the instantaneous force

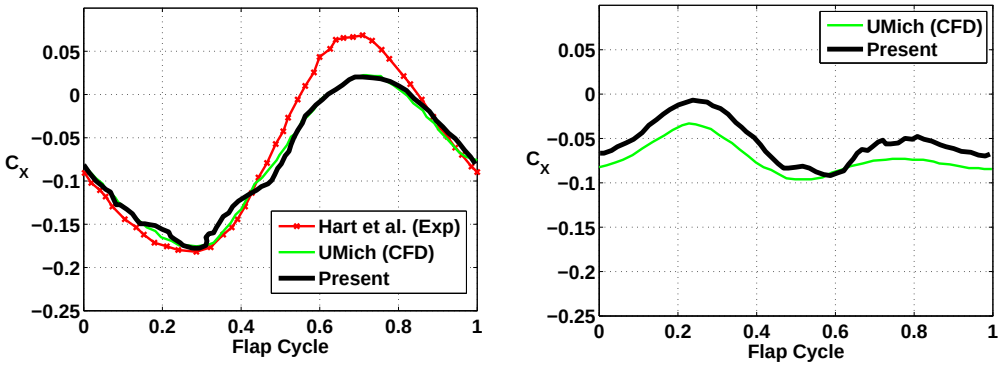

(a) **Case 1** (b) **Case 2**

Figure 3.23: **Instantaneous C_X variation over a flap cycle for 3D flat plate**

variation for case 2 so here comparison is shown with results from University of Michigan. Satisfactory co-relation is obtained with experiments and Michigan analysis.

The average vertical force coefficient over a cycle for the cases 1 (pure plunge) and 2 (combined pitch and plunge) from current study are 0.443 and 0.415, respectively. Even though, the mean vertical force between the two cases differ by only about 6%, the maximum instantaneous vertical force attained by case 1 is significantly higher compared to that of case 2. This is because of the larger maximum instantaneous effective angles seen by the blade in case 1 as compared to case 2 (Figure 3.21). The effective angle is defined here as the angle at quarter chord based on pitch angle (shown in Figure 3.22) and plunge velocity. Also, the maximum instantaneous value of vertical force coefficient for pure plunge (case 1) is 1.31 and differs by 6% from Hart et al.

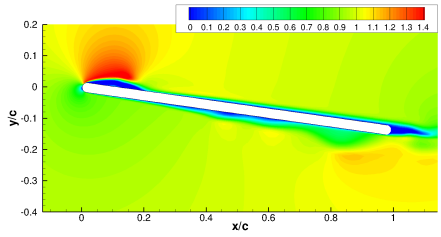

(a) **t=0, Present**

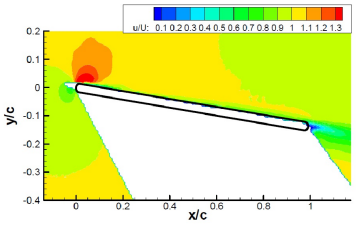

(b) **t=0, Hart et al.**

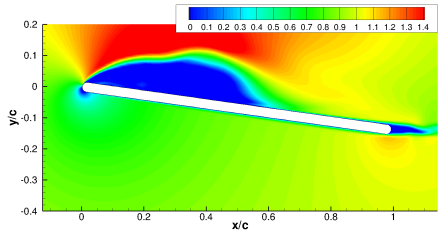

(c) **t=T/4, Present**

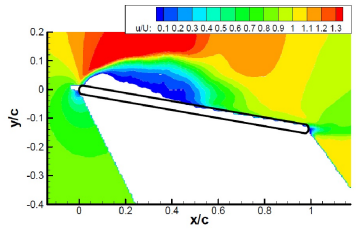

(d) **t=T/4, Hart et al.**

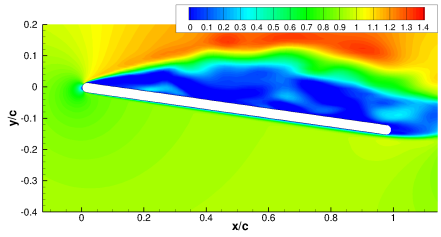

(e) **t=T/2, Present**

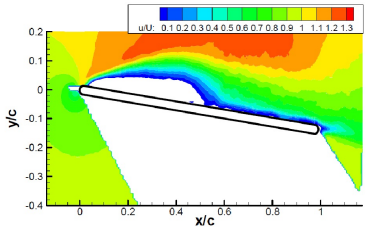

(f) **t=T/2, Hart et al.**

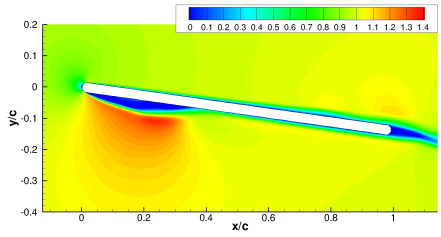

(g) **t=3T/4, Present**

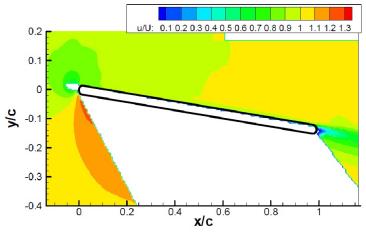

(h) **t=3T/4, Hart et al.**

Figure 3.24: **Velocity Contours for Case 1 at $3/4^{th}$ span, 3D flat plate**

The maximum angle of attack for this is 22° and occurs at $t/T = 0.25$. The static C_L for this flat plate at angle of attack of 22° is 0.73 from the result by Meuller [140]. Therefore, due to unsteady effects, the vertical force coefficient

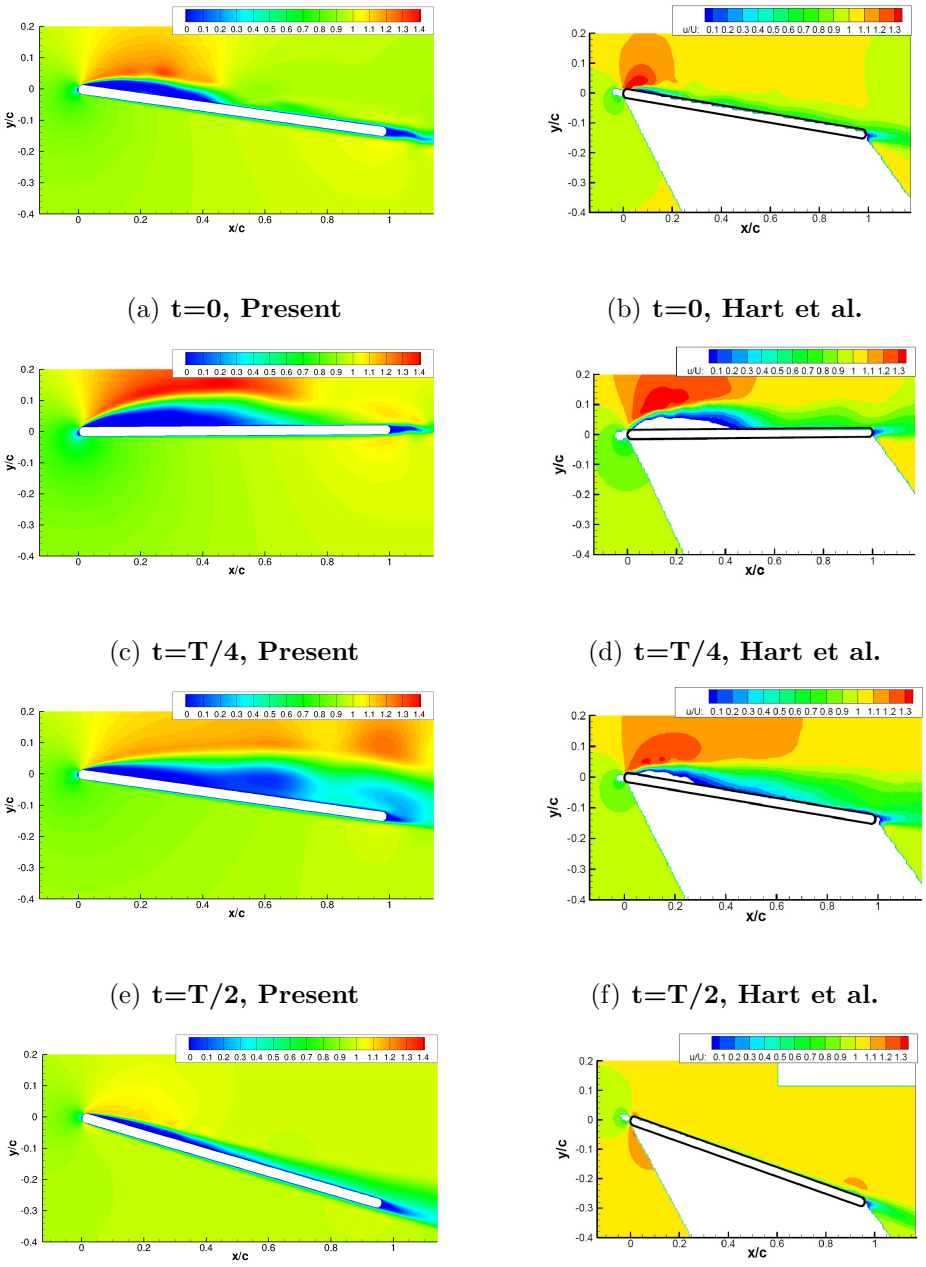

(a) **t=0, Present** (b) **t=0, Hart et al.**

(c) **t=T/4, Present** (d) **t=T/4, Hart et al.**

(e) **t=T/2, Present** (f) **t=T/2, Hart et al.**

(g) **t=3T/4, Present** (h) **t=3T/4, Hart et al.**

Figure 3.25: **Velocity Contours for Case 2 at** $3/4^{th}$ **span, 3D flat plate**

is much greater than the static value (79% increase) at the same effective angle of attack and clearly shows the benefit of unsteady effects.

Figure 3.23 shows the variation of C_X over a flap cycle for the pure plunge

(case 1) and combined plunge and pitch cases (case 2). From these results, cases 1 and 2 have a mean propulsive force value of -0.0742 and -0.0526 . Even though, the numbers look comparable, case 1 actually produces about 30% higher negative propulsive force compared to case 2. Case 1 also has larger maximum instantaneous propulsive force in the negative direction. Therefore, the use of pitching motion along with the plunge motion is helping in reducing the average negative propulsive force or drag.

Figures 3.24 and 3.25 compare the velocity contour (normalized by the freestream velocity) at $3/4^{th}$ span from the current simulation with experimental results for the respective cases. Even though, there are some differences in the magnitude, overall there is a good correlation between the PIV data of Hart et al. [80] and the current predictions. As expected, both the cases show separation during the mid-stroke due to the higher instantaneous effective angles seen during this period. For the same reason, case 1 shows larger separation when compared to case 2. Further, it can be seen from these plots, due to large flow separation, the force generated by its low pressure is vectored in the negative propulsive direction. This is consistent with what was seen before while looking at the instantaneous forces. In addition, this suggests that it might be possible to produce positive propulsive force instead of negative propulsive force for the same flow conditions by choosing the kinematics appropriately. One possibility would be to have a kinematics such that the wing is pitched in the opposite direction as compared to the effective angle due to the combined pitch and plunge motion during the mid-stroke. The lead-

ing edge vortex could thus be positioned to produce propulsive force. Such a kinematics was used in the next case studied.

3.2.2 Root based flapping (NACA 0005)

3.2.2.1 Description of Test Case

The second type of motion considered was a root flapping wing. A spanwise tapered wing with NACA 0005 airfoil cross section was experimentally studied by Yuan et al. [81] at the National Research Council (NRC), Canada in a water tunnel. The water tunnel has a 15 in (width) $\times$ 20 in (height) test section. The test set up is shown in Figure 3.26. The wing geometry is shown in Figure 3.27. It has a span of 0.15 m, root chord of 0.09 m and tip chord of 0.047 m. The reference section is chosen at a spanwise position of 0.25 m and has a chord of 0.07 m.

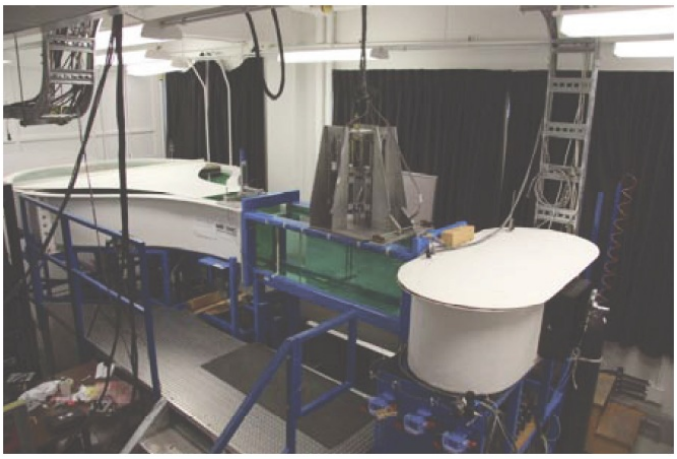

Figure 3.26: **The water tunnel at the NRC-IAR with the two-axis motion system installed[81]**

The flap kinematics are as follows:

Flap: $\gamma = \gamma_o cos(2\pi ft)$,

Pitch: θ = -$\theta_a sin(2\pi ft)$

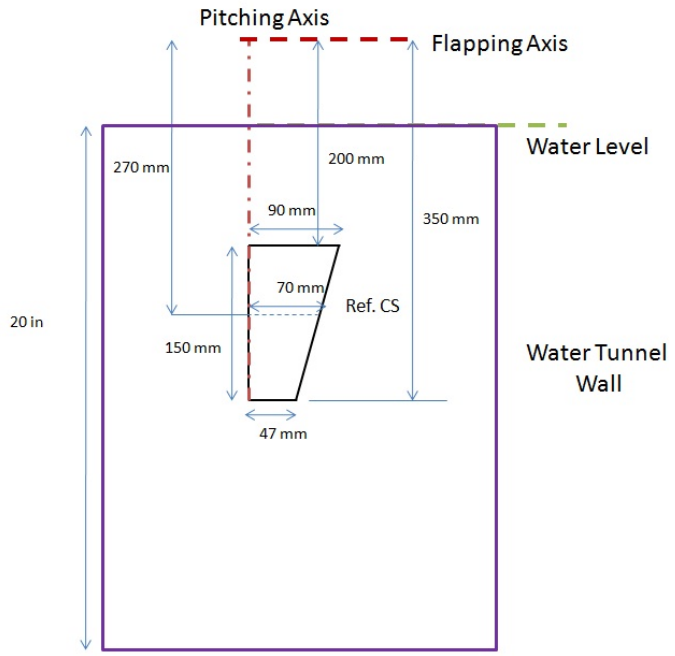

Figure 3.27: **Wing geometry for Yuan root flap case**

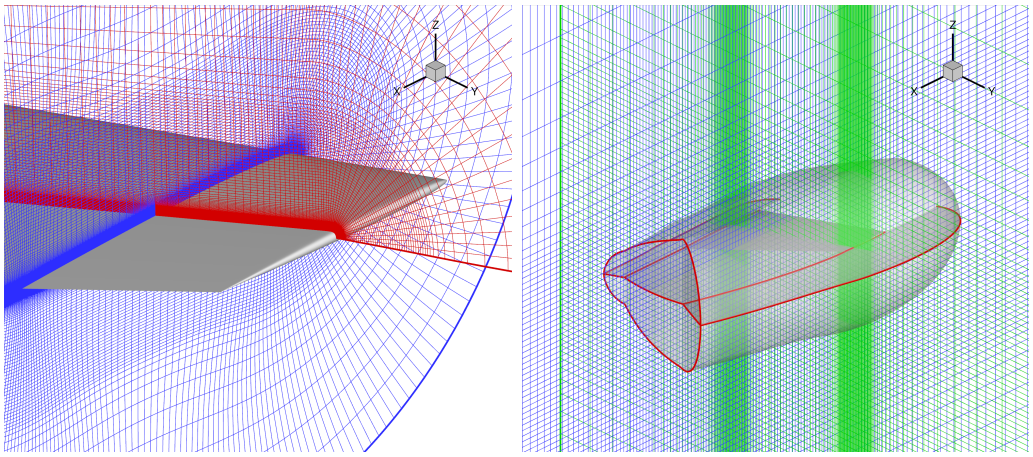

(a) **Blade mesh** ($267 \times 101 \times 93$)

(b) **Cartesian background mesh** ($172 \times 183 \times 92$) **with blade mesh boundary**

Figure 3.28: **Computational mesh for 3D root flapping wing simulation.**

with $\gamma_o = 15^\circ$ and $\theta_a = 40^\circ$. The flapping frequency was 0.46 Hz. The reduced frequency at the reference section was 1.6 based on reference chord and maximum tip velocity. The wing was pitched about the leading edge. The freestream velocity was 0.0635 m/s and the maximum tip velocity was 0.264 m/s. The reference velocity with which all the quantities are normalized is given by $\sqrt{(0.0635^2 + 0.264^2)} = 0.2715$ m/s. The Reynolds number at the reference section is about $19,000$ (based on the reference section chord and reference velocity).

Yuan et al. also carried out 3D computations using an incompressible solver to simulate their experiments. In their simulation, the flow was assumed to be laminar. In the current work, two separate simulations were carried out: one assuming fully turbulent flow and the other assuming fully laminar flow. No significant differences were found between the results. Therefore, only results from the laminar simulation are presented here.

3.2.2.2 Description of Computational Model

The simulation in the present work was carried out using a two mesh overset system consisting of a body-fitted curvilinear blade mesh overlayed onto a Cartesian background mesh. The blade mesh had clustering at the blade root and tip as well as leading and trailing edges. The Cartesian background was refined to resolve tip vortex evolution, see Figure 3.28. The blade mesh had 267 points in the wrap around, 101 points in the spanwise and 93 points

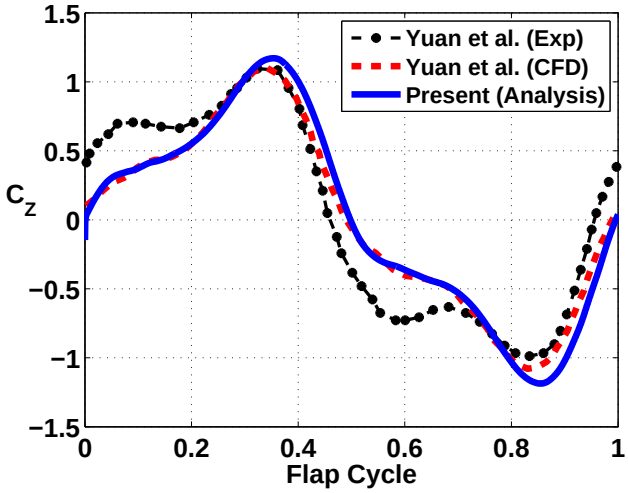

Figure 3.29: C_Z **variation over a flap cycle for 3D root flapping case,** 15° **flap amplitude,** 40° **pitch amplitude.**

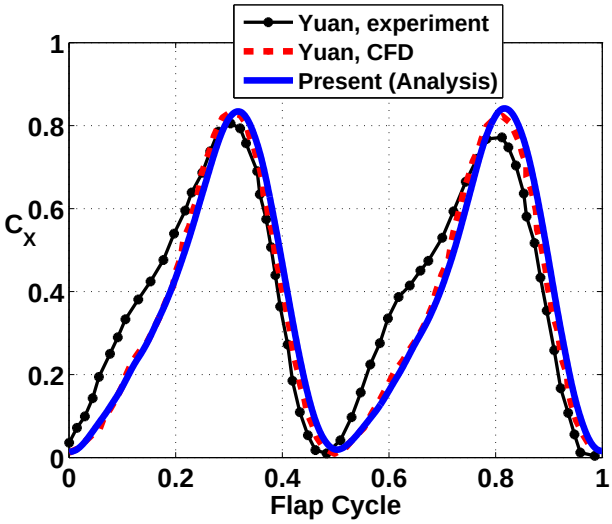

Figure 3.30: C_X **variation over a flap cycle for 3D root flapping case,** 15° **flap amplitude,** 40° **pitch amplitude.**

in the normal directions. The Cartesian background mesh had 172 points in the streamwise, 183 points in the spanwise and 92 points in the vertical directions. Implicit hole-cutting method developed by Lee [124] and refined by

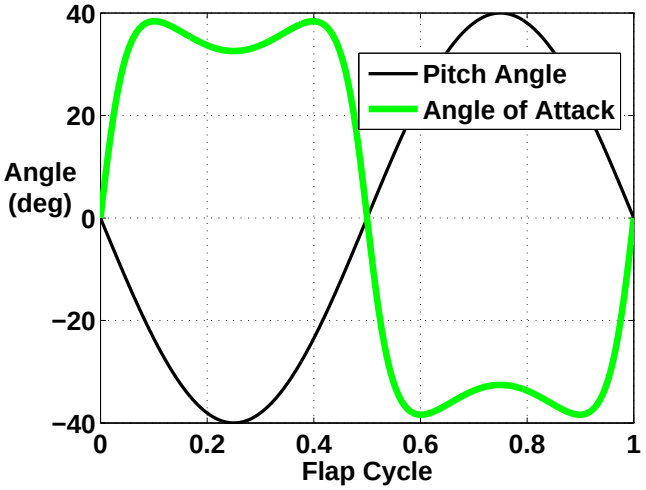

Figure 3.31: **Variation of pitch angle and effective angle of attack at reference section for 3D root flapping case.**

Lakshminarayan [105] was used to find the connectivity information between the overset meshes. Calculations were done using 1440 iterations per flap cycle and each iteration used 10 subiterations to remove linearization error. To help ensure an accurate and stable simulation, OVERTURNS was run at a Mach of 0.05 rather than the lower experimental value. Since the Mach numbers involved in these studies were well within the incompressible limit, it is expected that small variations in Mach number will not have a significant effect on the final results.

3.2.2.3 Results

Figures 3.29 and 3.30, respectively, show the variation of vertical force coefficient (C_Z) and propulsive force coefficient (C_X) over a flap cycle. Note that, the vertical and propulsive force coefficients were obtained by normaliz-

ing with the wing planform area and the reference velocity (described earlier). As can be seen in the figures, the current results correlate well with the numerical results of Yuan et al. When both the computational results are compared with the experimental data, there is satisfactory agreement between the results. However, there are some differences in the computed magnitude of the secondary peak found in the vertical force time history when compared to that in the experimental data. In addition, while both the computations predict zero net vertical force over a flap cycle, the experimental data show a small positive value due to dissimilar peaks obtained during upstroke and downstroke. Note that some of these differences are reflected even in the propulsive force time history. The reason for these differences between the computational and the experimental results is not clear at this point. Yuan et al. had mentioned that the differences could possibly be because the water tunnel wall effects in the simulation were ignored. However, a simulation with the inclusion of wall effects in the current study did not result in any significant change in the vertical and propulsive force time histories.

Looking at the variation of propulsive force over a flap cycle (Figure 3.30), we can see that it has a positive value at all times, thus producing a net propulsive force over a flap cycle. The net propulsive force coefficient predicted from the current simulation is 0.38 and it lies within 10% of the experimental value. Clearly, the kinematics used in this case helps in producing positive propulsive force as opposed to the earlier case of Hart et al. [80]. To understand the reason for the positive propulsive force generated, the variation of pitch

angle along with the effective angle of attack seen by the reference section (mid-span section) of the wing is plotted over a flap cycle, see Figure 3.31. The effective angle of attack is obtained by adding the angle of attack due to the wing pitch and that due to the flapping motion. The wing pitch angle follows the prescribed sinusoidal motion with 40° amplitude. The effective angle of attack, on the other hand, stays relatively constant over the middle part of the stroke and at all times it has a sign opposite to that of the wing pitch.

As a result, the leading edge vortex is always formed on the surface (upper or lower) of the wing that is facing the "thrusting" direction, thus vectoring the force in the forward direction. The low pressure created by the leading edge vortex is shown in Fig. 3.32, where the pressure coefficient (normalized by reference velocity) contours at the reference section are plotted at different instances in time as the wing moves from the topmost position to the bottommost position. The contour plots obtained from the current simulation are compared with those obtained by Yuan et al. [81] as a part of validation. Thus, it can be clearly seen that by optimizing flapping kinematics, the vertical force and propulsive force can be tailored for application to MAVs.

It should be noted that to carry out their simulations, Yuan et al. used a grid with $481 \times 129 \times 33$ points and 384 timesteps per cycle. The pressure coefficient contours from the current simulation seem to have better off-surface flow resolution due to better resolution of the grid in the normal direction and also higher number of iterations per cycle. Figures 3.33 and 3.34, respectively,

show the pressure contour plots at spanwise locations that are at 10% and 90% wing span location (from the root). Again, the presence of leading edge vortices are identified through mid portion of the wing stroke, but the strength of the vortex is slightly different at various sections.

A 2D simulation, which mimicked the motion of the reference section of the current case, was presented earlier in Section 3.1.4. Comparing to the 2D results shown earlier in Figure 3.18, we see that the vortices in 3D are smaller and dissipate into the flow quickly (also as observed by Yuan et. al). As a result, the maximum vertical force (F_Z) and propulsive force (F_X) produced in the 3D case is lower. Thus, 3D effects are seen to significantly alter the vertical and propulsive forces for a flapping wing MAV.

A good flow visualization can be obtained by looking at the iso-surfaces of the so-called q-criterion [114] colored with vorticity contour, as shown in Figure 3.35. The q-criterion, which is the second invariant of the velocity gradient tensor, extracts the rotational flow regions without including the highly strained regions, such that vortical regions are highlighted. As a result, leading edge vortex along with the root and tip vortices can be easily identified in Figure 3.35. The plot clearly shows the three-dimensionality of the flow-field. While the leading edge vortex is seen to be formed throughout the mid-sections of the wing, it is absent near the root and tip regions of the wing. At the root and tip, the flow feature is dominated by the root and tip vortices, respectively. All the vortices stay attached to the wing during the middle of the stroke, but are seen to get detached when the wing flips over.

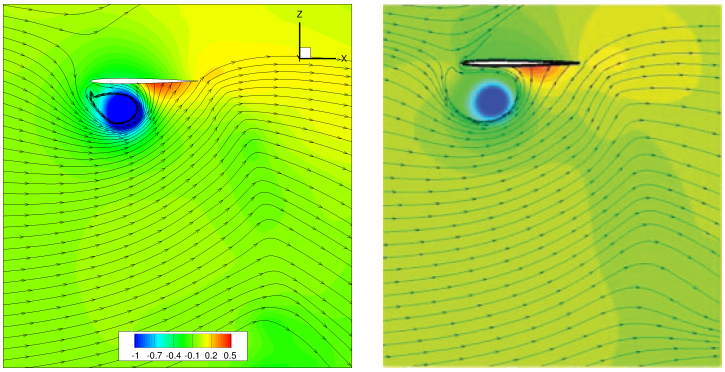

(a) t=0, Present (b) t=0, Yuan et al.

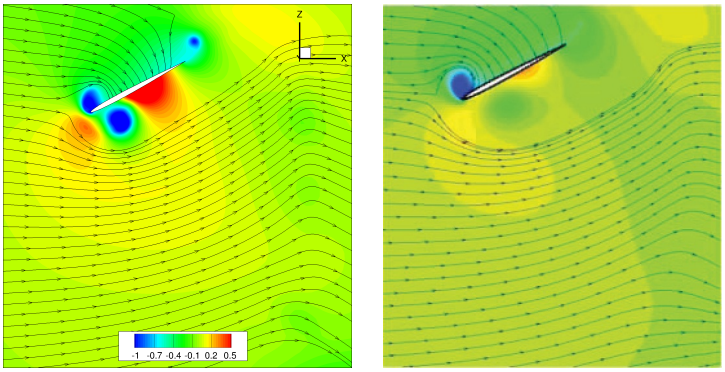

(c) t=T/8, Present (d) t=T/8, Yuan et al.

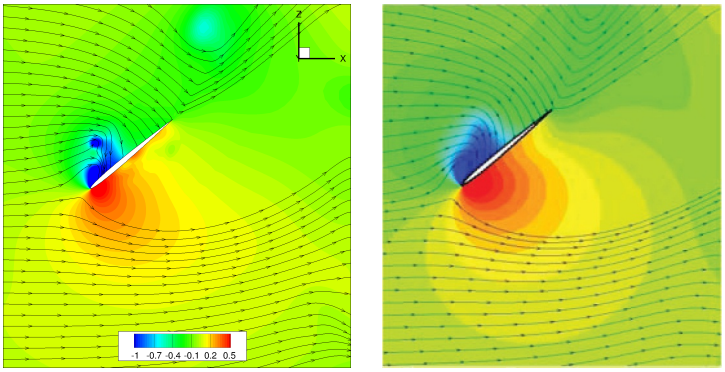

(e) t=T/4, Present (f) t=T/4, Yuan et al.

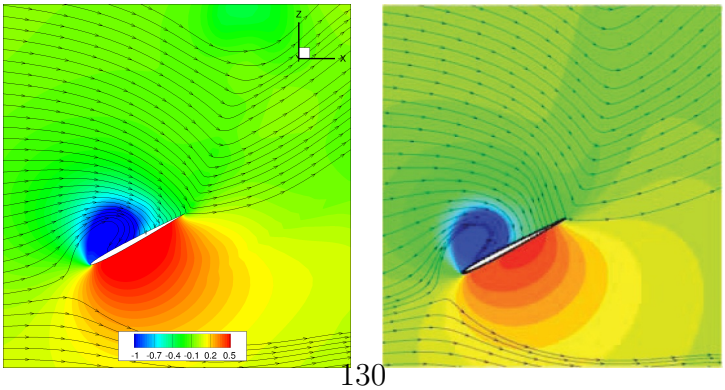

(g) t=3T/8, Present (h) t=3T/8, Yuan et al.

Figure 3.32: **Pressure contours at reference section for 3D root flapping case.**

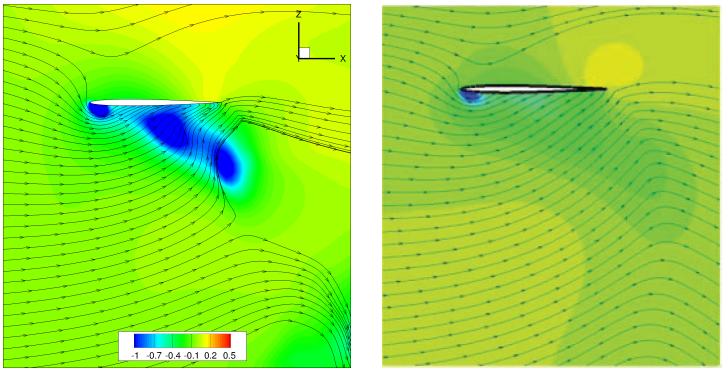

(a) t=0, Present (b) t=0, Yuan et al.

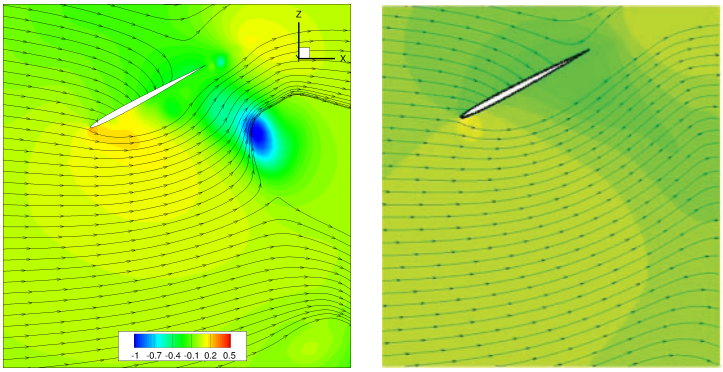

(c) t=T/8, Present (d) t=T/8, Yuan et al.

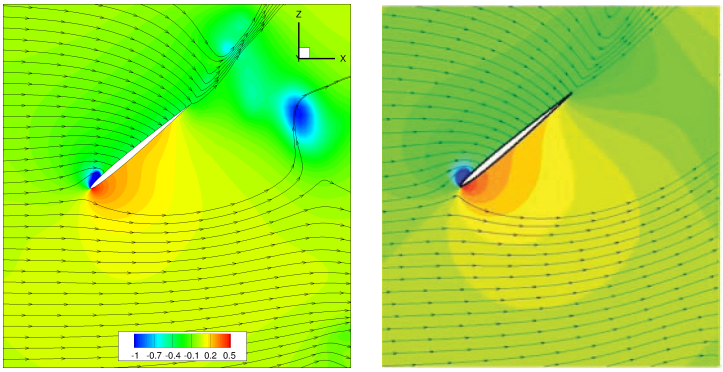

(e) t=T/4, Present (f) t=T/4, Yuan et al.

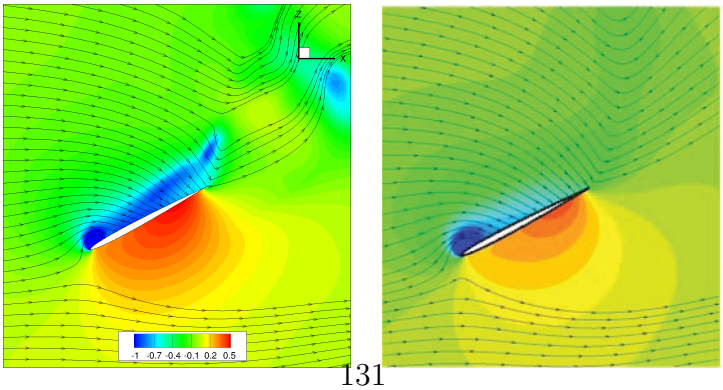

(g) t=3T/8, Present (h) t=3T/8, Yuan et al.

Figure 3.33: **Pressure contours at 10% wing span location for 3D root flapping case.**

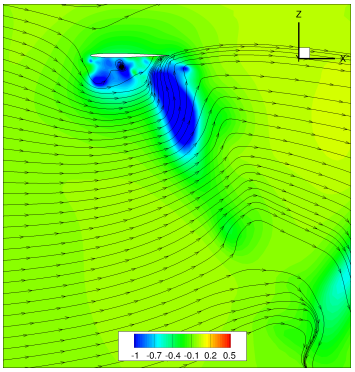

(a) t=0, Present

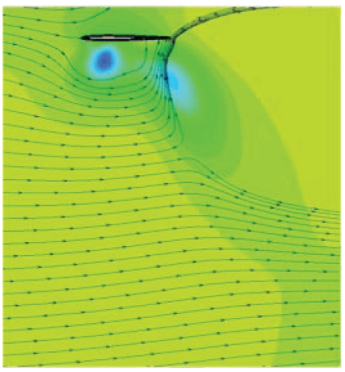

(b) t=0, Yuan et al.

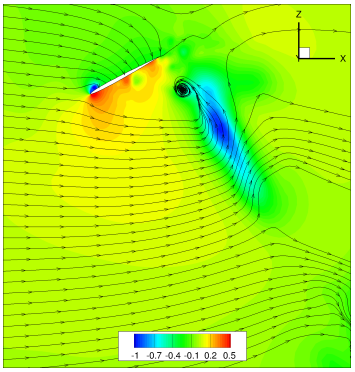

(c) t=T/8, Present

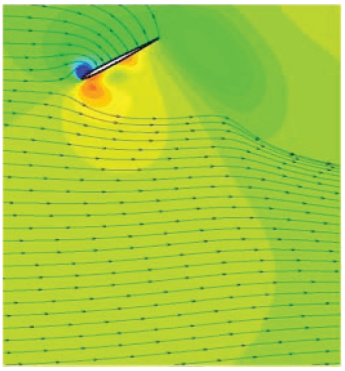

(d) t=T/8, Yuan et al.

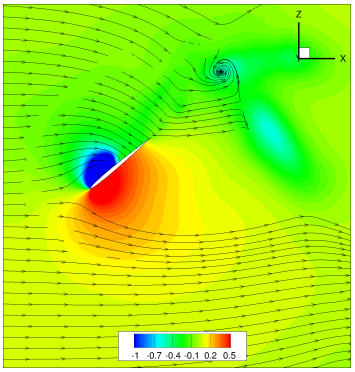

(e) t=T/4, Present

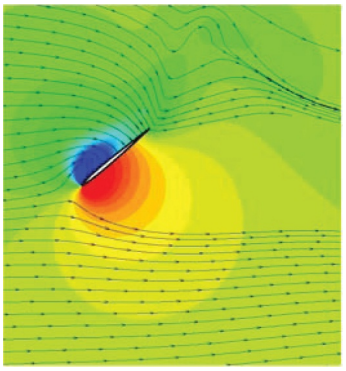

(f) t=T/4, Yuan et al.

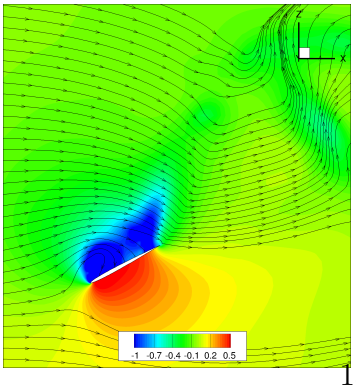

(g) t=3T/8, Present

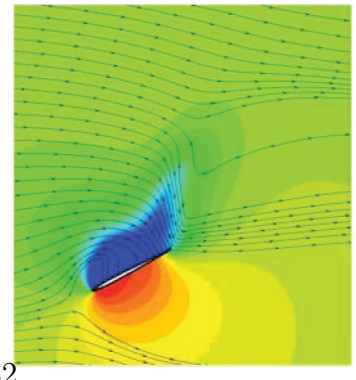

(h) t=3T/8, Yuan et al.

Figure 3.34: **Pressure contours at 90% wing span location for 3D root flapping case.**

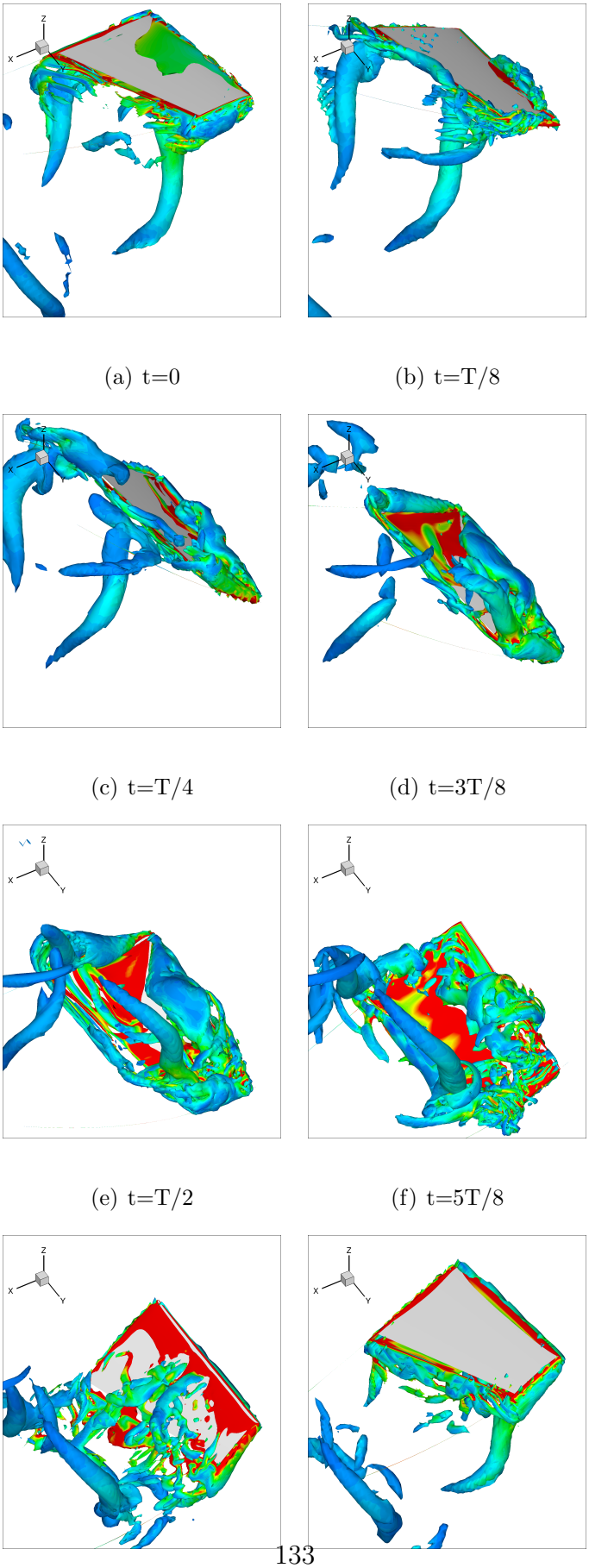

(a) t=0 (b) t=T/8

(c) t=T/4 (d) t=3T/8

(e) t=T/2 (f) t=5T/8

(g) t=3T/4 (h) t=7T/8

Figure 3.35: **Iso-surfaces of second invariant of the velocity gradient tensor colored with azimuthal vorticity contour**

3.3 Summary and Conclusions

A compressible RANS solver was used to simulate the aerodynamics of a flapping wing. The analysis was first validated in 2D flow cases and showed good correlation for all the cases considered. The first case was at relatively high Reynolds numbers. It was observed that propulsive force increases with plunge frequency due to the increasing leading edge suction of the leading edge vortex. At higher plunge amplitudes, a leading edge vortex is formed and as long as this vortex is ahead of the position of maximum thickness, it leads to a propulsive force. However, if this vortex convects aft, propulsive force drops.

Validation was then carried out for combined pitch and plunge motions at high Reynolds numbers. It was observed that the propulsive force generated was higher for this case as compared to pure plunge. The mechanism of propulsive force was again the suction force due to formation of leading edge vortex. But in this case, the vectoring of the resultant force is determined by combination of pitch angle and the position of the vortex. For the flapping wing to generate propulsive force, the vortex may be positioned on the top or bottom of the airfoil (which depends on the angle of attack), but the suction force should be vectored in the propulsive direction (which depends on the pitch angle and the phasing between pitch and plunge). Good correlation was achieved for both the cases.

Simulation was then carried out for a low Reynolds number case, which is applicable to MAVs. It should be noted that all the 2D cases were symmetric

in upstroke and downstroke and hence the average force in vertical direction was zero. For this case, the instantaneous vertical and propulsive force values were also validated. Very high value of maximum instantaneous vertical force coefficient was observed which was much greater than the corresponding static lift coefficient at the same effective angle of attack. This clearly shows the beneficial effect of unsteadiness in the aerodynamic forces.

3D validation was then carried out for two configurations. The first configuration was a heaving and pitching flat plate wing with low aspect ratio. Validation of instantaneous forces and flow fields was carried out with experimental data and PIV results. Two cases were considered, pure plunge at fixed positive angle and a case with pitch modulation superimposed over a constant pitch angle. Due to an asymmetry in the kinematics, an average vertical force (F_Z) was generated in both the cases. However, the kinematics was such that the wing generated mostly negative propulsive force throughout the entire cycle for both the cases.

The second 3D configuration was root based flapping that is more representative of natural flyers. A spanwise tapered wing was simulated in pitch and flap. Good correlation of instantaneous forces and flow fields was achieved with prior work. The flowfield was highly three dimensional with the flow dominated by leading edge vortices in the midsection but by the root and tip vortices near the ends of the wing. Unlike the flat plate case considered before, positive propulsive force (F_X) was produced as a result of the tailoring of pitch and plunge angles and flapping frequency.

As a concluding remark, this chapter demonstrates the capability of OVERTURNS to characterize the flowfield of a flapping wing MAV in 3D flow environment.

Chapter 4

Structural Modeling Methodology and Validation

4.1 Overview

Analysis of flapping wing MAVs requires the capability to address structural dynamics with significant geometrical nonlinearity, mechanism modeling capability to take into account the actual flap and pitch mechanism, and consistent fluid-structure coupling. Multibody System Dynamics (MSD) represents an ideal modeling environment to address this type of problem, since it directly provides sophisticated structural dynamics and mechanism modeling. At the same time, the analysis can be consistently coupled to external solvers like a Computational Fluid Dynamics (CFD) solver for the aerodynamic part of the problem. The free general-purpose multibody solver MBDyn is used here to model the structure.

A consistent geometrically nonlinear four-node shell element is used, in addition to an already available nonlinear beam element [141], to model a flapping wing MAV. The use of shell elements either in Finite Element (FE) or in MSD analysis to model flapping wing MAV has been recently proposed, for example, by Chandar and Damodaran [142] and Chimakurthi et al. [143]. The novelty of the approach used in this work is related to the use of a nonlinear shell model, as opposed to the co-rotational one of Ref. [143], and to the use of

a consistent mapping of the interaction between the structural and the CFD analysis. The basics of the modeling methodology are presented next.

4.2 Structural Modeling Methodology

4.2.1 Equations of Motion

At the core of its formulation, MBDyn integrates in time the equations of motion of constrained mechanical systems. The equations associated to linear and angular motion of a set of independent rigid bodies (Newton-Euler equations) are explicitly constrained by a set of algebraic equations that express the kinematic constraints between the bodies. The corresponding constraint reaction forces and moments are applied to the bodies using Lagrange multipliers. All dynamics equations are formulated as first-order differential equations. For each body b, momentum, β_b, and momenta moments, γ_b, are defined first,

$$\beta_b = m_b \dot{x}_b + \omega_b \times s_b \tag{4.1}$$

$$\gamma_b = s_b \times \dot{x}_b + J_b \omega_b. \tag{4.2}$$

The derivatives of momentum and momenta moments express the inertia forces in the equations of motion,

$$\dot{\beta}_b = f_b \tag{4.3}$$

$$\dot{\gamma}_b + \dot{x}_b \times \beta_b = c_b \tag{4.4}$$

where f_b and c_b are the active force and moment acting on the node.

When the node participates in a kinematic constraint $\phi_c(x_b)$ (only the case of dependence on the position of the node is considered for simplicity), the corresponding algebraic equation is added to the system, and the corresponding reaction forces are applied to the equations of motion of the node, i.e. the unconstrined equation of Eq. (4.3) becomes

$$\dot{\beta}_b + \sum_c \phi^T_{c/x_b} \lambda_c = f_b \tag{4.5}$$

where λ_c is the Lagrange multiplier associated to the kinematic constraint.

The problem is thus expressed as a system of Differential-Algebraic Equations (DAE). Its direct integration in time must be performed using A/L-stable integration schemes, which in turn must be implicit. In the present case, a two-step A/L-stable second-order accurate scheme is used. The algorithmic dissipation of the scheme, required to damp out high-frequency numerical oscillations associated with the infinitely fast dynamics of the algebraic equations, can be tuned to provide an asymptotic spectral radius ranging from 0 to 1.

4.2.2 Large Rotations

The efficient and accurate handling of arbitrary rotations is key for the success of rigid body dynamics. Let v be a vector in a three-dimensional domain: $v \in R^3$. Matrix R represents a rotation φ of the vector v from its initial orientation v_0 to a new orientation v_1: $v_1 = Rv_0$, namely a transformation that preserves the 'length' (the norm) of the vector, $v_1 \cdot v_1 = v_0^T R^T R v_0 = v_0 \cdot v_0$, which implies $R^{-1} = R^T$. The rotation matrix is defined according to Euler's

rotation vector φ as

$$R = I + \frac{\sin \|\varphi\|}{\|\varphi\|}\varphi \times + \frac{1 - \cos \|\varphi\|}{\|\varphi\|^2}\varphi \times \varphi \times \tag{4.6}$$

Because the trigonometric functions in matrix R are costly to evaluate, the modified Cayley-Gibbs-Rodriguez rotation parameters g are used instead. They are defined as $g = 2\tan(\|\varphi\|/2)n$, with $n = \varphi/\|\varphi\|$, and are obtained from the usual Gibbs-Rodriguez parameters by pre-multiplication by the factor 2. In this way, for small rotation perturbations about zero, the parameters Δg coincide with the rotation vector $\Delta\varphi$. The rotation matrix is

$$R = I + \frac{4}{4 + g \cdot g}\left(g \times + \frac{1}{2} g \times g \times\right) \tag{4.7}$$

The transformation is undefined for rotations that are integer multiples of the angle π, since $\lim_{\|\varphi\| \to \pi^{\pm}} g = \pm\infty n$, although R is defined (in fact, $\lim_{\|\varphi\| \to \pi} R = I - n \times n \times$) but this causes no harm if an incremental solution process is used and incremental rotations are limited. In this case, the matrix R_0 contains the reference rotation, while the rotation unknowns are the Gibbs-Rodriguez parameters that represent the incremental rotation R_Δ from the reference configuration R_0 to the new one R_1 at the end of the current integration step, namely $R_1 = R_\Delta(g)R_0$. The difference between the two configurations is assumed to be sufficiently small for an acceptable accuracy, so that no singularity should result. The kinematic unknowns of an arbitrary node and their time

derivatives are

$$q_b = \left\{ \begin{array}{c} x_b \\ g_b \\ \beta_b \\ \gamma_b \end{array} \right\} \tag{4.8}$$

where x are the Cartesian positions of the node, g are the Gibbs-Rodriguez parameters describing the incremental, finite rotation from the last completed step to the current iteration during the iterative solution of a nonlinear problem, and β_b and γ_b have been already defined.

The relationship between the rotation parameters and the angular velocity is $\omega = G\dot{g}$, where matrix G is

$$G = \frac{4}{4 + g \cdot g} \left(I + \frac{1}{2} g\times \right). \tag{4.9}$$

4.2.3 Finite Volume Multibody Beam Element

A finite volume beam element is used in MBDyn to give the code the capability to model the elastic deformation of bodies undergoing large displacements and rotations. Deformable beams can be interpreted as discrete elastic constraints that link independent rigid bodies. A computation for a three-node beam element has been implemented, which is sketched in Figure 4.1. A piece of beam is divided in three parts that are related to three reference points, i.e., the midpoint and the two endpoints. They are related to geometrical nodes by means of offsets o_n. This makes it possible to offset the elastic

axis of the beam from the center of mass. Every node is characterized by a position vector, x_n, and a rotation matrix, R_n. A reference line p describes the position of an arbitrary point $p(\xi)$ on the beam section; the configuration of the section at an arbitrary location ξ is described by a rotation matrix $R(\xi)$. The reference line is not required to have some physical significance (e.g., the center of axial stresses, the shear center, nor the center of mass). The direction e_1 of the section reference frame is normal to the section; directions e_2, e_3 are mutually orthogonal, are normal to e_1, and lie in the section plane. The angle between the unit vector e_1 and the reference line represents the shear strain. The effects of cross-section warping are assumed to be small, and are accounted for in the constitutive coefficients of the beam [146].

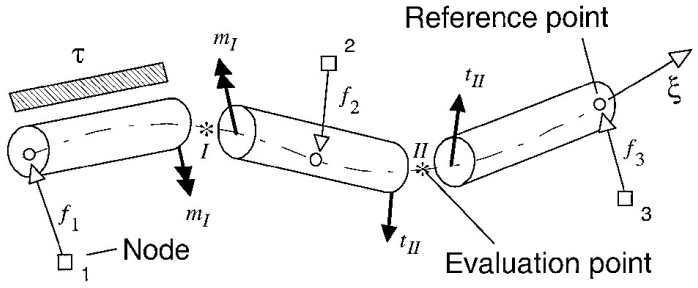

Figure 4.1: **Finite volume three-node beam**

4.2.4 Generalized Strains

The generalized strains can be expressed in terms of derivatives of the position and the rotation of the sections with regard to their initial configuration. The strains in the global reference frame are defined by

$$\epsilon = p' - R\overline{p}' \tag{4.10}$$

where the rotation matrix R represents a rigid rotation from the initial configuration of an arbitrary section. Overlined quantities denote the initial values of entities. Because the material constitutive matrix equation does not depend on the configuration when written in the material frame, the deformations ought to be translated in that frame to obtain the proper internal forces. The strains in the material frame become

$$\tilde{\epsilon} = R^T\epsilon = R^T p' - \tilde{\overline{p}}' \tag{4.11}$$

where the tilde $\tilde{(\cdot)}$ denotes entities expressed in the material frame. The rotation deformations, i.e., the elastic curvatures, are

$$\kappa\times = R'R^T - R\tilde{\overline{\rho}} \times R^T \tag{4.12}$$

Matrix $R'R^T = \rho\times$ is the current geometric curvature,whereas $\tilde{\overline{\rho}}\times$ is the geometric curvature of the undeformed beam. The transformation from the current to the material frame leads to

$$\tilde{\kappa}\times = R^T R' - \tilde{\overline{\rho}}\times = R^T\rho \times R - \tilde{\overline{\rho}}\times \tag{4.13}$$

The definitions of strains and curvatures, together with the equilibrium equation, characterize the beam as a one-dimensional continuum. Thereby, the formulation is implicitly valid for initially curved and twisted beams, even if

these are taken into account only in a discrete manner.

4.2.5 Generalized Deformations

The beam generalized strains have already been defined. The curvatures can be expressed in terms of updated rotation parameters g_Δ from Eq. 4.12:

$$\kappa\times = (Gg'_\Delta) \times + R_\Delta \kappa_r \times R_\Delta^T \tag{4.14}$$

From now on, the subscript Δ will be discarded from the incremental rotation parameters. The matrix R_Δ represents the variation of rotation matrix that occurs during the running iteration, namely $R = R_\Delta R_r$. Only the matrix R_Δ depends on the rotation parameters g, whereas the vector κ_r and the matrix R_r , respectively, represent the curvature and the rotation matrix at the last completed time step. Matrix G is defined in Eq.4.9 and depends on the finite rotation from the reference frame at the last iteration to that at the current iteration. In the material frame the elastic curvatures are

$$\tilde{\kappa} = R^T G g' + \tilde{\kappa}_r \tag{4.15}$$

and only the first addendum on the right-hand side depends on the unknown rotation parameters g, both in the matrices R and G and in the vector g'.

4.2.6 Equilibrium

The nodal equilibrium equations are summarized as follows:

$$AD\Psi = F \tag{4.16}$$

where A is the moment arms matrix; the matrix D is block diagonal and contains the constitutive matrices of the sections at the evaluation points, expressed in the global frame; vector Ψ represents the generalized deformations at the these points. Vector F represents the imposed nodal loads. Roman and Arabic subscripts denote entities related to the two evaluation points and the three nodes of a beam element, respectively. The matrices take the form

$$\mathrm{A} = \begin{bmatrix} -I & 0 & 0 & 0 \\ (p_I - x_1)\times & -I & 0 & 0 \\ I & 0 & -I & 0 \\ -(p_I - x_2)\times & I & (p_{II} - x_2)\times & -I \\ 0 & 0 & I & 0 \\ 0 & 0 & -(p_{II} - x_3)\times & I \end{bmatrix} \tag{4.17}$$

The variables p, having Roman subscripts, are the positions of the evaluation points, and the variables x, having Arabic subscripts, are the positions of the reference points of the beam.

4.2.7 Discretization

The position of the ith reference point is $p_i = x_i + R_i\overline{f_i}$, where x_i is the position of the ith node, R_i is its rotation matrix, and $\overline{f_i}$ is the offset in the node reference frame. The position of an arbitrary point of the reference line is interpolated from the positions of the nodes by means of parabolic shape functions $N(\xi)$:

$$p(\xi) = N_i(\xi)(x_i + R_i\overline{f_i}) \tag{4.18}$$

where subscript i refers to the ith node and summation over repeated indices is assumed. The shape functions are

$$N(\xi) = \begin{bmatrix} 1/2\xi(\xi-1) & 1-\xi^2 & 1/2\xi(\xi-1) \end{bmatrix} \tag{4.19}$$

Rotation parameters g are discretized using the same shape functions:

$$g(\xi) = N_i(\xi)g_i \tag{4.20}$$

The generalized deformations at an arbitrary point are

$$\varepsilon(\xi) = N_i'(\xi)(x_i + R_i\overline{f_i}) - R(\xi)\overline{p'} \tag{4.21}$$

$$\kappa(\xi) = G(\xi)N_i'(\xi)g_i + R_\Delta(\xi)\kappa_r \tag{4.22}$$

4.2.8 Linearization of Equilibrium Equations

The solution of the system requires local linearization of the equations with respect to the unknowns, i.e., the nodal position and rotation unknowns Δx_i and Δg_i. The following relations hold:

$$
\begin{aligned}
\Delta x_J &= N_{Jk}\Delta x_k \\
\Delta g_J &= N_{Jk}\Delta g_k \\
\Delta R_J &= \left[\left(G_J N_{Jk}\Delta g_k\right)\times\right]\left(R_r\right)_J \\
\Delta p_J &= N_{Jk}\left\{\Delta x_k - \left[\left(R_r\overline{f}\right)_k\times\right]G_k\Delta g_k\right\} \\
\Delta\tilde{\varepsilon}_J &= \left(R_r\right)^T{}_J\left(p'_J\times\right)G_J N_{Jk}\Delta g_k \\
&+ R_J^T N'_{Jk}\left\{\Delta x_k - \left[\left(R_r\overline{f}_k\right)\times\right]G_k\Delta g_k\right\} \\
\Delta\tilde{\kappa} &= \left(R_r\right)^T{}_J\left(G_J g'_J\times\right)G_J N_{Jk}\Delta g_k \\
&+ R_J^T\left[H g'_J N'_{Jk}\Delta g_k + G_J N'_{Jk}\Delta g_k\right]
\end{aligned}
$$

where subscript J denotes the Jth evaluation point, whereas subscript k denotes the kth node. The matrix H follows from the relation $\Delta\left(Gg'\right) = \Delta G g' + G\Delta g'$ and represents the differentiation of matrix G, such that $H\left(g'\right)\Delta g = \Delta G g'$:

$$
\begin{aligned}
\Delta G g' &= \frac{2}{4+g\cdot g}\left(-g\cdot\Delta g G + \Delta g\times\right)g' \\
&= -\frac{2}{4+g\cdot g}\left[\left(Gg'\right)g^T + g'\times\right]\Delta g
\end{aligned}
$$

The linearization of Eq. 4.16 gives

$$
\Delta A\Theta + A\Delta\Theta + A\Theta = 0 \tag{4.23}
$$

Differentiation of the matrix A involves the distance between the evaluation points p_I, p_{II} and the nodes of the beam:

$$\Delta A_{iJ}\vartheta_J = \left\{ \begin{array}{c} 0 \\ \\ -t_J \times (\Delta p_J - \Delta x_i) \end{array} \right\} \tag{4.24}$$

Differentiation of the internal forces gives

$$\Delta\vartheta_J = -\left\{ \begin{array}{c} (t_r)_J\times \\ \\ (m_r)_J\times \end{array} \right\} G_J\Delta g_J + \left[\begin{array}{cc} R_J & 0 \\ \\ 0 & R_J) \end{array} \right] \tilde{D}_J \left\{ \begin{array}{c} \Delta\tilde{\varepsilon}_j \\ \\ \Delta\tilde{\kappa}_j \end{array} \right\} \tag{4.25}$$

where the differentiation of strains and curvatures has already been defined. These elastic terms contribute to the already outlined multibody dynamic system, which already accounts for the contribution of lumped inertia. The consistent (i.e., distributed) inertia forces require numerical integration. The external loads should be linearized, too, because the deformation of the beam changes the moment arm of the forces, i.e., the matrix U, on the right-hand side of the equilibrium equation. This effect vanishes when forces are applied only at the nodes.

4.2.9 Shell Element Formulation

A four node C^0 shell element was recently implemented in MBDyn to allow the modeling of arbitrary 2-D structural elements. It is derived from the elements proposed by Witkowski [147], based on a combination of the Enhanced Assumed Strain (EAS) and Assumed Natural Strain (ANS) formulations. Some details of the formulation are mentioned in Ref. [144].

Let y be the position of the shell reference surface, and define a local

orthogonal coordinate system on the undeformed shell surface. Let T be a local orthonormal triad defined on the surface. Two Biot-like linear deformation vectors (e.g. [148, 149]) can be computed by comparing the deformed and undeformed back-rotated derivatives of the position, namely

$$\tilde{\epsilon}_k = T^T y_{/k} - {T_0}^T y_{0/k} \tag{4.26}$$

where $y_{/k}$ is the partial derivative with respect to the arc length coordinate k ($k = 1, 2$); the subscript $(\cdot)_0$ identifies the undeformed configuration. Vectors $\tilde{\epsilon}_k$ are work-conjugated with the force per unit length vectors $\tilde{n}_k$. The Biot-like angular deformation is defined as

$$\tilde{\kappa}_k = T^T \kappa_k - {T_0}^T \kappa_{0k} \tag{4.27}$$

where κ_k is the vector characterizing the spatial derivative of tensor T , with respect to arc length coordinate k, i.e.

$$\kappa_k \times = T_{/k} T^T \tag{4.28}$$

The angular strain vectors are work-conjugated with the internal couple per unit length vectors $\tilde{m}_k$. The straining of the shell is thus completely defined by the vector

$$\epsilon = \left\{ \begin{array}{c} \tilde{\epsilon}_1 \\ \\ \tilde{\epsilon}_2 \\ \\ \tilde{\kappa}_1 \\ \\ \tilde{\kappa}_2 \end{array} \right\}$$

which is work conjugated to

$$\sigma = \left\{ \begin{array}{c} \tilde{n}_1 \\ \\ \tilde{n}_2 \\ \\ \tilde{m}_1 \\ \\ \tilde{m}_2 \end{array} \right\}$$

The virtual internal work is thus equal to

$$\delta L_i = \int_A \delta\epsilon^T \sigma \mathrm{d}A \tag{4.29}$$

The proposed formulation departs from Witkowski's one [147] and from the earlier work of Chroscielewski and Witkowski [150] in the treatment of the rotation field. The orientation field T is interpolated resorting to a co-rotational framework, as in the above cited works. In the present one, however, the angular strain vectors $\tilde{\kappa}_k$ are computed from their definition Eq. 4.27, and not from the back-rotated gradient of the rotation tensor $\Phi = TT_0^T$. Furthermore, the direct use of the linear and angular strains of Eqs. 4.26, 4.27 and of their work-conjugated forces per unit length nullifies the need to resort to co-rotational derivatives in the definition of the strain vectors. The linearization of the ensuing virtual internal work differs as well, as the previously mentioned works seem to miss a term related to the second variation of the angular strain vectors, $\partial\delta\tilde{\kappa_k}$, described later.

The interpolation of the orientation field is performed after defining, in the reference configuration, a triad of unit orthogonal vectors t_{n1}, t_{n2}, t_{n3} for each node n, with t_{n1} and t_{n2} tangent to the shell surface and $t_{n3} = t_{n1} \times t_{n2}$. Let R_n be the orientation tensor of node n, and define the local shell orientation as

$$T_n = R_n R_{0n}^T [t_{n1}, t_{n2}, t_{n3}] \tag{4.30}$$

where R_{0n} is the nodal orientation in the reference configuration. The average orientation $\overline{T}$ of the shell is then computed as $\overline{T} = \exp(\log(1/4 \sum_{n=1,4} T_n))$, where function $\log(\cdot)$ is the inverse of function $\exp((\cdot)\times)$, which computes the rotation tensor defined by a rotation vector, such that $R = \exp(\log(R))$ and $a\times = \log(\exp(a\times))$. Standard bilinear interpolation shape functions $N_n(\xi)$ are defined for each node n and used to interpolate the relative rotation vectors that define the relative nodal rotations $\tilde{R}_n = \overline{T}^T T_n$ i.e.

$$\tilde{\varphi}_i(\xi)\times = log(\tilde{R}_i) = \sum_{n=1,4} N_n(\xi) log(\overline{T}^T T_n) \tag{4.31}$$

where the subscript $(\cdot)_i$ indicates interpolated quantities; the interpolated orientation can finally be recovered as $T_i = \overline{T} exp(\tilde{\varphi}_i\times)$. In short, the nodal rotation tensors are averaged to yield the tensor $\overline{T}$. The relative orientation vectors are then extracted from the relative rotation tensors between the orientation of each node and $\overline{T}$. These vectors are used to interpolate the relative orientation vector at arbitrary points within the domain of the shell element,

keeping the value of interpolated orientations limited although not necessarily small. Apart from approximations related to interpolation, orientations are always treated consistently, without resorting to any approximation nor small orientations assumption.

Computing the virtual internal work, Eq. 4.29, and its linearization involves computing the first (δ) and second ($\partial\delta$) variations of the linear and angular deformation vectors Eqs. 4.26, 4.27. These, in turn, require explicit expressions for the interpolated virtual rotation vector $\varphi_{i\delta}$, defined by $\varphi_{i\delta}\times = \delta T_i T_i^T$; recall that the virtual rotation vector φ_δ can be computed from the virtual variation of the rotation vector as $\varphi_\delta = \Gamma(\varphi)\delta(\varphi)$, with $\Gamma(\varphi)$ a second order tensor. The interpolated virtual rotation vector is

$$\varphi_{i\delta} = \sum_{n=1,4} \Phi_{in} N_{in} \varphi_{n\delta} \tag{4.32}$$

with

$$\Phi_{in} = \overline{T}\tilde{\Gamma}_i \tilde{\Gamma}_n^{-1} \overline{T}^T \tag{4.33}$$

and $N_{in} = N(\xi)$. The linear strain is then

$$\tilde{\epsilon_k} = T_i^T y_{i/k} = T_i^T \sum_{n=1,4} N_{in/k} y_n \tag{4.34}$$

Its first variation is then

$$\delta(T_i^T y_{i/k}) = T_i^T (y_{i/k} \times \varphi_{i\delta} + \delta y_{i/k}) \tag{4.35}$$

with the second variation equal to

$$\partial\delta(T_i^T y_{i/k}) = T_i^T \left(\left(y_{i/k} \times \varphi_{i\delta} + \delta y_{i/k} \right) \times \varphi_{i\partial} - \varphi_{i\delta} \times \partial y_{i/k} + y_{i/k} \times \partial\varphi_{i\delta} \right) \tag{4.36}$$

The back-rotated curvature is

$$\tilde{\kappa}_{ik} = T_i^T \kappa_{ik} = \tilde{\Gamma}_i^T \sum_{n=1,4} N_{in/k} \tilde{\varphi}_n \tag{4.37}$$

its first variation is

$$\begin{aligned} \delta(T_i^T \kappa_{ik}) &= T_i^T \kappa_{ik} \times \varphi_{i\delta} + T_i^T \delta\kappa_{ik} \\ &= T_i^T \varphi_{i\delta/k} \\ &= T_i^T \sum_{n=1,4} (\Phi_{in/k} N_{in} + \Phi_{in} N_{in/k}) \varphi_{n\delta} \end{aligned}$$

whereas second variations is

$$\begin{aligned} \partial\delta(T_i^T \kappa_{ik}) &= \partial(T_i^T \varphi_{i\delta/k}) = T_i^T (\varphi_{i\delta/k} \times \varphi_{i\partial} + \partial\varphi_{i\delta/k}) \\ &= T_i^T \Big(\sum_{n=1,4} (\Phi_{in/k} N_{in} + \Phi_{in} N_{in/k}) \varphi_{n\delta} \Big) \times \sum_{n=1,4} \Phi_{in} N_{in} \varphi_{n\partial} \\ &+ \sum_{n=1,4} (\partial\Phi_{in/k} N_{in} + \partial\Phi_{in} N_{in/k}) \varphi_{n\delta}) \end{aligned}$$

It is worth noticing that the last term of Eq. 4.38, whose explicit expression turns out to be rather complex, seems to be missing from Chroscielewski and Witkowskis works [147, 150]. Explicit formulae for the derivatives of the rotation tensor up to the third order, required in order to consistently linearize the approximated deformation field, can be found in Merlini and Morandini [151].

The constitutive law of the shell must be computed beforehand; it expresses the generalized stress vector as a function of the generalized deformation vector. As an example, the constitutive law of an isotropic flat plate is

$$\begin{Bmatrix} \tilde{n}_1 \\ \tilde{n}_2 \\ \tilde{m}_1 \\ \tilde{m}_2 \end{Bmatrix} = D \begin{Bmatrix} \tilde{\epsilon_1} \\ \tilde{\epsilon_2} \\ \tilde{\kappa_1} \\ \tilde{\kappa_2} \end{Bmatrix}$$

$$\mathrm{D} = \begin{bmatrix} C & 0 & 0 & 0 & \nu C & 0 & 0 & 0 & 0 & 0 & 0 & 0 \\ 0 & 2Gh & 0 & 0 & 0 & 0 & 0 & 0 & 0 & 0 & 0 & 0 \\ 0 & 0 & \alpha Gh & 0 & 0 & 0 & 0 & 0 & 0 & 0 & 0 & 0 \\ 0 & 0 & 0 & 2Gh & 0 & 0 & 0 & 0 & 0 & 0 & 0 & 0 \\ \nu C & 0 & 0 & 0 & C & 0 & 0 & 0 & 0 & 0 & 0 & 0 \\ 0 & 0 & 0 & 0 & 0 & 0 & 2F & 0 & 0 & 0 & 0 & 0 \\ 0 & 0 & 0 & 0 & 0 & 0 & 0 & D & 0 & -\nu D & 0 & 0 \\ 0 & 0 & 0 & 0 & 0 & 0 & 0 & 0 & \beta F & 0 & 0 & 0 \\ 0 & 0 & 0 & 0 & 0 & 0 & 0 & -\nu D & 0 & D & 0 & 0 \\ 0 & 0 & 0 & 0 & 0 & 0 & 0 & 0 & 0 & 0 & 2F & 0 \\ 0 & 0 & 0 & 0 & 0 & 0 & 0 & 0 & 0 & 0 & 0 & \beta F \end{bmatrix} \tag{4.38}$$

$C = E/(1-\nu^2)h$, $D = Ch^2/12$, $F = Gh^3/12$; E is Young's Modulus, ν is Poisson's coefficient, $G = E/(2(1+\nu))$ is the shear modulus, and h is the shell thickness; the coefficients α and β are the shear and moment factors.

The constitutive law for laminated plates can be easily estimated using the Classical Lamination Theory (CLT), but is better computed using appropriate formulations, as the one described in Masarati and Ghiringhelli [152], which take into account the effects of natural and kinematic inter-laminar boundary conditions on the stiffness of the shell.

4.3 Structural Model Validation

First, validation of the nonlinear shell model in MBDyn was carried out against some static benchmark cases which required the shell model to undergo significantly large deformations. Results of this study are presented by Masarati et al. [153].

The shell model was then validated for rotating and flapping plates against prior analysis and experiments conducted by Singh et al. [34]. Further, in-house experiments were conducted on flexible plates. Details of these validation cases are mentioned in the following subsections.

4.3.1 Rectangular Plate undergoing Rotational Motion

First, spin up motion of a cantilevered plate was studied as shown in Figure 4.2(a). It consists of a rectangular plate, hinged at one end and spun with a prescribed angular velocity. The rotational speed of the plate is given by,

$$\omega = \begin{cases} \omega_s\left(\frac{t}{t_s} - \frac{1}{2\pi}\sin\frac{2\pi t}{t_s}\right) & \text{if } 0 \le t \le t_s \\ \omega_s & \text{if } t > t_s \end{cases}$$

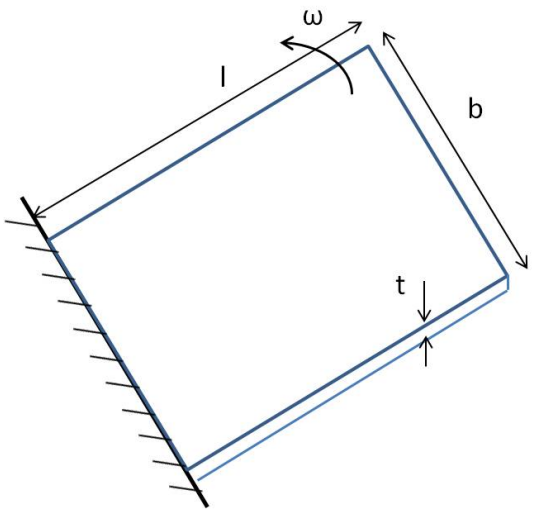

(a) **Schematic**

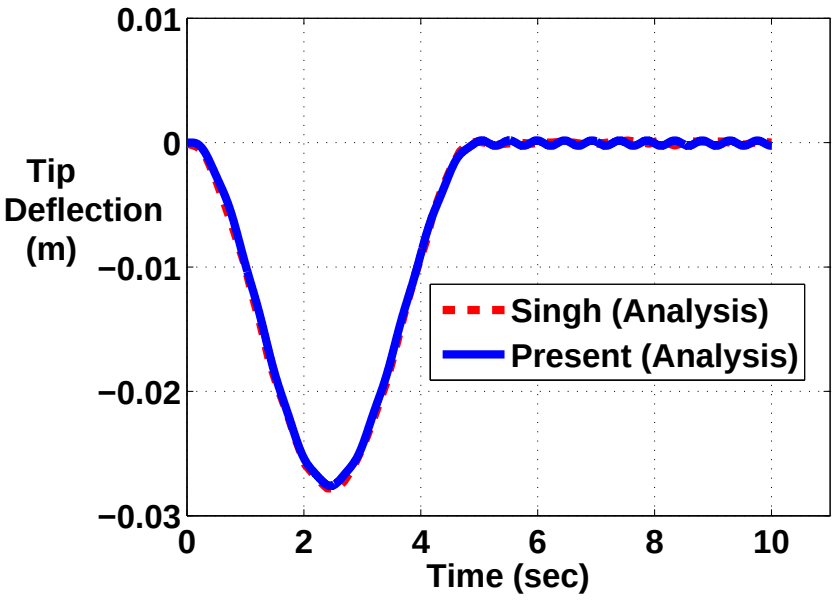

(b) **Tip deflection**

Figure 4.2: **Rotating cantilevered plate validation**

The geometric and material properties of the plate are:

$E = 70$ GPa, $\rho = 3000\ kg/m^3$, $l = 1.0$ m,

$b = 0.5$ m, $t = 0.0025$ m, $\nu = 0.3$.

The rotational speed was ramped up to $\omega_s = 10$ rad/sec over 5 seconds.

For the structural model, an evenly spaced mesh with 32×64 nodes is used. No structural damping is considered. Algorithmic dissipation of high-frequency dynamics is achieved using L-stable second-order BDF to integrate the problem in time. A time step of 0.005 s is used, as in Reference [34]. Good correlation of plate tip deflection was obtained with the analysis of Singh et al. as shown in Figure 4.2(b).

4.3.2 Aluminum Plate in Pure Flapping

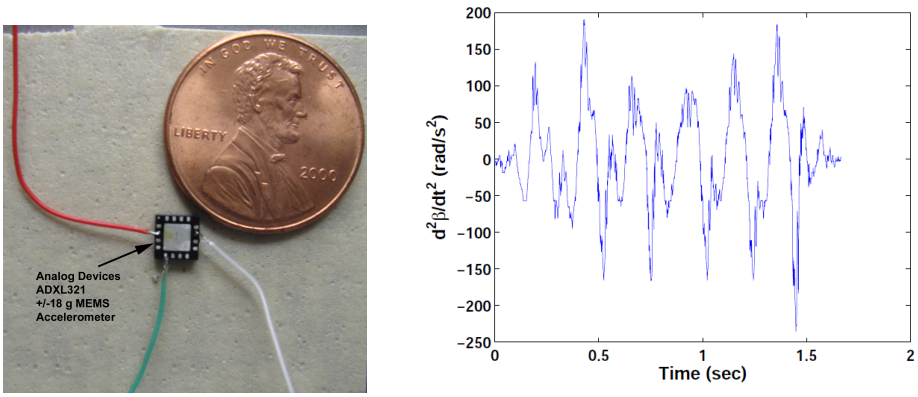

(a) **Schematic** (b) **Experimentally measured acceleration**

Figure 4.3: **Aluminum plate in pure flapping motion (slow support motion, flapping shaft shaken by hand**)

The shell model in MBDyn was then validated for a rectangular alu-

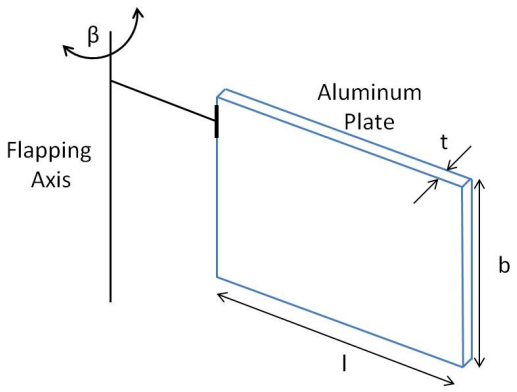

(a) **Schematic**

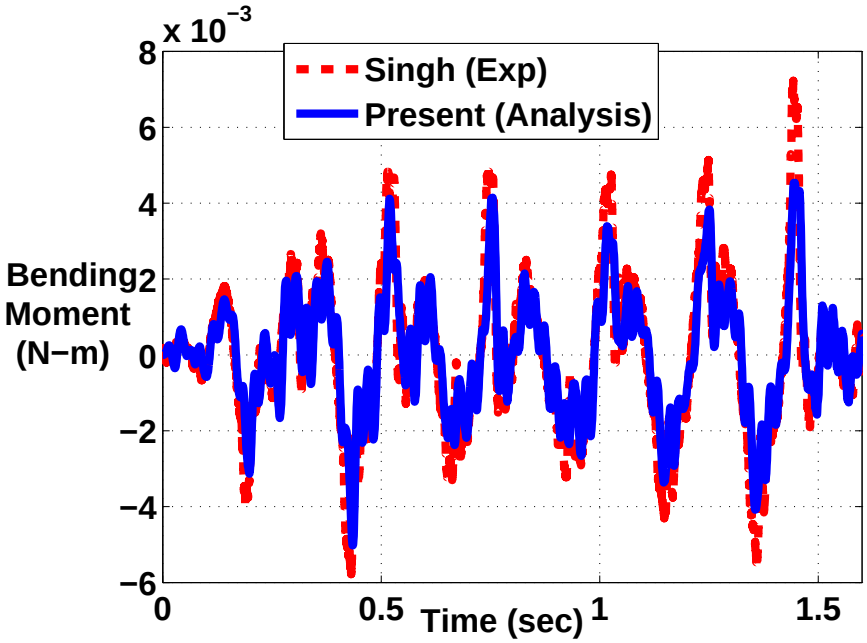

(b) **Comparison of measured and predicted bending moment**

Figure 4.4: **Aluminum plate in pure flapping motion (slow support motion, flapping shaft shaken by hand**)

minum plate undergoing pure flap motion (Figure 4.4(a)). The geometric and material properties of the plate are as follows:

$E = 70$ GPa, $\rho = 2750\ kg/m^3$, $l = 0.089$ m,

$b = 0.038$ m, $t = 0.00058$ m, $\nu = 0.3$

A MEMS accelerometer (Figure 4.3(a)) was used by Singh et al. to measure the wing flap acceleration. Experimentally measured acceleration is shown in Figure 4.3(b). This measured acceleration was input into MBDyn and the bending moment at the base of the wing was compared with experiments. Comparison of prediction with experiments is shown in Figure 4.4(b) and satisfactory correlation is obtained.

4.3.3 Cantilevered Delrin Plate

In-house experiments were carried out to generate more data for the structural model validation. A $1/8^{th}$ inch thick Delrin plate was cantilevered and loaded at the free end. Markers were placed on the plate at different spanwise and chordwise locations and the motion capturing system VICON was used to measure the positions of the markers. A set of four infrared cameras were used as shown in Figure 4.5. Loads were added along different chordwise locations of the free end and the deflections at all the markers (shown in Figure 4.5(b)) were measured experimentally. Figure 4.6 shows the plate schematically.

Using the properties of this isotropic Delrin plate, a structural model was built in MBDyn and the experiments were simulated. Figure 4.7 shows the deflections along the spanwise positions of the plate (blue markers) for load applied at red marker. Experimental measurements are represented by

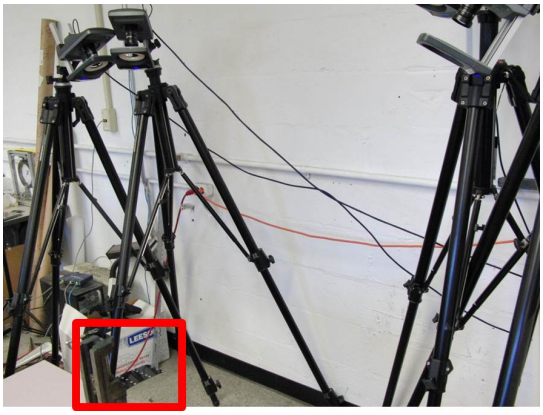

(a) **VICON Setup**

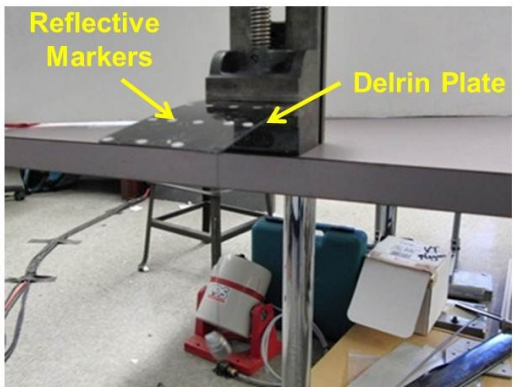

(b) **Zoomed in view of delrin plate with markers**

Figure 4.5: **Cantilevered Delrin plate in VICON setup**

squares and results from the analysis are shown by circles and lines. For the same load conditions, deflections along the purple line are shown by purple squares (experiments) and circles (analysis). As can be seen from the figure, good correlation is achieved and the shell model in MBDyn was satisfactorily validated.

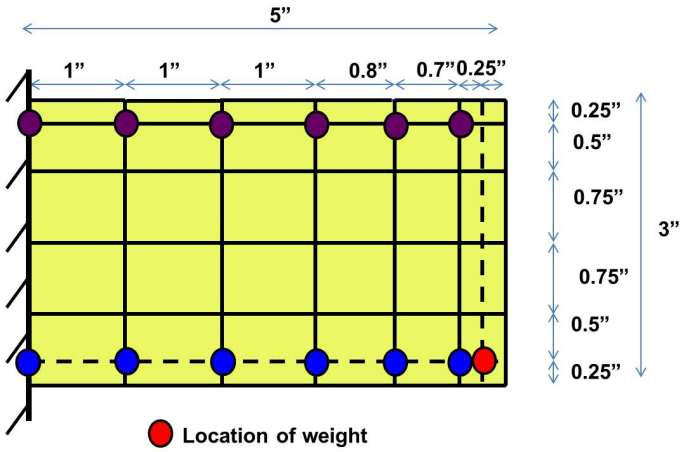

Figure 4.6: **Schematic showing cantilevered delrin plate**

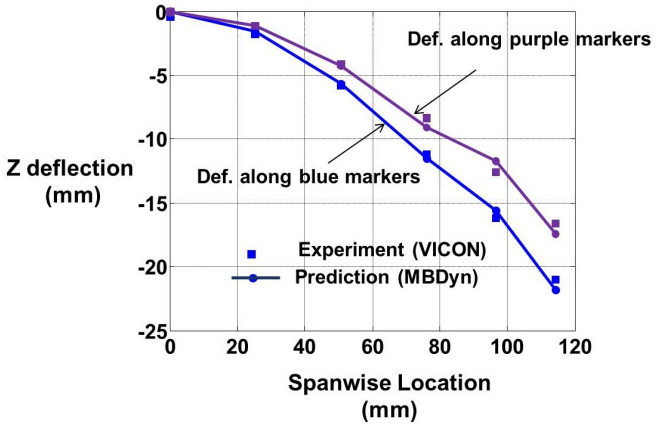

Figure 4.7: **Deflections for cantilevered plate from experiments (VICON) and analysis (MBDyn)**

4.4 Summary and Conclusions

The open source general-purpose multibody solver MBDyn is used here to model the structure of a flapping MAV wing. MBDyn has the capability to analyze geometrically exact non-linear beam elements. It has been used extensively for rotary wing applications but it was recently enhanced to take

into account geometrically exact non-linear shell elements. Validation of the shell model was carried out with prior experiments and analysis. In house experiments were also conducted and deflections were measured using VICON on a cantilevered Delrin plate. Satisfactory correlation was obtained for all the cases. To conclude, the capability of MBDyn to model plate structures with large deformations was successfully demonstrated.

Chapter 5

CFD-CSD Aeroelastic Analysis of Simplified Configurations

5.1 Overview

To obtain reliable predictions of a flexible flapping wing performance and the detailed flow field surrounding the wing, both the fluid and the structural domains need to be modeled accurately. Solving the two domains in a single monolithic solver is impractical. Instead, a coupled simulation using specialized solvers allows modeling of domain-specific features in a simple and efficient manner. Interactions between the fluid and the structural surface can then be modeled by exchanging information at the fluid-structure interface. The present work uses such a coupled simulation where independent CFD and CSD solvers are used together. The CFD solver (OVERTURNS) and structural solver (MBDyn) are coupled using the coupling methodology described here.

5.2 Coupling Strategy

A Python-based computational framework that facilitates the data exchange between the participating solvers is used. This coupling algorithm allows exchange of motion (which is the kinematics mapping from the CSD

to the CFD solver) and loads (from the CFD to the CSD solver) at the fluid-structure interface. This exchange is done in a quite tight manner, that is at each iteration of the nonlinear problem solution procedure for a given time step. Coupling between the two codes was accomplished using a first order as well as a staggered second order accurate approach, which satisfies the discrete geometric conservation law (DGCL) presented by Farhat et al. [128]. However, it was observed that both the approaches gave similar results. The domains and meshes of the two solvers are non conformal. The mapping of these incompatible domains is based on an original scheme that preserves the work exchanged between the structural and the aerodynamic domains [129]. This mapping is based on a Moving Least Squares (MLS) fitting of the discretization of the interface between the two domains using a compact support that consists of Radial Basis Functions (RBF).

5.3 CFD-CSD Validation

Validation of the coupled CFD-CSD solver was carried out for some flexible flapping wing configurations for which data is available in prior literature.

5.3.1 Description of Test Case

A lot of experiments have been carried out recently on flexible flapping wings. However, in most of these studies, the wings were not structurally characterized. Since the structural properties of these wings are not available,

they cannot be used to validate our aeroelastic analysis. One study where flexible wings were structurally characterized was carried out by Heathcote et al. [88] at University of Bath. Validation of the coupled analysis with these results is presented here. These experiments were carried out to understand the effect of spanwise flexibility on flapping wing aerodynamics on a straight, untapered wing, in pure plunging motion at Reynolds numbers ranging from 10,000 to 30,000. Reduced frequencies up to about 5 were considered. For the present validation, focus is on cases at $Re = 30,000$ and $k = 1.82$ for which instantaneous force and tip displacements are available. Some details of the test setup and wing construction are mentioned next.

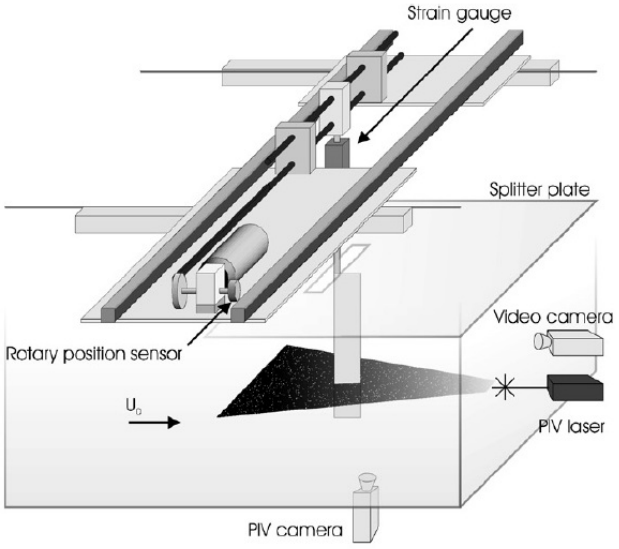

Figure 5.1: **Water tunnel experimental set-up for force measurements, wing deformation measurements and PIV measurements** [88]

Experiments were conducted in a free-surface closed-loop water tunnel (Eidetics Model 1520) with a 381 mm wide x 508 mm deep test-section and

flow speed range of $0 - 0.45$ m/s. The free stream velocity was measured with a Laser Doppler Velocimetry system. The driving mechanism is shown in Figure 5.1. The wing was mounted vertically with one end attached to a horizontal shaker. The displacement of the root is given by $s = h_{ROOT}cos(\omega t)$. A half-model wing with a splitter plate was tested. The wing was attached to a rod which moves in a narrow slit in the splitter plate.

Wings of 300 mm span, 100 mm chord, NACA0012 cross-section, and rectangular planform were used in the experiment. The model consisted of a rectangular stainless steel plate (Young's modulus, $E = 210$ GPa) of constant thickness, 1 mm. It was covered by a polydimethylsiloxane (PDMS) layer of very soft Young's modulus ($E = 250$ kPa), in order to reproduce the outer shape of the airfoil. The wing was designed to be stiff in the chordwise direction. In the experimental study, force measurements were made using strain gauges and wing deformations were captured using a motion tracking software. The root of the wing was subjected to a harmonic motion given by: $h_{root} = h_\circ \sin(\omega t)$, where $h_\circ = 0.175$ c, root displacement amplitude. Experiments were also conducted on an inflexible wing, made as stiff as possible, using a nylon structure stiffened by thick steel rods. Cross-section of the wings is shown in Figure 5.2(a). A wing with greater flexibility was also tested and details of that are mentioned in a later section.

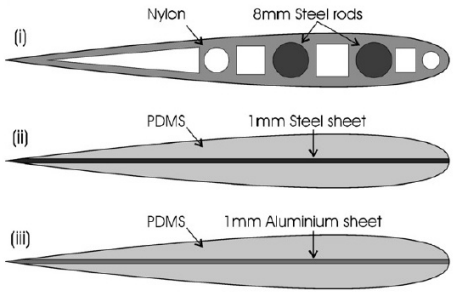

(a) **Cross-sections of the three NACA0012 wings: (i) inflexible, (ii) flexible, (iii) highly flexible [88]**

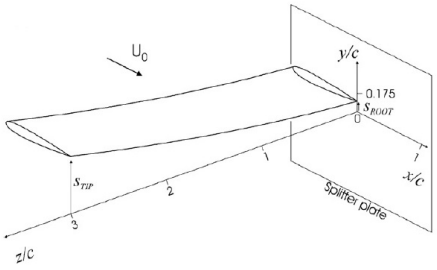

(b) **Schematic of the spanwise flexible wing heaving periodically**

Figure 5.2: **Schematics for spanwise flexible wings [88]**

5.3.2 Description of Computational Model

A C-H grid is used to simulate the wing having 277 points in the wrap around, 81 points in the spanwise and 85 points in the normal directions as shown in Figure 5.3. The main structural component of this model consists of a flat metal plate. Thus, it is modeled here using a single layer of non-linear shell elements, and actuated by prescribing the heave motion of the semi-span wing root. The structural model consists of 5×15 shell elements re-

spectively, in the chordwise and spanwise directions. These experiments have been used for validation in previous studies as well [104, 116]. Results from the present study are compared with those of Chimakurthi et al. [104]. They used a high-order Navier-Stokes solver coupled with a structural solver that decomposes the equations of three-dimensional elasticity into cross-sectional, small deformation and spanwise, large-deformation analyses for slender wings.

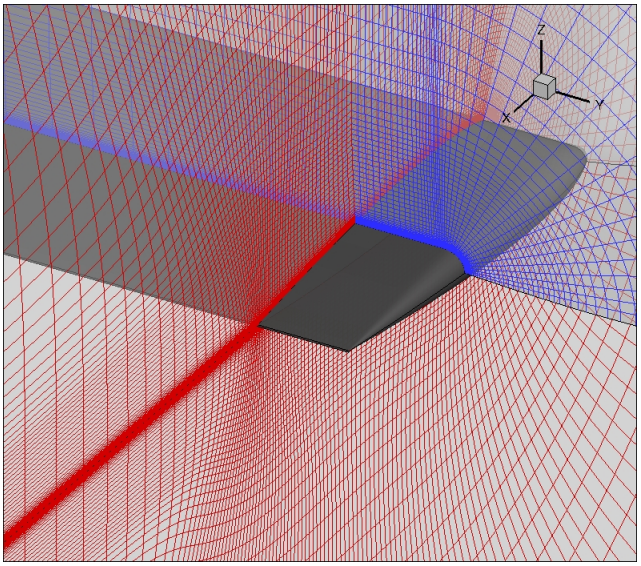

Figure 5.3: **Grid for spanwise flexible wing**

5.3.3 Rigid and Spanwise Flexible Wing Validation

Figure 5.4 shows the instantaneous propulsive force variation over a flap cycle for the rigid wing, starting from the top most position of the flap cycle. In the present analysis, the inflexible wing is modeled using an ideally rigid model. From the figure, it can be seen that the instantaneous propulsive force is positive almost throughout the flap cycle. The present simulation resulted in

an average C_X of 0.21, which is equal to the experimental value, as compared to 0.195 from the simulation by Chimakurthi et al. [104]. These results further validate the CFD solver. Note that, Heathcote et al. [88] have not presented the instantaneous vertical force values (F_Z) and therefore, a comparison of the vertical force variation is not shown.

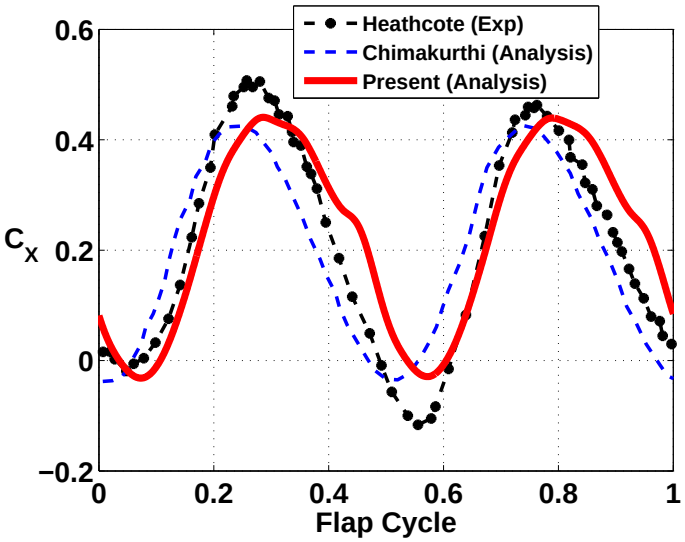

Figure 5.4: **Instantaneous C_X variation over a flap cycle for rigid wing**

Figure 5.5(a) shows the instantaneous tip position at mid chord normalized by the root amplitude for the flexible wing. Due to spanwise flexibility, tip deflections are higher than the prescribed root motion. Figure 5.5(b) shows the instantaneous propulsive force over the flap cycle for flexible wing. The present simulation resulted in an average C_X of 0.31 as compared to the experimental C_X of 0.32, and 0.278 from the simulation by Chimakurthi et al. [104].

Figures 5.6 and 5.7 show the comparison of vortical wake structures between the results by Chimakurthi et al. [104], experiments by Heathcote

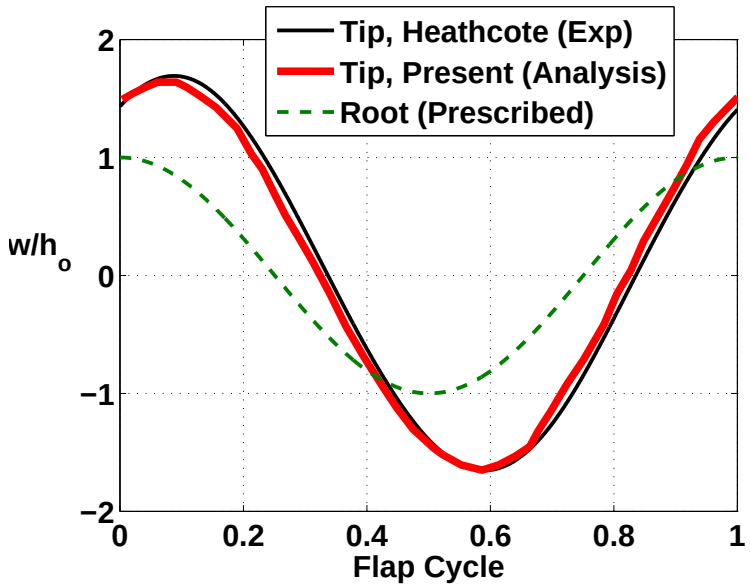

(a) **Tip displacement at mid chord for flexible wing**

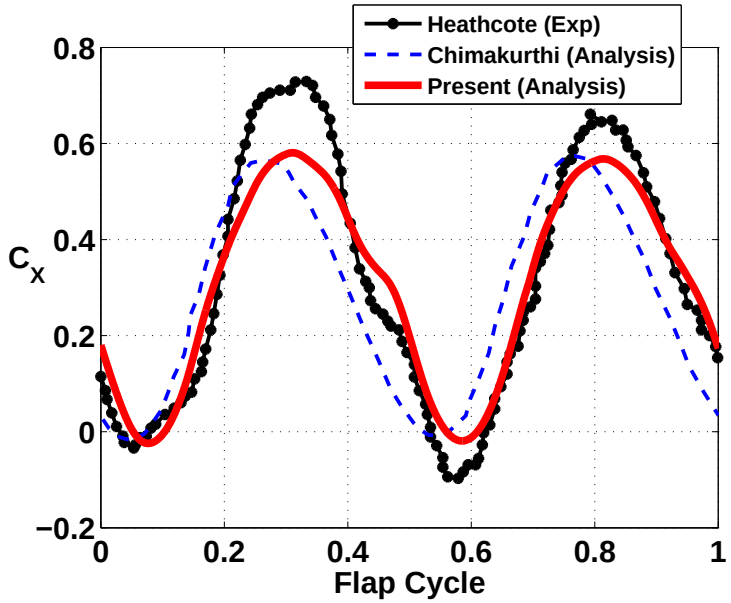

(b) **Instantaneous C_X variation over a flap cycle for flexible wing**

Figure 5.5: **Instantaneous tip deflection and C_X variation for spanwise flexible wing**

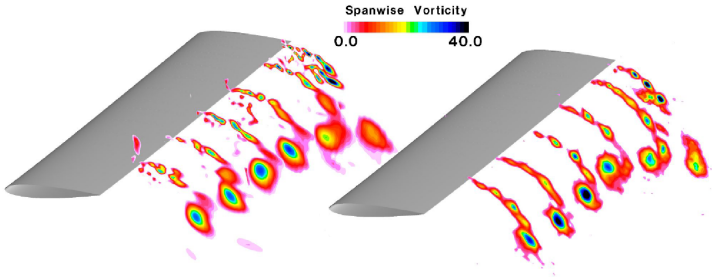

(a) **Predictions: Chimakurthi et al.[104] (left), Experiments: Heathcote et al.[88] (right)**

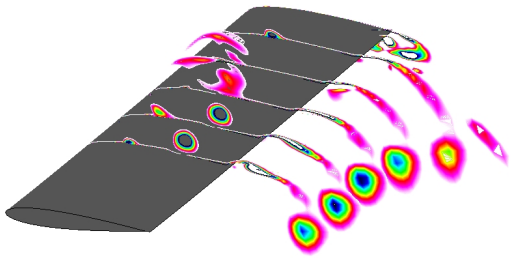

(b) **Predictions: Present**

Figure 5.6: **Comparison of wake structure at various spanwise stations at the peak of the upstroke, $t/T = 0.0$, for spanwise flexible wing**

et al. [88] and present simulation. Similar vortical structures are obtained as compared to prior research at two instants of time, $t/T = 0$ and $t/T = 0.25$, respectively.

A discussion on the effect of flexibility is presented in the next subsection.

5.3.4 Comparison Between Rigid and Spanwise Flexible Wing

Figure 5.8 shows the spanwise vorticity contours and surface pressure contours for the rigid and flexible wings (starting from the top most position

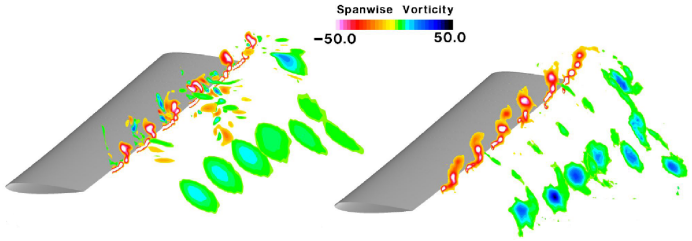

(a) **Predictions: Chimakurthi et al.[104] (left), Experiments: Heathcote et al.[88] (right)**

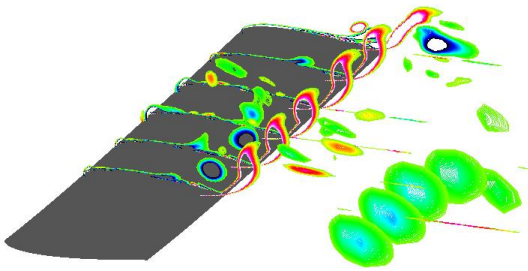

(b) **Predictions: Present**

Figure 5.7: **Comparison of wake structure at various spanwise stations at the midpoint of the downstroke,** $t/T = 0.25$**, for spanwise flexible wing**

in plunge cycle). Since this case is a pure plunge motion, for the rigid case, the flow is mostly 2D till about 75% span location. Beyond this the flow becomes 3D due to the tip effect. On the other hand, for the flexible case, since there is flap bending and the plunge amplitude varies over the span, the 2D nature is not preserved even at further inboard locations. The flow is more 3-D in the flexible wing case as compared to the rigid wing. As compared to the rigid wing, since the flexible wing has higher plunge amplitude near the wing

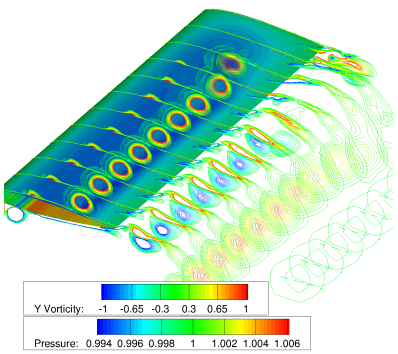

(a) **t=0, Rigid**

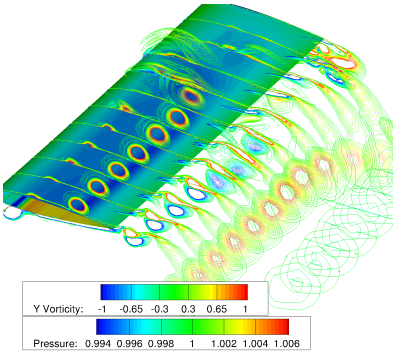

(b) **t=0, Flexible**

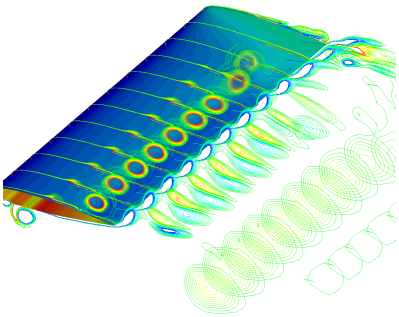

(c) **t=T/8, Rigid**

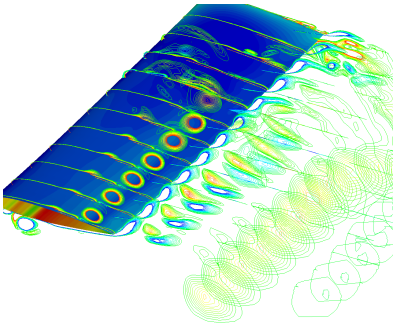

(d) **t=T/8, Flexible**

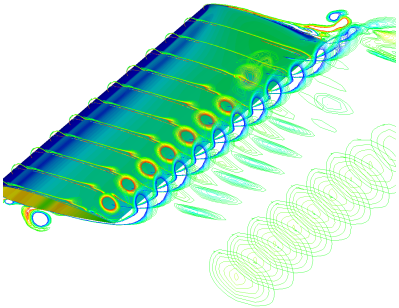

(e) **t=T/4, Rigid**

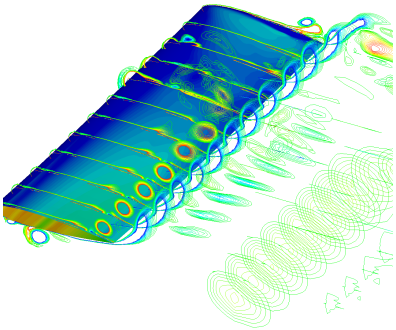

(f) **t=T/4, Flexible**

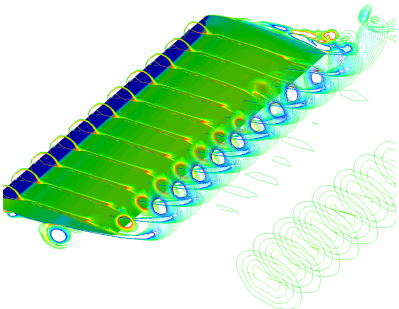

(g) **t=3T/8, Rigid**

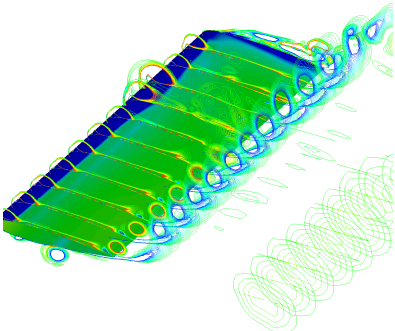

(h) **t=3T/8, Flexible**

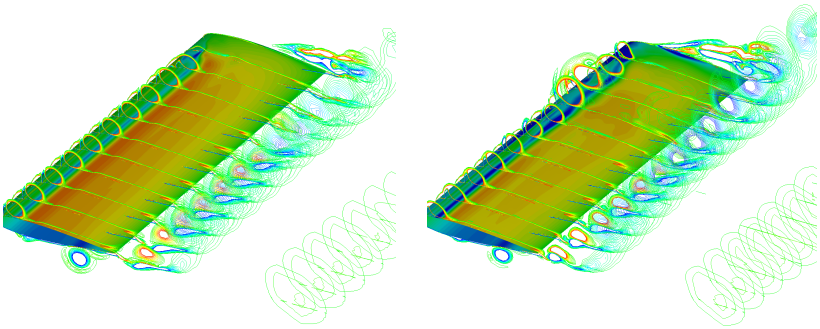

(i) **t=T/2, Rigid** (j) **t=T/2, Flexible**

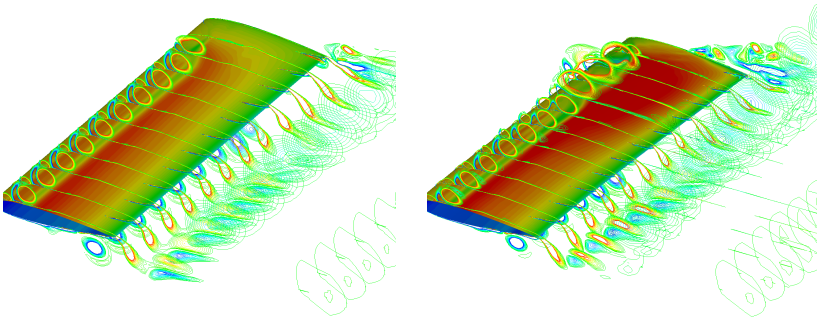

(k) **t=5T/8, Rigid** (l) **t=5T/8, Flexible**

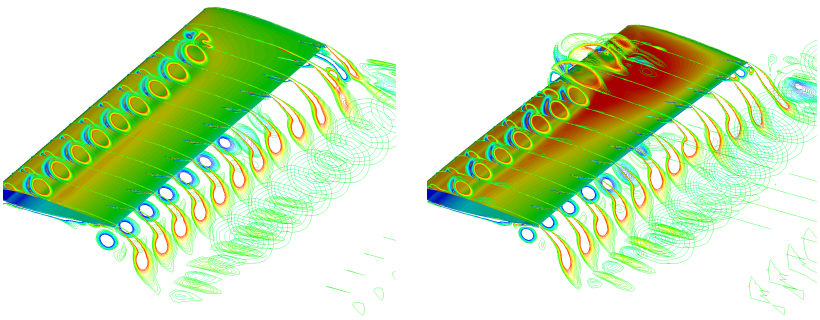

(m) **t=3T/2, Rigid** (n) **t=3T/2, Flexible**

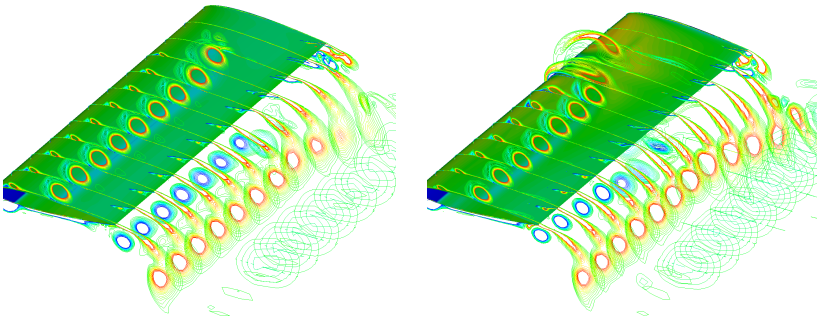

(o) **t=7T/8, Rigid** (p) **t=7T/8, Flexible**

Figure 5.8: **Y vorticity contours for rigid and spanwise flexible wings.**

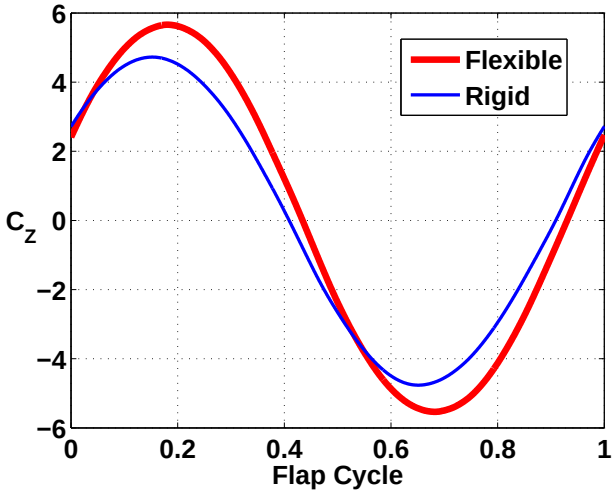

Figure 5.9: **Instantaneous C_Z variation over a flap cycle for rigid and spanwise flexible wings**

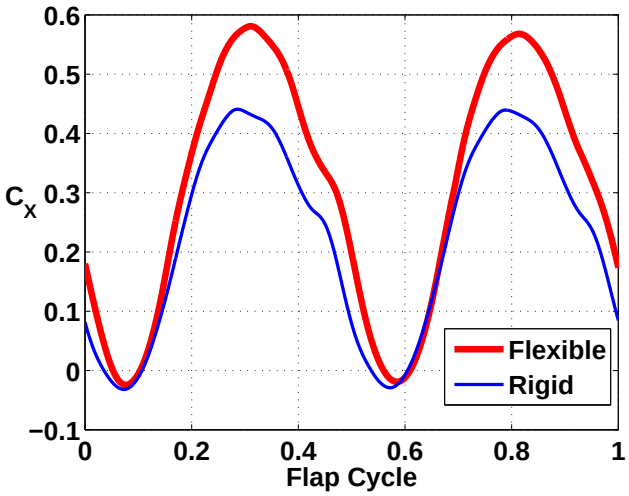

Figure 5.10: **Instantaneous C_X variation over a flap cycle for rigid and spanwise flexible wings**

tip, this leads to a higher effective angle of attack and higher propulsive (F_Z) and vertical forces (F_X). The leading edge vortices are stronger towards the outboard sections of the wing and also the strength of the tip vortex is higher.

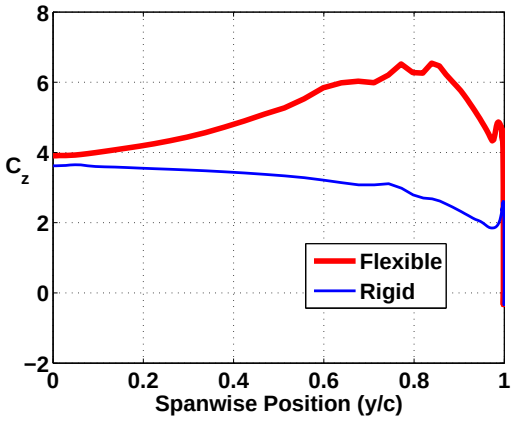

(a) C_z

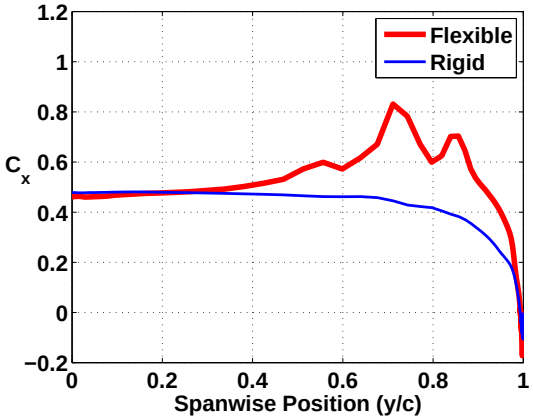

(b) C_x

Figure 5.11: **Spanwise C_z and C_x variation for rigid and spanwise flexible wings at $t/T = 0.25$ (middle of downstroke)**

These observations are consistent with those made by Chimakurthi et al. [104].

Figure 5.9 shows the instantaneous vertical force coefficient (C_Z) variation over the flap cycle for the rigid and flexible wings. Due to symmetry in the upstroke and downstroke, the average vertical force in this case is zero. However, due to flexibility, the maximum instantaneous vertical force coefficient is increased from 4.4 in case of a rigid wing, to 5.6 for the flexible wing.

Figure 5.10 shows the instantaneous propulsive force variation over a flap cycle for rigid and spanwise flexible wings. As compared to the rigid wing, higher propulsive force is obtained for the flexible wing. It increased from 0.21 to 0.31. Therefore, due to flexibility, the average C_X increased by 47%. These results are summarized in Table 5.1.

Figure 5.11 shows the spanwise C_z and C_x variation for the rigid and flexible wings at the same instant of time (t/T=0.25, middle of downstroke). Sectional vertical force coefficient (C_z) is higher for flexible wing, particularly towards the outer sections of the wing. Similar trend is seen for propulsive force. Thus, the increase in forces due to flexibility in this case comes mainly from the outer sections where the plunge amplitudes are higher. Higher plunge amplitude leads to a greater effective angle of attack and leading edge suction and therefore, greater forces.

Table 5.1: **Average propulsive force and maximum instantaneous vertical force coefficients for rigid and flexible wings**

	Rigid	**Flexible**	**% Increase**
Average C_X	0.21	0.31	47%
Max. Instantaneous C_Z	4.4	5.6	27%

5.3.5 Highly Flexible Wing Validation

Next, a wing with more flexibility referred to here as a highly flexible wing, was analyzed. The experimental model tested by Heathcote et al. was constructed using polydimethylsiloxane rubber (PDMS, $E = 250$kPa) cast in a NACA0012 mould and stiffened with 1 mm aluminum sheet (E = 70 GPa). This wing was tested with similar kinematic parameters as the flexible wing mentioned in the previous subsection. It should be noted that using the value of Young's modulus mentioned in the paper by Heathcote et al. [88] of 70 GPa, the analysis could not predict similar deflections and forces as the experiments. Through personal correspondence with Chimakurthi, it was discovered that the correct value of experimental Young's Modulus was 40 GPa, which is then used here. The instantaneous tip position (non-dimensionalized by root amplitude) of the highly flexible wing is shown in Figure 5.12. As can be seen from the figure, satisfactory correlation is obtained with the analysis by Chimakurthi et al. There is some phase difference with the experimental results and this might be because of the discrepancy in the value of Young's Modulus of this wing. Further, unlike the flexible wing, for this case, the root and tip move out of phase for a large portion of the flap cycle.

Figure 5.13 shows the instantaneous vertical force and instantaneous propulsive force coefficients from the experiment, analysis by Chimakurthi and present prediction. The present simulation resulted in an average C_X of 0.13, experimental value was 0.11, as compared to 0.121 from the simulation

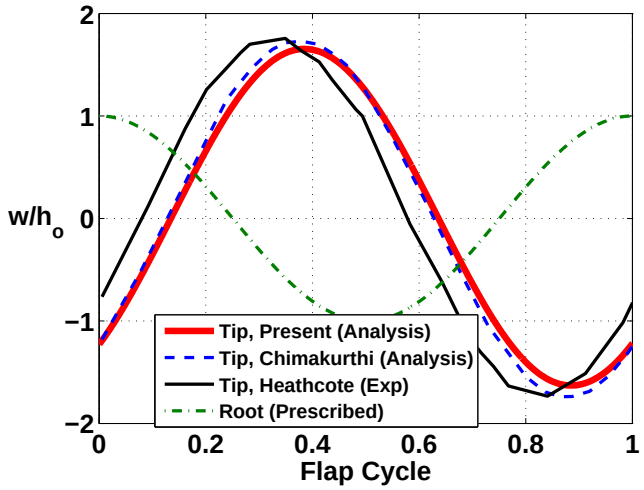

Figure 5.12: **Instantaneous tip positions for highly flexible wing**

by Chimakurthi et al. [104].

Figures 5.14 and 5.15 show the comparison of vortical wake structures between the results by Chimakurthi et al. [104], experiments by Heathcote et al. [88] and present simulation. Similar vortical structures are obtained as compared to prior research at two instants of time, $t/T = 0$ and $t/T = 0.25$, respectively.

5.3.6 Comparison Between Rigid, Flexible and Highly Flexible Wings

Finally, comparing the inflexible, flexible and highly flexible cases, it was observed that on introducing a small amount of flexibility, the average propulsive force coefficient (C_X) increased from 0.21 to 0.31 by 47% and the instantaneous vertical force coefficient (C_Z) increased from 4.4 to 5.6 by 27%.

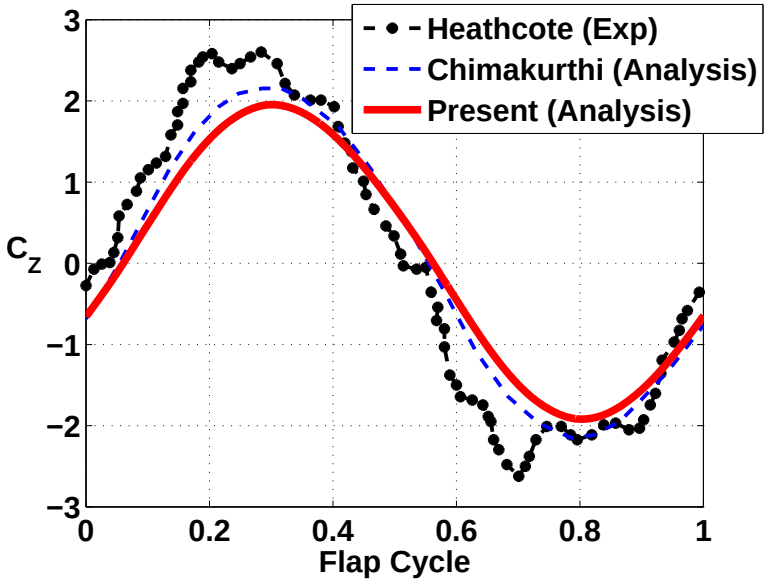

(a) C_Z

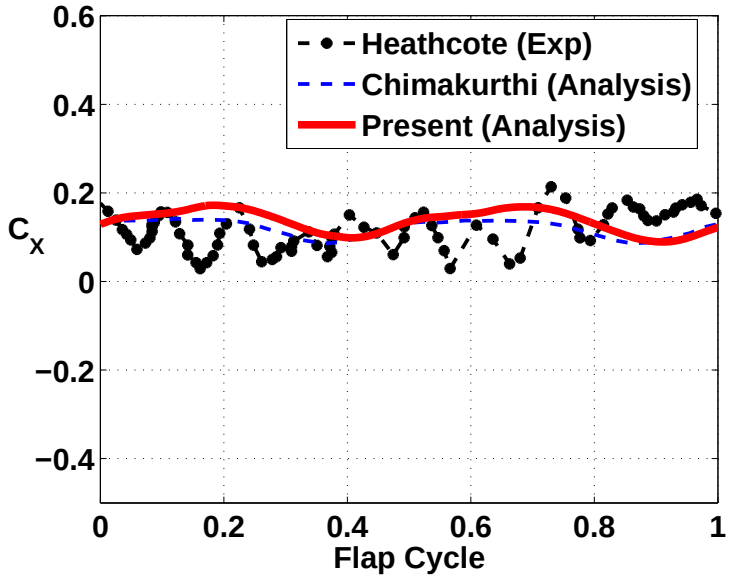

(b) C_X

Figure 5.13: **Instantaneous force variation over a flap cycle for highly flexible wing**

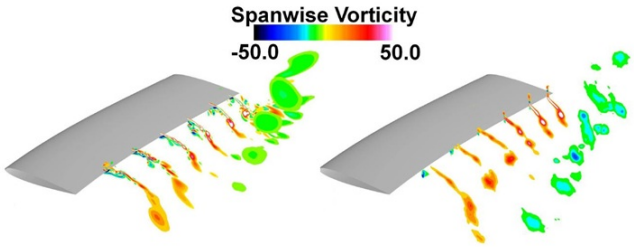

(a) **Predictions: Chimakurthi et al.[104] (left), Experiments: Heathcote et al.[88] (right)**

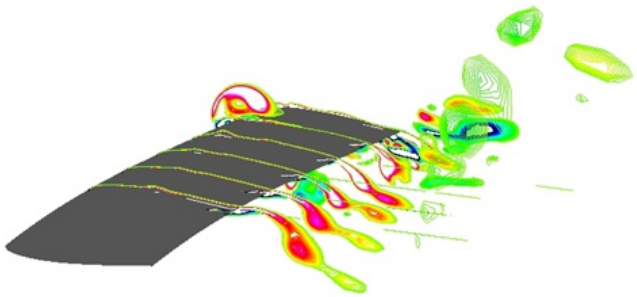

(b) **Predictions: Present**

Figure 5.14: **Comparison of wake structure at various spanwise stations at the peak of the upstroke,** $t/T = 0.0$ **for spanwise highly flexible wing**

However, for the highly flexible wing, the average propulsive force coefficient dropped to 0.13, (58% compared to flexible wing) and instantaneous vertical force coefficient dropped to 1.95 (65% compared to flexible wing). These results are summarized in Table 5.2. The instantaneous vertical and propulsive force coefficients for the three wings are plotted in Figure 5.16. The reason for the drop in forces for the highly flexible wing is that in this case, the wing root and tip move out of phase for a large portion of the flap cycle and this

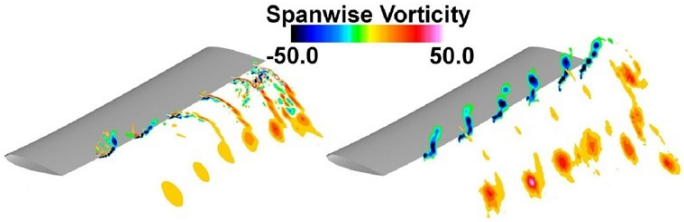

(a) **Predictions: Chimakurthi et al.[104] (left), Experiments: Heathcote et al.[88] (right)**

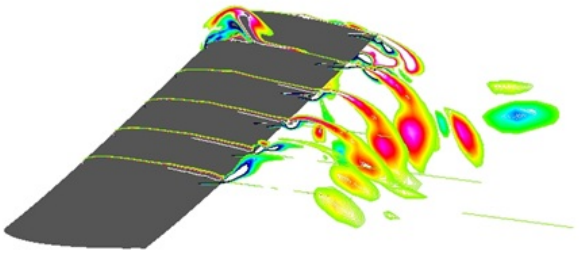

(b) **Predictions: Present**

Figure 5.15: **Comparison of wake structure at various spanwise stations at the midpoint of the downstroke,** $t/T = 0.25$ **for spanwise highly flexible wing**

results in leading edge vortices being formed on different sides of the wing at the root and tip. The instantaneous tip positions for all the cases is shown in Figure 5.17. Also, due to this out of phase motion, the angle of attack is reduced towards the outer sections and a drop in vortex strength is observed. Figure 5.18 shows the pressure coefficient contours for the $3/4^{th}$ spanwise location at middle of the downstroke for all three cases. To conclude, leading edge vortex strength increases from rigid wing to flexible wing but drops for

the highly flexible wing and similar trend is observed in the forces.

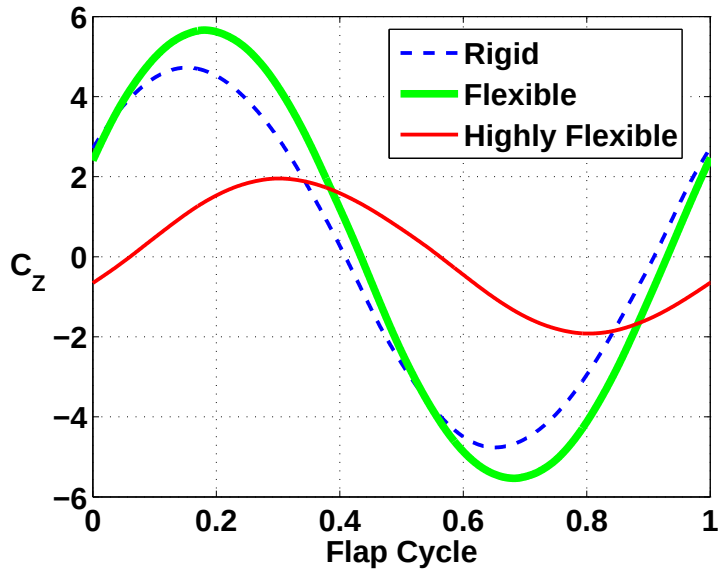

(a) C_Z

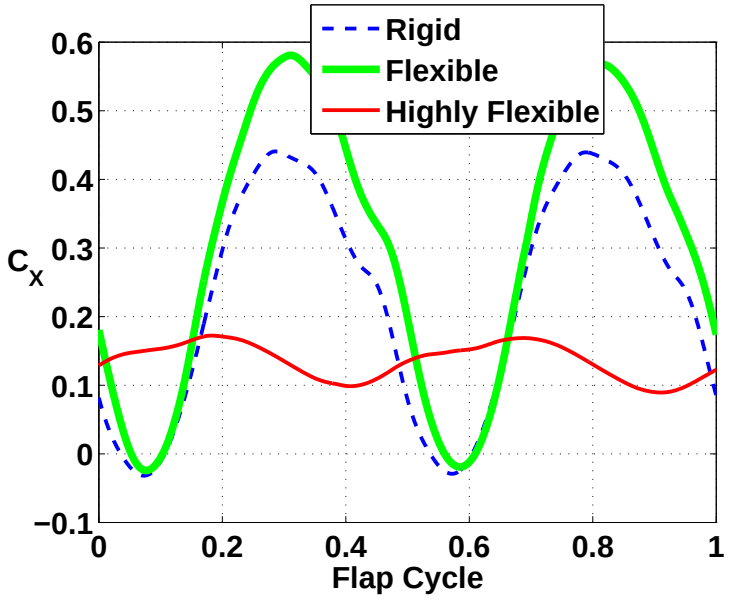

(b) C_X

Figure 5.16: **Instantaneous force variation over a flap cycle for three configurations**

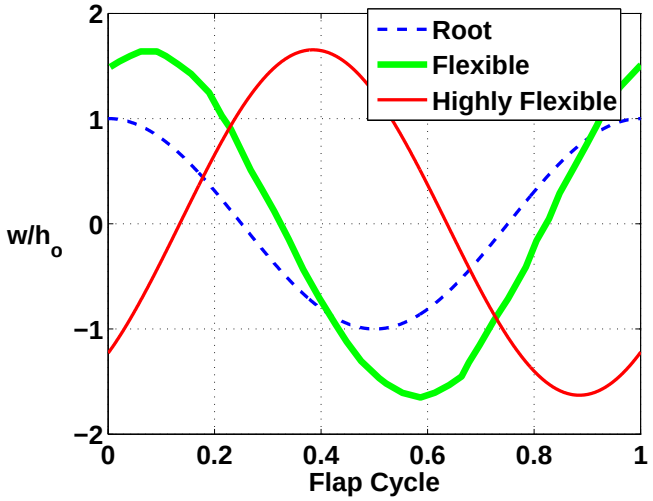

Figure 5.17: **Instantaneous tip positions for all configurations**

Table 5.2: **Average propulsive and maximum instantaneous vertical force coefficients for different wings**

	Rigid	**Flexible**	**Highly Flexible**
Average C_X	0.21	0.31	0.13
Max. Instantaneous C_Z	4.4	5.6	1.95

5.3.7 Power Calculation

Power calculations were available for the experiments by Heathcote et al. [88]. Thus, the aerodynamic power required to flap the wing was obtained from the simulation and compared to the experiments.

The time-averaged power input is given by:

$$\bar{C_P} = \frac{\bar{F_z v}}{\frac{1}{2}\rho V_\infty^3 cS} \tag{5.1}$$

where $F_z v$ is the instantaneous power input, and the overbar denotes an

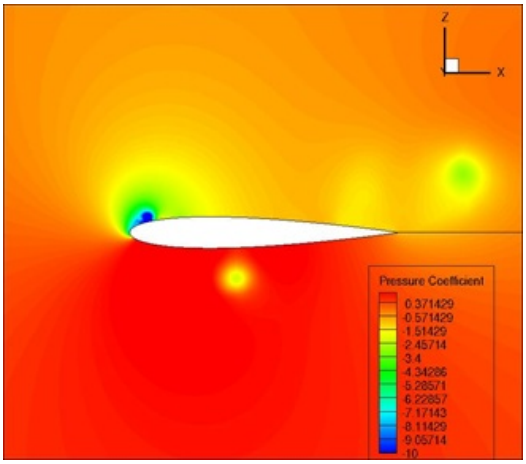

(a) **Rigid Wing**

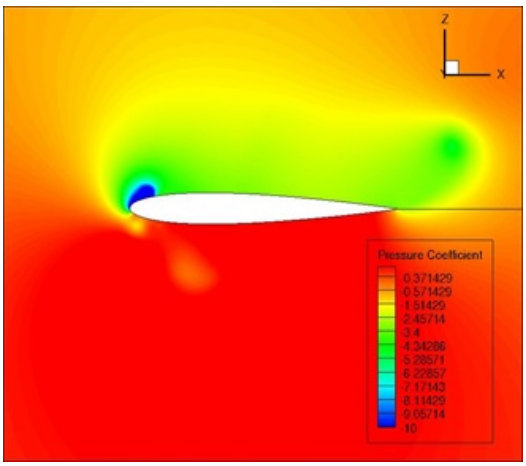

(b) **Flexible Wing**

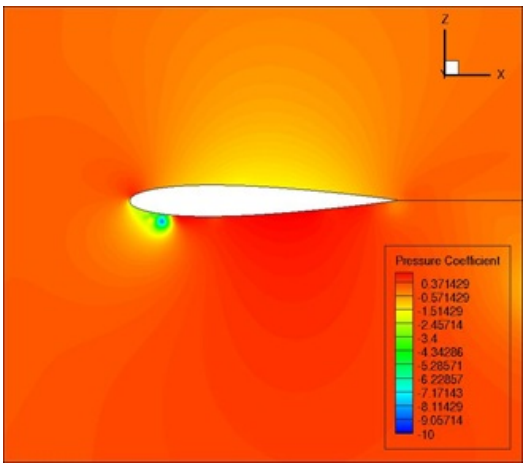

(c) **Highly Flexible Wing**

Figure 5.18: **Pressure coefficient contours at 3/4th spanwise section for different wings**

average over time. The propulsive efficiency is given by:

$$\eta = \frac{\bar{F_x} V_\infty}{\bar{F_z} v} = \frac{\bar{C_X}}{\bar{C_P}} \tag{5.2}$$

Both, power and efficiency are calculated for the three cases and the results are presented in Table 5.3 and 5.4. The results from the prediction are comparable to the experimental results by Heathcote et al. The power required is 56% higher for the flexible wing as compared to the rigid wing and the though efficiency is almost the same, it produces 47% more propulsive force than the rigid wing case. The highly flexible wing produces less propulsive force and also required the lowest input power.

Table 5.3: **Average power for different wings**

C_P	**Experiment**	**Present**
Rigid	1.2	1.1
Flexible	1.8	1.7
Highly Flexible	0.7	0.65

Table 5.4: **Propulsive efficiency for different wings**

η	**Experiment**	**Present**
Rigid	0.17	0.19
Flexible	0.17	0.18
Highly Flexible	0.14	0.17

5.4 Investigation of a Chordwise Flexible Wing

5.4.1 Description of Test Case

A chordwise flexible wing was simulated to further demonstrate the capability of the CFD-CSD solver. Note that there is no reliable experimental data available for validation. Therefore, the current analysis was performed based on an analysis by Gopalakrishnan et al. [103]. They simulated rigid as well as flexible root flapping wings by coupling an LES solver to a linear elastic membrane model. It should be noted that they studied the effect of prestress on flexible wing performance, but used a linear assumption for the prestress values. The present study is not limited to analyzing membrane models linearized about a prestressed condition, but allows the prestress to change accordingly. This is expected to improve the quality of the analysis compared to current literature. Therefore, we are not comparing the flexible wing results from the present study with those of Gopalakrishnan et al. [103], but instead just compare results of the flexible wing obtained from our analysis with those of rigid wing.

The wing considered here is a rectangular wing with an aspect ratio of 4 and root cutout of 0.5 chord (Figure 5.19). The wing thickness to chord ratio was 0.00125. Flapping frequency is 11.94 Hz and Reynolds number of the flow is $10,000$. The pitching axis is placed at the quarter-chord from the leading edge. The wing is held fixed at the root and flapped with the following parameters:

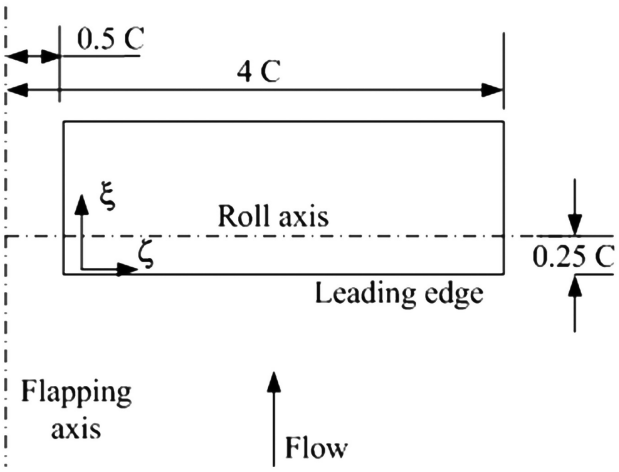

Figure 5.19: **Wing dimensions for chordwise flexible case [103]**

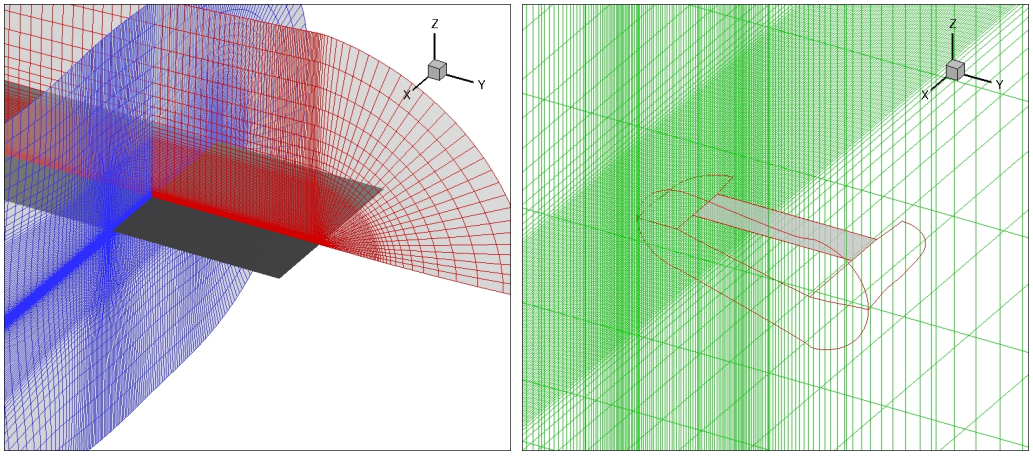

(a) **Blade mesh** ($267 \times 181 \times 85$) (b) **Cartesian background mesh** ($162 \times 195 \times 122$) **with wing mesh boundary**

Figure 5.20: **Computational mesh for 3D root flapping chordwise flexible wing simulation**

Flap: $\gamma = \gamma_o \cos(2\pi f t)$,

Pitch: $\theta = \theta_o - \theta_a \sin(2\pi f t)$

with $\gamma_o = 30^o$, $\theta_o = 12.5^o$, $\theta_a = 32.5^o$

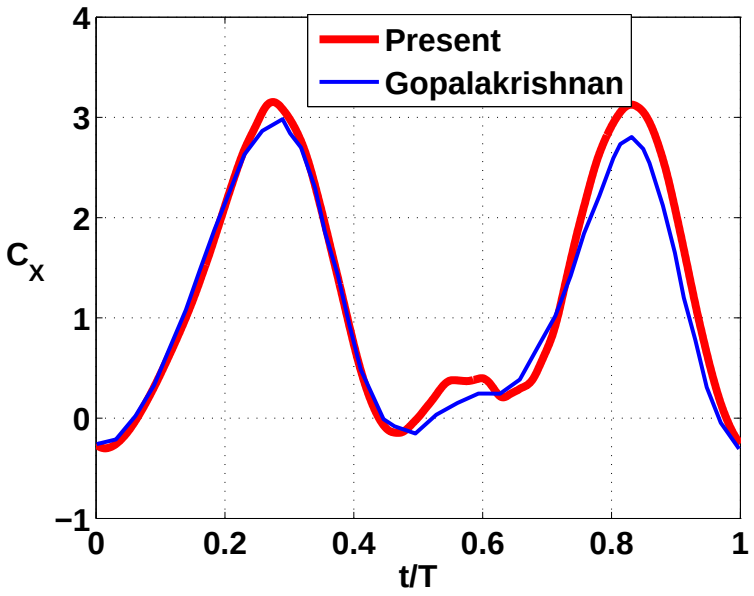

(a) C_X

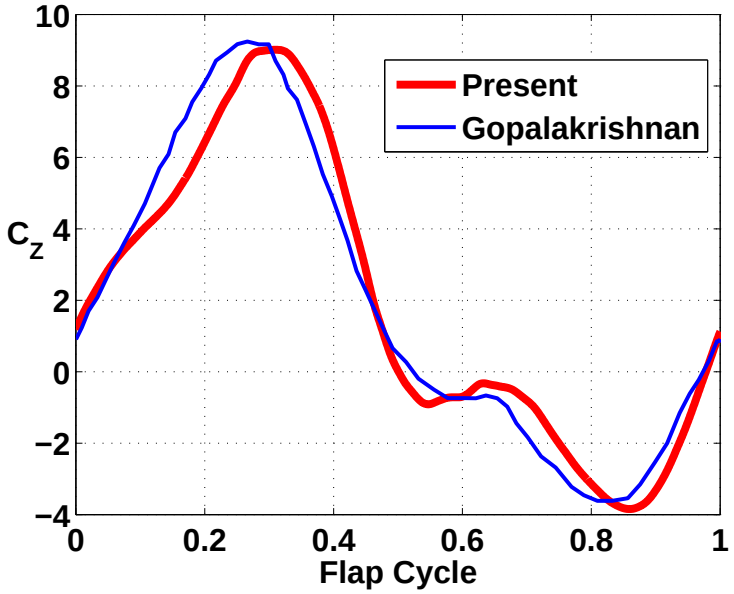

(b) C_Z

Figure 5.21: **Instantaneous C_X and C_Z variation over a flap cycle for 3D root flapping chordwise rigid case**

5.4.2 Description of Computational Model

A two mesh overset system consisting of a body-fitted curvilinear wing mesh overlayed onto a Cartesian background mesh is used for this case. The wing mesh has clustering at the wing root and tip as well as leading and trailing edges. The Cartesian background mesh is refined to resolve tip vortex evolution. The wing mesh has 267 points in the wrap around, 181 points in the spanwise and 85 points in the normal directions. The Cartesian background mesh has 162 points in the streamwise, 195 points in the spanwise and 122 points in the vertical directions. The mesh for this case is shown in Figure 5.20.

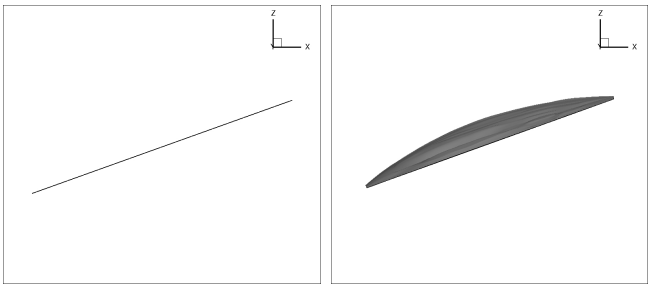

(a) **Rigid Wing** (b) **Flexible Wing**

Figure 5.22: **Side view of rigid and chordwise flexible wings at** $t/T = 0.25$ **(middle of downstroke)**

5.4.3 Results and Discussion

Figure 5.21 shows the rigid wing results from the present study and the simulation by Gopalakrishnan et al. [103] and satisfactory correlation is achieved. The average C_Z and C_X values are 1.9 and 1.2, respectively.

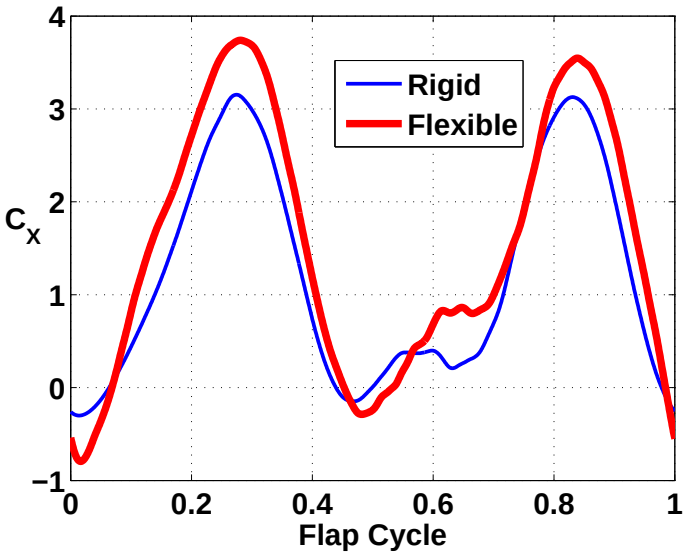

(a) C_X

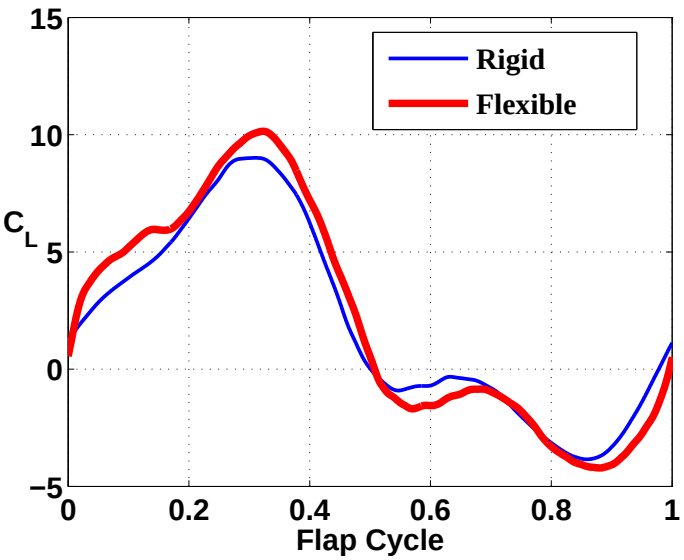

(b) C_Z

Figure 5.23: C_X **and** C_Z **variation with time for 3D root flapping chordwise flexible case**

A membrane model is then used to analyze a chordwise flexible wing with no prestress. The Young's Modulus is $E = 2 \times 10^6\ N/m^2$ and density

of the material, $\rho_w = 1350\ kg/m^3$. As a result of this flexibility, the wing produced a positive camber during the downstroke and negative camber during the upstroke over a large portion of the wing. A side view of the wing during the middle of the downstroke is shown in Figure 5.22.

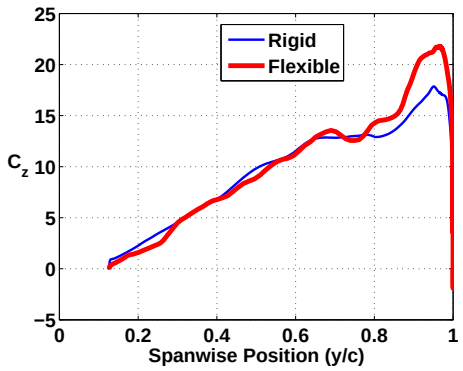

(a) C_z

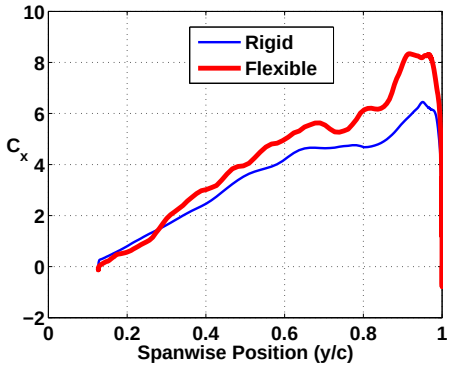

(b) C_x

Figure 5.24: **Spanwise C_z and C_x variation for rigid and chordwise flexible wings at $t/T = 0.25$ (middle of downstroke)**

Figures 5.23(a) and 5.23(b) show the instantaneous propulsive and vertical force coefficients, respectively, for the rigid and flexible wings. The average C_Z for the flexible wing increased by 10% to 2.1 and the average C_X increased

by 25% to 1.5 as compared to the rigid wing. These results are summarized in Table 5.5.

Table 5.5: **Average forces for rigid and chordwise flexible wings (root flap + pitch)**

	Rigid	**Flexible**	**% Increase**
Average C_X	1.2	1.5	25%
Average C_Z	1.9	2.1	10%

Figure 5.24 shows the spanwise variation of C_z and C_x for the rigid and flexible wings at the same instant of time (t/T=0.25, middle of downstroke). Similar to the spanwise flexible wing, the chordwise flexible wing has higher sectional C_z and C_x towards the tip. Figure 5.25 shows the comparison between the surface pressure contours for the rigid and flexible wings at 3/4th spanwise location for various instants of time. Due to the camber that develops for the flexible wing, a greater portion of the resultant force is vectored in the chordwise direction. Also, the strength of leading edge suction is higher in the flexible wing case and there is a greater high pressure at the bottom of the wing. This clearly shows the beneficial effect of chordwise flexibility on the aerodynamics of flapping wings.

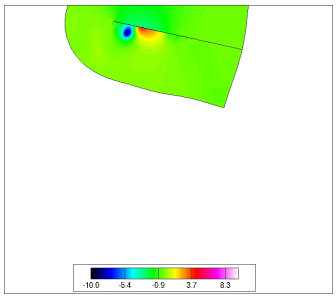

(a) **t=0, Rigid**

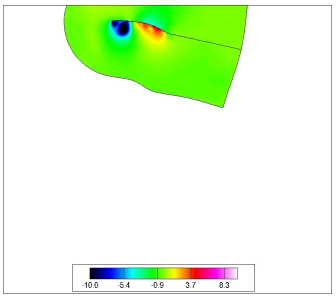

(b) **t=0, Flexible**

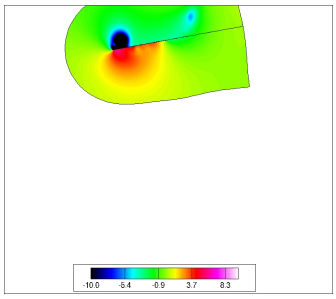

(c) **t=T/8, Rigid**

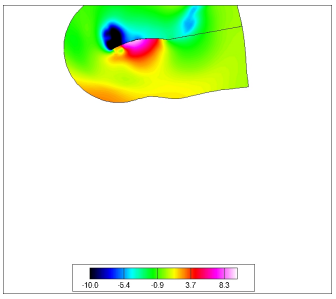

(d) **t=T/8, Flexible**

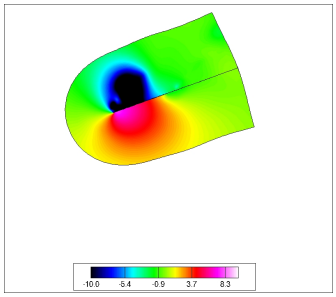

(e) **t=T/4, Rigid**

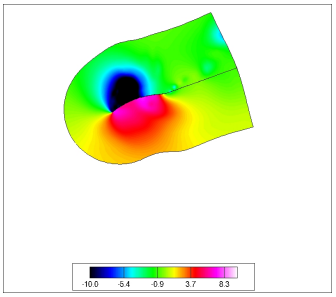

(f) **t=T/4, Flexible**

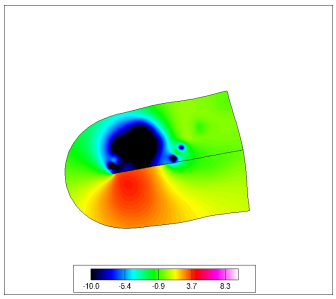

(g) **t=3T/8, Rigid**

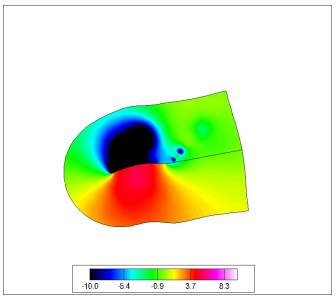

(h) **t=3T/8, Flexible**

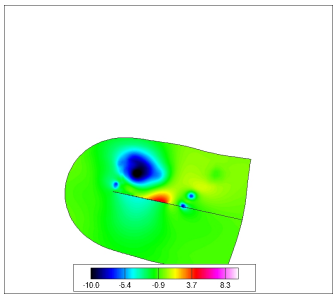

(i) **t=T/2, Rigid**

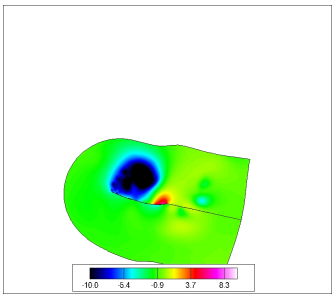

(j) **t=T/2, Flexible**

Figure 5.25: **Pressure contours at 3/4th spanwise section for rigid and chordwise flexible wings (continued)**

5.5 Summary and Conclusions

A coupled CFD-CSD solver was used to simulate the aerodynamics of a flexible flapping wing. The CFD solver was a compressible RANS solver, which was first validated for rigid 2D and 3D wings. Good correlation was obtained for all the cases considered. The structural solver used is called MBDyn which has been extended to take into account non linear shell straining, making it possible to analyze plate/shell structures with large deformations. It was validated with prior research on rotating and flapping plates. In this chapter, validation cases of the aeroelastic solver were presented. Some key conclusions are as follows.

Spanwise flexible wing Spanwise inflexible, flexible and highly flexible wings were simulated and good correlation was obtained with prior experiments and other analysis. Since this case is a pure plunge motion, for the inflexible case, the flow is mostly 2D till about 75% span location. Beyond this the flow becomes 3D due to the tip effect. On the other hand, for the flexible case, since there is flap bending and the plunge amplitude varies over the span, the 2D nature is not preserved even at further inboard locations and the flow field is more three dimensional. As compared to the rigid wing, since the flexible wing has higher plunge amplitude near the wing tip, this leads to a higher effective angle of attack. The leading edge vortices are stronger towards the outboard sections of the wing and also the strength of the tip vortex is higher. Sectional vertical force coefficient (C_z) is higher for flexible

wing, particularly towards the outer sections of the wing. Similar trend is seen for the sectional propulsive force coefficient (C_x). Thus, the increase in forces due to flexibility in this case comes mainly from the outer sections where the plunge amplitudes are higher. These observations are consistent with those made by Chimakurthi et al. [104].

A highly flexible wing was also analyzed and compared to prior experiments and other analysis. Satisfactory correlation was obtained. Comparing the inflexible, flexible and highly flexible cases, it was observed that on introducing a small amount of flexibility, the average propulsive force increased from 0.21 to 0.31 by 47% and the instantaneous vertical force increased from 4.4 to 5.6 by 27%. However, for the highly flexible wing, the average propulsive force dropped to 0.13, (58% compared to flexible wing) and instantaneous vertical force dropped to 1.95 (65% compared to flexible wing).

The reason for the drop in forces for the highly flexible wing is that in this case, the wing root and tip move out of phase for a large portion of the flap cycle and this results in leading edge vortices being formed on different sides of the wing at the root and tip. Also, due to this out of phase motion, the angle of attack is reduced towards the outer sections and a drop in vortex strength is observed. To conclude, leading edge vortex strength increases from rigid wing to flexible wing but drops for the highly flexible wing and similar trend is observed in the forces.

Chordwise flexible wing Next, a chordwise flexible wing was analyzed using the solver. This was a root flap case where the wing was held fixed at

the root and flapped. As a result of the flexibility, camber was produced towards outer sections of the wing as it flapped. Due to camber in the wing, the resultant force was vectored more in the chordwise direction as compared to rigid wings, which resulted in higher propulsive force.

The average vertical force coefficient C_z increased by 10% and the average propulsive force coefficient C_x increased by 25% due to flexibility in the

Similar to the spanwise flexible wing, the chordwise flexible wing has higher sectional vertical force and propulsive force towards the tip. Due to the camber that develops for the flexible wing, a greater portion of the resultant force is vectored in the chordwise direction. Also, the strength of leading edge suction is higher for the flexible wing and there is a greater high pressure at the bottom of the wing. This clearly shows the beneficial effect of chordwise flexibility on the aerodynamics of flapping wings.

As a concluding remark, these results demonstrate the capability of the current aeroelastic solver to characterize the flowfield of simplified flexible wing configurations in 3D.

Chapter 6

Experiments and Analysis of Flapping MAV Wings

The high-fidelity analysis developed can account for non-linearities in structure and fluid. Validation was shown in the previous chapter for some simplified configurations. However, there is a dearth of data on realistic, well characterized flexible flapping MAV wings. In order to fill this void in the literature, experiments were carried out on rigid and flexible flapping MAV wings in an open jet wind tunnel. First, a single degree of freedom was introduced and the wing was flapped while the pitch angle was held fixed. Next, second degree of freedom was added and flapping rigid wings were also pitched in a passive manner. Lastly, torsionally flexible wings were flapped while being held rigidly at the root.

Flexible wings were also structurally characterized by performing experimental testing of the wings. The structural properties of these wings were used to develop a model in MBDyn. This structural model was then coupled to the CFD solver to obtain a CFD-CSD coupled solution. Predictions from the simulation were compared to the experimental results and satisfactory correlation was obtained. This helped to further validate the analysis. Finally, the analysis was used to gain more insights into the flow physics.

6.1 Mechanism Design and Experimental Setup

This section describes the experimental test setup and instrumentation. A four-bar mechanism was used to provide the required flapping kinematics to the wing. Schematic of the four-bar is shown in Figure 6.1. The link AD is the driving link and link BC (driven link) is connected to the wing. Depending on required flapping kinematics, the linkage lengths, L_1, L_2, L_3, L_4 were chosen. If the link AD rotates by θ, the driven link rotates by ϕ (wing flap angle), which is calculated as follows:

$$x = L_1 - L_2 cos\theta \tag{6.1}$$

$$y = L_2 sin\theta \tag{6.2}$$

$$\phi = tan^{-1}\frac{y}{x} - cos^{-1}\frac{L_4^2 + x^2 + y^2 - L_3^2}{2L_4\sqrt{x^2 + y^2}} \tag{6.3}$$

For the experimental setup, these links were made using delrin to reduce the weight and thereby the inertial loads due to the linkages. The lengths of the links were chosen to replicate sinusoidal motion as closely as possible. The baseline linkage lengths were $L_1 = 0.42$ cm, $L_2 = 5.52$ cm, $L_3 = 6.41$ cm and $L_4 = 1.6$ cm. Flapping kinematics was designed to be close to harmonic variation with flapping amplitudes varying from 20° to 40° in steps of 5°. In the actual flapping mechanism, as shown in Figure 6.2, the four-bar was driven by a flywheel attached to the shaft of a motor. A 260 Watt outrunner motor manufactured by AXI (AXI 2217) was used. A 3:1 planetary gear box was used in order to provide the required torque. The flapping amplitude

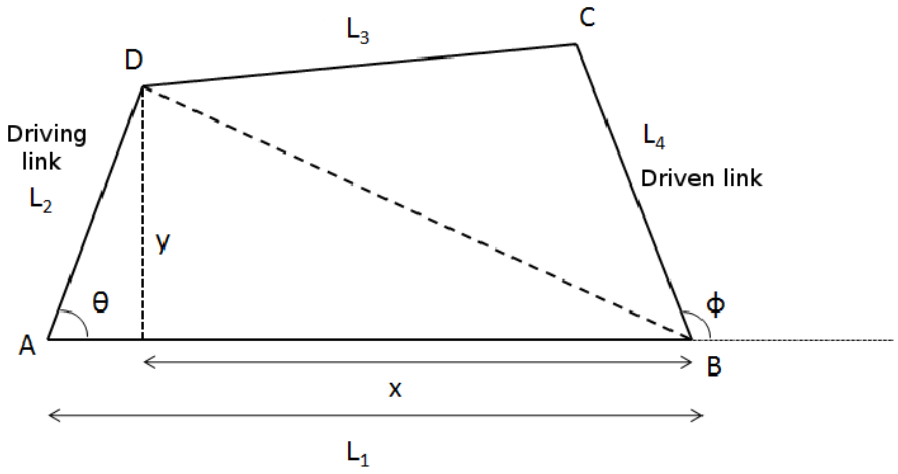

Figure 6.1: **Four-bar linkages**

could be varied by changing the offset (linkage length, L_2) on the flywheel. Instantaneous flap and pitch angles of the wing were measured using two low friction, light weight potentiometers (QP-2HC manufactured by Midori). The flapping frequency was measured from the 1/rev signal obtained using a Hall switch. For the pure flap tests (no wing pitching), the wing attachment was designed such that the wing can be set at the desired geometric pitch angle.

The second degree of freedom, which we wanted to simulate was the pitch kinematics. One way of introducing wing pitching is by an active pitch mechanism, where the pitch kinematics is prescribed throughout the flap motion. However, this mechanism can be complex and heavy and thus may not be suitable for use on an MAV. For example, an active pitch mechanism was used on the Robofly test bench set up developed at Caltech, as shown in Figure 6.3.

In the present study, a passive pitch mechanism was built to study the effect of wing pitching on the aerodynamic performance of the flapping wing.

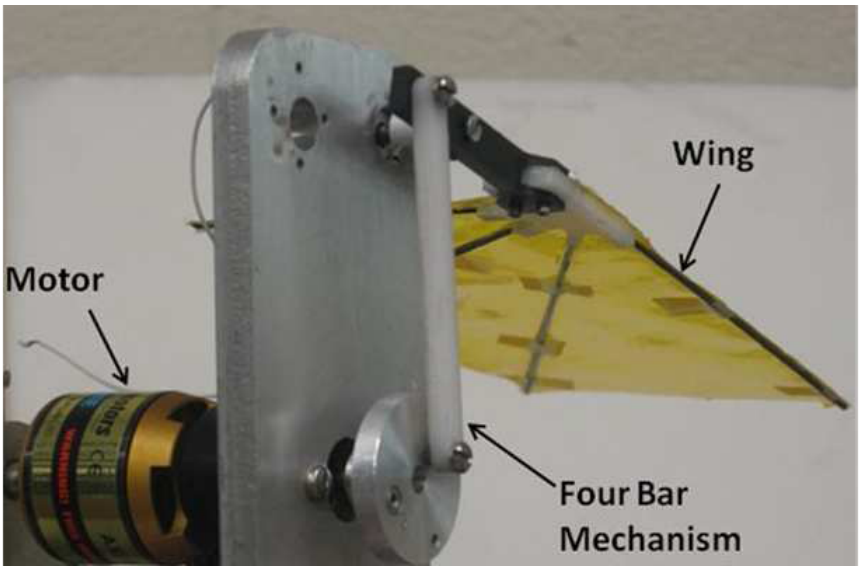

Figure 6.2: **Flapping mechanism**

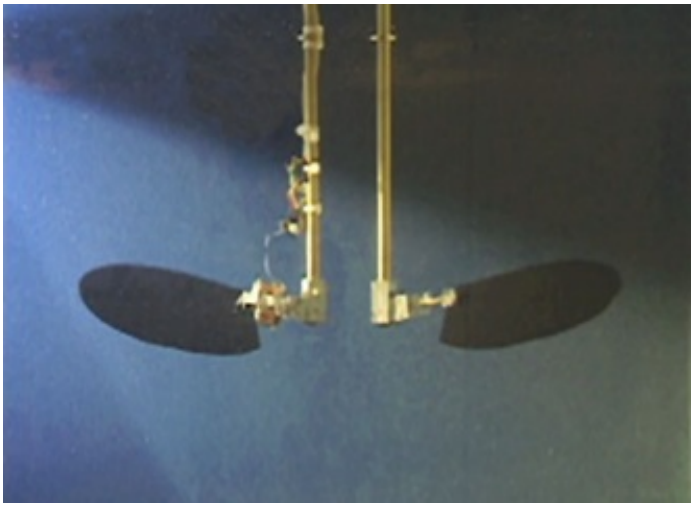

Figure 6.3: **Robofly active pitch mechanism[158]**

It is a simple, light weight mechanism compared to an active pitch mechanism. It relies on the aerodynamic and inertial forces acting on the wing to provide the required pitch modulation. The wing was allowed to pitch about a pitch bearing and this motion can be controlled using a torsion spring. Also, it should be noted that, to obtain the required pitching kinematics, it was impor-

tant to design the wing with the chordwise c.g. location behind the pitching axis. The required pitch kinematics is such that we wanted the wing to pitch nose down during the downstroke. This is because during the downstroke, the angle of attack induced due to the flapping motion is positive and we wanted to reduce it to avoid stall. During the upstroke, the angle of attack induced due to flapping is negative and we wanted to induce a nose up pitch. In the present mechanism, such a kinematics was achieved as a result of a combination of aerodynamic and inertial forces acting on the wing. If the C.G is placed behind the pitching axis, inertial moments will help to pitch the wing in the appropriate directions. Figure 6.4 shows a schematic of the passive pitch mechanism. The actual passive pitch mechanism is shown in Figure 6.5.

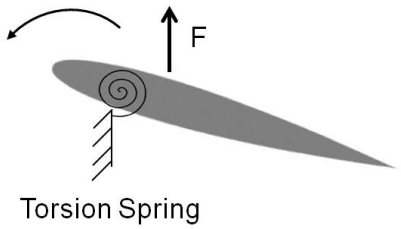

Figure 6.4: **Schematic of passive pitch mechanism**

In the present set-up, spring steel shims were used to provide the required root torsion stiffness. By varying the thickness of these shims, torsion stiffness can be varied, which in turn varies the pitching amplitude. An extremely low friction potentiometer was used at the pitching axis to measure the instantaneous wing pitch angles during flapping. Figure 6.6 shows the experimental flap angles and pitch angles with two different torsion stiffness.

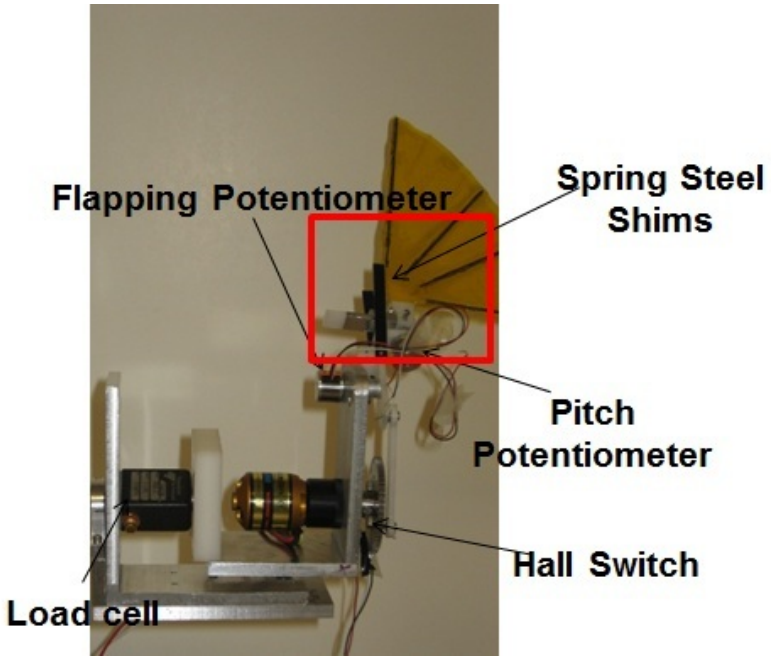

Figure 6.5: **Passive pitch mechanism**

If same shims are used on top and bottom, the geometric pitch angle during upstroke and downstroke are same, resulting in "symmetric pitching". However, shims of different stiffness can also be used at the top and bottom ends to provide different torsion stiffness during the pitch up and pitch down motions. Thus, using this mechanism, differential pitching could be obtained during upstroke and downstroke. Such a kinematics where the geometric pitch angle is not the same during the upstroke and downstroke is referred to here as "asymmetric pitching". A schematic for the symmetric and asymmetric pitch kinematics is shown in Figure 6.7.

Performance of the flapping wing was evaluated in terms of the forces generated. The directions of vertical force (F_Z) and propulsive force (F_X) are defined in Figure 6.8. Load cells were used to measure the forces in the vertical

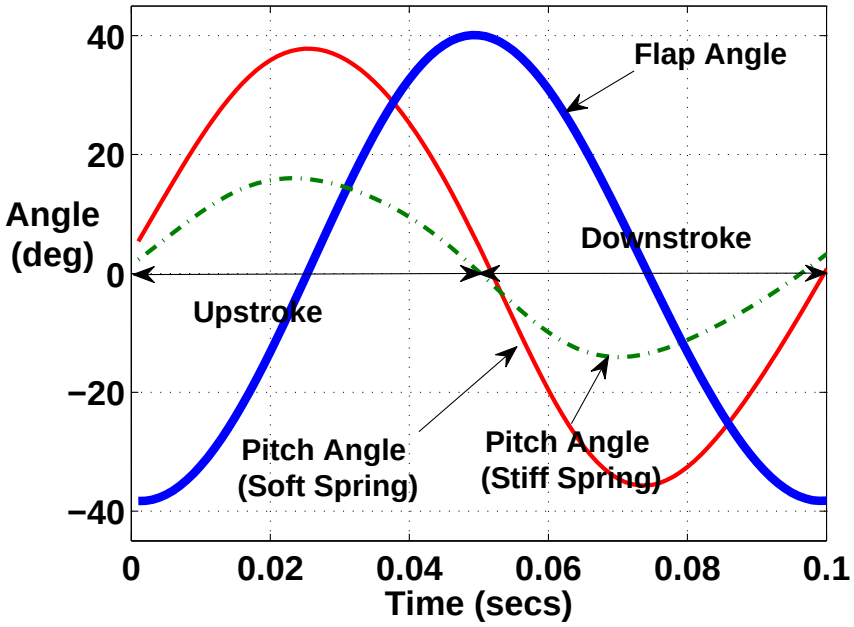

Figure 6.6: **Instantaneous flap and pitch angles over a flap cycle measured experimentally**

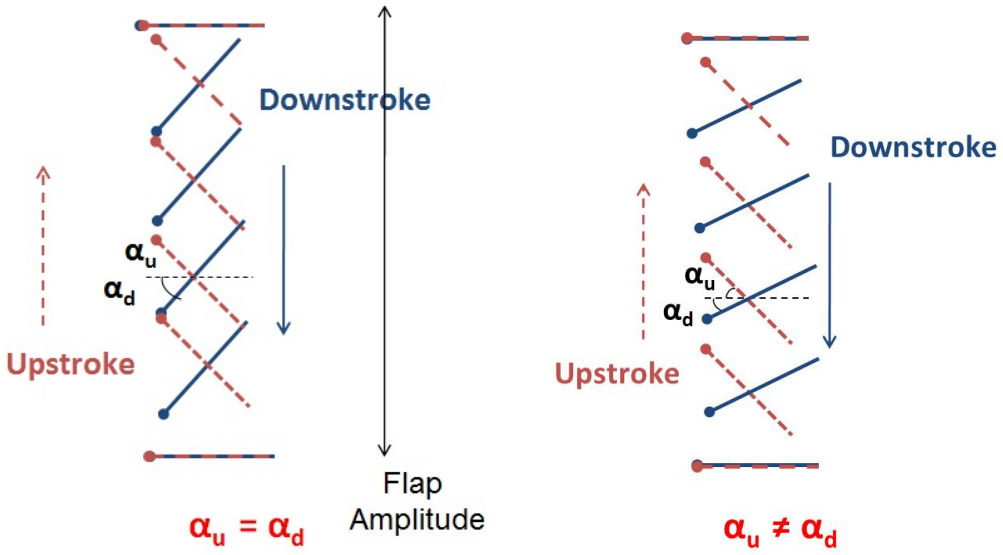

(a) **Symmetric Pitching** (b) **Asymmetric Pitching**

Figure 6.7: **Symmetric and Asymmetric Pitch Kinematics**

and propulsive directions. Although the manufacturer provided a calibration for the load cells, calibrations tests were performed in-house to confirm the accuracy of this calibration curve.

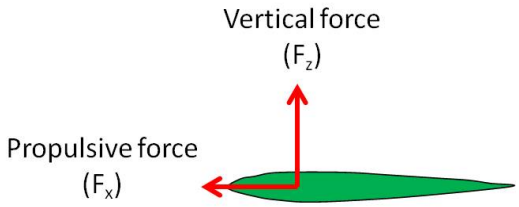

Figure 6.8: **Definition of F_Z and F_X**

The load cells were connected to a National Instruments USB DAQ device (NI USB-6251). Raw data from the sensors was transmitted to a computer using a software called LabView. These voltages were later post-processed with the calibration factor to extract the observed forces.

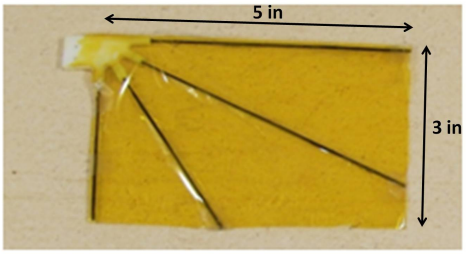

(a) Rigid Wing

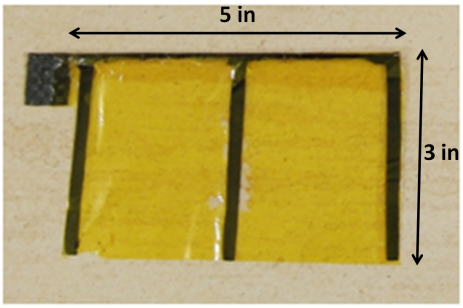

(b) Flexible wing

Figure 6.9: **Wing construction**

Rigid wings were fabricated using unidirectional carbon rods, which are 1.5 mm in diameter as shown in Figure 6.9(a). High speed videos of these wings while flapping showed no visible deformation. Flexible wings were also

constructed which can twist about the leading edge. For the flexible wings, chord-wise ribs were made of single layered unidirectional carbon fiber and leading edge spar is again a 1.5 mm diameter carbon rod (Figure 6.9(b)). These wings had a rectangular planform with a span of 12.7 cm (5 in) and a chord of 7.62 cm (3 in). The wings were covered with Mylar film. The weight of the flexible and rigid wings were 1.5 grams and 2.8 grams respectively.

Using sizing data available in literature, the target F_Z and F_X for an MAV with these wings was determined to be 16 grams and 8 grams respectively [154-157] for a wind speed of 3 m/s. These forces are required to sustain the vehicle weight and propel it in forward flight by overcoming the vehicle drag. Therefore, the required F_Z and F_X from each of these wings is 8 grams and 4 grams respectively.

6.2 Pure Flap (Rigid Wings)

6.2.1 Experimental Results

The goal of these experiments was to examine the effect of pure flapping (no pitching or twisting) of rigid wings at different fixed pitch angles (geometric angles of attack). The wing was flapped in a vertical plane in the open-jet wind tunnel. The flap kinematics are as follows:

Flap: $\gamma = \gamma_o \cos(2\pi f t)$,

Pitch: $\theta = \theta_o + \theta_a \cos(2\pi f t + \phi)$

with $\gamma_o = 40°$, $\theta_a = 0°$, $\phi = 0°$, θ_o was varied from $0°$ to $24°$.

Figure 6.10 shows the variation of average vertical force (F_Z) and average propulsive force (F_X) with frequency for different pitch angles flapping with a flap amplitude of 40° in a forward speed of 3 m/s obtained from experiments. It is interesting to note that a flapping rigid wing generates a propulsive force even at 0° pitch. This effect is called the Knoller-Betz effect [73]. Figures 6.11(a) and 6.11(b) show schematically how a change in effective angle of attack due to flapping motion generates a positive aerodynamic force in the chordwise direction providing propulsive force during both, upstroke and downstroke. However, for the wing with 0° pitch angle, there is symmetry in the vertical forces during upstroke and downstroke resulting in about zero average F_Z. From Figure 6.10, it can also be seen that, as the pitch angle is increased, the propulsive force decreases and at higher pitch angles there is a negative propulsive force (or drag force). Thus, a trade-off is seen between the vertical and propulsive forces.

Based on these results, from an MAV perspective, for the required 8 grams of F_Z from this wing, the pitch angle should be at least 24° for a flap frequency of 10 Hz. However, as shown in Figure 6.10, for $\theta_o = 24°$ this wing generates negative propulsive force. This shows that pure flapping of this rigid wing may not be a practical solution for a forward-flying flapping-wing MAV at this wind speed.

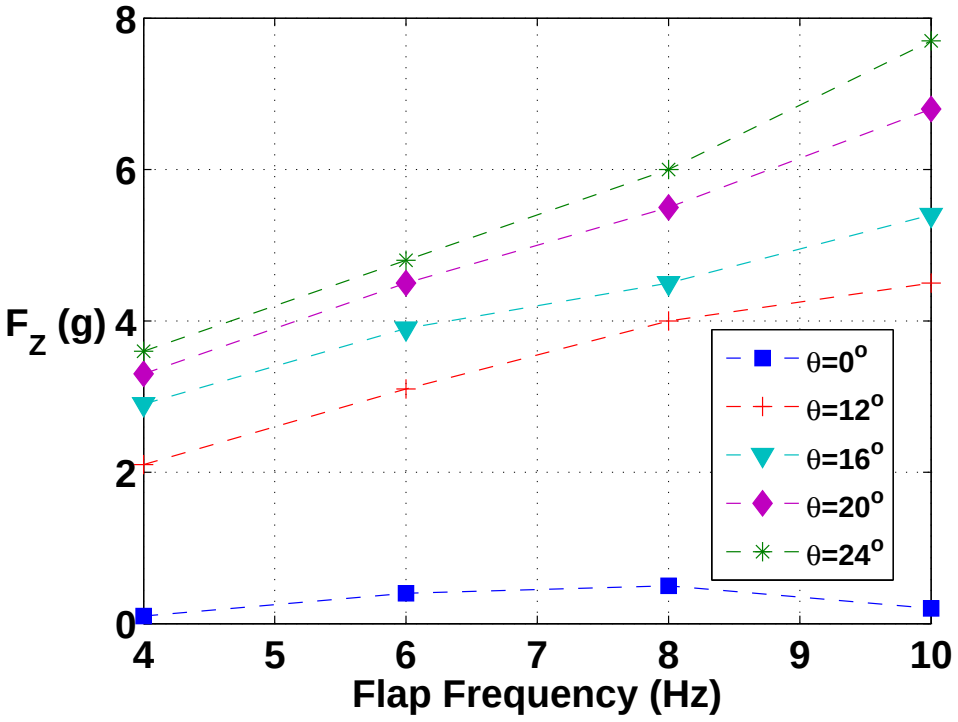

(a) Average vertical force, F_Z

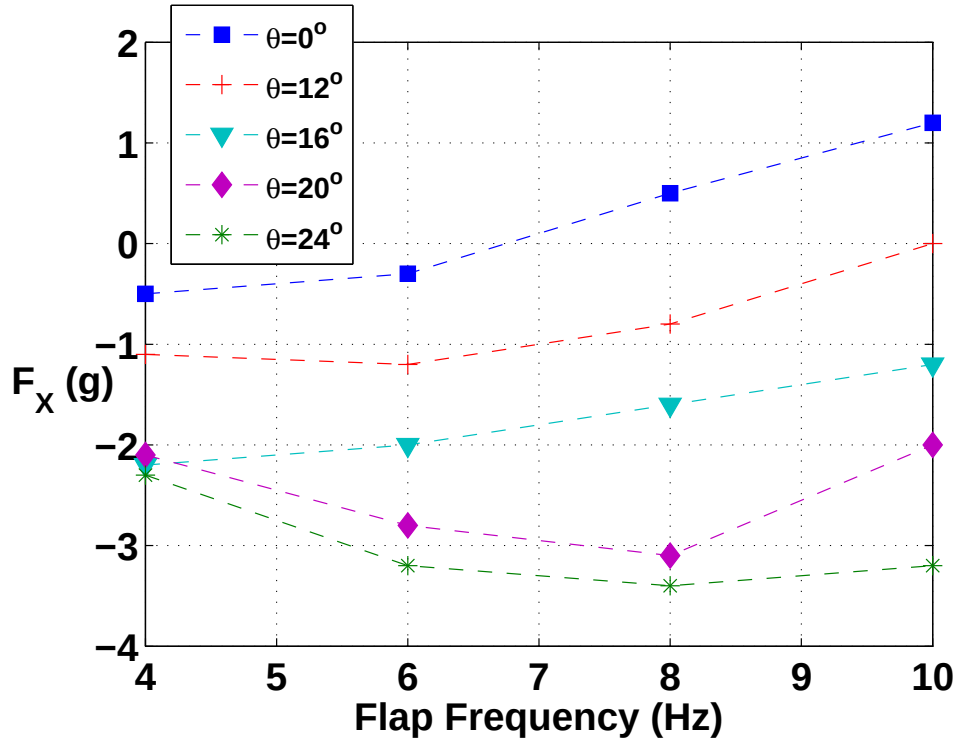

(b) Average propulsive force, F_X

Figure 6.10: **Variation of average vertical and propulsive force with frequency for rigid wings in pure flap from experiments (40° flapping amplitude, $V_\infty = 3$ m/s)**

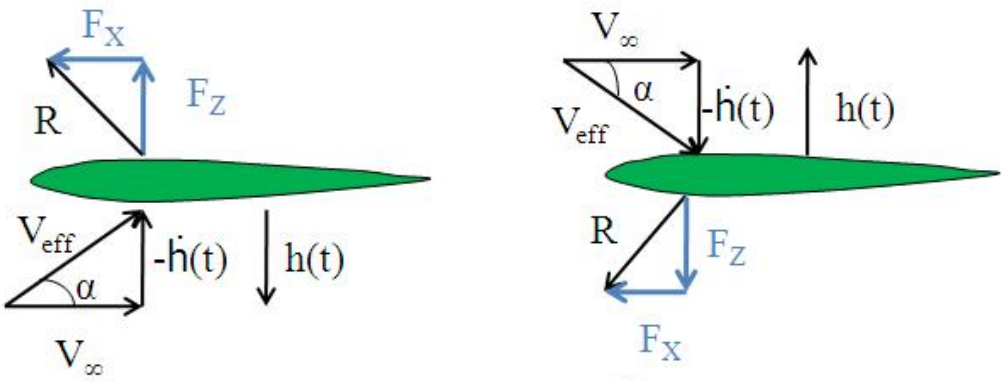

(a) **Downstroke** (b) **Upstroke**

Figure 6.11: **Knoller Betz effect of flapping**

6.2.2 CFD Analysis of Rigid Wings in Pure Flap

The experimental results presented above were simulated using our CFD solver, OVERTURNS. Overset meshes were used for this case. The blade mesh had $267 \times 141 \times 85$ points. The background cartesian mesh had $162 \times 195 \times 122$ points. 1440 iterations were used per flap cycle. Analysis was carried out for pitch angles, $\theta_o = 0°, 12°$ and $24°$. Figure 6.12 shows the average F_Z and F_X from the analysis as compared to the experiments. Since the correlation is satisfactory, the analysis was used to gain further insights into the flow physics. Results for flap frequency of 10 Hz are presented next in greater detail.

Figure 6.13 shows the pressure coefficient contours for rigid wing with $0°$ pitch angle, $40°$ flap amplitude and 10 Hz flap frequency at different instants of the flap cycle. The results shown here are for the mid-span location of the wing. A strong leading edge vortex is formed on top of the wing at the middle of downstroke ($t/T = 0.25$, Figure 6.13(b)) which results in a large instantaneous force in the vertical direction as shown in Figure 6.14(a). Similarly, during the upstroke, a leading edge vortex is formed at the bottom of the wing which leads to a force in the negative vertical direction ($t/T = 0.75$, Figure 6.13(d)). Due to symmetry in the upstroke and downstroke, the average F_Z is zero. A slight positive propulsive force is seen at higher flap frequencies for the $0°$ pitch case, due to the Knoller-Betz effect, similar to the experimental results.

Now, consider the results for the case with mean pitch angle, $\theta_o = 24°$ at flap frequency of 10 Hz. Figure 6.15 shows the pressure coefficient contours

from the analysis at mid span section. Similar to the 0° pitch case, leading edge vortices are formed at top and bottom of the wing during the downstroke and upstroke. Due to the positive pitch angle, a greater component of the net force is vectored in the "x" direction (because of the inclination of the wing) than the 0° pitch angle case. This results in a large negative instantaneous propulsive force (F_X) at the middle of downstroke ($t/T = 0.25$) and positive instantaneous propulsive force at the middle of the upstroke ($t/T = 0.75$) as shown in Figure 6.14(b). The average propulsive force is negative. The positive mean pitch angle results in an asymmetry in the kinematic. The magnitude of positive instantaneous force is larger during the downstroke than the magnitude of negative instantaneous vertical force during the upstroke(Figure 6.14(a)). Therefore, a positive average force is generated in the vertical direction and a negative average propulsive force is generated for this rigid wing in pure flap with a positive mean pitch angle.

In order to sustain an MAV in forward flight, the target propulsive and vertical forces must be generated by the wing. Since pure flap of a rigid wing cannot generate a positive propulsive force and positive vertical force at the same time, it is not a feasible configuration for this forward flight condition.

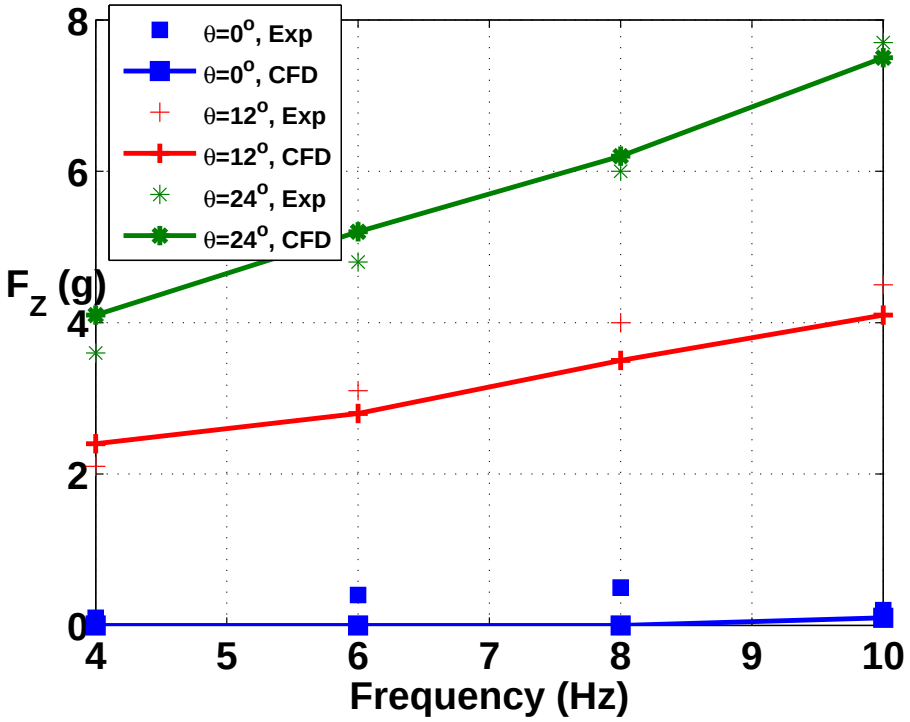

(a) Average vertical force, F_Z

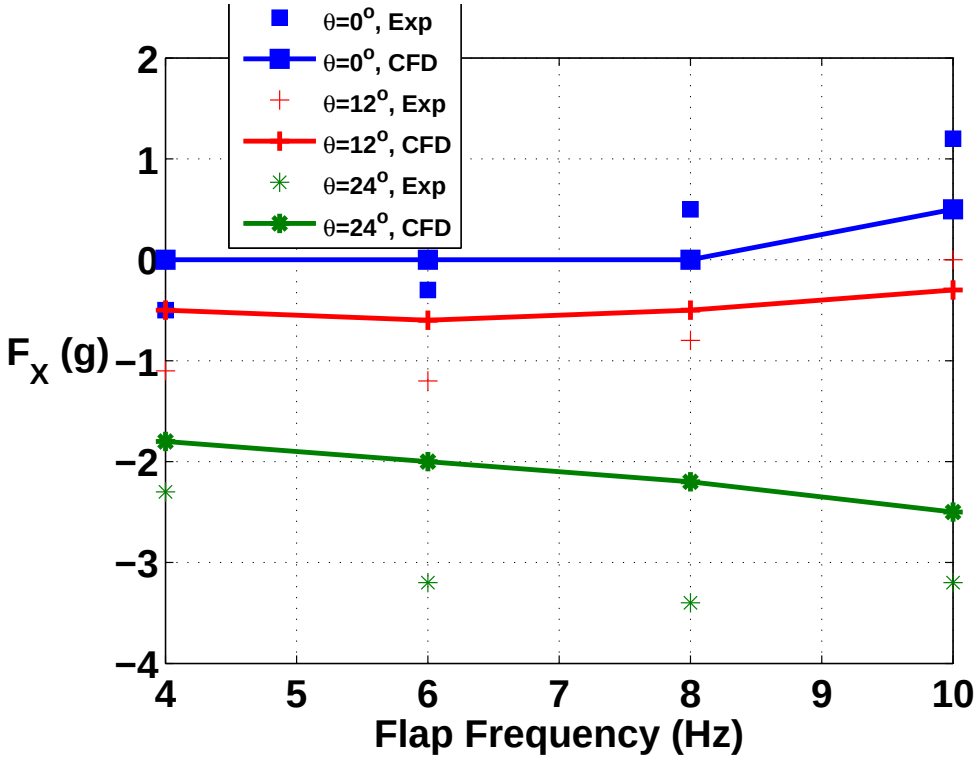

(b) Average propulsive force, F_X

Figure 6.12: **Variation of average vertical and propulsive forces with frequency for rigid wings in pure flap from experiments and analysis (40° flap amplitude, $V_\infty = 3$ m/s).**

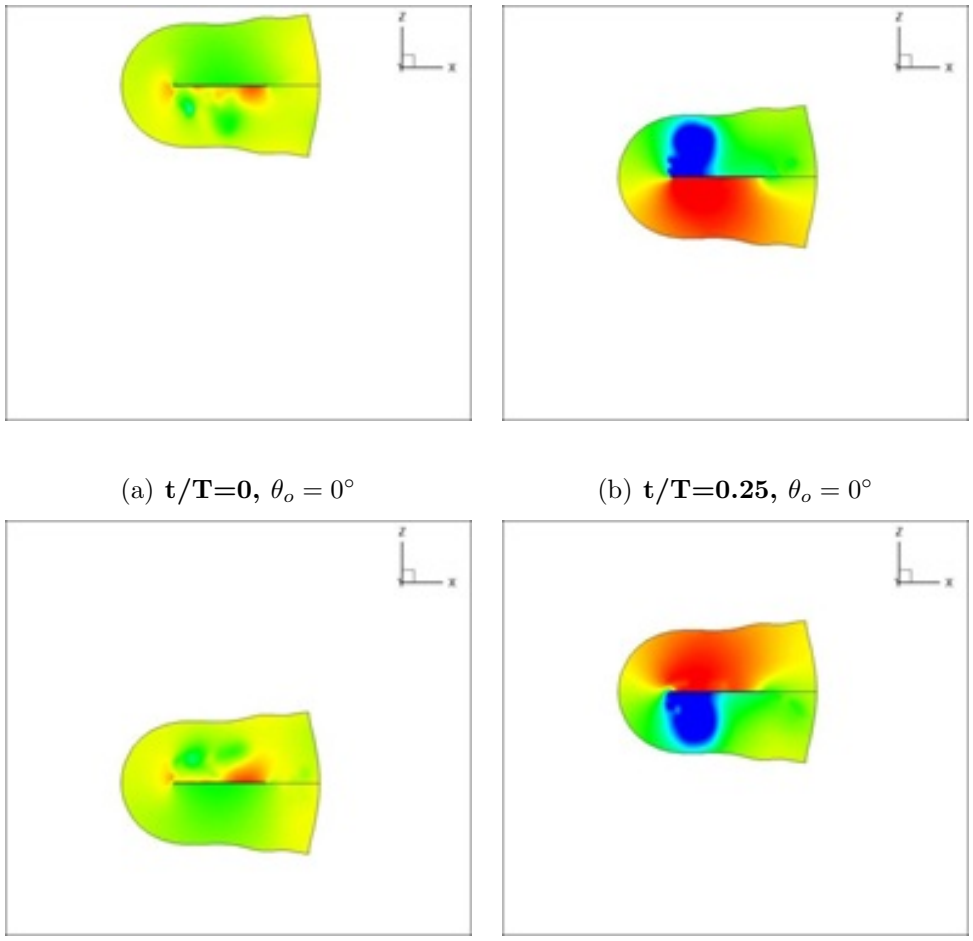

(a) **t/T=0,** $\theta_o = 0°$

(b) **t/T=0.25,** $\theta_o = 0°$

(c) **t/T=0.5,** $\theta_o = 0°$

(d) **t/T=0.75,** $\theta_o = 0°$

Figure 6.13: **Pressure coefficient contours at mid span section for pure flap of rigid wing with** $0°$ **pitch angle (**$40°$ **flap amplitude,** $V_\infty = 3$ **m/s,** 10 **Hz flap frequency)**

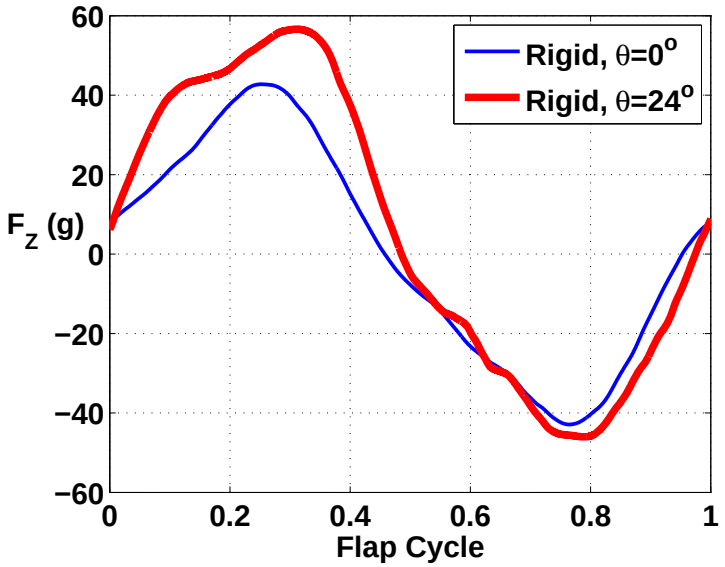

(a) **Instantaneous vertical force**

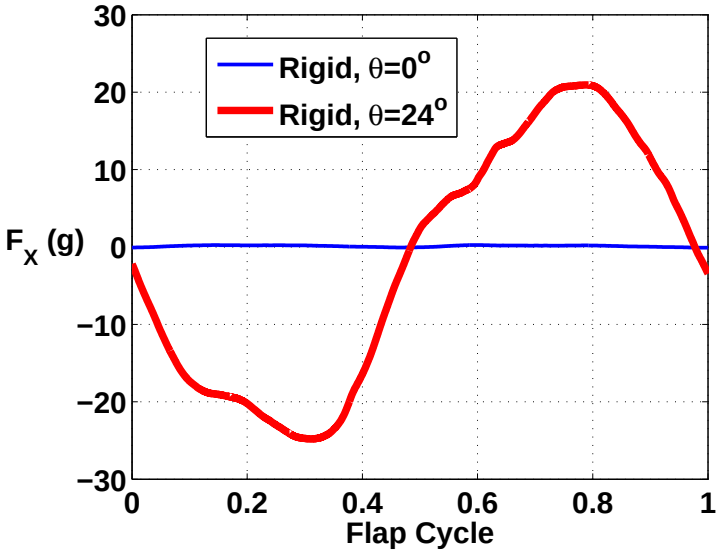

(b) **Instantaneous propulsive force**

Figure 6.14: **Instantaneous force variation over a flap cycle for rigid wing in pure flap obtained from analysis** (40° **flap amplitude,** $V_\infty = 3$ **m/s,** 10 **Hz flap frequency)**

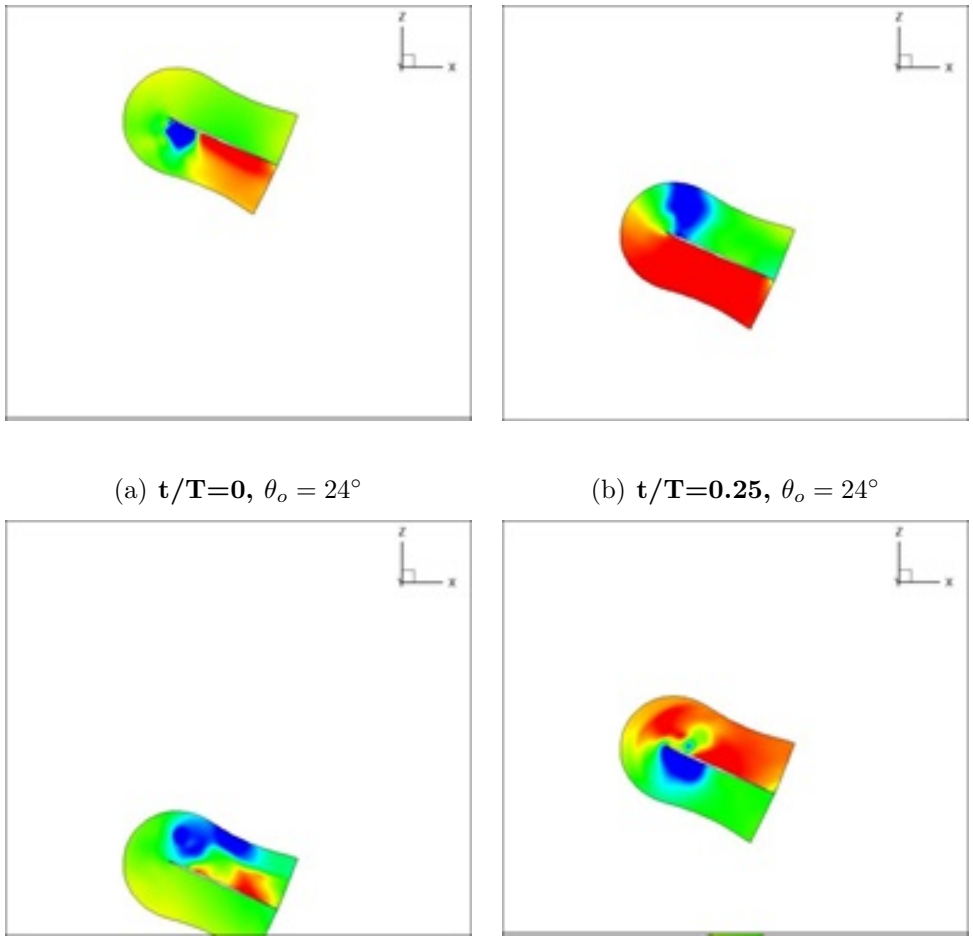

(a) **t/T=0,** $\theta_o = 24°$ (b) **t/T=0.25,** $\theta_o = 24°$

(c) **t/T=0.5,** $\theta_o = 24°$ (d) **t/T=0.75,** $\theta_o = 24°$

Figure 6.15: **Pressure coefficient contours at mid span section for rigid wing in pure flap with** $24°$ **pitch angle (**$40°$ **flap amplitude,** $V_\infty = 3$ **m/s,** 10 **Hz flap frequency)**

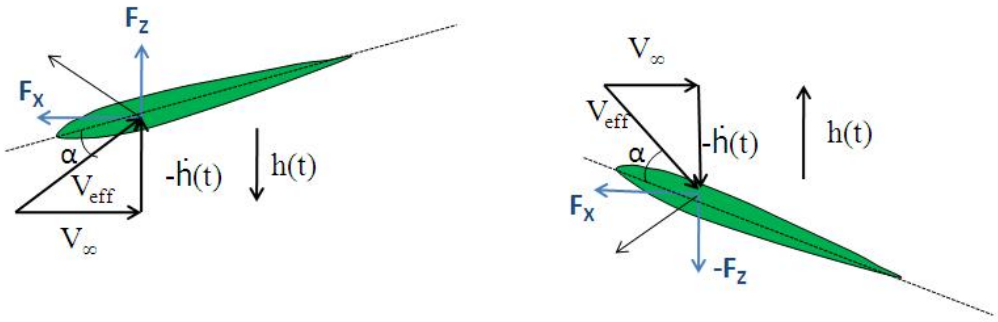

(a) **Downstroke, nose down pitch**

(b) **Upstroke, nose up pitch**

Figure 6.16: **Effect of symmetric pitching in forward flight**

6.3 Passive Pitching (Rigid Wings)

6.3.1 Experimental Results

As mentioned earlier, for an MAV capable of forward flight, both, vertical and propulsive target forces must be generated by the wing. Since pure flapping of a rigid wing may not be a viable option, passive pitch mechanism was then tested in the wind tunnel to determine if this could provide the required propulsive force (F_X) in forward flight along with the required vertical force (F_Z). The wing kinematics are as follows:

Flap: $\gamma = \gamma_o \cos(2\pi f t)$,

Pitch: $\theta = \theta_o + \theta_a \cos(2\pi f t + \phi)$

with $\gamma_o = 40°$, $\phi = 90°$, θ_o and θ_a varied depending on the stiffness of the passive pitch mechanism.

If the wing pitches symmetrically, the positive vertical force on the down-

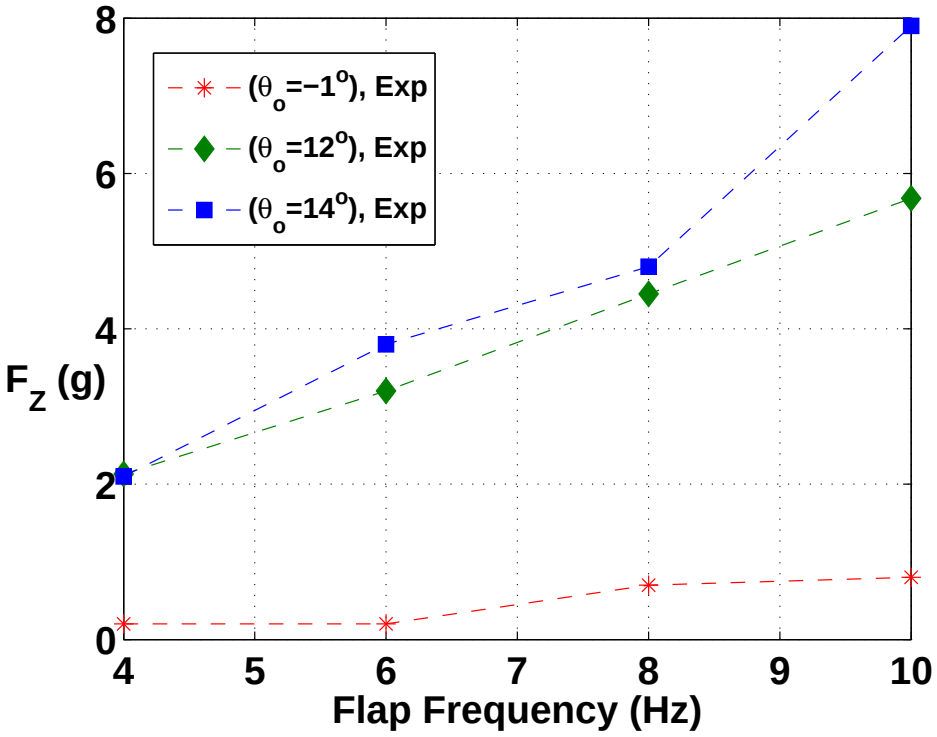

(a) Average vertical force, F_Z

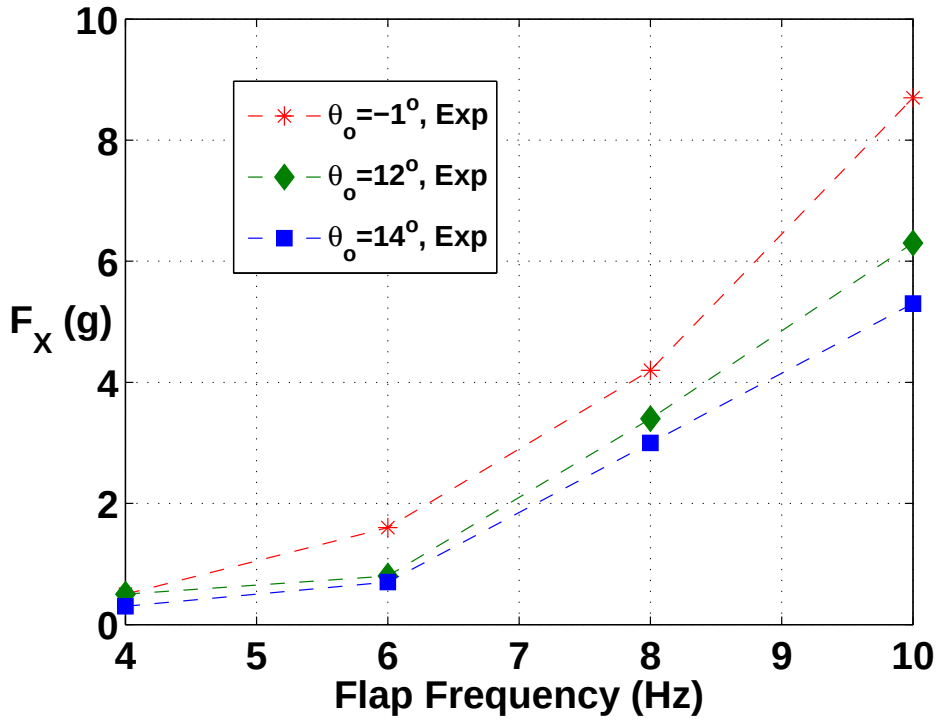

(b) Average propulsive force, F_X

Figure 6.17: **Variation of average vertical and propulsive forces with frequency for passive pitch kinematics from experiments (40° flap amplitude, $V_\infty = 3$ m/s, rigid wing)**

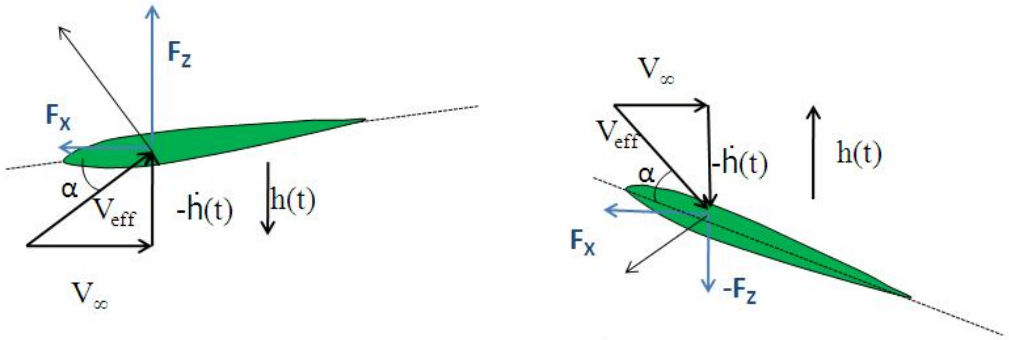

(a) **Downstroke, nose down pitch**

(b) **Upstroke, nose up pitch**

Figure 6.18: **Effect of asymmetric pitching in forward flight**

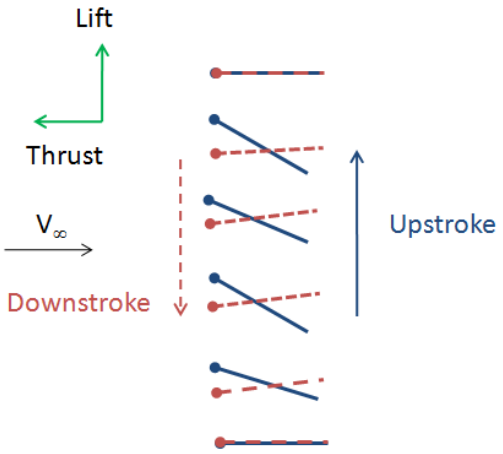

Figure 6.19: **Asymmetric pitch kinematics (Angles measured experimentally in forward wind speed)**

stroke is canceled out by the negative vertical force on the upstroke. This is shown schematically in Figures 6.16(a) and 6.16(b). In order to generate a mean vertical force, F_Z, a positive pitch angle is required about which the wing pitches. Asymmetric pitching was tested using dissimilar spring steel shims on the top and bottom which gives unequal nose-up and nose-down torsional stiffness. The pitch angle on the downstroke was progressively decreased by using thicker shims at the bottom.

The experimental results are shown in Figures 6.17(a) and 6.17(b). The pitch angle for the symmetric case varied from -33° (nose down) at the middle of the downstroke to $+31^\circ$ (nose up) at the middle of the upstroke at 10 Hz flapping frequency. The mean pitch angle, θ_o was -1° and pitch amplitude, $\theta_a = 32^\circ$. This will be referred to here as the "symmetric passive pitching" case.

It was hypothesized that on introducing an asymmetry, with a positive mean pitch angle (θ_o), the vertical force generated during the downstroke would be greater than the magnitude of negative vertical force during the upstroke. Therefore, the average vertical force F_Z should increase. Figures 6.18(a) and 6.18(b) show this effect schematically. Looking back at Figure 6.17, on increasing the mean pitch angle to 12°, the average vertical force increased to 5.8 grams at 10 Hz. For the case with mean pitch angle, $\theta_o = 14^\circ$, 8 grams of average vertical force, F_Z was generated. The pitch angle for this configuration varied from -7° at the middle of the downstroke to $+35^\circ$ at the middle of the upstroke. This last case will be referred to here as the

"asymmetric passive pitching". The pitching kinematics for this asymmetric case is shown schematically in Figure 6.19.

In terms of propulsive force, it is seen in Figure 6.17(b) that the symmetric pitch kinematics ($\theta_o = -1°$) produced the maximum propulsive force, F_X. Up to 8 grams of F_X was produced using symmetric pitching at 10 Hz. As the pitch angle is reduced on the downstroke and the kinematics becomes asymmetric, the propulsive force reduces. Using the best F_Z case (8 grams) from above which employed asymmetric passive pitching kinematics ($\theta_o = 14°$), F_X of up to 5 grams was produced. Thus, both target vertical and propulsive forces can be achieved using this configuration.

To summarize, the first observation from these tests is that a positive mean pitch angle is required for positive average vertical force. Secondly, pitching is the key for generating propulsive force. Thirdly, a trade-off exists between the vertical and propulsive forces for the different pitching kinematics.

Further details of the flow field and instantaneous forces are obtained using CFD analysis.

6.3.2 CFD Analysis of Rigid Wings in Combined Flap and Pitch

CFD analysis was carried out using OVERTURNS for the cases with symmetric pitching ($\theta_o = -1°$) and asymmetric pitching ($\theta_o = 14°$), 40° flap amplitude and 3 m/s forward speed at different flap frequencies.

Figure 6.20 shows the average forces in vertical and propulsive directions

from the experiments and analysis. The analysis is able to predict the average vertical force, F_Z quite well. Though the analysis can capture the trend in the average propulsive force, F_X, there are some differences in magnitude.

The results for flap frequency of 10 Hz are shown in greater detail next. Pressure coefficient contours at mid span section for the symmetric pitching case ($\theta_o = -1°$) are shown in Figure 6.21. The contours are symmetric during the downstroke and upstroke. The instantaneous force variation over a flap cycle is shown in Figure 6.22. The net force in vertical direction cancels out. However, a positive instantaneous force in propulsive direction is observed during the both the strokes. This is because the leading edge vortex is formed during both the strokes on that portion of the wing which is facing upstream.

Pressure coefficient contours at mid span section for the asymmetric pitching ($\theta_o = 14°$) case are shown in Figure 6.23. It can be clearly seen that the strength of leading edge vortex is higher during the downstroke ($t/T = 0.25$) than the upstroke ($t/T = 0.75$). Therefore, due to a positive mean pitch angle, the entire vertical force (F_Z) curve is shifted upwards and results in a positive average force in the vertical direction. The instantaneous force variation over a flap cycle is shown in Figure 6.22. Further, positive instantaneous force in propulsive direction is observed during the downstroke and upstroke.

Comparing the average forces for the symmetric ($\theta_o = -1°$) and asymmetric pitching ($\theta_o = 14°$) cases, it can be seen from Figure 6.20 that on introducing an asymmetry, the vertical force increases but propulsive force drops. Looking at the instantaneous force variation (Figure 6.22), the entire vertical force (F_Z) curve shifts upwards for the asymmetric pitching case. On the other hand, the propulsive force reduces, particularly during the downstroke ($t/T = 0.25$). The reason for this drop in propulsive force and increase in vertical force becomes clear if we look at the pressure coefficient contours at this instant of the flap cycle ($t/T = 0.25$) for both the cases (Figures 6.21(b) and 6.23(b)). The strength of the Leading Edge Vortex is stronger for the asymmetric pitching kinematics and also, the geometric angle of the wing is $-7°$ as compared to $-35°$ for symmetric pitching case. Due to the combined effect of higher strength of LEV and the lower negative geometric pitch angle, the resultant force is vectored more in the vertical direction, hence, there is an increase in vertical force and drop in propulsive force for the asymmetric pitch kinematics. During the upstroke ($t/T = 0.75$), the geometric pitch angles are $31°$ and $35°$ for the symmetric and asymmetric pitching cases, respectively. The strength of LEV is lower for the asymmetric pitching kinematics which leads to a smaller force in both the directions.

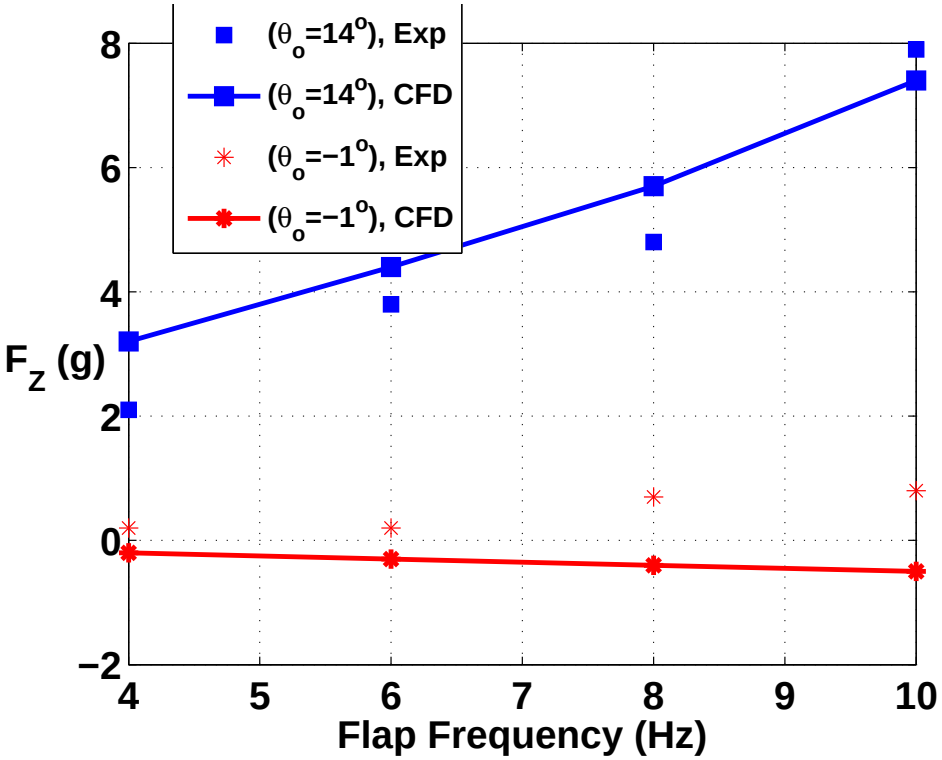

(a) Average vertical force, F_Z

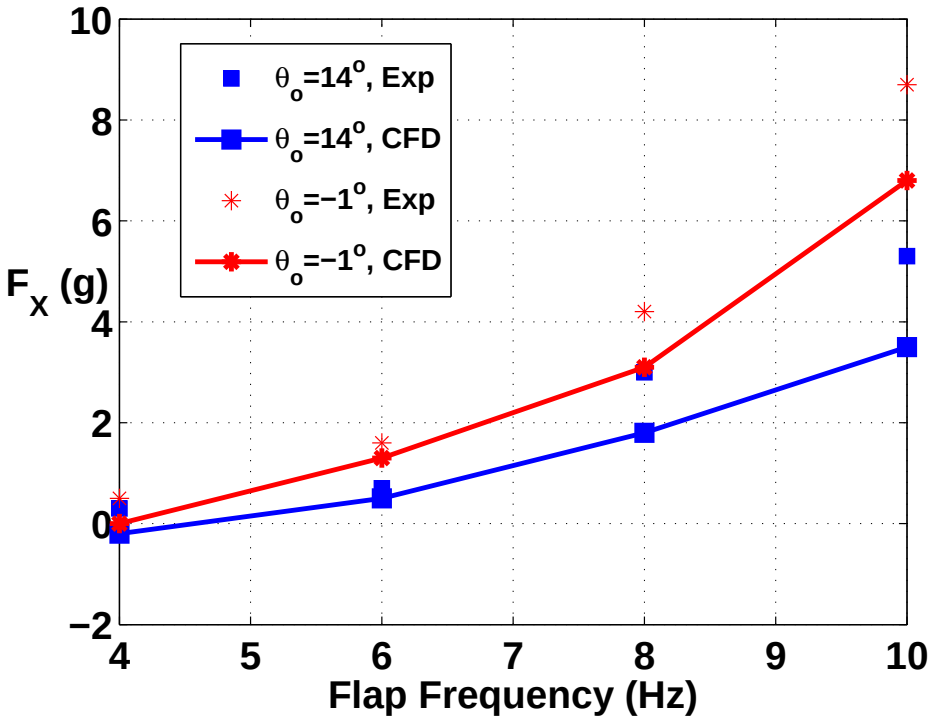

(b) Average propulsive force, F_X

Figure 6.20: **Variation of average vertical and propulsive forces with frequency for rigid wing in flap plus passive pitch from experiments and analysis** (40° **flap amplitude,** $V_\infty = 3$ **m/s)**

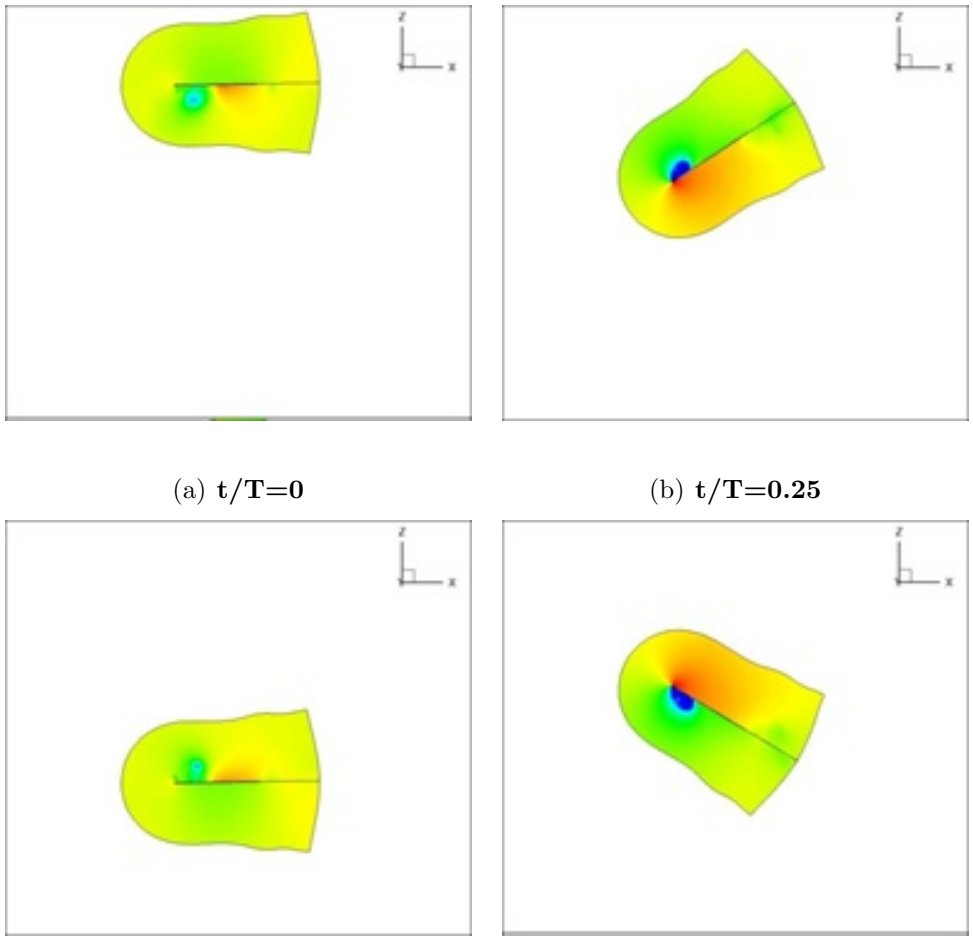

(a) **t/T=0** (b) **t/T=0.25**

(c) **t/T=0.5** (d) **t/T=0.75**

Figure 6.21: **Pressure Coefficient Contours at mid-span section for symmetric pitching of rigid wing (**40° **flap amplitude,** V_∞ = 3 **m/s, flap frequency=**10 **Hz)**

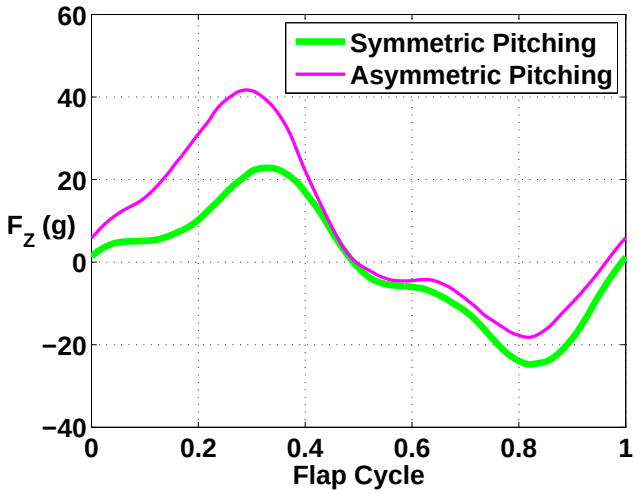

(a) **Instantaneous vertical force**

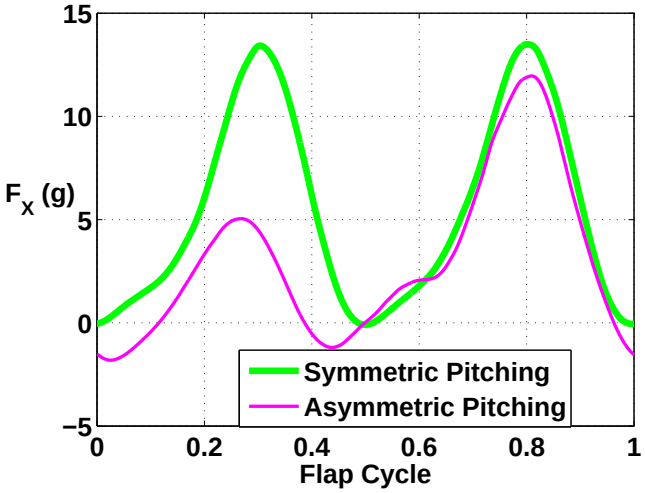

(b) **Instantaneous propulsive foce**

Figure 6.22: **Instantaneous forces for rigid wing, flap plus passive pitch (40° flap amplitude, $V_\infty = 3$ m/s, $f = 10$ Hz) obtained from analysis**

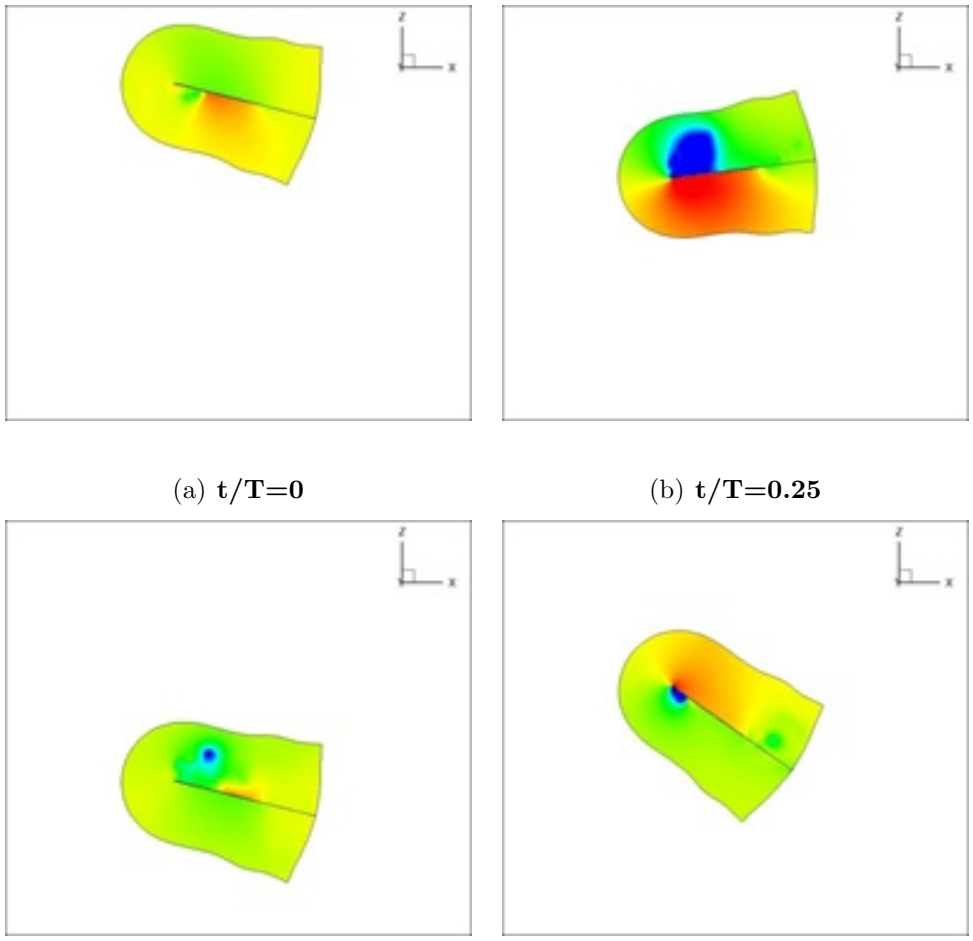

(a) **t/T=0** (b) **t/T=0.25**

(c) **t/T=0.5** (d) **t/T=0.75**

Figure 6.23: **Pressure coefficient contours at mid-span section for asymmetric pitching of rigid wing (**40° **flap amplitude,** $V_\infty = 3$ **m/s, flap frequency=**10 **Hz)**

6.4 Dynamic Twist using Flexible Wings

Experimental results and predictions presented in previous sections helped to understand the role of flapping and pitching separately. From these studies, it can be concluded that flapping was the main contributor to the enhancement in vertical force generated, and pitch modulation over a flap cycle plays a significant role in the propulsive force. Temporal variation of wing pitch angle (passive pitching) is important because the effective angle of attack of the wing changes at different instants of flap. One key disadvantage of passive pitching is that the entire wing pitches by the same angle, and therefore there is no variation in pitch modulation in the spanwise direction. However, when wing undergoes root flap actuation, plunge velocity (as shown in Figure 6.24), and hence the effective angle of attack, varies from wing root to tip. Therefore, in order to achieve the best efficiency from a wing, both temporal and spanwise variation of pitch angle are required. In other words, the wing should undergo dynamic twisting and not dynamic pitching alone. "Dynamic" refers to the fact that there is a temporal variation in pitch (for rigid wings) and twist (for flexible wings).

The easiest way to obtain dynamic twisting (with higher pitch modulation at the tip and lower pitch modulation at the root) is to use structurally well tailored, flexible (torsionally compliant) wings. Looking at natural flyers, it is observed that the bending stiffness of their wings is one to two orders of magnitude higher than the torsion stiffness [82]. Flexible wings used in

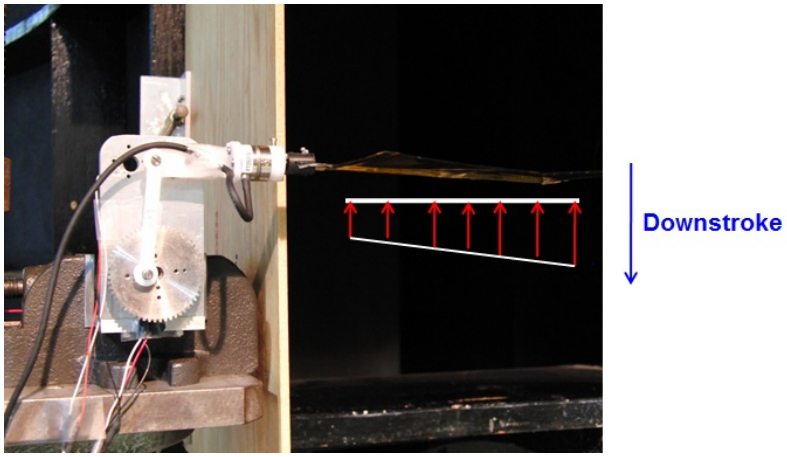

Figure 6.24: **Spanwise variation of flap velocities for root flapping wing**

this study were made with a unidirectional carbon-fiber rod as leading edge and thin unidirectional single layered carbon fiber strips for the chordwise ribs (Figure 6.9(b)), so that the wing is stiff in bending and compliant in torsion. By tailoring the flexibility, it is expected that the various spanwise sections of the flexible wing would pitch in a much more efficient way due to dynamic twist of the wing caused by aerodynamic and inertial loads, which vary temporally and also along the span.

6.4.1 Experimental Results

The flexible wing was held fixed at the root and no additional torsion spring was used. Figures 6.25(a) and 6.25(b) show the variation of average vertical force and propulsive force respectively, with flapping frequency for the flexible wing. It can be observed that with root pitch angle, θ_o of 0° the wing generated almost zero average vertical force, F_Z and 9.5 grams of average

propulsive force, F_X. On increasing the root pitch angle, the vertical force increases, but propulsive force reduces. Both, the target F_Z and F_X can be achieved using this flexible wing at 16° and 24° root pitch angles. For example, for the case with $\theta_o = 24°$, F_Z of 12 grams and F_X of 5 grams was generated. This was more than the target F_Z of 8 grams and target F_X of 4 grams per wing.

6.4.2 Structural Modeling of Flexible Wing

Flexible wing used in this study was constructed using the following structural members (Figure 6.26):

1. Leading edge spar: 1.5 mm diameter carbon rod
2. Chordwise Ribs (Root, Mid, Tip): Unidirectional single layered carbon fiber strips
3. Membrane: Mylar film

The structural properties of each of these members was obtained experimentally and these were then used to build up a structural model in MBDyn. Bending and torsion tests were carried out for the chorwise ribs (Figure 6.27) and the leading edge spar (Figure 6.28). Loads were added to simulate bending and torsion and a height gauge was used to measure the deflections. The bending and torsion stiffness properties (EI and GJ) were then obtained from these results. Manufacturer specified properties were used for the Mylar film.

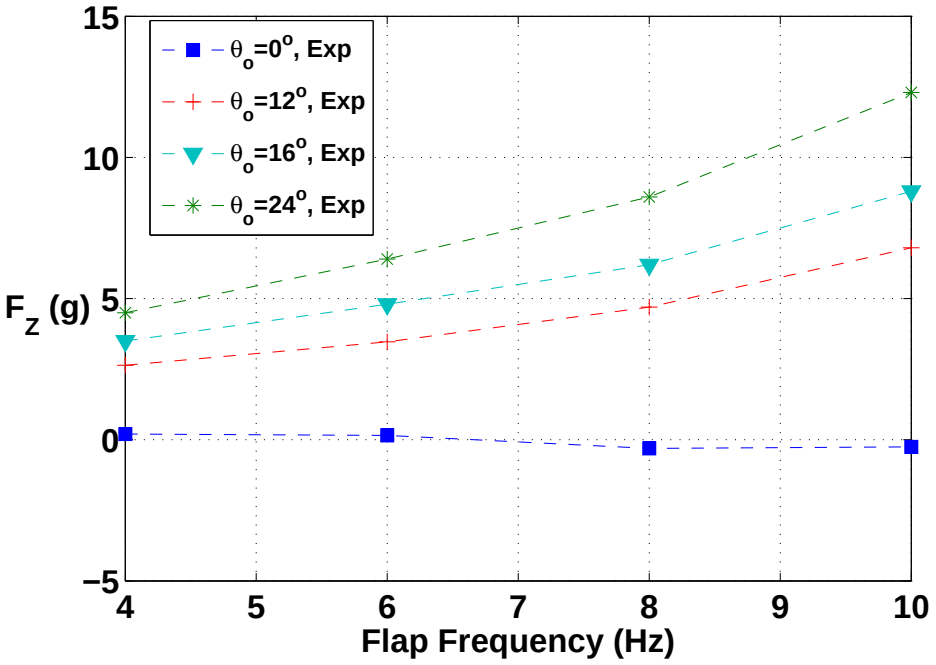

(a) **Average vertical force, F_Z**

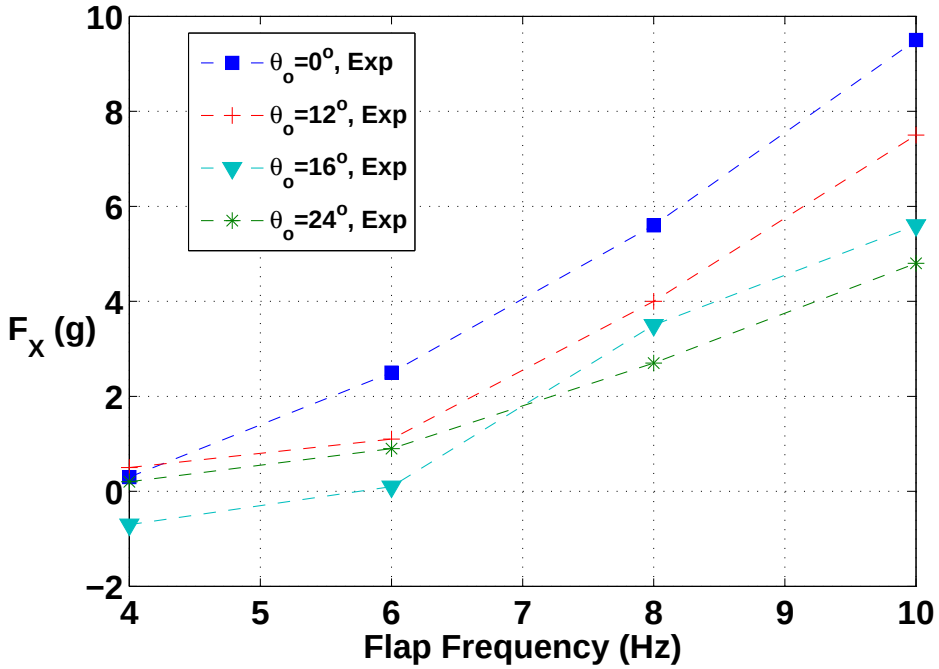

(b) **Average propulsive force, F_X**

Figure 6.25: **Variation of vertical and propulsive forces with frequency for flexible wings obtained from experiments** (40° **flap amplitude,** $V_\infty = 3$ **m/s)**

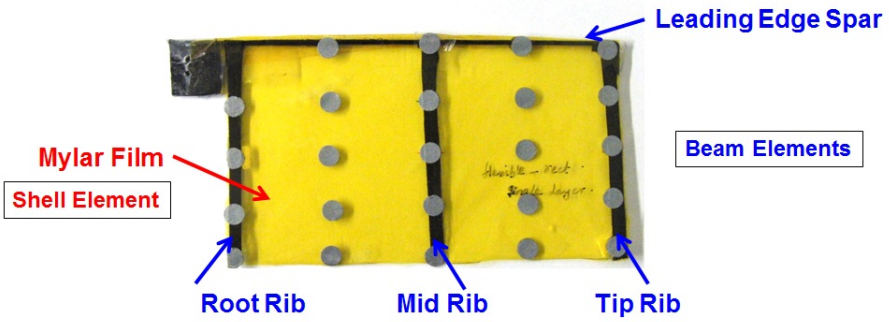

Figure 6.26: **Structural members of flexible wing**

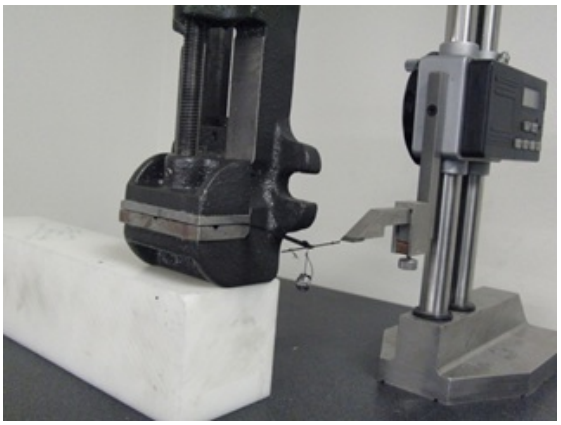

(a) **Bending test**

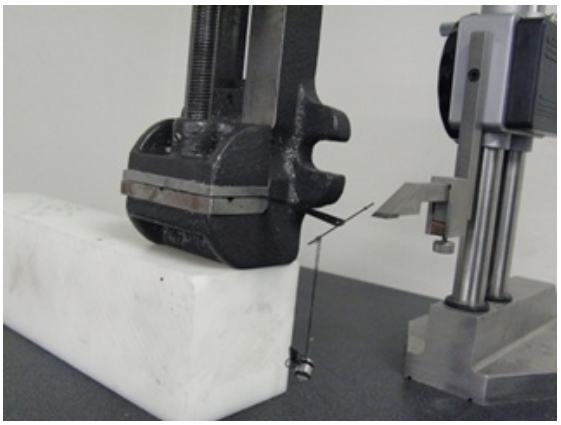

(b) **Torsion test**

Figure 6.27: **Bending and torsion tests on chordwise ribs**

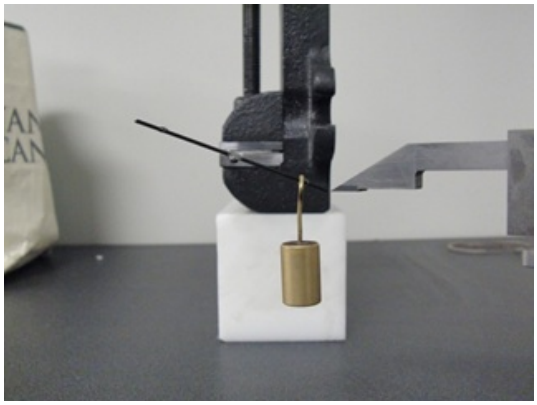

Figure 6.28: **Torsion test on leading edge spar**

The geometric and structural properties of the flexible wing are mentioned in Table 6.1

Using the properties of these different components, a complete structural model of the wing was developed in MBDyn. The spar and ribs were modeled as beam elements and the Mylar film was modeled as a 2D shell element. Experiments were then carried out on the entire wing using VICON which is a motion capturing system. The details of VICON were mentioned earlier in Chapter 4. Loads were added at different markers attached on the wing and deflections were measured using four infra-red cameras. The experimental test set-up is shown in Figure 6.29

Analysis was then carried out for the entire wing model developed in MBDyn with the different loading conditions and the deflections were compared to experiments. Figures 6.30 show the results for the cases where the loads were added at tips of the chordwise ribs. As can be seen from the figure, satisfactory correlation is obtained from analysis (MBDyn) and experiments

Table 6.1: **Properties of flexible wing**

Member	**Properties**
Wing span (m)	0.127
Wing chord (m)	0.0762
Leading edge spar, EI (Nm^2)	2.9×10^{-2}
Leading edge spar, GJ (Nm^2)	2.1×10^{-3}
Root Rib, GJ (Nm^2)	4.2×10^{-5}
Mid Rib, GJ (Nm^2)	3.5×10^{-5}
Tip Rib, GJ (Nm^2)	3×10^{-5}
Root rib, EI (Nm^2)	4.6×10^{-4}
Mid rib, EI (Nm^2)	1.2×10^{-4}
Tip rib, EI (Nm^2)	0.97×10^{-4}
Mylar film, E (N/m^2)	5.02×10^{9}
Mylar film, ν	0.45

(VICON). Surface contour plots were also compared from MBDyn and VICON. The results for a case with 5 grams of load applied at the tip are shown in Figure 6.31. With this, the structural model of the wing was satisfactorily validated.

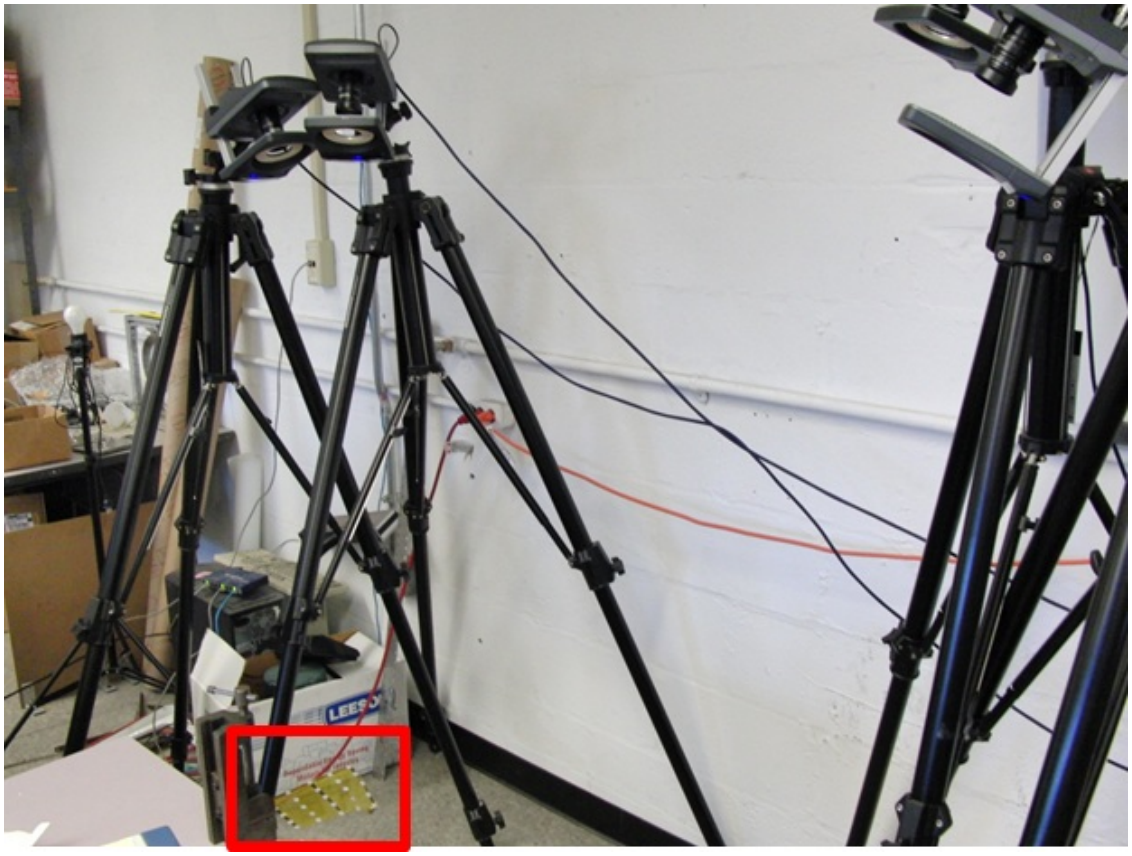

(a) **VICON Motion Capturing System**

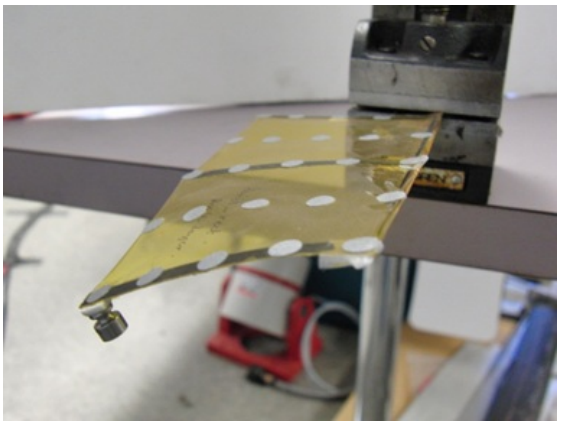

(b) **Zoomed in view of wing with load added on it**

Figure 6.29: **VICON tests to determine wing deflections under various loading conditions**

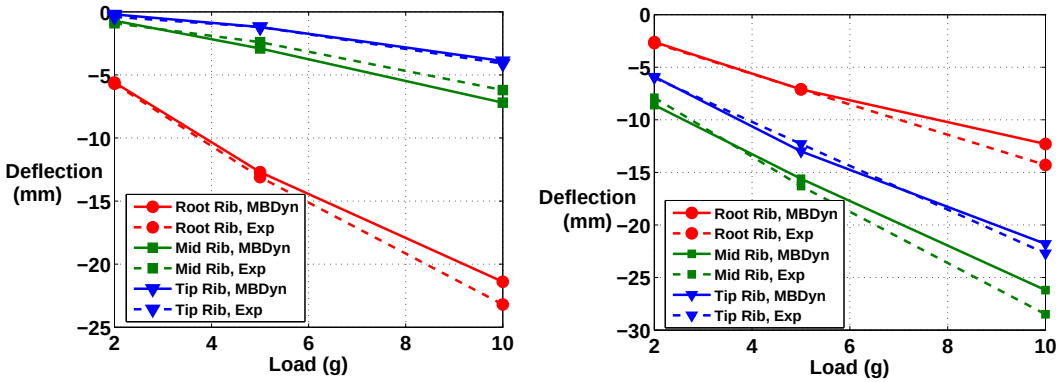

(a) **Load at trailing edge of root rib** (b) **Load at trailing edge of mid rib**

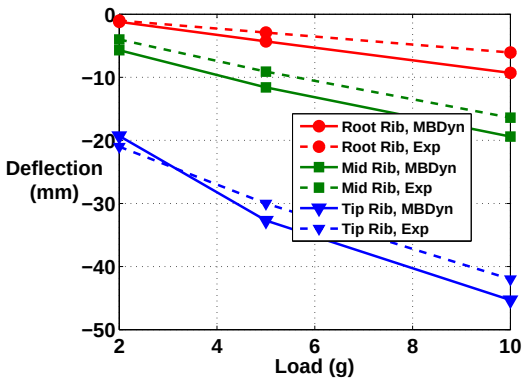

(c) **Load at trailing edge of tip rib**

Figure 6.30: **Load deflection curves for chordwise ribs**

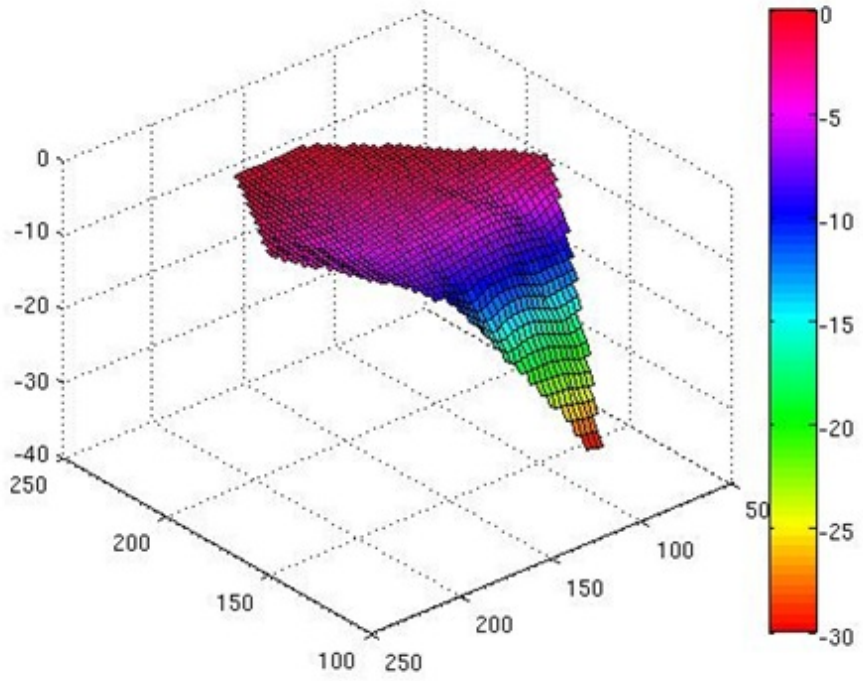

(a) **VICON**

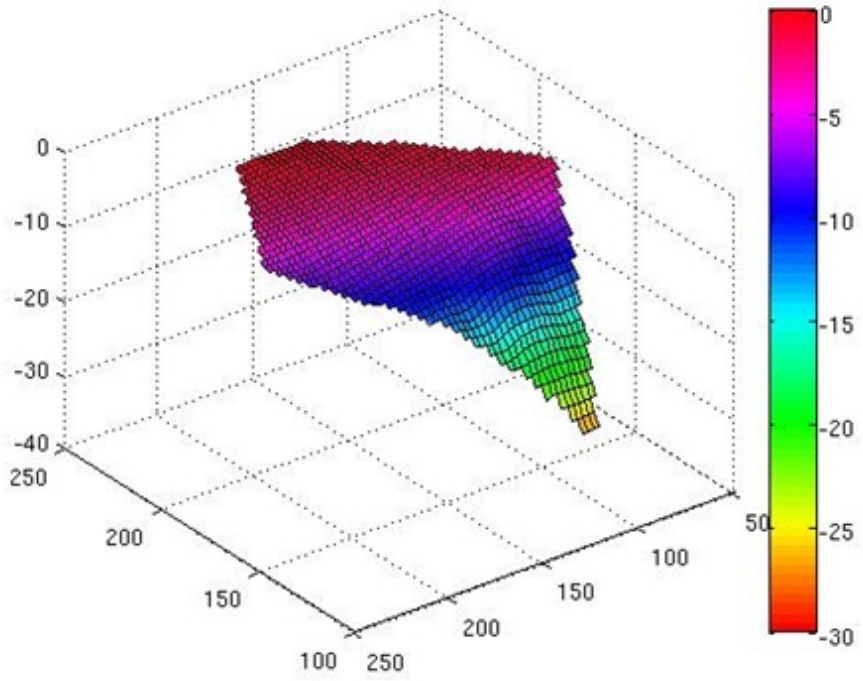

(b) **MBDyn**

Figure 6.31: **Wings surface contours from experiment and analysis for weight added at tip trailing edge**

6.4.3 CFD-CSD Analysis of Flexible Wings

The structural model of the wing was coupled to the CFD solver to obtain a coupled CFD-CSD analysis. Analysis was carried out for flexible wings with root pitch angles, $\theta_0 = 0°, 12°$ and $24°$, flap amplitude of $40°$, 3 m/s forward speed and different flap frequencies. Results from the coupled simulation are presented in this section. Figure 6.32 shows the average forces in vertical and horizontal directions from experiments and the coupled CFD-CSD analysis. As can be seen from the figure, satisfactory correlation is obtained. The analysis was then used to gain further insights into the flow physics for the case with flap frequency of 10 Hz.

Figure 6.33 shows the pressure coefficient contours at the mid-span section of flexible wing with $0°$ root pitch angle at different instants of flap cycle for the 10 Hz flap frequency. As was seen earlier for the symmetric cases (rigid wing: pure flap with $0°$ pitch angle, flap plus symmetric passive pitch), in this case also, symmetry is observed in the flow features in the upstroke and downstroke. Figure 6.34 shows the instantaneous forces over a flap cycle for the 10 Hz case. The positive instantaneous force during the downstroke in vertical direction (F_Z) cancels out the negative instantaneous force in the upstroke for the wing with root pitch angle, $\theta_o = 0°$ (Figure 6.34(a)). Due to flexibility in the wing, the wing undergoes twisting and there is a change in wing pitch angle along the different spanwise locations. As a result of the wing twist, a part of the net force is vectored in the propulsive direction and a positive propulsive

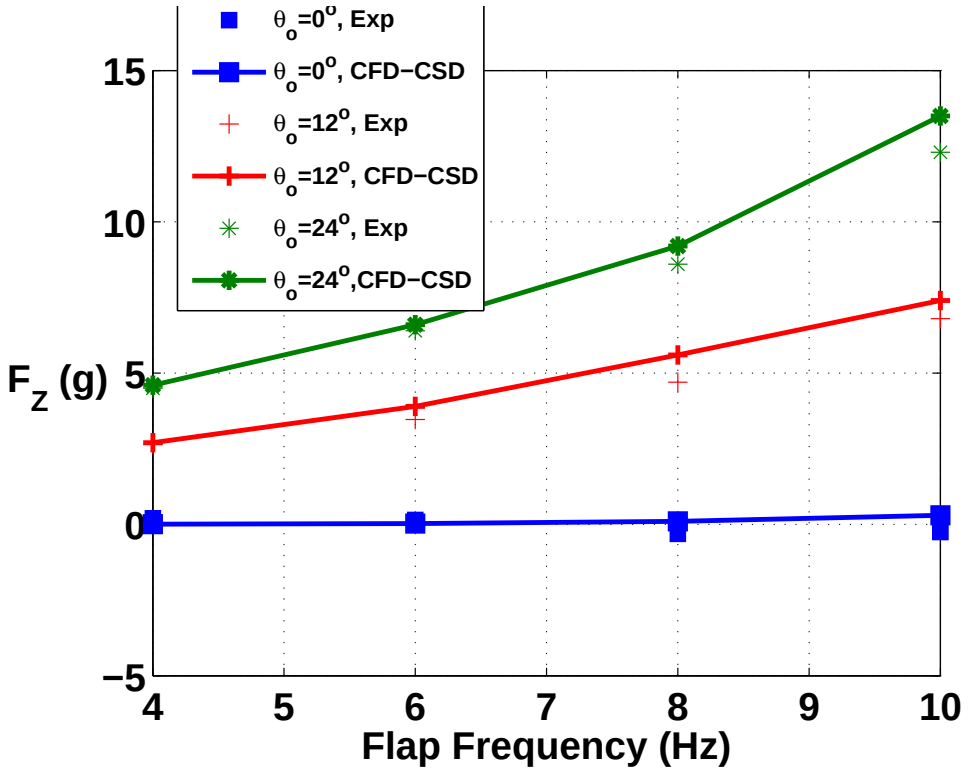

(a) Average vertical force, F_Z

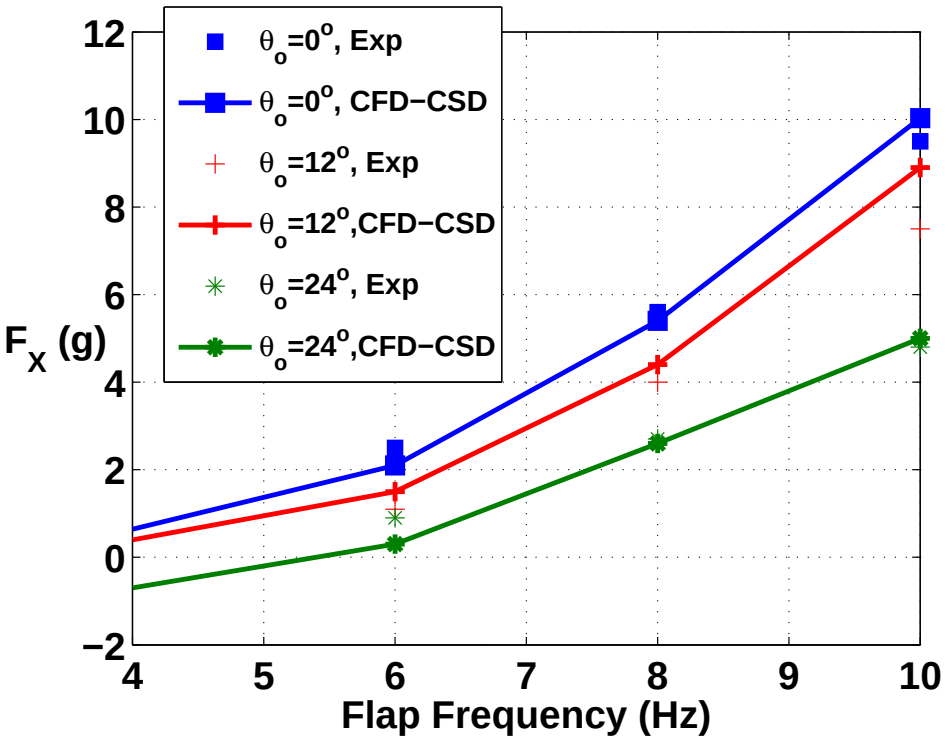

(b) Average propulsive force, F_X

Figure 6.32: **Variation of vertical and propulsive forces with frequency for flexible wings obtained from experiments and analysis** (40° **flap amplitude,** $V_\infty = 3$ **m/s).**

force is obtained throughout the flap cycle. To summarize, a positive average propulsive force (F_X) is obtained using the dynamic twisting of this flexible wing with 0° root pitch angle and the average force in vertical direction (F_Z) is zero.

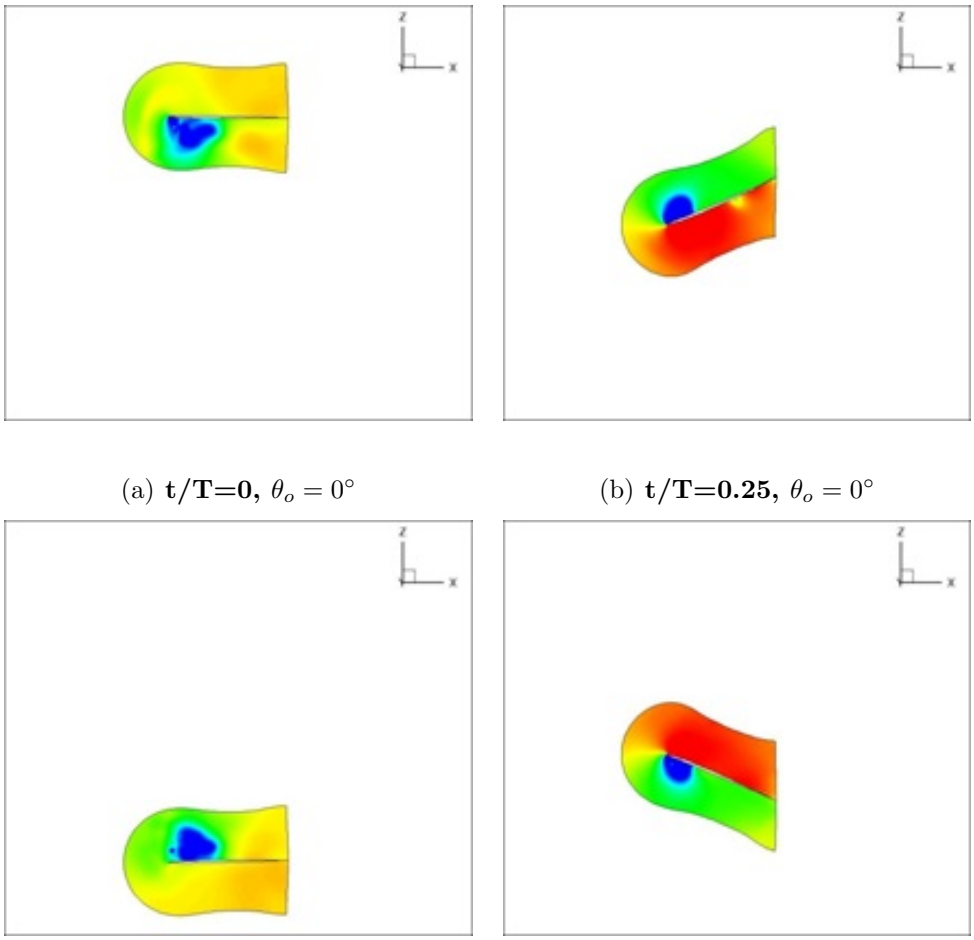

(a) **t/T=0,** $\theta_o = 0°$ (b) **t/T=0.25,** $\theta_o = 0°$

(c) **t/T=0.5,** $\theta_o = 0°$ (d) **t/T=0.75,** $\theta_o = 0°$

Figure 6.33: **Pressure coefficient contours at mid span section of flexible wing in flap plus dynamic twist with** 0° **root pitch angle (**40° **flap amplitude,** $V_\infty = 3$ **m/s)**

Figure 6.35 shows the mid-span pressure coefficient contours for the flex-

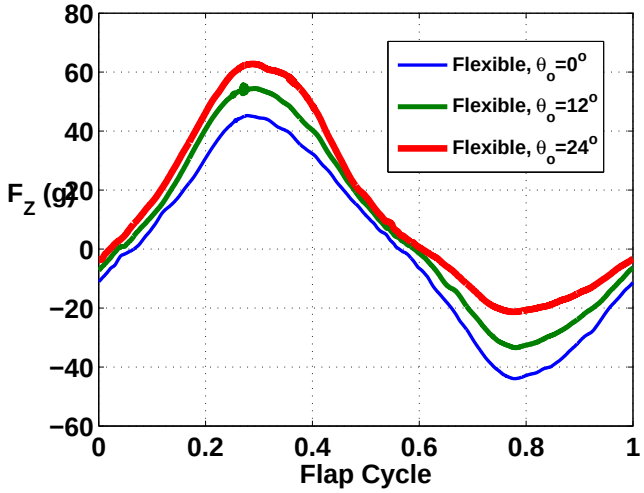

(a) **Instantaneous vertical force**

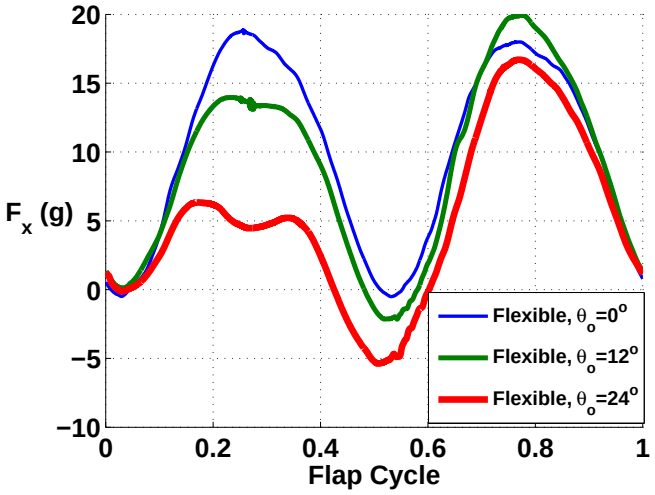

(b) **Instantaneous propulsive force**

Figure 6.34: **Instantaneous forces for flexible wing, flap plus dynamic twist** (40° **flap amplitude,** $V_\infty = 3$ **m/s,** 10 **Hz flap frequency)**

ible wing with 24° root pitch angle for 10 Hz flap frequency. A strong leading edge vortex is observed at top of the wing at middle of the downstroke ($t/T = 0.25$). As a result of twisting of the wing, the wing pitch angle at the

mid span location, for example (shown here), is reduced from the root pitch angle of 24°. The actual geometric pitch angle varies along the span. For the mid-span section as shown in the figure, the wing pitch angle is $-2°$ at the middle of downstroke ($t/T = 0.25$). Due to this, a large part of the resultant force is vectored in the vertical direction (F_Z) and this results in a larger force in the vertical direction and a smaller force in the propulsive direction (F_X) as compared to wing with 0° root pitch angle. The instantaneous forces are shown in Figure 6.34. For the 24° root pitch case, the entire vertical force curve (F_Z) is shifted upwards as compared to the 0° case and reduction in propulsive force is observed, particularly during the downstroke ($t/T = 0.25$).

To conclude, the flexible wing with 0° root pitch angle generated positive F_X but zero average F_Z. On increasing the root pitch angle to 24° the propulsive force dropped but was still higher than the target F_X and also target F_Z was achieved. Similar to the rigid wing results, a trade-off was seen in vertical and propulsive forces. The effect of flexibility on the aerodynamics is explored in more detail in the next section.

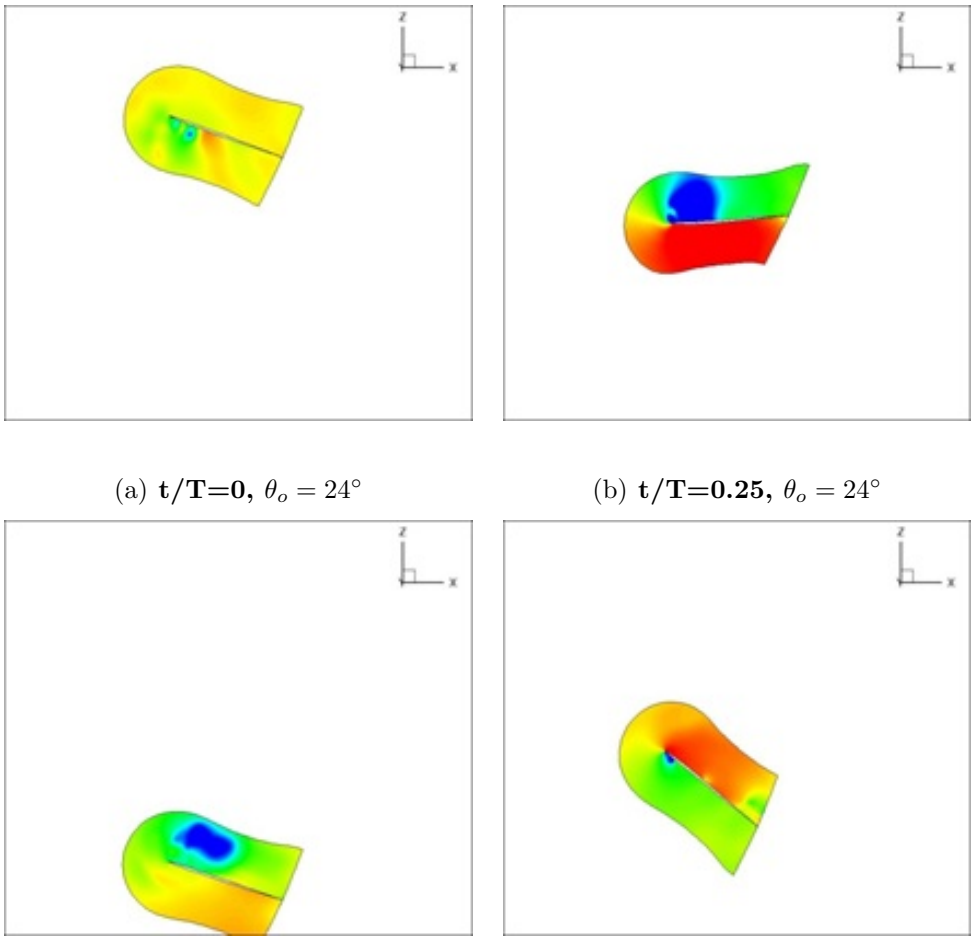

(a) **t/T=0,** $\theta_o = 24°$ (b) **t/T=0.25,** $\theta_o = 24°$

(c) **t/T=0.5,** $\theta_o = 24°$ (d) **t/T=0.75,** $\theta_o = 24°$

Figure 6.35: **Pressure coefficient contours at mid span section flexible wing in flap plus dynamic twist with** $24°$ **root pitch angle,** $40°$ **flap amplitude,** $V_\infty = 3$ **m/s,** 10 **Hz flap frequency**

6.5 Comparison between Rigid and Flexible Wing with Root Flap Actuation

This section compares the rigid wing in pure flap and dynamic twisting of flexible wing in root flap actuation with fixed root pitch angle, $\theta_o = 24°$. The pressure coefficient contour plots at mid span sections for the rigid and flexible wings at different instants of the flap cycle for flap frequencies of 4 Hz, 6 Hz, 8 Hz and 10 Hz are shown in figs. 6.36 to 6.39 respectively.

The first observation is that on increasing the flap frequency, there is an increase in the strength of vortices for both, the rigid and flexible wings. Secondly, due to higher forces acting on the wing at a higher flap frequency, the flexible wing twist increases. This has a significant effect on the forces. Figure 6.40 shows the variation of average forces for the rigid and flexible wing with flap frequency. As was mentioned earlier in Section 6.2, rigid wing in pure flap with pitch angle of 24° produces a positive vertical force (F_Z) but negative propulsive force (F_X). Comparing the flexible wing results, we see that not only is there an increase in the F_Z magnitude but also, the flexible wing produces a positive propulsive force, F_X.

Now consider the wings at flap frequency of 10 Hz in more detail. Figure 6.41 is a plot of instantaneous forces for both the wings over a flap cycle. It can be seen that at middle of downstroke (t/T=0.25), negative instantaneous propulsive force (as shown in Figure 6.41(b)) is generated by the rigid wing. The reason for this negative propulsive force becomes clear if we look

at the pressure coefficient contour shown in Figure 6.39(c). The force due to the LEV on the rigid wing is vectored such that it results in a positive force in vertical direction and negative propulsive force. However, in the case of a flexible wing, its twisting leads to a reduction in the negative geometric pitch angle as shown in Figure 6.39(d). As a result, the negative "x" component of the force is reduced and instead, a positive instantaneous propulsive force is generated. Further, looking at the upstroke ($t/T = 0.75$), the strength of LEV at bottom of wing is reduced for the flexible wing (Figure 6.39(h)) as compared to the rigid wing (Figure 6.39(g)). While a negative instantaneous force was generated in the vertical direction (F_Z) during the uptroke ($t/T = 0.75$) by the rigid wing, a positive propulsive force is generated by the flexible wing as shown in Figure 6.41. Therefore, a benefit is seen in both, vertical as well as propulsive force due to flexibility. The rigid wing with root flap actuation studied here may not be a viable option on an MAV at this forward speed. However, the well tailored flexible wing may be used to generate both, the target vertical and propulsive forces.

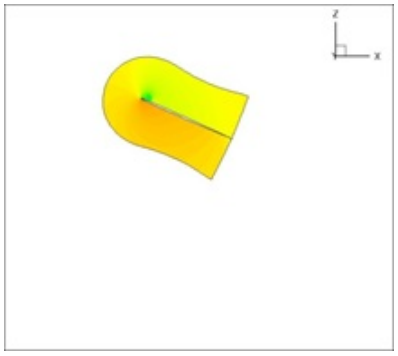

(a) **t/T=0, Rigid Wing**

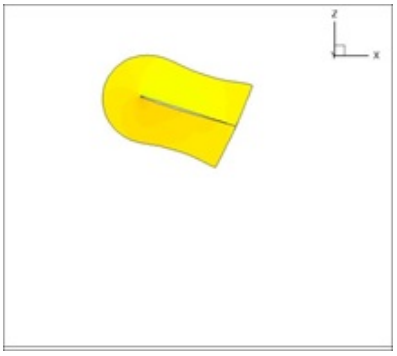

(b) **t/T=0, Flexible Wing**

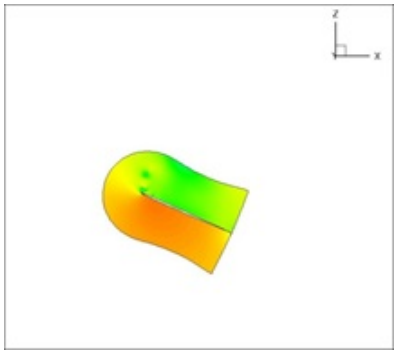

(c) **t/T=0.25, Rigid Wing**

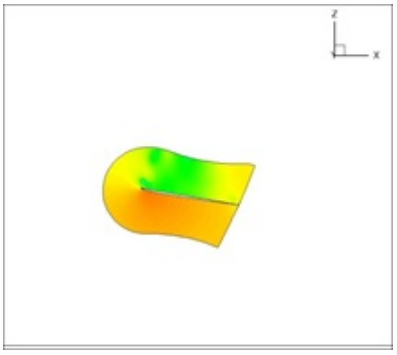

(d) **t/T=0.25, Flexible Wing**

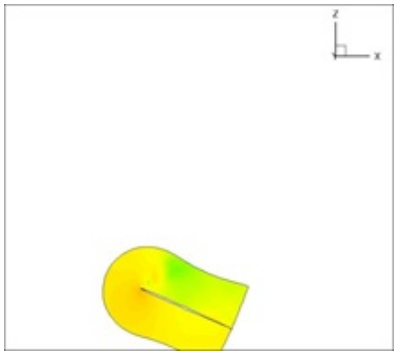

(e) **t/T=0.5, Rigid Wing**

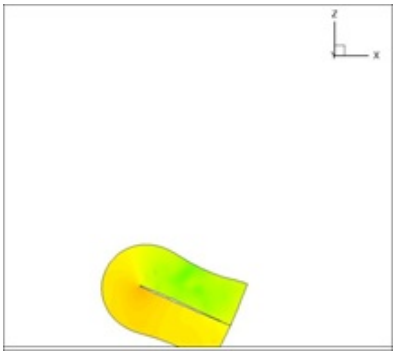

(f) **t/T=0.5, Flexible Wing**

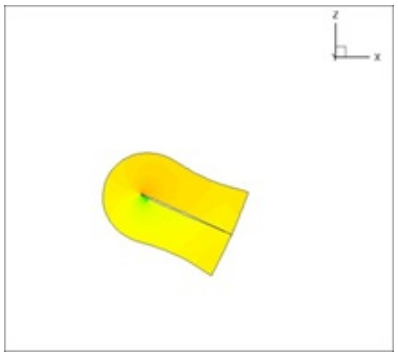

(g) **t/T=0.75, Rigid Wing**

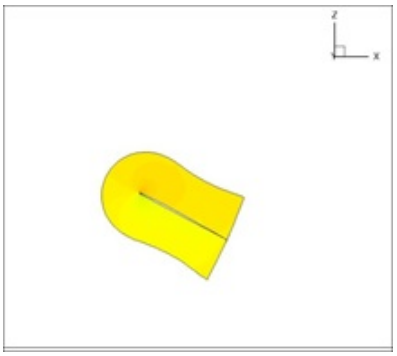

(h) **t/T=0.75, Flexible Wing**

Figure 6.36: **Pressure contours at mid span location for rigid and flexible wings (**40° **flap amplitude,** 24° **pitch angle,** $4Hz$ **flap frequency,** $3m/s$ **forward speed)**

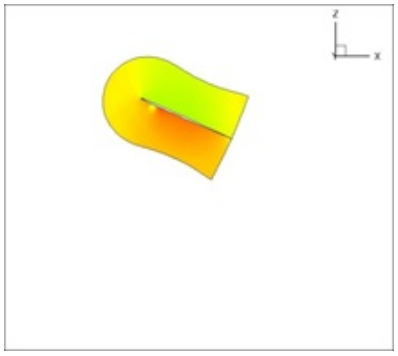

(a) **t/T=0, Rigid Wing**

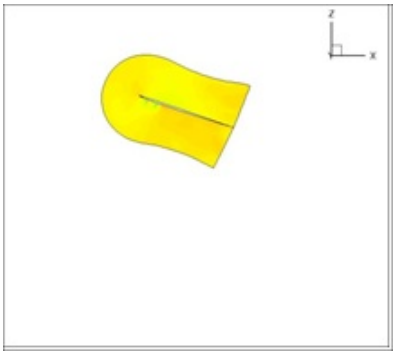

(b) **t/T=0, Flexible Wing**

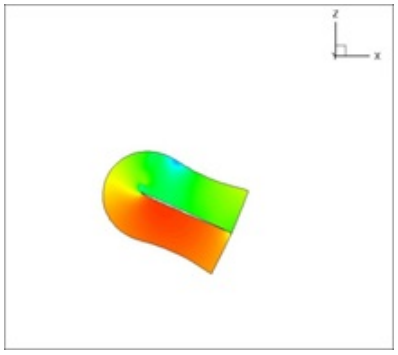

(c) **t/T=0.25, Rigid Wing**

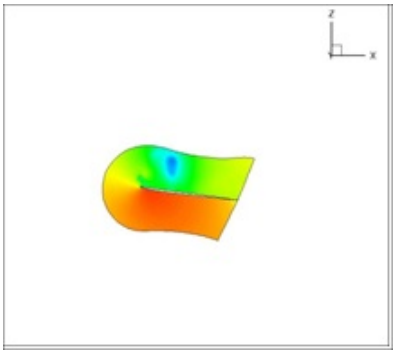

(d) **t/T=0.25, Flexible Wing**

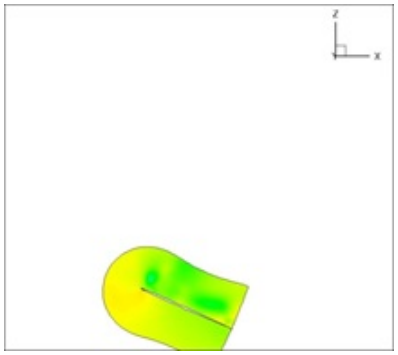

(e) **t/T=0.5, Rigid Wing**

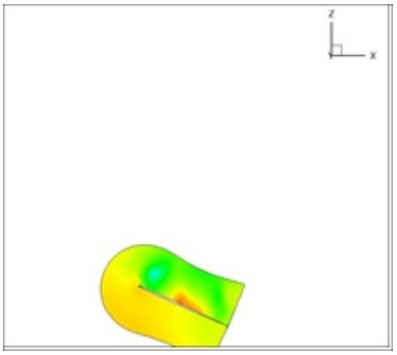

(f) **t/T=0.5, Flexible Wing**

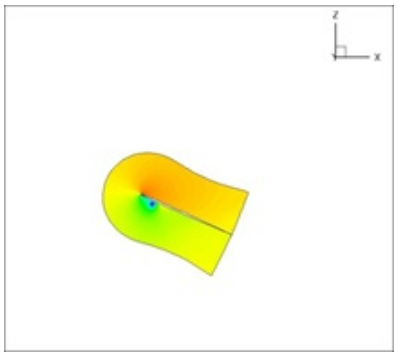

(g) **t/T=0.75, Rigid Wing**

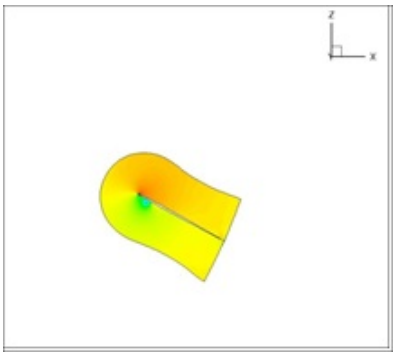

(h) **t/T=0.75, Flexible Wing**

Figure 6.37: **Pressure contours at mid span location for rigid and flexible wings (**40° **flap amplitude,** 24° **pitch angle,** $6Hz$ **flap frequency,** $3m/s$ **forward speed)**

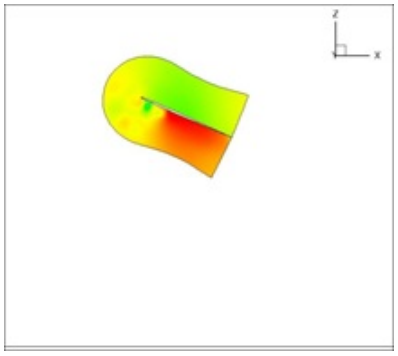

(a) **t/T=0, Rigid Wing**

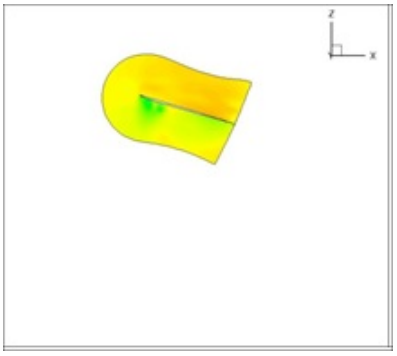

(b) **t/T=0, Flexible Wing**

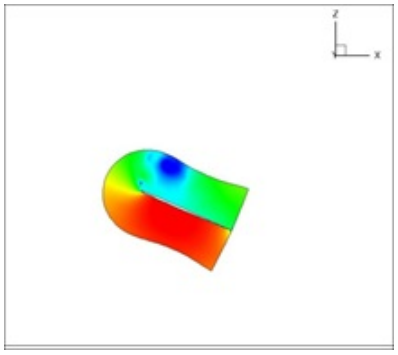

(c) **t/T=0.25, Rigid Wing**

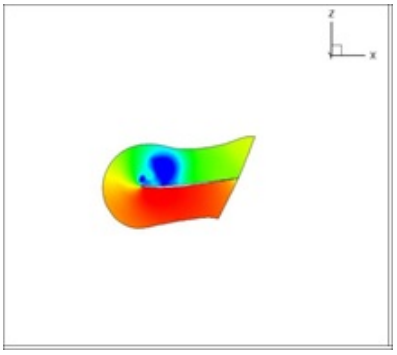

(d) **t/T=0.25, Flexible Wing**

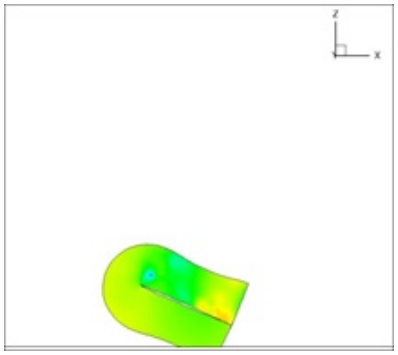

(e) **t/T=0.5, Rigid Wing**

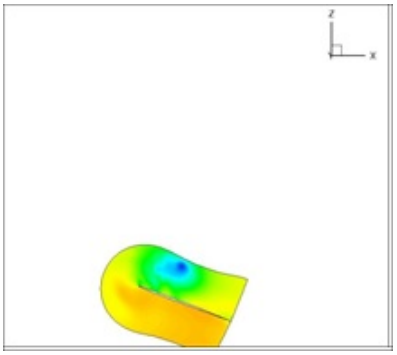

(f) **t/T=0.5, Flexible Wing**

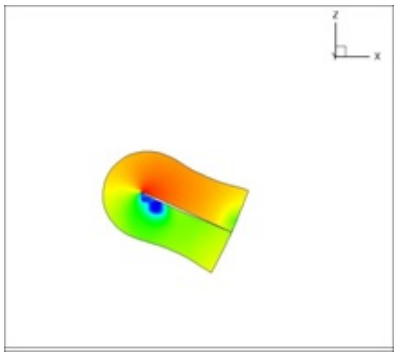

(g) **t/T=0.75, Rigid Wing**

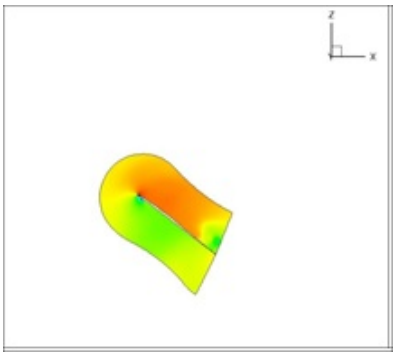

(h) **t/T=0.75, Flexible Wing**

Figure 6.38: **Pressure contours at mid span location for rigid and flexible wings (**40° **flap amplitude,** 24° **pitch angle,** $8Hz$ **flap frequency,** $3m/s$ **forward speed)**

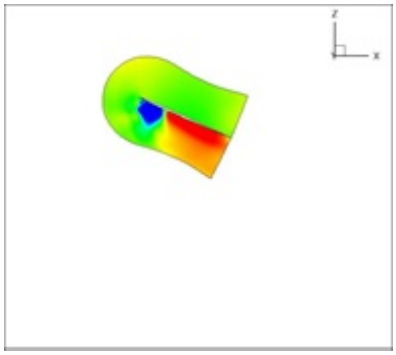

(a) **t/T=0, Rigid Wing**

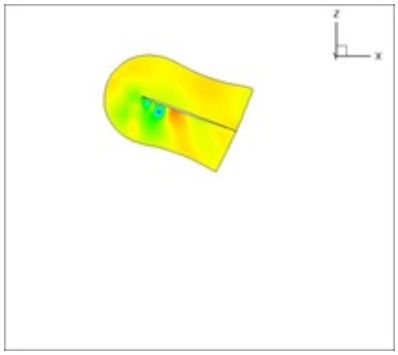

(b) **t/T=0, Flexible Wing**

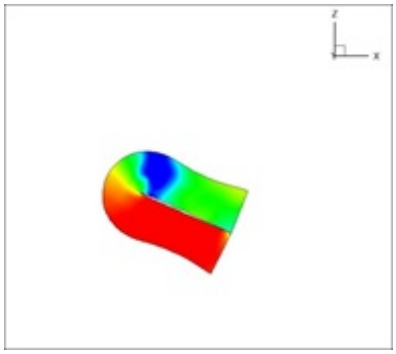

(c) **t/T=0.25, Rigid Wing**

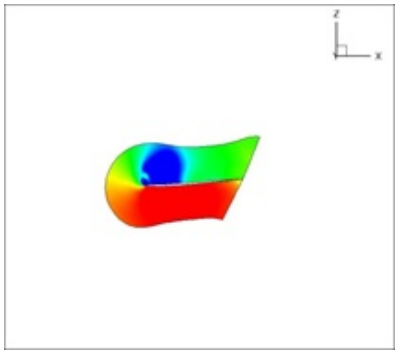

(d) **t/T=0.25, Flexible Wing**

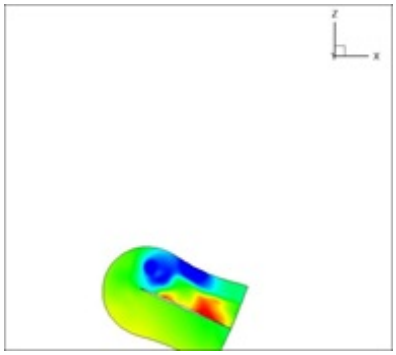

(e) **t/T=0.5, Rigid Wing**

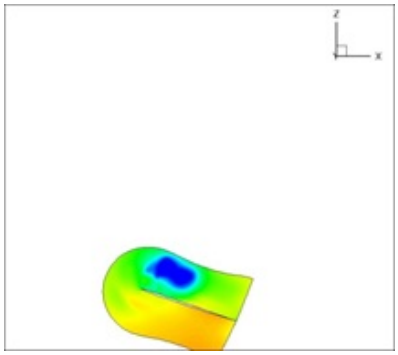

(f) **t/T=0.5, Flexible Wing**

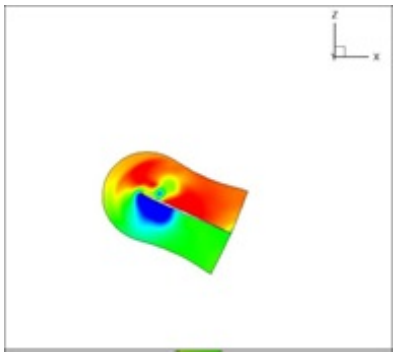

(g) **t/T=0.75, Rigid Wing**

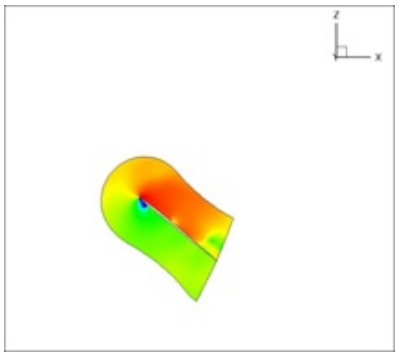

(h) **t/T=0.75, Flexible Wing**

Figure 6.39: **Pressure contours at mid span location for rigid and flexible wings (**$40°$ **flap amplitude,** $24°$ **pitch angle,** $10Hz$ **flap frequency,** $3m/s$ **forward speed)**

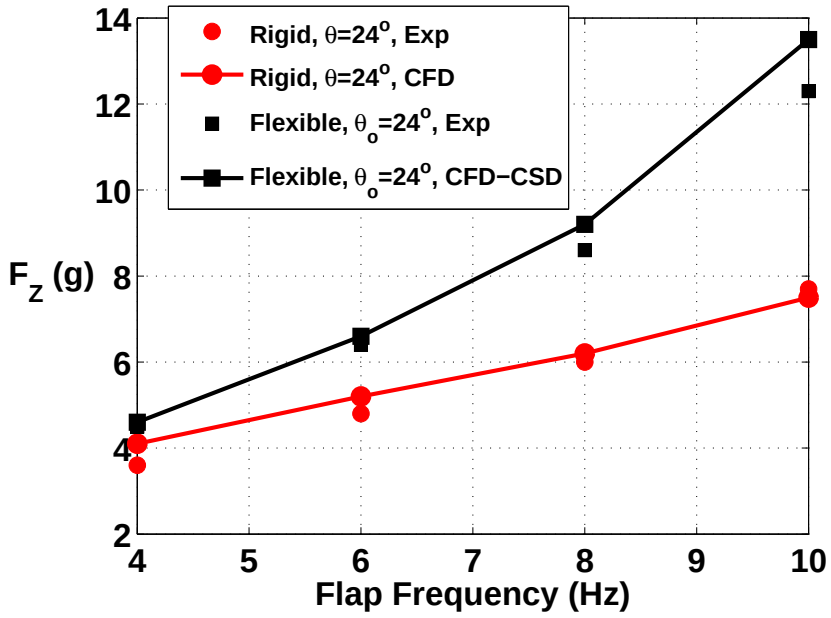

(a) **Average vertical force, F_Z**

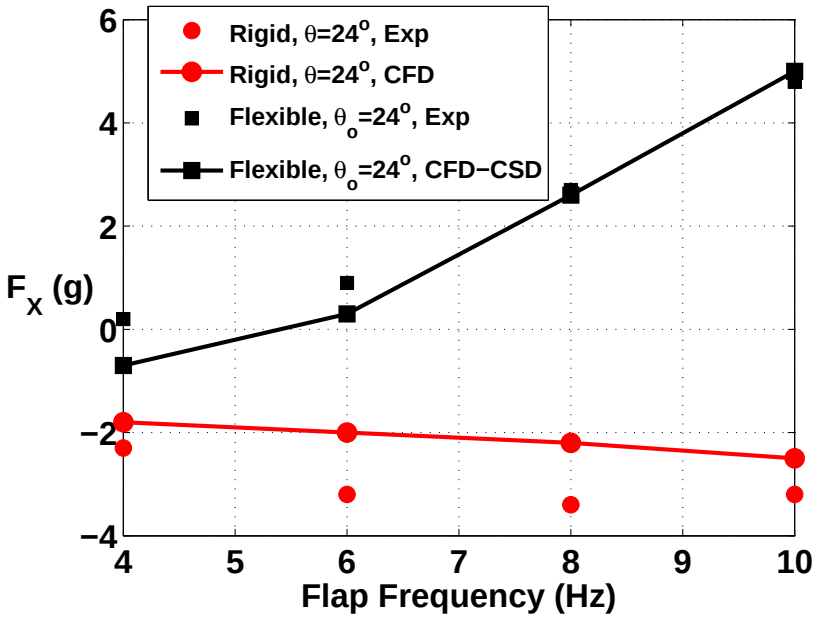

(b) **Average propulsive force, F_X**

Figure 6.40: **Variation of average forces with frequency for rigid and flexible wings** (40° **flap amplitude,** $V_\infty = 3$ **m/s)**

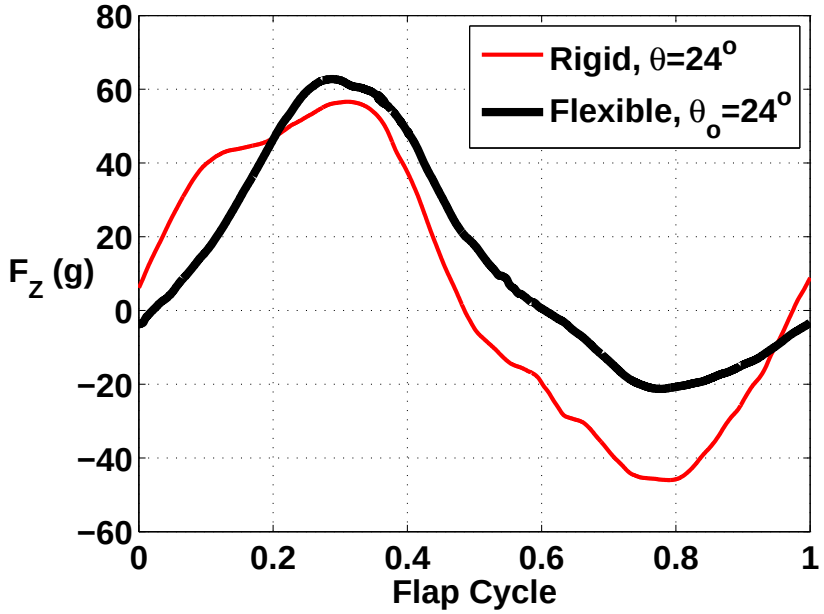

(a) **Instantaneous vertical force**

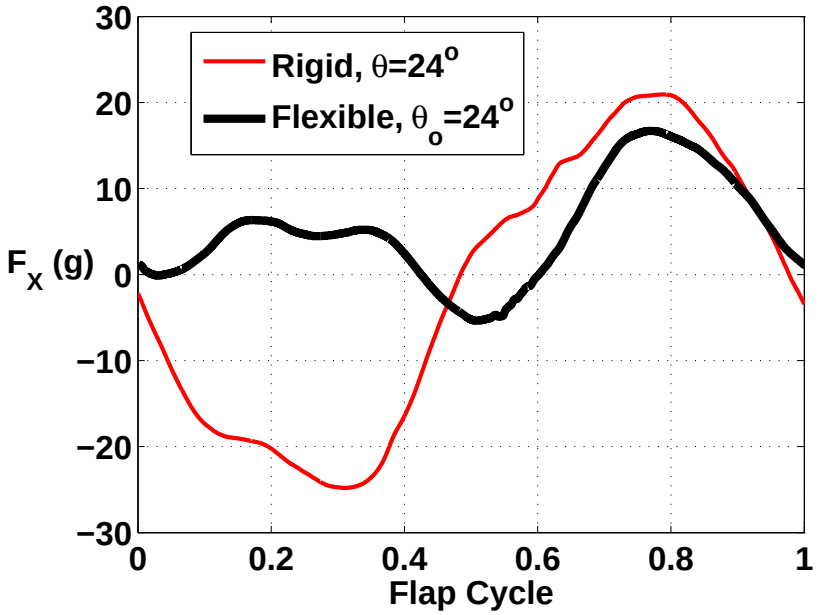

(b) **Instantaneous propulsive force**

Figure 6.41: **Instantaneous forces for rigid and flexible wings** (40° **flap amplitude,** $V_\infty = 3$ **m/s,** 10 **Hz flap frequency)**

6.6 Comparison between Passive Pitching of Rigid Wing and Dynamic Twist of Flexible Wing

Figures 6.42(a) and 6.42(b) summarize all the above tests and show how the kinematics affects the aerodynamic performance. For an MAV in forward flight, both, positive vertical and propulsive forces are required to be generated by the wing. This can be achieved using either asymmetric passive pitch of a rigid wing (with positive mean pitch angle) as mentioned in Section 6.3, or by dynamic twist of a flexible wing with positive root pitch angle as mentioned in Section 6.4. Also, it was mentioned in Section 6.4 that due to variation of spanwise flow velocities and angle of attack, dynamic twisting of flexible wing might be better aerodynamically than the entire wing pitching by the same pitch angle. The results from these two viable configurations are compared here to determine which could offer a better solution.

Figure 6.43 shows the average force variation with flap frequency for the two cases from experiments as well as analysis. From the analysis, 50% higher F_Z and 42% higher F_X is generated by the flexible wing as compared to the rigid wing. In order to analyze the effect of spanwise twist, the spanwise force coefficient variations are plotted for the two configurations at the middle of downstroke ($t/T = 0.25$) in Figure 6.44. It can be clearly seen that each section produces greater forces in the case of flexible wing because of better wing pitch modulation.

Also, it should be noted that the flexible wing did not have any additional

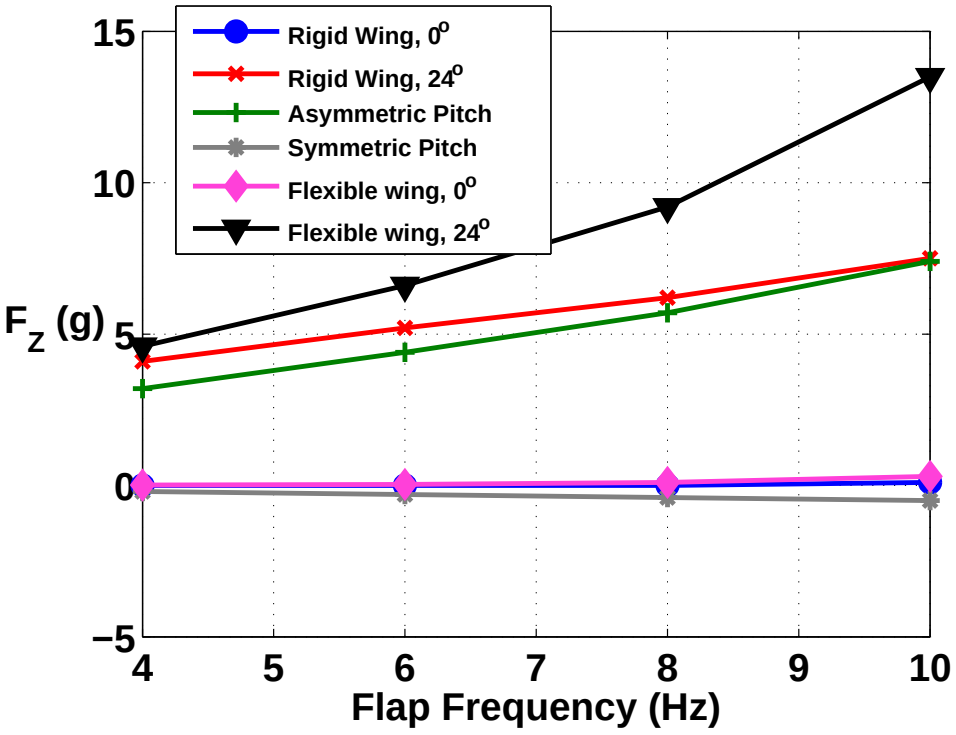

(a) Variation of F_Z with frequency

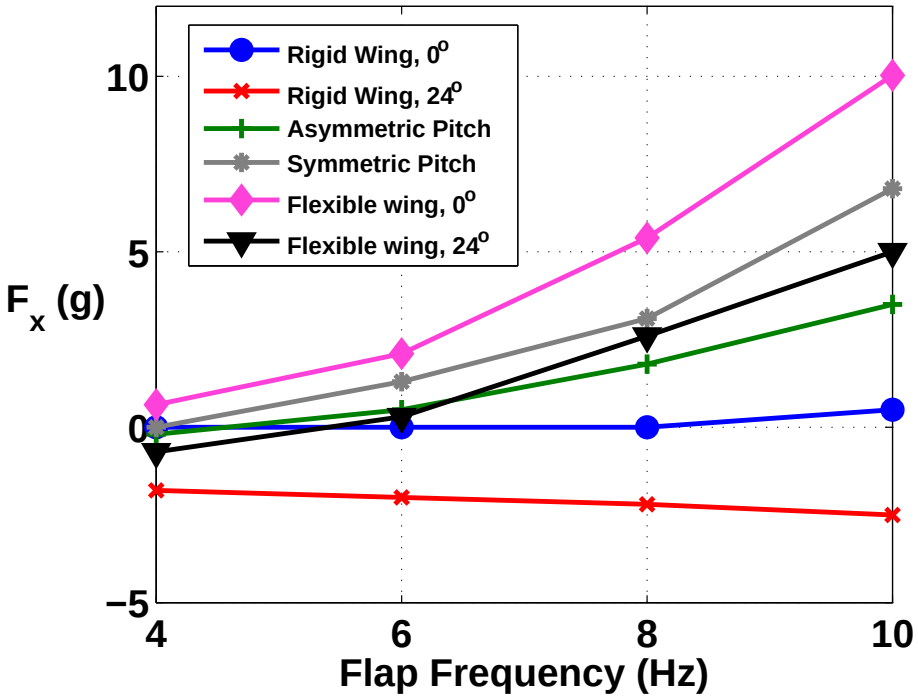

(b) Variation of F_X with frequency

Figure 6.42: **Comparison of average vertical and propulsive forces for all different configurations (40° flap amplitude, $V_\infty = 3$ m/s).**

torsion spring, as a result of which the mechanism was much simpler and lighter than the passive pitch mechanism. Both the mechanisms are shown in Figure 6.45. Further, since the flexible wing did not have to be stiffened as much as the rigid wing, it was lighter by 46%. Since the entire passive pitch mechanism has to be flapped, having a much lighter mechanism is definitely advantageous. Thus, the optimal configuration for a flapping wing MAV in forward flight might be dynamic twisting of a properly tailored flexible wing with a positive root pitch angle.

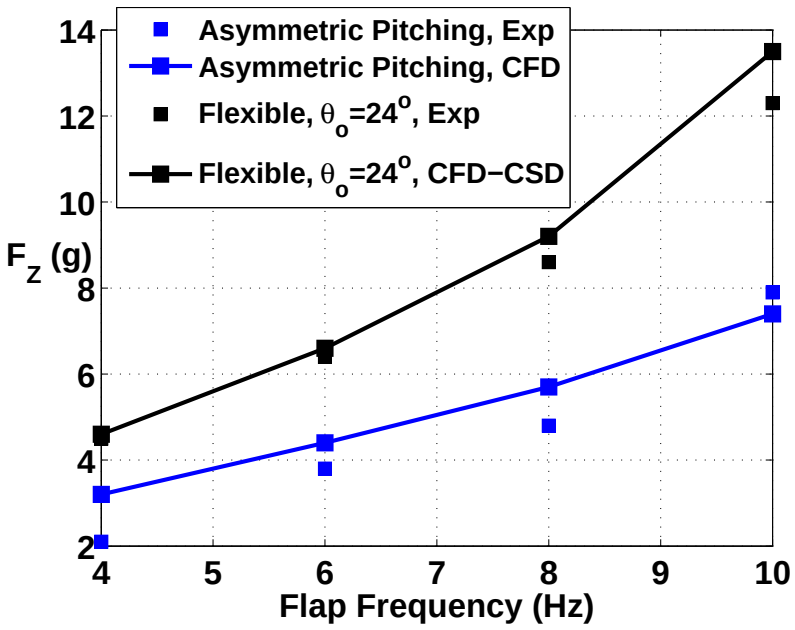

(a) **Average vertical force, F_Z**

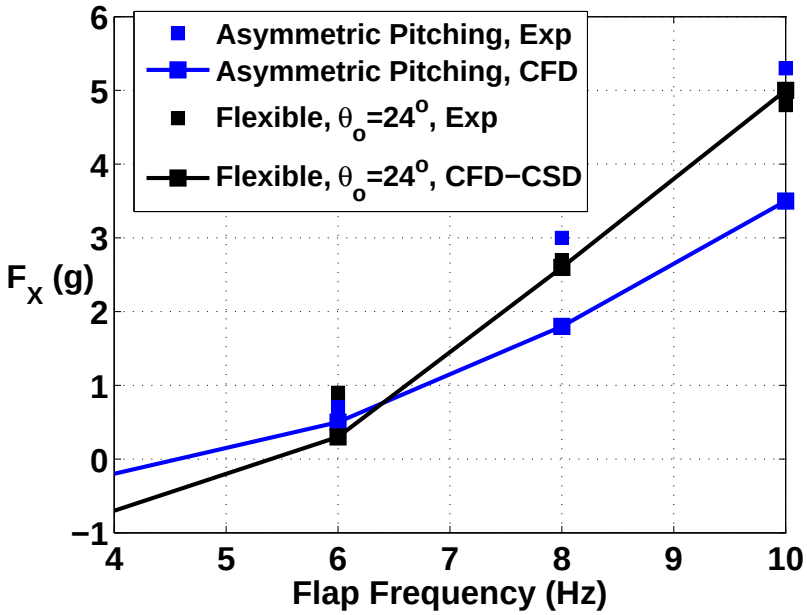

(b) **Average propulsive force, F_X**

Figure 6.43: **Variation of average forces with frequency for passive pitching rigid wing and dynamic twisting flexible wing (40° flap amplitude, $V_\infty = 3$ m/s)**

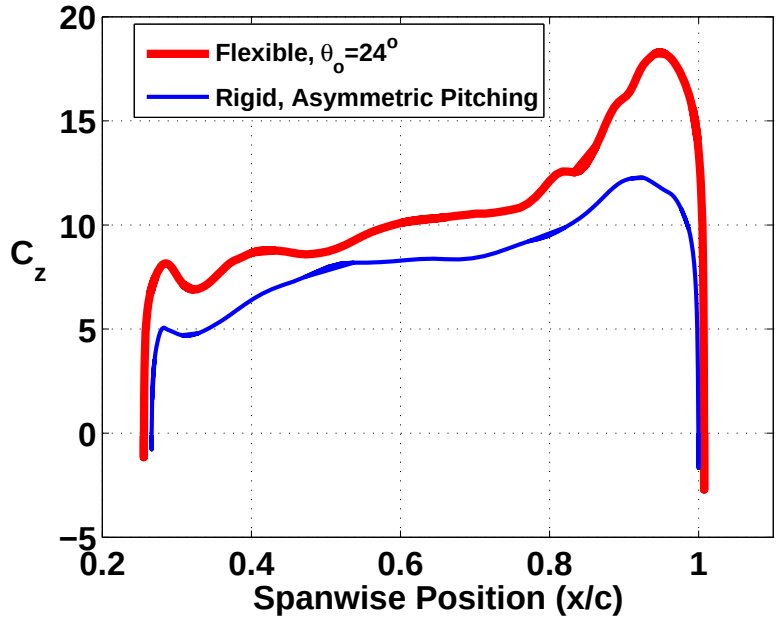

(a) C_z

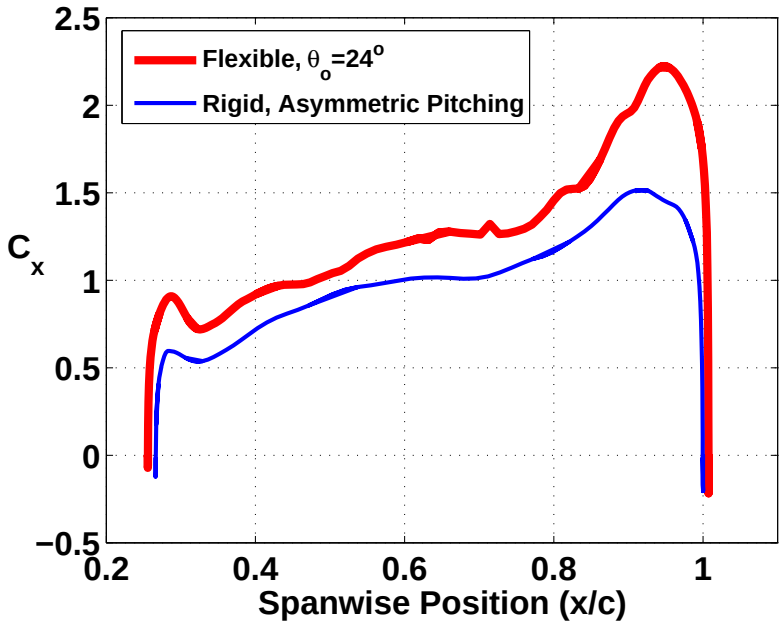

(b) C_x

Figure 6.44: **Spanwise force variation for passive pitching rigid wing and dynamically twisting flexible wing at middle of downstroke obtained from analysis (40° flap amplitude, $V_\infty = 3m/s$, 10 Hz flap frequency)**

(a) **Passive pitch mechanism** (b) **Flexible wing mechanism**

Figure 6.45: **Passive pitch and dynamic twist mechanisms**

6.7 Power Calculation for Rigid and Flexible Wings

Aerodynamic power was calculated for the rigid and flexible wings from the analysis. The time-averaged power input is given by:

$$\bar{C_P} = \frac{\bar{F_z v}}{\frac{1}{2}\rho V_\infty^3 cS} \tag{6.4}$$

where $F_z v$ is the instantaneous power input, and the overbar denotes an average over time. The propulsive efficiency is given by:

$$\eta = \frac{\bar{F}_x V_\infty}{\bar{F_z v}} = \frac{\bar{C_X}}{\bar{C_P}} \tag{6.5}$$

Both, power and efficiency are calculated for the rigid wing with asymmetric pitching and flexible wing with dynamic twist. The instantaneous aerodynamic power coefficient over the flap cycle is shown in Figure 6.46 for a flap frequency of 10 Hz. Figure 6.47 shows the instantaneous propulsive force variation. The average results for power and propulsive efficiency are presented in Table 6.2 and 6.3, respectively.

The power required for the flexible wing is 50% higher as compared to the rigid wing with asymmetric pitching. The propulsive efficiency of the flexible wing is 15% higher and it generates 71% more propulsive force than the rigid wing. The propulsive efficiency of these wings lie in the ball park of other studies on flapping wings [159] and highlights the need for future studies to improve the efficiency of such flapping wing concepts.

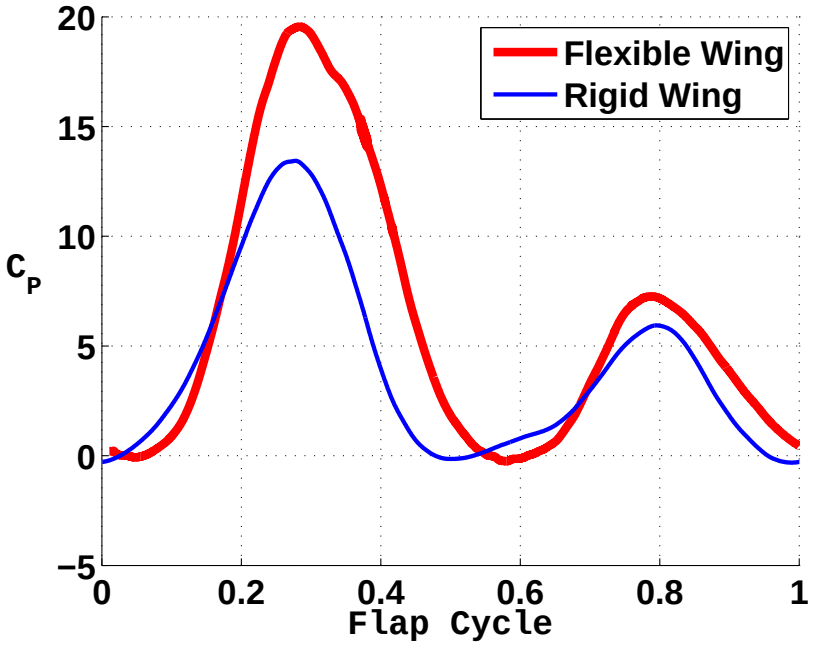

Figure 6.46: **Instantaneous aerodynamic power for rigid wing (asymmetric pitch) and flexible wing (dynamic twist) at 10 Hz flap frequency**

Table 6.2: **Average power and propulsive force for rigid and flexible wings**

	C_P	C_X
Rigid (Asymmetric Pitch)	3.98	0.53
Flexible (Dynamic Twist)	5.97	0.91

Table 6.3: **Propulsive efficiency for rigid and flexible wings**

	η
Rigid (Asymmetric Pitch)	0.13
Flexible (Dynamic Twist)	0.15

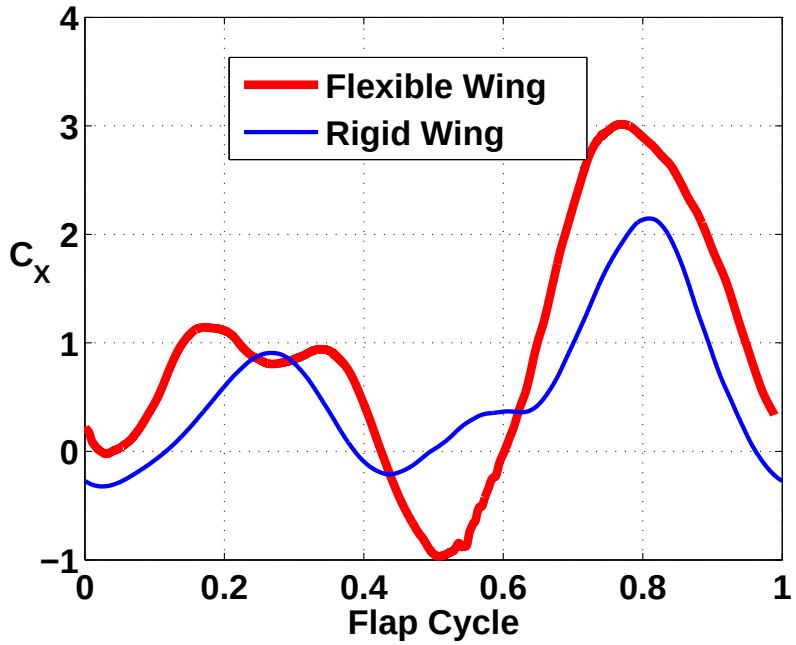

Figure 6.47: **Instantaneous propulsive force for rigid wing (asymmetric pitch) and flexible wing (dynamic twist) at 10 Hz flap frequency**

6.8 Summary and Conclusions

There is a dearth of data on flexible MAV wings with well characterized structural properties. Therefore, experiments were carried out on realistic rigid and flexible MAV flapping wings in an open jet wind tunnel. These experiments were also simulated using the high-fidelity tools developed. Three types of configurations were studied: pure flap of rigid wings, flap plus passive pitch of rigid wings, flap plus dynamic twist of flexible wings. Good correlation was obtained between the average forces from experiments and analysis. Following conditions were studied:

Pure flap of rigid wings

Pure flap tests were carried out on a rigid wing. It was observed that with a root pitch angle, $\theta_o = 0°$, positive propulsive force (F_X) was generated at 10 Hz flap frequency due to the Knoller-Betz effect. However, the average force in vertical direction (F_Z) was zero for $V_\infty = 3$ m/s. On increasing the root pitch angle, F_Z increased but F_X became negative. Since both, positive propulsive and vertical forces are required to be generated for forward flight, pure flap of a rigid wing may not be a viable configuration.

Combined flap and passive pitching of rigid wings

Passive pitch modulation was used along with flap motion of rigid wings. Two types of kinematics were studied: symmetric (with zero mean pitch angle, θ_o) and asymmetric (with positive mean pitch angle). Symmetric pitching generated positive propulsive force during the upstroke and downstroke. However,

due to symmetry in the kinematics in upstroke and downstroke, the average force in vertical direction (F_Z) was negligible. On introducing an asymmetry in the kinematics, the propulsive force (F_X) dropped (though it was still higher than the target propulsive force). Further, a positive average force in vertical force was generated. Therefore, both, the target propulsive and vertical forces can be achieved using asymmetric pitching of the rigid wing.

Flap plus dynamic twist of flexible wings

When a wing undergoes root flap actuation, plunge velocity and hence the effective angle of attack, varies from wing root to tip. Therefore, in order to achieve the best efficiency from a wing, both temporal and spanwise variation of pitch angle are required. In other words, the wing should undergo dynamic twisting and instead of passive pitching alone. Experiments and analysis on a flexible wing with root flap actuation showed that it generated zero vertical force, F_Z and a positive propulsive force, F_X with a root pitch angle of $\theta_o = 0°$. On increasing the root pitch angle, trade off was observed between the vertical and propulsive forces. For this wing, with root pitch angle, $\theta_o = 24°$, the target forces in both the directions were generated.

From these tests, it can be concluded that in order to generate a net F_Z force, a positive mean pitch angle is required. The target F_Z of the MAV can be met by

1. Pure flap of rigid wing at high pitch angle

2. Flap plus asymmetric passive pitch of rigid wing (with a mean positive

pitch angle)

3. Dynamic twist of flexible wing with positive root pitch angle

In order to generate a propulsive force, a pitch variation is required over the flap cycle. The target propulsive force of the MAV can be achieved by

1. Flap plus symmetric passive pitch of a rigid wing

2. Flap plus asymmetric passive pitch of a rigid wing

3. Dynamic twist of flexible wing

For an MAV application, both, target F_Z and F_X must be generated. In order to achieve this, either rigid wings can be pitched asymmetrically or, dynamic twisting of flexible wings with positive root pitch angle can be employed.

Further, it was shown that by using dynamic twisting, better wing modulation is obtained, which leads to greater forces at all spanwise sections as compared to passive pitching rigid wings. Also, the flexible wing mechanism is less complex and lighter. Finally, the flexible wing itself is also much lighter than the rigid wing. These results show the beneficial effects of flexibility and a well tailored flexible wing may be a suitable configuration for use on an MAV.

As a concluding remark, the current work demonstrates the capability of an aeroelastic solver to characterize the flowfield of a flexible flapping wing

MAV in 3D. This high fidelity solver may be used to drive the design of the next generation MAVs.

Chapter 7

Summary Remarks, Conclusions and Future Work

The growing interest in unmanned aircrafts, especially for surveillance and reconnaissance missions in confined areas, has spurred research activities in the area of Micro Air Vehicles (MAVs). MAVs can be considered as aerial robots or 6 degree of freedom machines which are required to carry out a variety of missions. Potential applications for MAVs, both military and civilian, are numerous. A few applications are: search and rescue, biochemical sensing, power line inspection, targeting, fire rescue, communications and traffic monitoring. In order to successfully carry out these missions, we need MAVs that are compact, maneuverable, can operate in constrained environments, efficient (with good hover and loiter endurance), have low noise signature and low detectability, and superior tolerance to wind gusts. Both fixed wings and rotary wings appear to provide well-known technologies, but all the flight envelope specifications of MAVs cannot be achieved using these scaled down concepts. This motivated researchers to investigate alternative typologies. The basic idea for bio-inspired MAVs is to adapt from nature and use similar flying technique as insects and birds: flapping wings. At MAV scales, flapping-wing vehicles may offer many advantages and superior flight stability in gusty environments over fixed wing/rotary-wing vehicles such as high maneuverability

and efficiency. Also, flapping wing aircraft have the potential to take-off and land vertically and can blend more easily into the environment. Recently, a lot of studies have been carried out in order to investigate the efficiency of such concepts and the possibility to reproduce them in the laboratory. In fact, the principal motivation seems to be the possibility of integrating vertical and propulsive forces together with stability and control mechanisms. With the introduction of a constantly accelerating and decelerating wing, the aerodynamics of such vehicles is highly unsteady in addition to the high viscous effects because of low operating Reynolds numbers. The aim of this work was to develop analytical tools as well as generate an experimental data to gain a fundamental understanding of the aerodynamics and aeroelasticity of flapping MAV wings.

7.1 Conclusions

7.1.1 Analysis of Rigid Flapping Wings

A compressible RANS solver, OVERTURNS, was used to simulate the aerodynamics of a flapping wing. Following are the key conclusions from this study.

1. The analysis was first validated for 2D flow cases and showed good correlation for all the cases considered. The first case was at relatively high Reynolds numbers. It was observed that propulsive force increases with plunging frequency due to the increasing suction of the leading edge

vortex. As long as this vortex is ahead of the position of maximum thickness, the wing generates a propulsive force. However, if this vortex convects aft, propulsive force drops.

2. Validation was then carried out for combined pitch and plunge motions at high Reynolds numbers. It was observed that the propulsive force generated was higher for this case as compared to pure plunge motion. The mechanism of propulsive force was again the suction force due to formation of leading edge vortex. But in this case, the vectoring of the resultant force is determined by combination of pitch angle and the position of the vortex. For the flapping wing to generate propulsive force, the vortex may be positioned on the top or bottom of the airfoil (which depends on the angle of attack), but the suction force should be vectored in the propulsive direction (which depends on the pitch angle and the phasing between pitch and plunge). Good correlation was achieved with other analyses.

3. Simulation was then carried out for a low Reynolds number case, which is applicable to MAVs. It should be noted that all the 2D cases were symmetric in upstroke and downstroke and hence the average force in vertical direction was zero. For this case, the instantaneous vertical and propulsive force values were also validated. Very high value of maximum instantaneous vertical force coefficient was observed, which was much greater than the corresponding static vertical force coefficient at the

same effective angle of attack. This clearly shows the beneficial effect of unsteadiness in the aerodynamic forces.

4. 3D validation was then carried out for two configurations. The first configuration was a heaving and pitching flat plate wing with low aspect ratio. Validation of instantaneous forces and flow fields was carried out with experimental data and PIV results. Two cases were considered, pure plunge at fixed positive angle and a case with pitching modulation over a constant pitch angle. Due to an asymmetry in the kinematics, an average vertical force (F_Z) was produced in both the cases. However, the kinematics was such that the wing produced mostly positive propulsive force throughout the entire cycle for both the cases.

5. The second 3D configuration was root based flapping which is more representative of natural flyers. A spanwise tapered wing was simulated in pitch and flap. Good correlation of instantaneous forces and flow fields was seen with prior work. The flowfield was highly three dimensional with the flow dominated by leading edge vortices in the midsection but by the root and tip vortices near the ends of the wing. Unlike the flat plate case considered before, high propulsive force (F_X) was generated as a result of the tailoring of pitch and plunge angles and flapping frequency.

As a concluding remark, this study demonstrated the capability of OVERTURNS to characterize the flowfield of a flapping wing MAV in 3D flow environment.

7.1.2 Analysis of Simplified Flexible Wing Configurations

In order to include the effects of flexibility, a structural solver, MBDyn was used. It had geometrically exact non-linear beam and shell elements, which could be used to analyze composite wing structures undergoing large non-linear deformations. The structural model was validated for different cases and satisfactory correlation was obtained. A coupled CFD-CSD analysis was then developed by coupling OVERTURNS and MBDyn using python framework. The following simplified configurations were analyzed for which data was available in literature.

Spanwise flexible wing

Spanwise inflexible, flexible and highly flexible wings were simulated and good correlation was obtained with prior experiments and other analyses. The first case was a pure plunge motion, for the inflexible wing. The flow was mostly 2D until about 75% span location. Beyond this, the flow becomes 3D due to the tip effect. On the other hand, for the flexible case, since there is flap bending and the plunge amplitude varies over the span, the 2D nature is not preserved even at further inboard locations and the flow field is more three dimensional. As compared to the rigid wing, because the flexible wing has higher plunge amplitude near the wing tip, this leads to a higher effective angle of attack. The leading edge vortices are stronger towards the outboard sections of the wing and also the strength of the tip vortex is higher. Sectional lift is higher for flexible wing, particularly towards the outer sections of the

wing. Similar trend is seen for the propulsive force. Thus, the increase in forces due to flexibility in this case comes mainly from the outer sections where the plunge amplitudes are higher.

A highly flexible wing was also analyzed and compared to prior experiments and other analyses. Satisfactory correlation was obtained. Comparing the inflexible, flexible and highly flexible cases, it was observed that on introducing a small amount of flexibility, the average propulsive force (C_X) increased from 0.21 to 0.31 by 47% and the instantaneous vertical force (C_Z) increased from 4.4 to 5.6 by 27%. However, for the highly flexible wing, the average propulsive force dropped to 0.13, (58% compared to flexible wing) and instantaneous vertical force dropped to 1.95 (65% compared to flexible wing).

The reason for the drop in forces for the highly flexible wing is that, the wing root and tip move out of phase for a large portion of the flap cycle and this results in leading edge vortices being formed on different sides of the wing at the root and tip. Also, due to this out of phase motion, the angle of attack is reduced towards the outer sections and a drop in vortex strength is observed. To conclude, leading edge vortex strength increases from rigid wing to flexible wing but drops for the highly flexible wing and similar trend is observed in other forces.

Chordwise flexible wing

Next, a chordwise flexible wing was analyzed using the solver. This was a root flap case where the wing was held fixed at the root and flapped. As a result of the flexibility, camber was produced towards outer sections of the

wing as it flapped. Due to camber in the wing, the resultant force was vectored more in the chordwise direction as compared to rigid wings, which resulted in higher propulsive force.

The average vertical force coefficient C_Z increased by 10% and the average propulsive force coefficient C_X increased by 25% due to flexibility.

Similar to the spanwise flexible wing, the chordwise flexible wing has higher sectional vertical force and propulsive force towards the tip. Due to the camber that develops in the flexible wing, a greater portion of the resultant force is vectored in the chordwise direction. Also, the strength of leading edge suction is higher in the flexible wing case and there is a greater high pressure at the bottom of the wing. This clearly showed the beneficial effect of chordwise flexibility on the aerodynamics of flapping wings.

7.1.3 Experiments and Analysis of Rigid and Flexible MAV Wings

There is a dearth of data on MAV wings with well characterized structural properties. Therefore, experiments were carried out on realistic rigid and flexible MAV flapping wings in an open jet wind tunnel. These experiments were also simulated using the high-fidelity tools developed. Three types of configurations were studied: pure flap of rigid wings, flap plus passive pitch of rigid wings, flap plus dynamic twist of flexible wings. Good correlation was obtained between the average forces from experiments and analysis. Following conditions were studied:

Pure flap of rigid wings

Pure flap tests were carried out on a rigid wing. It was observed that with a root pitch angle, $\theta_o = 0°$, positive propulsive force (F_X) was generated at 10 Hz flap frequency due to the Knoller-Betz effect. However, the average force in vertical direction (F_Z) was zero for $V_\infty = 3$ m/s. On increasing the root pitch angle, F_Z increased but F_X became negative, implying a net negative propulsive force. Since both, positive propulsive and vertical forces are required to be generated for forward flight, pure flap of a rigid wing may not be a viable configuration for these conditions.

Combined flap and passive pitching of rigid wings

Passive pitch modulation was used along with flap motion of rigid wings. Two types of kinematics were studied: symmetric (with zero mean pitch angle, θ_o) and asymmetric (with positive mean pitch angle). Symmetric pitching generated positive propulsive force during the upstroke and downstroke. However, due to symmetry in the kinematics in upstroke and downstroke, the average force in vertical direction (F_Z) was negligible. On introducing an asymmetry in the kinematics, the propulsive force (F_X) dropped (though it was still higher than the target propulsive force). Further, a positive average force in vertical direction was generated. Therefore, both, the target propulsive and vertical forces can be achieved using asymmetric pitching of the rigid wing.

Flap plus dynamic twist of flexible wings

When a wing undergoes root flap actuation, plunge velocity and hence the effective angle of attack, varies from wing root to tip. Therefore, in order to

achieve the best efficiency from a wing, both temporal and spanwise variation of pitch angle are required. In other words, the wing should undergo dynamic twisting instead of passive pitching alone. Experiments and analysis on a flexible wing with root flap actuation showed that it generated zero vertical force, F_Z and a positive propulsive force, F_X with a root pitch angle of $\theta_o = 0°$. On increasing the root pitch angle, trade off was observed between the vertical and propulsive forces. For this wing, with root pitch angle, $\theta_o = 24°$, the target forces in both the directions were generated.

From these tests, it could be concluded that in order to generate a net F_Z force, a positive mean pitch angle is required. The target F_Z of the MAV could be met by

1. Pure flap of rigid wing with positive pitch angle
2. Flap plus asymmetric passive pitch of rigid wing (with a mean positive pitch angle)
3. Dynamic twist of flexible wing with positive root pitch angle

In order to generate a propulsive force, a pitch variation is required over the flap cycle. The target propulsive force of the MAV could be achieved by

1. Flap plus symmetric passive pitch of a rigid wing
2. Flap plus asymmetric passive pitch of a rigid wing
3. Dynamic twist of flexible wing

For an MAV application, both, target F_Z and F_X must be generated. In order to achieve this, either rigid wings can be pitched asymmetrically or, dynamic twisting of flexible wings with positive root pitch angle can be employed.

Further, it was shown that by employing dynamic twisting, better wing modulation is obtained, which leads to greater forces at all spanwise sections as compared to passive pitching rigid wings. Also, the flexible wing mechanism is less complex and lighter. Finally, the flexible wing itself is also much lighter than the rigid wing. These results show the beneficial effects of flexibility and a well tailored flexible wing may be a suitable configuration for use on an MAV.

7.2 Contributions to the State of the Art

Insects and birds make use of different unsteady lift mechanisms to make their flight possible. These unsteady aerodynamic effects need to be investigated thoroughly in order to understand them and use them to our advantage while building the next generation MAVs. Though a lot of experimental works have been carried out on flapping wings, a large number of them are performed by biologists on insect wings at very low Reynolds numbers (~ 100), which are far below the current MAV regime. In the Reynolds number regime of MAVs ($\sim 10^3 - 10^5$), a number of studies have been carried out on rigid wings. Though these provide some insights into unsteady aerodynamics, but many

other studies have shown that natural flyers use flexibility to their advantage. It is extremely important to understand not only unsteady aerodynamics, but also the aeroelastic effects need to be modeled in order to be able to accurately predict the performance of flapping wing MAVs.

Experimental testing of different wings is a very time consuming and inefficient way to drive the design of flapping wing MAVs as well as to understand their flow physics. Also, experiments may not be able to provide the level of details in flow physics, which can be achieved through analysis. In recent years, a number of aeroelastic analyses have been developed. The three major components of the analyses are: the aerodynamic solver, structural solver and the coupling between the solvers. Majority of the analyses either have a simplified aerodynamic model that cannot accurately represent all the unsteady, viscous effects (based on thin airfoil theory, unsteady panel methods, euler methods) or, have a linear finite element model (mostly based on linear finite elements with beam elements). It should be noted that to model all the complex unsteady and aeroelastic effects of these highly flexible low aspect ratio wings, both the solvers should be of high fidelity and able to take into account the three dimensional unsteady aerodynamics at low Reynolds numbers and large non linear deformations of 2D membrane wings with anisotropic construction. In addition, the coupling between the two solvers should be robust.

The main contribution of the current work to the state of the art was to extend the limited body of work on 3D flapping wings and develop a high fidelity CFD-CSD solver to study the performance and flow physics of realis-

tic flexible flapping wing MAVs. Proper understanding of the aerodynamics and aeroelasticity of flapping wings will reduce the amount of time and effort spent on experimental trial and error platform development. A high fidelity, well validated solver may then be used to drive the design for the next generation flapping wing MAVs. The CFD-CSD solver developed was validated systematically with other analyses and experiments.

Though the analysis is able to handle non-linearities of structures and fluids, it was found that there is a dearth of data on realistic flexible, structurally characterized flapping wings. The current flapping wing MAVs are built using membrane wings, strengthened by carbon spars and these are normally based on a trial and error approach through testing a variety of wings and kinematic configurations. In most of these studies, the flexible wings are not even structurally characterized. Therefore, there is clearly a need of reliable experimental data on structurally well characterized realistic, flexible, lightweight wings. Another key contribution was to carry out experiments on realistic flexible wings to determine the kinematics suitable for generating appropriate vertical and propulsive forces in forward flight. These wings were then structurally characterized to generate a comprehensive data set, currently unavailable in literature, which can be used for validation of aeroelastic analyses of flapping wings. This experimental data set was also used to validate the analysis and gain further confidence in its prediction capabilities. Once satisfactory correlation was achieved, the analysis was used to obtain more insights into the flow physics.

7.3 Recommendations for Future Work

There are several areas where more research needs to be performed to extend and improve upon the understanding gained from the present research. This entire study was carried out for flapping wings in forward flight. The analysis can be extended to hovering flapping kinematics. Further experiments (force measurements and PIV) can be carried out to generate test data in hover. Once the code is validated using these experimental results, detailed parametric studies can be carried out, which will be aimed at understanding the effect of various wing kinematics parameters (flapping-pitching amplitude, phasing and frequency) and wing geometric and structural parameters (wing span, planform, aspect-ratio, twist, spanwise/chordwise flexibility and mass distribution, wing natural frequencies and mode-shapes) on performance. The results from these studies can be used to design an optimized flapping wing MAV configuration with aeroelastically tailored wings for both efficient hover and forward flight.

In order for the flapping-wing MAVs to be used in the various mission scenarios, stability and gust tolerance of these vehicles need to be determined. The analysis can be used to derive the stability derivatives to develop high-fidelity flight dynamics simulations for flapping-wing MAVs and quantitatively estimate the gust-tolerance capability of flapping-wing based MAVs. Finally, the code can be extended to much smaller scales (Reynolds Numbers less than 1000) in order to analyze the performance of sub-gram millimeter scale

flappers, which may require further changes to the CFD and structural solvers. This will provide insights into the scalability of flapping wings which is not clear at this point and also identify the scales at which flapping wings could be more efficient than rotary wings. Finally, a well validated, robust, high-fidelity comprehensive aeroelastic analysis can be developed which can be routinely used for the design of next-generation flapping wing MAVs.

Bibliography

[1] James, M. and McMichael, C. M. S. F., "Micro Air Vehicles - Toward a New Dimension in Flight," Website http://www.fas.org/irp/program/collect/docs/mavauvsi.htm, Accessed on September 3, 2012.

[2] Grasmeyer, J. M. "Development of the Black Widow Micro Air Vehicle," 39th AIAA Aerospace Sciences Meeting and Exhibit, M. T. Keennon, Ed., American Institute of Aeronautics and Astronautics, 2000.

[3] Aerovironment, Inc., Website http://www.aerovironment.com/, Morovia, CA, Accessed on January 6, 2012.

[4] Sankaranarayanan, S., Antony, R. and Suraj, C. S., "Technology Driven Program for the Development for the Development of a Fixed wing micro Air Vehicle at NALDRIVEN," MAV Workshop - Challenges and Preferred Outcomes, National Aerospace Laboratories, Bangalore, 13 November 2008.

[5] University of Arizona Micro Air Vehicle Club, Website http://clubs.engr.arizona.edu/mav/, Accessed on October 15, 2009.

[6] Null, W., and Shkarayev, S., "Effect of Camber on the Aerodynamics of Adaptive Wing Micro Air Vehicles," 2nd AIAA Flow Control Conference,

Portland, OR, July 2004.

[7] Ifju, P. G., Stanford, B., Sytsma M. and Albertani, R., "Analysis of a Flexible Wing Micro Air Vehicle", 25th AIAA Aerodynamic Measurement Technology and Ground Testing Conference, San Francisco, California, 5-8 June 2006.

[8] Ifju, P. G., Jenkins, D. A., Ettinger, S., Lian, Y., Shyy, W., and Waszak, M. R., "Flexible-Wing-Based Micro Air Vehicles," 40th AIAA Aerospace Sciences Meeting and Exhibit, Reno, Nevada, January 14-17, 2002.

[9] Petersen, B., Erath, B., Henry, K., Lyon, M., Walker, B., Powell, N., Fowkes, K., and Bowman, W. J., "Development of a Micro Air Vehicle for Maximum Endurance and Minimum Size," 41st AIAA Aerospace Sciences Meeting and Exhibit, Reno, Nevada, January 6-9, 2003.

[10] Brion, V., Aki, M., and Shkarayev, S., "Numerical Simulations of Low Reynolds Number Flows Around Micro Air Vehicles and Comparison against Wind Tunnel Data," 24th AIAA Applied Aerodynamics Conference, San Francisco, California, June 5-8, 2006.

[11] Lian, Y. and Shyy, W., "Numerical Simulations of Membrane Wing Aerodynamics for Micro Air Vehicle Applications," *Journal of Aircraft*, Vol. 42, (4), July-August 2005, pp. 865-873.

[12] Stanford, B., Viieru, D., Albertani, R., Shyy, W., and Ifju, P., "A Numerical and Experimental Investigation of Flexible Micro Air Vehicle Wing Deformation," 44th AIAA Aerospace Sciences Meeting and Exhibit, Reno, Nevada, January 9-12, 2006.

[13] Abdulrahim, M., Garcia, H., and Lind, R., "Analysis and Estimation of the Lift Components of Hovering Insects," *Journal of Aircraft*, Vol. 42, (1), January-February 2005, pp. 131-137.

[14] Abdulrahim, M., Garcia, H., Ivey, G. F., and Lind, R., "Flight Testing a Micro Air Vehicle Using Morphing for Aeroservoelastic Control," 45th AIAA/ASME/ASCE/AHS/ASC SDM conference, Palm Springs, California, April 19-22, 2004.

[15] DeLuca, A. M., Reeder, M. F., Freeman, J., and Ol, M. V., "Flexible and Rigid-Wing Micro Air Vehicle: Lift and Drag Comparison," *Journal of Aircraft*, Vol. 43, (2), March-April 2006, pp. 572-575.

[16] Smedresman, A., Yeo, D. and Shyy, W.,"Design, Fabrication, Analysis, and Testing of a Micro Air Vehicle Propeller," 29th AIAA Applied Aerodynamics Conference, Honolulu, Hawaii, 27-30 June 2011.

[17] Ahn, J. and Lee, D., "A Computational Study on the Aerodynamic Characteristics of a Flying-Wing MAV Design," 30th AIAA Applied Aerodynamics Conference, New Orleans, Louisiana, 25-28 June 2012.

[18] Ahn, J. and Lee, D., "Airfoil Designs and Free-Flight Tests of a Fixed Wing MAV Design," 30th AIAA Applied Aerodynamics Conference, New Orleans, Louisiana, 25-28 June 2012.

[19] Bohorquez, F., Samuel, P., Sirohi, J., Pines, D., Rudd, L., and Perel, R., "Design, Analysis and Hover Performance of a Rotary Wing Micro Air Vehicle," *Journal of the American Helicopter Society*, Vol. 48, (2), April 2003, pp. 80-90.

[20] Sirohi, J., Tishchenko, M., and Chopra, I., "Design and Testing of a Micro Aerial Vehicle with a Single Rotor and Turning Vanes," American Helicopter Society 61st Annual Forum Proceedings, Grapevine, TX, June 1-3, 2005.

[21] Bohorquez, F., Pines, D., and Samuel, P. D., "Small Rotor Design Optimization Using Blade Element Momentum Theory and Hover Tests," *Journal of Aircraft*, Vol. 47, (1), pp. 268-283, 2010.

[22] Hrishikeshavan, V., "Experimental Investigation of a Shrouded Rotor Micro Air Vehicle in Hover and in Edgewise Gusts," *Ph.D. Dissertation*, Department of Aerospace Engineering, University of Maryland at College Park, 2011.

[23] Airhogs, Website http://www.airhogs.com/en/products/havoc-heli, Accessed on March 4, 2009.

[24] Chopra, I., "Hovering Micro Air Vehicles: Challenges and Opportunities" Proceedings AHS International Meeting on Advanced Rotorcraft Technology and Safety Operations (Heli Japan), Ohmiya, Japan, November 2010.

[25] Daedalus Flight Systems, LLC, Website ¡http://daedalusflightsystems.com/¿, Accessed March 4, 2009.

[26] Harrington, A. M., "Optimal Propulsion System Design for a Micro Quad Rotor," Masters of Science, Department of Aerospace Engineering, University of Maryland at College Park, 2011

[27] Kroo, I., and Kunz, P. "Mesoscale Flight and Miniature Rotorcraft Development," Fixed, Flapping and Rotary Wing Vehicles at Very Low Reynolds Numbers, University of Notre Dame, 5-7 June 2000.

[28] Parrot, Website http://ardrone2.parrot.com/usa/, Accessed on April 5, 2012.

[29] Bouabdallah, S., Murrieri, P., and Siegwart, R., "Towards Autonomous Indoor Micro VTOL," *Autonomous Robots*, Vol. 18, (2), 2005, pp. 171-183.

[30] Tarascio, M., and Chopra, I., "Design and Development of a Thrust Augmented Entomopter: An Advanced Flapping Wing Micro Hovering Air

Vehicle," 59th American Helicopter Society Forum, Phoenix, AZ, May 2003.

[31] Spedding, G. R. and Lissaman, P. B. S., "Technical Aspects of Microscale Flight Systems," *Journal of Avian Biology*, Vol. 29, (4), 1998, pp. 458-468.

[32] Conn, A., Burgess, S., Hyde R., and Ling, C. S.,"From Natural Flyers to the Mechanical Realization of a Flapping Wing Micro Air Vehicle," Proceedings of the 2006 IEEE International Conference on Robotics and Biomimetics, Kunming, China, December 17-20, 2006.

[33] Petricca, L., Ohlckers, P., and Grinde, C.,"Micro and Nano-Air Vehicles: State of the Art," *International Journal of Aerospace Engineering*, Vol. 2011, Article ID 214549.

[34] Singh, B., "Dynamics and Aeroelasticity of Hover Capable Flapping Wings: Experiments and Analysis," *Ph.D Dissertation*, Department of Aerospace Engineering, University of Maryland at College Park, 2006.

[35] Dickinson, M. H., Lehman, F.O. and Sane, S.P., "Wing Rotation and the Aerodynamic Basis of Insect Flight," *Science*, 284, June 1999.

[36] Weis-Fogh T., "Quick Estimates of Flight Fitness in Hovering Animals", *Journal of Experimental Biology*, 1973, pp. 169-230.

[37] Harmon, R., L., "Aerodynamic Modeling of a Flapping Membrane Wing using Motion Tracking Experiments," Masters of Science, Department of Aerospace Engineering, University of Maryland at College Park, 2008.

[38] Videler, J.V., "Avian Flight," Oxford University Press, New York City, NY, 2005.

[39] Biewener, A. A.,"Muscle Function in Avian Flight: Achieving Power and Control," Philosophical Transactions of the Royal Society, Vol. 366, 2011, pp. 1496-1506.

[40] Shyy, W., Lian, Y., Tang, J., Viieru, D. and Liu, H., "Aerodynamics of Low Reynolds Number Flyers," Cambridge University Press, New York, NY, 2008.

[41] Azuma, A., "The Biokinetics of Flying and Swimming (2nd Ed). Reston, VA: American Institute of Aeronautics and Astronautics.

[42] Zdunich, P., "Development and Testing of the Mentor Flapping-Wing Micro Air Vehicle," *Journal of Aircraft*, Vol. 44, (5), September-October 2007.

[43] Schenato, L., Deng, X., and Sastry, S. "Flight Control System for a Micromechanical Flying Insect: Architecture and Implementation," IEEE

International Conference on Robotics and Automation, Seoul, Korea, May 2001.

[44] Perez-Arancibia, N.,"First Controlled Vertical Flight of a Biologically Inspired Microrobot," *Bioinspiration and Biomimetics*, Vol. 6 (3), 2011.

[45] Pornsin-sirirak, T. N., Lee, S. W., Nassef, H., Grasmeyer, J., Tai, Y. C., Ho, C. M., and Keennon, M., "Titanium-Alloy MEMS Wing Technology for a Battery-Powered Ornithopter," 13th IEEE Annual International Conference on MEMS, Miyazaki, Japan, January 23-27, 2000.

[46] DelFly, Website http://www.delfly.nl/?site=DIImenu=lang=nl, Accessed on September 2, 2012.

[47] Keennon, M., Klingebiel, K., Won, H. and Andriukov, A., "Development of the Nano Hummingbird: A Tailless Flapping Wing Micro Air Vehicle," 50th AIAA Aerospace Sciences Meeting including the New Horizons Forum and Aerospace Exposition, Nashville, Tennessee, 9-12 January 2012.

[48] Sher, I., Sher, L. D., and Sher, E.,"Miniaturization Limitations of HCCI Internal Combustion Engines," Applied Thermal Engineering, Vol. 29, (2-3), 2009, pp. 400-411.

[49] Mehra, A., Zhang, X., Ayon, A. A., Waitz, I. A., Schmidt, M. A., and Spadaccini, C. M., "Six-wafer Combustion System for a Silicon Micro Gas

Turbine Engine," *Journal of Microelectromechanical Systems*, Vol. 9, (4), 2000, pp. 517-527.

[50] Onera company, http://www.onera.fr/defa/micro-machinesthermiques-mems, Accessed on February 6, 2011.

[51] Shan, X. C., Wang, Z. F., Maeda, R., Sun Y. F., Wu, M., and Hua, J. S., "A Silicon-based Micro Gas Turbine Engine for Power Generation," Symposium on Design, Test, Integration and Packaging of MEMS/MOEMS (DTIP 06), Stresa, Italy, April 2006.

[52] Glassock, R. R., "Multimodal Hybrid Powerplant for Unmanned Aerial Systems (UAS) Robotics," Proceedings of the 24th Bristol International Unmanned Air Vehicle Systems Conference, University of Bristol, Bristol, UK, 2009.

[53] Meuller, D. C., "Energy Storage: Strong Momentum in High-End Batteries," Credit Suisse, Suisse, 2007.

[54] Mandal, S. K., Bhojwani, P. S., Mohanty, S. P., and Mahapatra, R. N., "IntellBatt: Towards Smarter Battery Design," Proceedings of the 45th Design Automation Conference (DAC08), pp. 872-877, June 2008.

[55] FuelCellStore, Website http://www.fuelcellstore.com, Accessed on 21 December, 2011.

[56] IEEE Spectrum, Circuit Could Swap Ultracapacitors for Batteries, http://spectrum.ieee.org/semiconductors/ design/circuit-could-swap-ultracapacitors-for-batteries, Accessed on January 5, 2012.

[57] Liu, J., Yang, Z., Zhao, H., and Cheng, G., "Novel Precision Piezoelectric Step Rotary Actuator," Frontiers of Mechanical Engineering in China, Vol. 2, (3), 2007, pp. 356-360.

[58] Spinella, I., Mammano, G., S., and Dragoni, E.,"Conceptual Design and Simulation of a Compact Shape Memory Actuator for Rotary Motion," *Journal of Materials Engineering and Performance*, Vol. 18, (5-6), 2009, pp. 638-648.

[59] McArthur, J., "Aerodynamics of Wings at Low Reynolds Numbers," *Ph.D. Dissertation*, Department of Aerospace and Mechanical Engineering, University of Southern California, 2007.

[60] Schmitz, F. W., "Aerodynamics of Model Aircraft wing Measurements," R.T.P. Translation No 2460. Issued by Ministry of Aircraft Production. 1983.

[61] Abbott, I. H., Von Doenhoff, A. E., and Stivers, J., "Summary of airfoil data," NACA Technical Report 824 (1945).

[62] Riegels, F. W., "Airfoil Sections," Butterworth, London, 1961.

[63] Althaus, D., and Wortmann, F. X., "Stuttgarter profilkatalog I - Experimental Results for the Laminar Wind Tunnel of the University of Stuttgart," Friedr. Vieweg and Sohn, Braunschweig, 1972 (English version in 1981).

[64] MCMasters, J. H., and Henderson, M. L., "Low-Speed Single-Element Airfoil Synthesis," Technical Soaring 4, 2 (1979), pp. 1-21.

[65] Mueller, T. J., and Batill, S. M., "Experimental Studies of Separation on a Two-dimensional Airfoil at Low Reynolds Numbers," AIAA Journal Vol. 20, (4), 1982, pp. 457-463.

[66] Lissaman, P. B. S., "Low-Reynolds-number Airfoils," Annual Review of Fluid Mechanics Vol. 15, 1983, pp. 223-239.

[67] Laitone, E. V., "Wind Tunnel Tests of Wings at Reynolds Numbers Below 70,000," *Experiments in Fluids*, Vol. 23, 1997, pp. 405-409.

[68] Pelletier, A. and Mueller, T. J., "Low Reynolds Number Aerodynamics of Low-Aspect-Ratio, Thin/Flat/Cambered-Plate Wings," *Journal of Aircraft*, Vol. 37, (5), September-October 2000, pp. 825-832.

[69] Thielicke, W., Kesel, A. B., and Stamhuis, E. J., "Vortex-lift Modeling Provides Reliable Force Predictions for Flapping-wing Micro Air Vehi-

cles," International Micro Air Vehicle Conference and Competitions 2011, 't Harde, The Netherlands, September 12-15, 2011.

[70] Lighthill, M. J., "On the Weis-Fogh Mechanism of Lift Generation," *Journal of Fluid Mechanics*, Vol. 60, (1), 1973, pp. 1-17.

[71] Ellington, C. P., Van Den Berg, C., Willmott, A. P., and Thomas, A. L. R., "Leading-edge Vortices in Insect Flight," *Nature*, Vol. 384, 1996, pp. 626-630.

[72] Srygley, R. B., and Thomas, A. L. R., "Unconventional Lift Generating Mechanisms in Free-Flying Butterflies," *Nature*, Vol. 420, 2002, pp. 660-664.

[73] Knoller, R., "Die Gesetze des Luftwiderstandes," *Flug- und Motortechnik (Wien)*, Vol. 3, (21), 1909, pp. 1-7.

[74] Betz, A., "Ein Beitrag zur Erklaerung des Segelfluges," *Zeitschrift fur Flugtechnik und Motorluftschiffahrt*, Vol. 3, 1912, pp. 269-272.

[75] Katzmayer, R., "Effect of Periodic Changes of Angle of Attack on Behavior of Airfoils," NACA TM 147, Oct. 1922.

[76] McCroskey, W.J., "Unsteady Airfoils", *Annual Review Fluid Mechanics*, Vol. 14, 1982, pp. 285-311.

[77] Carr, L., "Progress in Analysis and Prediction of Dynamic Stall," *Journal of Aircraft*, Vol. 25, 1988, pp. 6-17.

[78] Anderson, J. M., Streitlin, K., Barrett, D. S., and Triantafyllou, M. S., "Oscillating Foils of High Propulsive Efficiency," *Journal of Fluid Mechanics*, Vol. 360, 1998, pp. 41-72.

[79] Jones, K. D., Dohring, C. M., and Platzer, M. F., "Experimental and Computational Investigation of the KnollerBetz Effect," *AIAA Journal*, Vol. 36, (7), July 1998, pp. 1240-1246.

[80] Hart, A. and Ukeiley, L., "Low Reynolds Number Unsteady Aerodynamics over a Pitching-Plunging Flat Plate," 48th AIAA Aerospace Sciences Meeting Including the New Horizons Forum and Aerospace Exposition, Orlando, Florida, 4-7 January 2010.

[81] Yuan, W., Lee, R., Hoogkamp, E., and Khalid, M., "Numerical and Experimental Simulations of Flapping Wings," *International Journal of Micro Air Vehicles*, Vol. 2, (3), September 2010, pp. 181-209.

[82] Wang, H., Zeng, L., Liu, H. and Yin, C., "Measuring Wing Kinematics, Flight Trajectory and Body Attitude During Forward Flight and Turning Maneuvers in Dragonflies," *The Journal of Experimental Biology*, Vol. 206, 2003, pp. 745-757.

[83] Tobalske, B. W., Warrick, D. R., Clark, C. J., Powers, D. R., Hedrick, T. L., Hyder, G. A., and Biewener, A. A., "Three-Dimensional Kinematics of Hummingbird Flight," *The Journal of Experimental Biology*, Vol. 210, 2007, pp. 2368-2382.

[84] Liu, T., Kuykendoll, K., Rhew, R., and Jones, S., "Avian Wing Geometry and Kinematics," AIAA Journal, Vol. 44, (5), May 2006, pp. 954-963.

[85] Frampton, K., Goldfarb, M., Monopoli, D., and Cveticanin, D., "Passive Aeroelastic Tailoring for Optimal Flapping Wings," In T.J.Mueller, editor, Fixed and Flapping Wing Aerodynamics for Micro Air Vehicle Applications, Vol. 195, pp. 473-482, New York, 2001. Progress in Astronautics and Aeronautics, AIAA.

[86] Combes, S. A. and Daniel, T. L., "Into Thin Air: Contributions of Aerodynamic and Inertial-elastic Forces to Wing Bending in the Hawkmoth Manduca Sexta," *The Journal of Experimental Biology*, Vol. 206, pp. 2999-3006

[87] Ho, S., Nassef, H., Pornsinsirirak, N., Tai, Y. C., and Ho, C. M., "Unsteady Aerodynamics and Flow Control for Flapping Wing Flyers," *Progress in Aerospace Sciences*, Vol. 39, 2003, pp. 635-681.

[88] Heathcote, S., Wang, Z. and Gursul, I., "Effect of Spanwise Flexibility on Flapping Wing Propulsion," *Journal of Fluids and Structures*, Vol. 24,

(2), February 2008, pp. 183-199.

[89] DeLaurier, J. D., "An Aerodynamic Model for Flapping-Wing Flight," Aeronaut. J. 97(964), pp.125-130, 1993.

[90] Stanford, B. K., and Beran, P. S., "Analytical Sensitivity Analysis of an Unsteady Vortex-Lattice Method for Flapping-Wing Optimization," *Journal of Aircraft*, Vol. 47, (2), March-April 2010, pp. 647-662.

[91] Tuncer, I. H., and Platzer, M. F., "Thrust Generation Due to Airfoil Flapping," *AIAA Journal*, Vol. 34, (2), Feb. 1996, pp. 324-331.

[92] Tuncer, I. H., Walz, R., and Platzer, M. F., "A Computational Study of the Dynamic Stall of a Flapping Airfoil," AIAA Paper 98-2519, June 1998.

[93] Isogai, K., Shinmoto, Y., and Watanabe, Y., "Effects of Dynamic Stall on Propulsive Efficiency and Thrust of Flapping Airfoil," *AIAA Journal*, Vol. 37, (10), Oct. 1999, pp. 1145-1151.

[94] Visbal, M. R., "High-Fidelity Simulation of Transitional Flows past a Plunging Airfoil," *AIAA Journal*, Vol. 47, (11), November 2009, pp. 2685-2697.

[95] Yu M., Wang, J. Z., Hu H.,"High-Fidelity Flapping-Wing Aerodynamics Simulations with a Dynamic Grid Spectral Difference Method," Seventh

International Conference on Computational Fluid Dynamics (ICCFD7), Big Island, Hawaii, July 9-13, 2012.

[96] Lim, S. C., "Computational Investigation of Flapping-Wing Propulsion for a Micro Air Vehicle," Master of Science, Naval Postgraduate School, 2006.

[97] RTO Technical Report, "Unsteady Aerodynamics of Micro Air Vehicles," Final Report of Task Group AVT-149, September 2010.

[98] Tang, J., Viieru, D., and Shyy, W., "A Study of Aerodynamics of Low Reynolds Number Flexible Airfoils," 37th AIAA Fluid Dynamics Conference and Exhibit, Miami, FL, 25 - 28 June 2007.

[99] Liani, E., Guo, S. and Allegri, G., "Aeroelastic Effect on Flapping Wing Performance," 48th AIAA/ASME/ASCE/AHS/ASC Structures, Structural Dynamics, and Materials Conference, Honolulu, Hawaii, 23-26 April 2007.

[100] Willis, D. J., Israeli, E. R., Persson, P., Drela, M., Peraire, J., Swartz, S. M. and Breuer, K. M., "A Computational Framework for Fluid Structure Interaction in Biologically Inspired Flapping Flight," 25th AIAA Applied Aerodynamics Conference, Miami, FL, 25-28 June 2007.

[101] Kima, D, K., Lee, J. S., Lee, J. Y., Han J H.,"An Aeroelastic Anal-

ysis of a Flexible Flapping Wing Using Modified Strip Theory," SPIE 15th Annual Symposium Smart Structures and Materials, 2008, Vol. 6928, 69281O.

[102] Smith, M. J. C. "Simulating Moth Wing Aerodynamics: Towards the Development of Flapping-Wing Technology," *AIAA Journal*, Vol. 34, (7), July 1996, pp. 1348-1355.

[103] Gopalakrishnan, P., Tafti, D. K., "Effect of Wing Flexibility on Lift and Thrust Production in Flapping Flight," *Journal of Aircraft*, Vol. 48, (5), May 2010, pp. 865-877.

[104] Chimakurthi, S. K., Tang, J., Palacios, R., Cesnik, C. E. S., Shyy, W., "Computational Aeroelasticity Framework for Analyzing Flapping Wing Micro Air Vehicles," *AIAA Journal*, Vol. 47, (8), August 2009.

[105] Lakshminarayan, V. K., "Computational Investigation of Micro-Scale Coaxial Rotor Aerodynamics in Hover," *Ph.D. Dissertation*, Department of Aerospace Engineering, University of Maryland at College Park, 2009.

[106] Young, J., and Lai, J. C. S., "Mechanisms Influencing the Efficiency of Oscillating Airfoil Propulsion," *AIAA Journal*, Vol. 45, (7), July 2007, pp. 1695-1702.

[107] Lakshminarayan, V. K., and Baeder, J. D., "Computational Investiga-

tion of Micro Hovering Rotor Aerodynamics," *Journal of the American Helicopter Society*, Vol. 55, (2), April 2010.

[108] Lakshminarayan, V. K., and Baeder, J. D., "Computational Investigation of Micro-Scale Coaxial Rotor Aerodynamics in Hover," *Journal of Aircraft*, Vol. 47, (3), June 2010, pp. 940-955.

[109] Pulliam, T., and Chaussee, D., "A Diagonal Form of an Implicit Approximate Factorization Algorithm," *Journal of Computational Physics*, Vol. 39, (2), February 1981, pp. 347-363.

[110] Buelow P. E. O., Schwer D. A., Feng J., and Merkle C. L., "A Preconditioned Dual-Time, Diagonalized ADI scheme for Unsteady Computations," 13th AIAA Computational Fluid Dynamics Conference, Snowmass Village, CO, June 29-July 2, 1997.

[111] Pandya, S. A., Venkateswaran, S., and Pulliam, T. H., "Implementation of Preconditioned Dual-Time Procedures in OVERFLOW," 41st AIAA Aerospace Sciences Meeting and Exhibit, Reno, NV, January 6-9, 2003.

[112] Spalart, P.R., and Allmaras, S.R., "A One-equation Turbulence Model for Aerodynamic Flows," 30th AIAA Aerospace Sciences Meeting and Exhibit, Reno, NV, January 6-9, 1992.

[113] Lee, Y. "On Overset Grid Connectivity and Automated Vortex Tracking

in Rotorcraft," *Ph.D Dissertation*, Department of Aerospace Engineering, University of Maryland at College Park, 2008.

[114] Jeong, J. and Hussain, F., "On the Identification of a Vortex," *Journal of Fluid Mechanics*, Vol. 285, 1995, pp. 69-94.

[115] Wu, P., Ifju P., Stanford B., "Flapping Wing Structural Deformation and Thrust Correlation Study with Flexible Membrane Wings," *AIAA Journal*, Vol. 48, (9), Sept. 2010, pp. 2111–2122.

[116] P. Masarati, M. Morandini, G. Quaranta, D. Chandar, B. Roget and J. Sitaraman, "Tightly Coupled CFD/Multibody Analysis of Flapping-Wing MAV," 41st AIAA Fluid Dynamics Conference, 2011, Honolulu, Hawaii, USA.

[117] Lakshminarayan, V. K., Baeder and J. D., "Computational Investigation of Micro Hovering Rotor Aerodynamics," *Journal of the American Helicopter Society*, Vol. 55, (2), April 2010.

[118] Lakshminarayan, V. K. and Baeder, J. D., "Computational Investigation of Micro-Scale Coaxial Rotor Aerodynamics in Hover," *Journal of Aircraft*, Vol. 47, (3), June 2010, pp. 940-955.

[119] Malhan, R., Lakshminarayan, V., Baeder, J. and Chopra, I., "Investigation of Aerodynamics of Rigid Flapping Wings for MAV Applications:

CFD Validation," American Helicopter Society Specialists Conference on Unmanned Rotorcraft and Network Centric Operations, Tempe, Az, Jan 2011.

[120] Pulliam, T. and Chaussee, D., "A Diagonal Form of an Implicit Approximate Factorization Algorithm," *Journal of Computational Physics*, Vol. 39, (2), February 1981, pp. 347-363.

[121] Buelow P. E. O., Schwer D. A., Feng J. and Merkle C. L., "A Preconditioned Dual-Time, Diagonalized ADI scheme for Unsteady Computations," 13th AIAA Computational Fluid Dynamics Conference, Snowmass Village, CO, July 1997.

[122] Pandya, S. A., Venkateswaran, S. and Pulliam, T. H., "Implementation of Preconditioned Dual-Time Procedures in OVERFLOW," 41st AIAA Aerospace Sciences Meeting and Exhibit, Reno, NV, January 2003.

[123] Spalart, P. R. and Allmaras, S. R., "A One-equation Turbulence Model for Aerodynamic Flows," 30th AIAA Aerospace Sciences Meeting and Exhibit, Reno, NV, January 1992.

[124] Lee, Y., "On Overset Grid Connectivity and Automated Vortex Tracking in Rotorcraft," *Ph.D Dissertation*, Department of Aerospace Engineering, University of Maryland at College Park, 2008.

[125] Masarati, P. and Sitaraman, J., "Tightly Coupled CFD/Multibody Analysis of NREL Unsteady Aerodynamic Experiment Phase VI Rotor," 49th AIAA Aerospace Sciences Meeting, Orlando, Florida, January 2011.

[126] Baron, A., Boffadossi, M., and De Ponte, S., "Numerical Simulation of Vortex Flows Past Impulsively Started Wings," AGARD-CP-494 Vortex Flow Aerodynamics, 1990, pp. 33/1-33/14.

[127] Ghiringhelli, G., L., Masarati, P. and Mantegazza, P., "A Multi-Body Implementation of Finite Volume Beams," *AIAA Journal*, Vol. 38, (1), January 2000, pp. 131-138.

[128] Farhat, C. and Lesoinne, M., "Two Efficient Staggered Algorithms for the Serial and Parallel Solution of Three-dimensional Nonlinear Transient Aeroelastic Problems," Computer Methods in Applied Mechanics and Engineering, 182:499-515, 2000.

[129] Quaranta, G., Masarati, P. and Mantegazza, P., "A Conservative Mesh-Free Approach for Fluid Structure Interface Problems," Coupled Problems, Santorini, Greece, May 2005.

[130] Barth, T. J., Puliam, T. H., and Buning P. G., "Navier-Stokes Computations for Exotic Airfoils," 23rd AIAA Aerospace Sciences Meeting, Reno, NV, January 1985.

[131] Duraisamy, K., "Studies in Tip Vortex Formation, Evolution and Control," *Ph.D. Dissertation*, Department of Aerospace Engineering, University of Maryland at College Park, 2005.

[132] Baldwin, B. S. and Lomax, H., "Thin Layer Approximation and Algebraic Model for Separated Turbulent Flows," AIAA Paper 78-257, 1978.

[133] Spalart, P. R. and Allmaras, S. R., "A One-equation Turbulence Model for Aerodynamic Flows," 30th AIAA Aerospace Sciences Meeting and Exhibit, Reno, NV, Jan. 1992.

[134] Van Leer, B., "Towards the Ultimate Conservative Difference Scheme V. A Second-Order Sequel To Godunov's Method," *Journal of Computational Physics*, Vol. 135, (2), August 1997, pp. 229-248.

[135] Roe, P., "Approximate Riemann Solvers, Parameter Vectors and Difference Schemes," *Journal of Computational Physics*, Vol. 135, (2), August 1997, pp. 250-258.

[136] Turkel, E., "Preconditioning Techniques in Computational Fluid Dynamics," *Annual Review of Fluid Mechanics*, Vol. 31, 1999, pp. 385-416.

[137] Jameson, A., "Time Dependent Calculations Using Multigrid, with Applications to Unsteady Flows Past Airfoils and Wings," AIAA Paper 91-1596, 199

[138] Hirsch, C., "Numerical Computation of Internal and External Flows," Vol. 2, Wiley Publishers, 1990.

[139] Yang, K., "Aerodynamic Analysis of an MAV Scale Cycloidal Rotor System Using a Structured OVERSET RANS Solver," M.S. Thesis, Department of Aerospace Engineering, University of Maryland at College Park, 2010.

[140] Mueller, T. J., "Fixed and Flapping Wing Aerodynamics for Micro Air Vehicle Applications," Danvers, Massachusetts, 2001, Vol. 195.

[141] Ghiringhelli, G. L., Masarati, P., and Mantegazza, P.,"A Multi-Body Implementation of Finite Volume Beams," *AIAA Journal*, Vol. 38 (1), January 2000, pp. 131-138.

[142] Chandar D., and Damodaran, M.,"Computational Study of the Free Flight of a Flapping Wing at Low Reynolds Numbers," 46th AIAA Aerospace Sciences Meeting, Reno, Nevada, January 7-10, 2008.

[143] Chimakurthi, S. K., Stanford, B. K., Cesnik, C. E. S., and Shyy, W., "Flapping wing CFD/CSD aeroelastic formulation based on a Co-rotational Shell Finite Element," 50th SDM Conference, Palm Springs, California, May 47 2009.

[144] Masarati, P., Morandini, M., and Vescovini, R., "A 4-Node Shell Ele-

ment for Multibody Analysis of Flapping Wing Micro-Aerial Vehicles," Brussels, Belgium, July 2011.

[145] Brenan, K. E., Campbell, S. L., and Petzold, L. R., "Numerical Solution of Initial-Value Problems in Differential-Algebraic Equations," North-Holland, New York, 1989, pp. 17-39.

[146] Borri, M., and Merlini, T., "A Large Displacement Formulation for Anisotropic Beam Analysis," *Meccanica*, Vol. 21, (1), 1986, pp. 30-37.

[147] Witkowski, W., "4-node Combined Shell Element with Semi-EAS-ANS Strain Interpolations in 6-parameter Shell Theories with Drilling Degrees of Freedom," *Computational Mechanics*, Vol. 43, (2), 2009, pp. 307-319.

[148] Merlini, T and Morandini, M., "The helicoidal Modeling in Computational Finite Elasticity. Part I: Variational Formulation," *International Journal of Solids and Structures*, Vol. 41 (1819), September 2004, pp. 5351-5381.

[149] Pietraszkiewicz, W and Eremeyev, V., A., "On Natural Strain Measures of the Non-linear Micropolar Continuum," *International Journal of Solids and Structures*, Vol. 46, (34), February 2009, pp. 774-787.

[150] Chroscielewski J., and Witkowski, W., "Four-node Semi-EAS Element in Six-Field Nonlinear Theory of Shells," *International Journal for Nu-*

merical Methods in Engineering, Vol. 68 (11), 2006, pp. 1137-1179.

[151] Merlini, T., and Morandini, M., "The Helicoidal Modeling in Computational Finite Elasticity. Part II: Multiplicative Interpolation," *International Journal of Solids and Structures*," Vol. 42, p. 1269 (2005).

[152] Masarati, P. and Ghiringhelli, G., L., "Characterization of Anisotropic, Non-homogeneous Plates with Piezoelectric Inclusions," *Computers and Structures*, Vol. 83 (15-16), June 2005, pp. 1171-1190.

[153] Masarati, P., Morandini, M., Quaranta, G. and Vescovini, R., "Multibody Analysis of a Micro-Aerial Vehicle Flapping Wing," Multibody Dynamics, edited by Samin J. C., and Fisette, P., Brussels, Belgium, July 2011.

[154] Beasley, B., and Chopra, I., "Planar and Nonplanar Membrane Wing Planform for the Design of a Flapping-Wing Micro Air Vehicle," American Helicopter Society 62nd Annual Forum Proceedings, Phoenix, AZ, May 2006.

[155] Khan, A., and Agrawal, S., "Force and Moment Characterization of Flapping Wings for Micro Air Vehicle Application," Proceedings of the 2005 American Control Conference, Portland, OR, June 8-10, 2005.

[156] Vest, M., and Katz, J., "Aerodynamic Study of a Flapping Wing Micro-

UAV," 37th AIAA Aerospace Sciences Meeting and Exhibit, Reno, NV, January 11-14, 1999.

[157] Mueller, D., Bruck, H. A., and Gupta, S. K., "Measurement of Thrust and Lift forces Associated with Drag of Compliant Flapping Wing for Micro Air Vehicles using a New Test Stand Design," *Journal of Experimental Mechanics*, Vol. 50, (6), July 2009, pp. 725-735.

[158] Website http://www.berkeley.edu/news/media/releases/99legacy/6-15-1999pix.html, Accessed on April 5, 2012.

[159] Demasi, L., Gordnier, R. E., Santarpia, E., Dipace, A., "High-Fidelity Simulations of a Flexible Flapping Wing in Forward Flight," 54th AIAA/ASME/ASCE/AHS/ASC Structures, Structural Dynamics, and Materials Conference, Boston, Massachusetts, April 8-11, 2013.